MOLECULAR DYNAMICS SIMULATIONS OF LIPID MEMBRANES: THE EFFECTS OF PROBES, LIPID COMPOSITION AND PEPTIDES

A Dissertation

Presented to the Faculty of the Graduate School

of Cornell University

In Partial Fulfillment of the Requirements for the Degree of

Doctor of Philosophy

by

David Geoffrey Ackerman

August 2015

MOLECULAR DYNAMICS SIMULATIONS OF LIPID MEMBRANES: THE EFFECTS OF PROBES, LIPID COMPOSITION AND PEPTIDES

David Geoffrey Ackerman, Ph.D.

Cornell University 2015

The cell plasma membrane is comprised of hundreds of different lipid species as well as a variety of integral and peripheral proteins. The diversity of molecular constituents leads to the formation of functional lateral heterogeneities within the plane of the membrane, known as lipid rafts, which are distinct from the surrounding membrane. Given the complexity of the plasma membrane, and the importance of rafts in the life of a cell, simplified model mixtures capturing the characteristics of the plasma membrane have been essential for unraveling its underlying behavior. In this work, we use molecular dynamics simulations to study model membranes at resolutions not possible with experimental techniques.

We first investigated a fundamental assumption in model membrane experiments: that extrinsic probes added to the membrane do not disrupt membrane behavior. We addressed this issue by simulating single component model membranes that contained commonly used fluorescent lipid analogs. We found that the probes are able to disorder the bilayer and reorient lipid headgroups due to the probes' large, positively charged headgroups and long, interdigitating acyl chains. Importantly though, these effects die off within a couple of nanometers of the probe. This means that the probes do not disrupt large-scale membrane behavior and can effectively be used for experimental membrane studies. However, the short-ranged perturbations also indicate that probes may provide incorrect information if they report directly on their local, disrupted, environment.

Next, we studied the behavior of more complex model membranes containing multiple lipid species. Experimentally, model membranes comprised of four lipid components can yield coexisting phases, mimicking raft and non-raft environments, ranging in size from nanometers to microns. Through simulations, we found that domain size and alignment are highly coupled and that they both change abruptly at certain lipid compositions. We also found that the phase interface between domains was only a couple of nanometers wide regardless of the properties of the two coexisting phases. Addition of transmembrane α-helical peptides of various lengths to the lipid-only mixtures significantly increased both domain size and alignment. These effects were largest for the shortest peptides and increased with peptide concentration. Thus cells may be able to control raft size and alignment, and in turn a variety of cellular processes, simply by altering lipid and protein concentrations.

BIOGRAPHICAL SKETCH

David Ackerman grew up on the south side of the tracks in Westfield, New Jersey. He persevered in a childhood without cable, often finding solace in public broadcasting and a variety of science and nature shows. Thanks to parents who never grew frustrated of his non-stop questions, and instead fed his curiosity with science articles and toys, David continued to find joy in science. Though set on pursuing a scientific education, in typical lazy David fashion, he did not enjoy putting in effort to actively seek out undergraduate institutions. Due to a suggestion by his father, David applied to and joined Northwestern University's interdisciplinary Integrated Science Program in 2006.

At Northwestern, David majored in integrated sciences, physics and math. Outside of classes, David performed theoretical research on extrasolar planets for Professor Fred Rasio. When it came time for graduate school, David decided to apply to institutions where he could use his broad scientific background to study problems at the boundaries between fields.

David joined the Ph.D. program in Biophysics at Cornell University in 2010. He was interested in performing simulations, so logically he joined a predominantly experimental lab in a field in which he had no experience: Professor Gerald Feigenson's membrane physical chemistry lab. As a member of Jerry's lab, David has enjoyed performing research which links simulations to experiments. He hopes to continue using similar research methodologies in his next career, whenever and wherever that might be.

To My Parents

ACKNOWLEDGMENTS

I would first like to thank my advisor Dr. Gerald Feigenson. Jerry is a constant source of knowledge and advice, and is invested in every project going on in the lab. His scientific integrity, passion and dedication are both inspirational and infectious. These traits, along with his willingness to let me pursue molecular dynamics even though neither he nor I had any experience with them, convinced me to join his lab. Throughout my 5 years at Cornell, he has been encouraging throughout my various projects spanning from simulations to experiments. It has been a real joy to work in his lab.

Lab members past and present have also provided unique points of view which have benefited my work. These close friends and labmates include Dr. Fred Heberle, Dr. Lynda Goh, Dr. Robin Smith Petruzielo, (Fighting Mongeese Teammate) Dr. Jon Amazon, Dr. Tatyana Konyakhina, Milka Doktorova, Michael Weiner, Rebecca Simpson, Yi Wen, Dr. Kai Yang and the undergraduates Sanjula Wickramsinghe, Nimit Sohoni and Mary Kim.

Additionally, I would like to thank my committee members Dr. John Brady and Dr. Warren Zipfel who provided guidance during my dissertation work and who took the time to attend my presentations and read my thesis.

Importantly, my time in Ithaca has been made exponentially better by the friendships I have made here. Huimin Chen, Avtar Singh, Joshua Tokuda, Stella Li, Vinh Le, Jeahoo Kwon, Digbijay Mahat and Rupa Shah Mahat have put up with my annoying questions and stupid get rich quick schemes and have shown me how creativity, fun, a sense of adventure, and stupidity can thrive well into adulthood. Huimin has been an especially supportive, helpful, encouraging, adventurous, informative and important person during my years at Cornell.

Finally I would like to thank my family. My parents, Susan (aka Suebert) and Louis (aka Loubert), have been extremely caring and supportive throughout my life and always make sure I am prepared for what comes next, including making sure I always have my phone charger. My sisters Rachel and Sara have been successful in their very different careers and hobbies showing me what it takes to be successful when venturing out on my own. And of course my niece Esme, who always provides advice, whether it is in English, French or our own private language.

Though research is often a somewhat independent endeavor, all these people have been essential to the successful completion of my dissertation. And for that, I am extremely grateful.

TABLE OF CONTENTS

LIST OF FIGURES

LIST OF TABLES

LIST OF ABBREVIATONS

CG	coarse-grained
DiI-C12:0	1,1′-didodecyl-3,3,3′,3′-tetramethylindocarbocyanine perchlorate (12:0, 12:0 chains)
DiI-C18:0	1,1′-dioctadecyl-3,3,3′,3′-tetramethylindocarbocyanine perchlorate (18:0, 18:0 chains)
DiI-C18:2	1,1′-dilinoleyl-3,3,3′,3′-tetramethylindocarbocyanine perchlorate (18:2, 18:2 chains)
DOPC	dioleoyl-phosphatidylcholine (18:1, 18:1 chains)
DPPC	dipalmitoyl-phosphatidylcholine (16:0, 16:0 chains)
DSPC	distearoyl-phosphatidylcholine (18:0, 18:0 chains)
DUPC	dilinoleoyl-phosphatidylcholine (18:2, 18:2 chains)
ESR	electron spin resonance
FRET	fluorescence resonance energy transfer
GPI	glycosylphosphatidylinositol
GUV	giant unilamellar vesicle
Lβ	lamellar gel
Ld	liquid disordered
Lo	liquid ordered
MD	molecular dynamics
NMR	nuclear magnetic resonance
PC	phosphatidylcholine
PE	phosphatidylethanolamine
PI	phosphatidylinositol
PME	particle-mesh ewald
POPC	palmitoyl,oleoyl-phosphatidylcholine (16:0, 18:1 chains)
PS	phosphatidylserine
PUPC	palmitoyl,linoleoyl-phosphatidylcholine (16:0, 18:2 chains)
SANS	small-angle neutron scattering
Tm	melting temperature
UA	united atom

CHAPTER 1
Introduction

1.1 Overview

Fundamental lipid bilayer physical chemistry provides a wealth of interesting phenomena to study. The bilayer itself is a pseudo two-dimensional material which exhibits complex phase behavior, existing as solids, liquids, or some combination of phases. The properties and phase(s) of the bilayer can be controlled both by temperature and lipid composition. Though bilayers are predominantly lipids, they can contain a variety of other molecules, including proteins, which affect and are affected by the underlying lipid-only behavior. Alone, the diversity of even simple bilayer mixtures makes them a particularly intriguing topic. Yet there is also a practical component driving fundamental membrane research: the nature of the cell plasma membrane. The plasma membrane is a lipid bilayer with hundreds of lipid and protein species that interact to form functional heterogeneities, or "rafts", within the plane of the bilayer, similar to the coexisting phases of simple lipid bilayers. How exactly these rafts are manipulated and used by the cell is not yet known. Experiments both *in vivo* and *in vitro* have been invaluable for increasing our understanding of raft behavior by revealing the properties of a plethora of membrane systems, generally on the scale of several nanometers to many microns. Molecular dynamics simulations of lipid bilayers go beyond the capabilities of experiments and provide information on smaller, otherwise inaccessible size-scales. In this work, we used molecular dynamics simulations to study lipid bilayer behavior at a near-atomistic level to better understand membrane phase behavior and its relation to rafts.

This chapter lays the general framework of membrane research which motivates the molecular dynamics studies in the remaining chapters. We start by reviewing lipid bilayer phases. Next, we describe the characteristics of cell plasma membranes and rafts. We then

discuss the utility of simplified membrane systems in modeling plasma membrane behavior. This is followed by a description of molecular dynamics. Finally, we outline the research reported in the remainder of this work.

1.2 Lipid bilayer phases

Bilayer-forming phospholipids, such as glycerolipids and sphingolipids, frequently have two hydrophobic acyl chains and a hydrophilic headgroup. In aqueous solutions, the amphiphilic nature of these lipids can drive them to form bilayers with their tails in the hydrophobic interior, shielded from water by the headgroups at the bilayer/water interface. Some lipid species, such as cholesterol, that do not form bilayers on their own can still exist as bilayers when mixed with bilayer-forming lipids.

Lipid bilayers can generally exist in three distinct thermodynamic phases: a solid gel phase (Lβ), and two liquid phases (liquid-disordered: Ld, and liquid-ordered: Lo) (Figure 1.1*A*). While the Lβ and Ld phases can form in bilayers containing just one type of phospholipid, the Lo phase requires a phospholipid and cholesterol. In addition to compositional requirements, the three bilayer phases are distinguished by long-range positional order, diffusion coefficients, and lipid acyl chain order. Here, chain order corresponds to how straight the chains are with respect to the bilayer normal: higher order means straighter acyl chains aligned with the bilayer normal, and lower order means more kinked acyl chains. The Lβ phase, being a typical solid, has long-range positional order, slow diffusion and high chain order (1). The Ld and Lo phases both have the characteristic liquid properties of fast diffusion and low positional order (1). However, while the Ld phase has low acyl chain order, the Lo phase has high acyl chain order comparable to the gel (1).

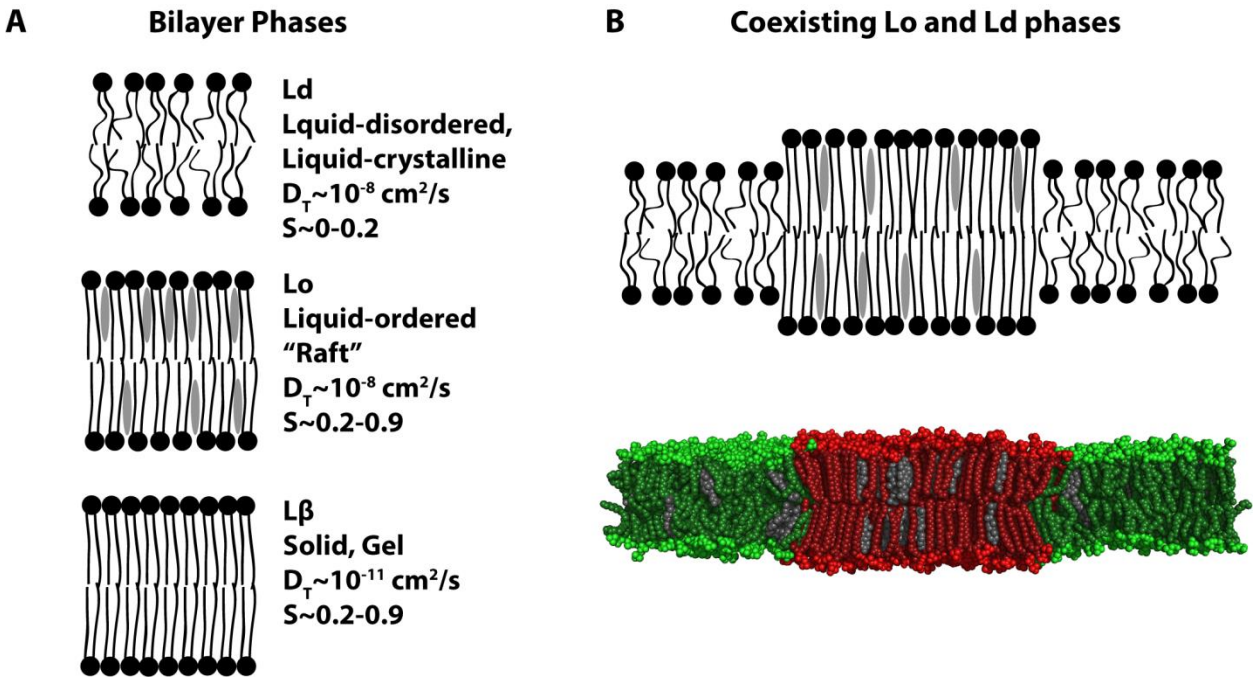

Figure 1.1 Lipid bilayer phases and phase coexistence. A) The three main phases found in lipid bilayers are the Ld phase, the Lo phase and the Lβ phase, differentiated by the presence of cholesterol (gray), long range positional order, diffusion (D_T) and acyl chain order (S). B) (top) Schematic of coexisting Lo and Ld phases, and (bottom) simulation snapshot of coexisting Lo and Ld phases for a ternary mixture of the low-Tm lipid dioleoylphosphatidylcholine (green), the high-Tm lipid distearoylphosphatidylcholine (red) and cholesterol (gray). Adapted from (2).

Transitioning between the different bilayer phases can be achieved by changes in temperature or lipid composition. For simplicity, we discuss these transitions using the minimum number of required components, but note that each phase can contain an unlimited number of unique molecular species. When a single component phospholipid bilayer is above the lipid's melting temperature (Tm), it exists in the Ld phase. When the bilayer is below the Tm, it solidifies and exists in the Lβ phase. Addition of cholesterol to the Lβ phase can then produce the Lo phase. This can be understood in terms of the largely hydrophobic nature of cholesterol (3). At low cholesterol fractions the bilayer remains in the Lβ phase since the small lipid area associated with high Lβ chain order means that hydrophilic lipid headgroups are freed up to shield small amounts of nearby cholesterol from water. At higher cholesterol concentrations, the cholesterol does not pack well in the highly structured Lβ phase. This has a fluidizing effect on the bilayer and leads to coexistence of Lβ and Lo, where both phases have the high chain order required for shielding, but the less structured Lo phase is able to accommodate more cholesterol than the Lβ phase. As the fraction of cholesterol increases, the amount of Lβ decreases until only the Lo phase remains. The Lo phase can accommodate large (> 50 mol%) cholesterol fractions until shielding is no longer possible; at this point cholesterol crystals precipitate out (3).

Generally, lipids with longer, saturated chains have higher Tms than lipids with shorter, unsaturated chains. Coexistence of phases is also possible (Figure 1.1*B*), and in particular Lo + Ld coexistence may underlie functional heterogeneities, known as lipid rafts, within the cell plasma membrane (4, 5).

1.2 The cell plasma membrane

1.2.1 Plasma membrane composition

The plasma membrane acts as a boundary between the internal cellular environment and the external world. Though a seemingly simple and passive task, the plasma membrane turns out to be a complex environment that fulfills a variety of additional cellular functions. The functionality of the plasma membrane is in part made possible by its diversity of lipid species, of which there are ~ 180,000 possible types based on the number of different lipid tails, linkages and headgroups (6). Determining the exact composition of the plasma membrane is non-trivial since separating the plasma membrane from other cellular membranes is difficult. Thus, the human erythrocyte, whose only membrane is the plasma membrane, has greatly aided in determining plasma membrane composition (7). Still, the vast amount of different lipid types requires simplified classification schemes for studies to be of any practical use.

To make the plasma membrane composition more comprehensible, a common technique is to group the different lipid species based on common characteristics. Some of the largest groups of lipids in the eukaryotic cell plasma membrane include cholesterol, sphingolipids, and glycerolipids with the headgroups phosphatidylcholine (PC), phosphatidylserine (PS), phosphatidylinositol (PI), or phosphatidylethanolamine (PE). All cellular membranes contain large fractions of glycerolipids, but compared to other cellular membranes, the plasma membrane also has a large fraction of cholesterol and sphingolipid, with a ratio of glycerolipid/sphingolipid/cholesterol ~ 0.4/0.1/0.5 (1). The glycerolipid headgroups are not equally represented in the plasma membrane, and in decreasing order of concentration are: PC, PE, PS and PI. Chains also vary between the lipid types; glycerolipids often have one saturated

chain and one chain with a *cis* unsaturation, and sphingolipids have chains that are either saturated or contain *trans* unsaturations (1).

Further heterogeneity of the plasma membrane appears on the level of individual bilayer leaflets. The extracellular leaflet of the plasma membrane is enriched in PC and sphingomyelin, while the cytoplasmic leaflet is enriched in PE and PS. Specifically, the extracellular leaflet contains 76% of all membrane PC and 82% of all membrane sphingomyelin, and the cytoplasmic leaflet contains 80% of the membrane PE and all of the membrane PS (7). To maintain the asymmetry, proteins within the bilayer actively flip lipids between the extracellular and cytoplasmic leaflets (7, 8).

It is important to note that while the membrane is thought of as a predominantly lipid bilayer, proteins such as those that maintain lipid asymmetry, comprise a large fraction of the bilayer. By mass, membrane proteins make up ~ 50% of the plasma membrane (9). However, since only small portions of the membrane proteins are integral membrane domains, about ~ 15-20% of the bilayer interior is actually protein by volume (9, 10). As we shall see later, proteins play a large role in the behavior and functionality of the cell plasma membrane.

1.2.2 Lateral membrane heterogeneity

The early 1970s saw the popularization of the so-called fluid mosaic model of the plasma membrane, where lipids formed a passive and homogenous fluid sea in which proteins function and interact (11). This seemed to discount the vast complexity of membrane lipid types. As time progressed, the important role of the lipidome in plasma membrane functionality became more evident. Spanning the scale of microns to nanometers, the cell plasma membrane was shown to be both compositionally and functionally more heterogeneous than suggested by the fluid mosaic model.

Some of the first evidence of lateral plasma membrane compositional heterogeneity came from mammalian epithelial cells. Epithelial cells are asymmetric with a rippled apical end facing the external environment and a smoother basolateral end facing the internal environment (12). The compositions of the two ends are distinct, with the phospholipid/glycosphingolipid/ cholesterol composition of the apical and basolateral ends equal to 0.33/0.33/0.33 and 0.5/0.2/0.3, respectively (13). Tight junctions between epithelial cells act as barriers between the apical and basolateral ends, inhibiting diffusion of molecules and maintaining the compositional polarity (14). While the tight junctions helped to explain how large scale heterogeneity was maintained, they did not explain how the heterogeneity arose. This led to the hypothesis that much smaller lateral heterogeneities must be present at the level of membrane trafficking, namely in the golgi (13). These small scale heterogeneities would be driven by lipid-lipid interactions (15), resulting in the clustering of glycosphingolipids and glycosphingolipid-associated proteins (13). The glycosphingolipid-enriched environments would then be targeted to the apical plasma membrane of epithelial cells, and the remaining glycerolipid-enriched regions of the golgi would be targeted to the basolateral plasma membrane (13). Seeming to confirm the hypothesis of nanoscale heterogeneities, experiments revealed that the golgi and apical plasma membrane of epithelial cells contained detergent-resistant membranes enriched in glycosphingolipid, cholesterol and glycosyl-PI (GPI)-anchored proteins (16). Though detergent-resistant membrane experiments could be plagued by artifacts dependent on experimental conditions (17), the existence of small-scale sphingolipid/cholesterol-rich heterogeneities has been repeatedly proven using other techniques (5). The role of these heterogeneities in cell functionality has been a driving force in the field of plasma membrane research since the late 1990s.

1.2.3 Lipid rafts

The small scale lateral heterogeneities detected in epithelial cells helped to inspire the popular lipid raft hypothesis: nanodomains of sphingolipid, cholesterol and sphingolipid-associated proteins exist in the cell plasma membrane, and they play an active role in a variety of membrane functions (18). Given their size, rafts would be below the optical resolution of conventional microscopy. However, techniques more sensitive to small size-scales and time-scales make measurements of raft properties possible.

Initially, rafts were thought of as small, stable, Lo-like diffusing patches of sphingolipid and cholesterol within an Ld-like sea enriched in glycerolipids (18, 19). Coexistence of Lo-like and Ld-like order within the membrane was confirmed with electron spin resonance (ESR) (20), and the submicron size of rafts was confirmed with fluorescence resonance energy transfer (FRET) (21), single particle tracking (22), super resolution optical microscopy (23), fluorescence correlation spectroscopy (24) and electron microscopy (25), with current evidence suggesting rafts are on the order of 10 nm (26). Conversely, the stability of rafts was disproven with FRET, single-particle tracking and ESR, which showed that raft lifetimes must be shorter than 100 μs in order to be consistent with experimental findings (19). How then can these spatially and temporally ephemeral entities exert any influence on the behavior of the cell plasma membrane?

The current model of lipid rafts involves lipid- or protein-induced clustering and stabilization of smaller-scale transient heterogeneities into larger-scale, stable, functional environments (5, 19) (Figure 1.2). In this model, sphingolipids, cholesterol and associated proteins are constantly forming transient clusters within the plasma membrane (5, 19). The clusters coalesce and are stabilized by activation events which enhance the interactions of raft molecules, such as by protein oligomerization or crosslinking of raft lipids by raft-associated

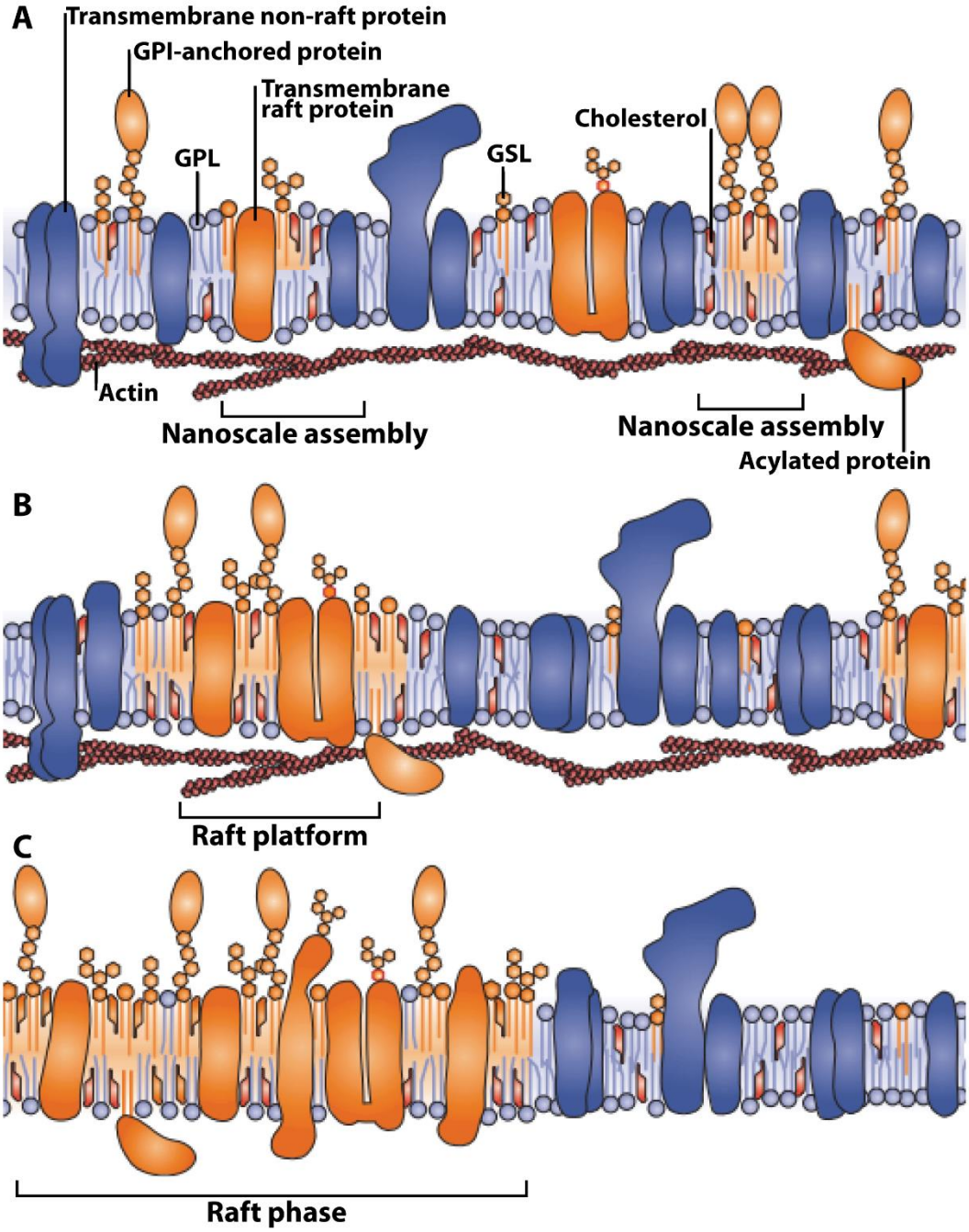

Figure 1.2 Current state of the raft hypothesis. A) Transient nanoscale heterogeneities enriched in sphingolipids and cholesterol exist within the plasma membrane. Abbreviations: glycerophospholipids (GPL), glycosphingolipids (GSL), glycosyl-phosphatidylinositol (GPI). B) Activation, for example by protein-induced crosslinking, can induce the formation of larger-scale, more stable raft platforms with distinct lipid and protein compositions. C) Separating the membrane from the actin cytoskeleton results in large-scale phase separation. Image taken from (17).

proteins (5, 19, 27). The functional rafts remain nanoscopic, in part because interactions with the cytoskeleton prevent large-scale diffusion, equilibration and phase separation of lipids (27–29). One of the key pieces of evidence supporting this model of raft formation and stabilization comes from experiments involving plasma membranes separated from the cytoskeleton. In these plasma membrane spheres, crosslinking by proteins induces the formation of micron-sized patches of lipid and protein with distinct properties and compositions (30). Additional support of the model comes from the fact that rafts can be destabilized by cholesterol depletion (25, 31). Together, these results emphasize the importance of lipid and protein composition on the formation of rafts.

The existence of stable sphingomyelin- and cholesterol-rich rafts within the plasma membrane is inherently tied to the vast array of functions the cell performs. At a basic level, the unique environments of the raft and non-raft regions means that proteins and other molecules can preferentially partition into one region over another. Thus, simply the existence of rafts provides a means to control molecular interactions by forcing partitioning-based segregation or aggregation of different molecules, which plays a key role during immune cell signaling (5, 32) and neurotransmitter signaling (33). Rafts and raft-associated proteins are also thought to be involved in reconstruction of the cell membrane via exocytosis, fusion (34) and endocytosis (35), which may affect membrane trafficking, vesicle generation and viral entry and exit (34–38). Evidently, the plasma membrane is more complex and dynamic than the fluid-mosaic model would suggest.

Based on the diverse roles that rafts play in the life of a cell, the fact that the plasma membrane composition seems tuned to allow for raft formation is likely not an accident of evolution. But if it is not a coincidence, how can the cell possibly finely control the composition

of thousands of different lipid components to perform its tasks? To better understand the formation and control of lipid rafts in the plasma membrane, scientists have turned to model membranes which capture much of the complexity of the plasma membrane behavior while using a select few representative lipid types.

1.3 Model membranes

1.3.1 Model membrane components

The vast array of different lipids in the eukaryotic cell plasma membrane can be grouped into three main categories. The first category are lipids which melt at higher temperatures than the cellular environment (high-Tm lipids), and they include saturated sphingolipids and glycerolipids. The second category are lipids which melt at lower temperatures than the cellular environment (low-Tm lipids), which are most frequently the unsaturated glycerolipids. The third category is cholesterol. Model membranes containing mixtures of these three components can lead to a wide array of phase properties and phase coexistence. Importantly, ternary mixtures can give rise to coexistence of an Lo phase (enriched in saturated lipids and cholesterol) and an Ld phase (enriched in unsaturated lipids), which respectively model the raft and non-raft regions within the cell plasma membrane (4, 39, 40).

However unlike the cell plasma membrane which has asymmetric leaflet compositions, most model membranes are symmetric. Methods for producing asymmetric membranes do exist (41, 42), but they are often more difficult than creating symmetric membranes. Furthermore, the phase coexistence that mimics raft behavior is ubiquitous in outer-leaflet membrane model membranes (enriched in cholesterol and saturated and unsaturated PCs and sphingolipids) (43), whereas inner leaflet model membranes (enriched in cholesterol and unsaturated PE and PS) do not exhibit similar Lo + Ld phase coexistence (1, 44). While raft-dependent coupling of

asymmetric leaflets seems likely *in vivo* (39, 45), and asymmetric model membrane studies have been aimed at investigating that possibility *in vitro* (46, 47), by far the most popular form of model membrane experiments involve outer leaflet model mixtures. These will be discussed in the following sections, with a key focus placed on the biologically relevant coexistence of Lo and Ld domains.

1.3.2 Ternary lipid mixtures

Ternary lipid mixtures of a high-Tm lipid (such as distearoyl-PC (DSPC) or sphingomyelin), a low-Tm lipid (such as palmitoyl,oleoyl-PC (POPC) or dioleoyl-PC (DOPC)) and cholesterol often have similar phase diagrams. A model phase diagram is shown in Figure 1.3, which does not correspond to any particular phase diagram, but instead captures the essential features from a broad range of ternary mixtures (48). The left axis of the phase diagram is the mole fraction of the low-Tm lipid, the right axis is the mole fraction of cholesterol and the bottom axis is the mole fraction of the high-Tm lipid. Each axis then corresponds to a binary mixture, and each corner corresponds to a single component system. The ternary composition of any other point in the phase diagram can be found by connecting it to the three axes, following the gridlines shown; as an example, the star in the phase diagram has a composition of high-Tm lipid/low-Tm lipid/cholesterol = 0.2/0.4/0.4. First-order phase transition boundaries are shown by thick black lines. In the two phase regions, compositions of coexisting phases are connected by tielines (thin black lines); a system within this region will phase separate into phases having compositions equal to the endpoints of the corresponding tieline. We now describe some of the key features of these ternary mixtures.

On the left hand side of the phase diagram, and following Arrow 1, the membrane exists in the Ld phase. This makes sense since the low-Tm lipid is above its melting temperature and so

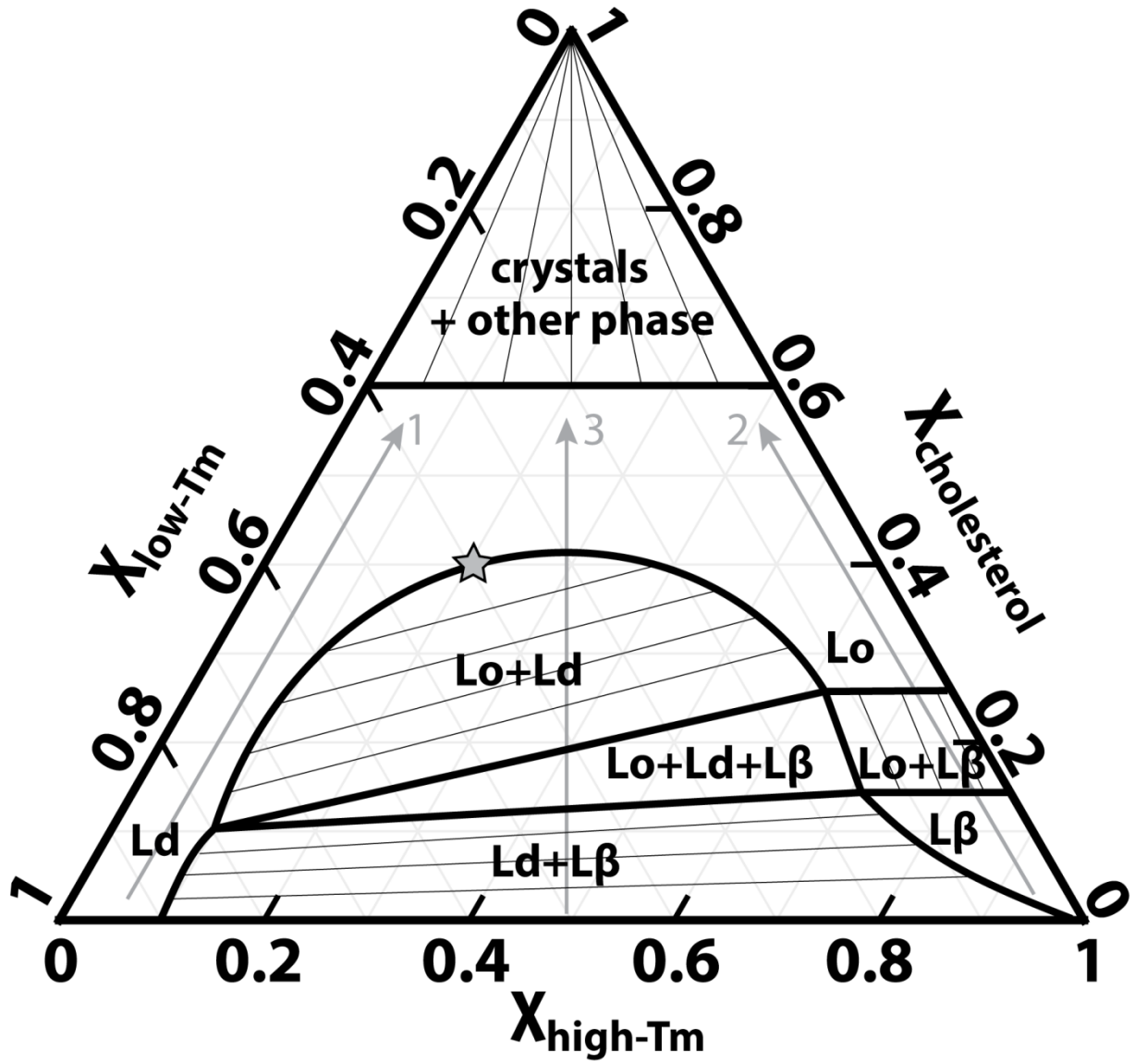

Figure 1.3 Representative phase diagram for ternary mixture of a high-Tm lipid, a low-Tm lipid and cholesterol. First order phase boundaries are shown by thick black lines, and tielines connecting coexisting phase compositions in the two phase regions are shown by thin black lines. Arrows show ways to traverse the phase diagram passing through the different phase coexistence regions. The star marks the critical point for the Lo + Ld coexistence region, here at a composition of high-Tm lipid/low-Tm lipid/cholesterol = 0.2/0.4/0.4.

should be a liquid; adding cholesterol to this Ld phase does not induce the formation of the Lo phase. At high cholesterol concentrations, cholesterol monohydrate crystals precipitate out.

On the right hand side of the phase diagram, and at low cholesterol fractions, the membrane is predominantly in the Lβ phase since the high-Tm lipid (the major component) is below its melting temperature. Adding cholesterol to this system, following Arrow 2, induces the formation of Lo in coexistence with Lβ, with Lo being enriched in cholesterol. As more cholesterol is added, only the Lo phase remains.

At the bottom-middle of the phase diagram, the membrane has coexisting Ld + Lβ phases since it is enriched in low-Tm and high-Tm lipids. As cholesterol concentration increases, following Arrow 3, the Lo phase also begins to form. This results in the three-phase coexistence region of Lo + Ld + Lβ. At high enough cholesterol concentrations, the Lβ phase can no longer form and the two-phase coexistence of Lo + Ld emerges, where the Lo is enriched in the high-Tm lipid and cholesterol and the Ld phase is enriched in the low-Tm lipid. Unlike the Lo + Lβ two-phase region, the Lo + Ld two-phase region terminates in a critical point (marked by the star). As membrane compositions approach this critical point from within the two-phase region, the coexisting Lo and Ld phases remain distinct but their compositions become more similar (shorter tielines).

In the single-phase region outside those marked by phase boundaries, there is a second-order phase transition where the Lo and Ld phases smoothly change from one to the other as composition is varied; for example, going from the word “Ld” to the word “Lo” in the one-phase region of the phase diagram results in the transition of Ld to Lo as the fraction of high-Tm lipid and cholesterol is increased.

Which phases are present can in part be understood in terms of mixing energies of the lipids (48). If there is no energy penalty difference for having like or unlike lipid neighbors, random mixing will occur and the system will be in a single phase. If there is any difference in interaction energies between pairs of lipid types, then non-ideal mixing can occur in which the system is in a single phase, but small, distinct clusters form. If the interaction energy differences become large enough, large-scale phase separation can occur dependent on specifics of the lipid compositions (48).

1.3.3 Type I and Type II ternary lipid mixtures

Ternary mixtures that produce Lo + Ld phase coexistence can be placed into one of two categories, called Type I and Type II mixtures, based on the size of the coexisting Lo + Ld domains (49). Type II mixtures produce Lo and Ld domains that are microns in size and can be observed using fluorescence microscopy. Type I mixtures produce nanoscopoic Lo and Ld domains that are below the optical resolution limit of fluorescence microscopy, but can instead be detected using FRET, ESR and small-angle neutron scattering (SANS), which show that the nanodomains, like rafts, are on the order of 10 nm (50–53). Thus while both Type I and Type II mixtures are comprised of a high-Tm lipid, a low-Tm lipid and cholesterol, and have similar phase diagrams (as discussed in Section 1.3.2), their Lo + Ld domain sizes vary by orders of magnitude.

The difference between a Type II mixture and a Type I mixture often seems to rely heavily on the type of low-Tm lipid used. Type II mixtures have been observed for a plethora of systems, often involving cholesterol, a high-Tm lipid such as dipalmitoyl-PC (DPPC), DSPC or sphingomyelin, and a low-Tm lipid such as DOPC and diphytanoyl-PC (53–57). However, DOPC and diphytanoyl-PC are not biologically relevant and are specifically chosen for their

ability to induce large-scale domains that are useful for fluorescence microscopy. On the other hand, Type I mixtures are formed from cholesterol, high-Tm lipids such as DSPC or sphingomyelin and a more biologically relevant low-Tm lipid such as POPC (51, 53). The ability to alter domain size through manipulation of the low-Tm lipid has led to the development of quaternary lipid mixtures, which show interesting behavior not observed in their ternary mixture counterparts.

1.3.4 Quaternary lipid mixtures

The first systematically studied quaternary lipid mixture was DSPC/DOPC/POPC/chol, which combined the Type I mixture DSPC/POPC/cholesterol with the Type II mixture DSPC/DOPC/cholesterol (58). The overall composition of DSPC/[POPC + DOPC]/cholesterol = 0.45/0.3/0.25 was fixed so that mixtures would remain within the Lo + Ld coexistence region regardless of the relative amounts of DOPC and POPC. For simplicity, the replacement ratio of POPC by DOPC was defined as ρ = [DOPC]/[POPC + DOPC]. At $\rho = 0$, the low-Tm lipid is entirely POPC and domains are nanoscopic. At $\rho = 1$, the low-Tm lipid is all DOPC and domains are macroscopic. By incrementally replacing POPC by DOPC along a so-called ρ-trajectory, the transition from nanoscopic domains to macroscopic domains was examined (58).

Three distinct regimes of domain morphology were found along this ρ-trajectory in giant unilamellar vesicles (GUVs) (58). For $\rho < 0.15$, domains are nanoscopic. For $\rho > 0.25$, domains are macroscopic. For $0.15 < \rho < 0.25$, domains are macroscopic and patterned. These patterns, termed “modulated phases”, ranged from thin stripes to honeycombs. The discovery of modulated phases in model membranes inspired an effort to determine what factors influence domain size and morphology in quaternary lipid mixtures.

One leading hypothesis is that modulated phases arise as a result of competing interactions; an interaction that favors small domain size competes with an interaction that favors large domain size (59, 60). The interaction that favors large domains in membranes is thought to be line tension, which is the energy per unit length of the phase interface. Line tension arises, in part, due to the thickness mismatch between the thicker Lo phase and the thinner Ld phase (61). For macroscopic domains, an interaction that favors domain break-up might be the rigidities of the coexisting phases, with large patches of the stiffer Lo phase being energetically unfavorable (60, 62, 63). For nanodomains, dipole-dipole interactions could also play a role in favoring the break-up of a higher-potential Lo phase (59, 64). Indeed, the transitions from nanodomains, to modulated phase patterns, to macroscopic domains can be captured in Monte Carlo simulations of coexisting phases when they include bending energies, electrostatics and a line tension which increases with ρ (62–64).

Evidence supporting the competing interactions model in quaternary mixtures comes from a variety of sources. SANS has shown that domain size along a ρ-trajectory increases with thickness mismatch – and implicitly line tension – between coexisting phases (52). We and others have also directly measured line tension for many four-component mixtures, and have explicitly shown that line tension increases with ρ (65, and unpublished). For interactions that favor small domain size, experiments have confirmed that the Lo phase is significantly stiffer than the Ld phase (66), and simulations indicate that a cholesterol-rich Ld membrane, and perhaps in turn an Lo phase, can have a higher dipole potential than a cholesterol-poor membrane (67). These results imply that at low ρ, line tension is small and some competing interactions favor the breakup of domains. As ρ increases, line tension increases and domains grow but are still nanoscopic due to the competing interaction. At some critical ρ value, line

tension and the competing interactions are of comparable magnitude and produce modulated phases. At high ρ values, line tension dominates leading to macroscopic domains. This supports the Monte Carlo simulation predictions (62), as well as our findings that the nano-modulated and modulated-macro transitions always occur at well-defined line tensions (unpublished).

1.3.5 Relevance to lipid rafts

Though the Lo phase in model membranes may be of higher order than rafts in the plasma membrane (68), model mixtures still act as a useful tool for understanding raft behavior. Lipid-only ternary and quaternary mixtures showed that biologically relevant lipid concentrations can indeed yield raft-like coexistence of distinct liquid phases. That the size of these domains can be tuned by slight changes in lipid composition hints that cells may similarly be able to control raft size, morphology and connectivity by changing lipid concentrations. Proteins, abundant in the cell plasma membrane, can also be added to lipid-only systems in order to more closely examine protein-protein, protein-lipid and protein-phase interactions relevant to rafts (69–71). Indeed, in model membranes containing sphingomyelin, PC and cholesterol, protein-induced crosslinking of raft-associated monosialotetrahexosylganglioside (GM1) drives the formation of coexisting Lo + Ld phases, which in turn alters the partitioning of transmembrane peptides (72); this is reminiscent of the experiments in plasma membrane spheres discussed in Section 1.2.3 (30). The ability of model membranes to capture so many important features of plasma membrane raft behavior is a testament to the utility of reducing complex systems to their most fundamental units.

In the following section, we describe how molecular dynamics simulations can be used to explore aspects of model membranes inaccessible with other methods.

1.4 Molecular dynamics (MD) simulations

1.4.1 Basic MD methodology

At their basis, most MD simulations work by integrating Newton's equations of motion for a system of interacting molecules (73, 74). The potential energy functions are generally comprised of non-bonded interactions (eg. Coulomb and Lennard-Jones), bonded interactions (eg. bond stretching) and restraints (eg. fixation of bond angles) (74). The set of parameters that define all of these interactions is called a "force field". Additionally, specific molecules often have their own topology files which explicitly list the intramolecular bonds, angles and charges that may differ from the generic force field. Together, these sets of parameters are used to calculate the forces necessary to update the positions and velocities for a certain configuration of atoms.

Fundamentally, MD simulations conserve the number of atoms (N), volume (V) and energy (E) of a system, and so are in the NVE ensemble (73, 74). However, it is often useful to study systems in other ensembles. For membrane simulations, the NPT ensemble is frequently used to mimic experiments, where the number of molecules, pressure (P) and temperature (T) are fixed. In these cases, temperature can be fixed by coupling the system to an external heat source, and pressure can be maintained by rescaling the simulation size (74).

1.4.2 Atomistic and coarse-grained (CG) MD

MD simulations can differ drastically in the level of resolution they use to represent molecules. At the highest level of resolution are all-atom force fields, where every atom of a molecule is included in its representation, as in the Charmm force field (75, 76). Another near-atomistic representation method is the United-Atom (UA) force field (77, 78). In the UA approach, nonpolar and uncharged hydrogens are grouped together with the atoms to which they

are attached. So a 130 atom DPPC molecule is only 50 united atoms. This saves computational cost while still preserving much of the essential chemical nature of the molecules. CG MD goes beyond UA by coarse-graining the molecules even further. Martini is one of the most widely used CG force fields, and groups ~ 4 heavy atoms into one CG bead (79). In this representation, DPPC would be represented by just 12 CG beads. Due to the simplicity of molecular representations in the Martini model, large time steps can be used, each time step can be calculated quickly, and molecules can diffuse ~ 2-10 times faster than their atomistic counterparts (79). This provides CG access to longer time-scales and larger size-scales than would be possible with more atomistic approaches, at the cost of molecular accuracy.

1.4.3 Atomistic simulations of phase separated model membranes

In atomistic simulations, computational limitations preclude access to the sizes and times necessary to observe phase separation taking place from an initially mixed state. Instead, phase separation is often studied by either starting from pre-formed phase separated bilayers based on some existing information about the coexisting phases, or by starting from an initially mixed state and observing just the early stages of clustering and phase separation (80–83). Atomistic simulations can then be used to identify favorable molecular interactions, lipid areas, lipid tilts, lipid order as a function of distance to the phase interface, lipid distributions and lipid diffusion in the different phases (80–84). Due to the accuracy of the atomistic models, the properties they report on can often be directly compared to corresponding experiments. For instance, the order parameter of lipids from a recent DPPC/DOPC/cholesterol all-atom simulation were used to calculate a ^{2}H nuclear magnetic resonance (NMR) spectra, which matched well with the experimentally determined spectra (83).

The accuracy and high resolution of the all-atom models makes them essential for improving our understanding as to how phase separation acts on an atomistic level. However, until computers advance further, all-atom simulations will remain relegated to small, short simulations and will not be able to provide much information regarding the large-scale formation of phases. Currently, CG simulations fill this gap.

1.4.4 CG simulations of phase separated model membranes

Unlike their atomistic counterparts, CG simulations can produce phase separation from initially mixed lipid bilayers (85–88). For mixtures of various lipid compositions, phase separating CG model membranes have provided a wealth of information on large-scale phase separation characteristics, such phase domain growth, phase domain alignment, phase compositions, phase thicknesses, surface tensions between domains in different leaflets, line tension between domains and the distinction between non-ideal mixing and phase separation (81, 84, 87, 89–92). The efficiency with which CG simulations phase separate also provides a means for analyzing the effects of non-lipid molecules on phase behavior, important for domains *in vitro* and *in vivo*.

CG simulations have been particularly useful at elucidating the interactions between phase separated bilayers and peripheral, and integral, membrane proteins. Peripheral membrane protein anchors were found to preferentially partition in phase separated bilayers, altering line tension, and determining the phase preference of the peripheral protein domain (93, 94). To model the interaction of integral membrane proteins with the bilayer, simple α-helical peptides are often used since they are a common transmembrane motif (95). The insertion of α-helical peptides, and α-helical anchored proteins, into phase separating bilayers revealed their

partitioning, clustering, and ability to enhance lipid demixing and domain formation (70, 92, 96–98).

As with atomistic simulations, CG simulations of phase separated systems provide predictions which can be, and to some extent have been, experimentally verified (70). These predictions include the partitioning of proteins, as well as protein-induced changes in phase behavior. Indeed, the strength of CG is in its ability to provide large size-scale and long time-scale experimentally testable results while also providing near-atomistic, non-experimentally accessible, resolution.

However, the ease of using CG to do such large simulations can also lead to the development of overly complex systems which outpace the fundamental knowledge required to understand them. At one extreme, a recent CG simulation study was published which modeled the plasma membrane as accurately as possible; this involved an asymmetric bilayer with 63 different lipid species (88). While interesting from a technical standpoint, the complexity of such a simulation is not necessarily useful until the underlying behavior of simplified model mixtures is better established.

1.5 Summary of research

In this work we use MD simulations to reveal traits of model lipid bilayers that cannot be studied with experimental techniques. We examine overall bilayer behavior, but also focus on the localization of different phenomena. In Chapter 2 we show how fluorescent probes commonly used to study lipid bilayers can alter their surrounding environment. In Chapter 3 we measure how composition alters phase and interface properties in quaternary lipid mixtures. In Chapter 4 we quantify the effects of different transmembrane peptides on phase behavior in the quaternary lipid mixtures of Chapter 3. Chapter 5 summarizes our findings and expounds on

possible future directions of MD simulations and experiments that will help deepen our knowledge of fundamental bilayer behavior.

REFERENCES

1. Van Meer, G., D.R. Voelker, and G.W. Feigenson. 2008. Membrane lipids: where they are and how they behave. Nat. Rev. Mol. Cell Biol. 9: 112–124.

2. Dick, R. a., and V.M. Vogt. 2014. Membrane interaction of retroviral Gag proteins. Front. Microbiol. 5: 1–11.

3. Huang, J., and G.W. Feigenson. 1999. A microscopic interaction model of maximum solubility of cholesterol in lipid bilayers. Biophys. J. 76: 2142–57.

4. Schroeder, R., E. London, and D. Brown. 1994. Interactions between saturated acyl chains confer detergent resistance on lipids and glycosylphosphatidylinositol (GPI)-anchored proteins: GPI-anchored proteins in liposomes and cells show similar behavior. Proc. Natl. Acad. Sci. U.S.A. 91: 12130–12134.

5. Lingwood, D., and K. Simons. 2010. Lipid Rafts as a Membrane-organizing Principle. Science. 327: 46–50.

6. Yetukuri, L., K. Ekroos, A. Vidal-Puig, and M. Orešič. 2011. Informatics and computational strategies for the study of lipids. Mol. Biosyst. 4: 121–127.

7. Roelofsen, B., and J.A.F. Op den Kamp. 1994. Plasma Membrane Phospholipid Asymmetry and Its Maintenance: The Human Erythrocyte as a Model. In: Hoekstra D, editor. Cell Lipids. San Diego, California: Academic Press, Inc. pp. 7–46.

8. Daleke, D.L. 2007. Phospholipid flippases. J. Biol. Chem. 282: 821–825.

9. Sheetz, M.P. 1993. Glycoprotein motility and dynamic domains in fluid plasma membranes. Annu. Rev. Biophys. Biomol. Struct. 22: 417–431.

10. Golan, D.E., M.R. Alecio, W.R. Veatch, and R.R. Rando. 1984. Lateral mobility of phospholipid and cholesterol in the human erythrocyte membrane: effects of protein-lipid interactions. Biochemistry. 23: 332–339.

11. Singer, S.J., and G.L. Nicolson. 1972. The fluid mosaic model of the structure of cell membranes. Science. 175: 720–731.

12. Alberts, B., D. Bray, A. Johnson, J. Lewis, M. Raff, K. Roberts, and P. Walter. 2010. Essential Cell Biology. Third. New York, NY: Garland Science Pub.

13. Simons, K., and G. van Meer. 1988. Lipid sorting in epithelial cells. Biochemistry. 27: 6197–6202.

14. Van Meer, G. 2005. Cellular lipidomics. EMBO J. 24: 3159–65.

15. Thompson, T.E., and T.W. Tillack. 1985. Organization of Glycosphingolipids in Bilayers and Plasma Membranes of Mammalian Cells. Ann. Rev. Biophys. Biophys. 14: 361–86.

16. Brown, D.A., and J.K. Rose. 1992. Sorting of GPI-anchored proteins to glycolipid-enriched membrane subdomains during transport to the apical cell surface. Cell. 68: 533–544.

17. Simons, K., and M.J. Gerl. 2010. Revitalizing membrane rafts: new tools and insights. Nat. Rev. Mol. Cell Biol. 11: 688–99.

18. Simons, K., and E. Ikonen. 1997. Functional rafts in cell membranes. Nature. 387: 569–72.

19. Hancock, J.F. 2006. Lipid rafts: contentious only from simplistic standpoints. Nat. Rev. Mol. Cell Biol. 7: 456–462.

20. Swamy, M.J., L. Ciani, M. Ge, A.K. Smith, D. Holowka, B. Baird, and J.H. Freed. 2006. Coexisting domains in the plasma membranes of live cells characterized by spin-label ESR spectroscopy. Biophys. J. 90: 4452–4465.

21. Varma, R., and S. Mayor. 1998. GPI-anchored proteins are organized in submicron domains at the cell surface. Nature. 394: 798–801.

22. Pralle, A., P. Keller, E.-L. Florin, K. Simons, and J.K.H. Hörber. 2000. Sphingolipid-cholesterol rafts diffuse as small entities in the plasma membrane of mammalian cells. J. Cell Biol. 148: 997–1007.

23. Van Zanten, T.S., J. Gómez, C. Manzo, A. Cambi, J. Buceta, R. Reigada, and M.F. Garcia-Parajo. 2010. Direct mapping of nanoscale compositional connectivity on intact cell membranes. Proc. Natl. Acad. Sci. U.S.A. 107: 15437–15442.

24. Bacia, K., D. Scherfeld, N. Kahya, and P. Schwille. 2004. Fluorescence correlation spectroscopy relates rafts in model and native membranes. Biophys. J. 87: 1034–1043.

25. Vereb, G., J. Matkó, G. Vámosi, S.M. Ibrahim, E. Magyar, S. Varga, J. Szöllősi, A. Jenei, R. Gáspár, Jr., T.A. Waldmann, and S. Damjanovich. 2000. Cholesterol-dependent clustering of IL-2Ralpha and its colocalization with HLA and CD48 on T lymphoma cells suggest their functional association with lipid rafts. Proc. Natl. Acad. Sci. U.S.A. 97: 6013–6018.

26. Goswami, D., K. Gowrishankar, S. Bilgrami, S. Ghosh, R. Raghupathy, R. Chadda, R. Vishwakarma, M. Rao, and S. Mayor. 2008. Nanoclusters of GPI-anchored proteins are formed by cortical actin-driven activity. Cell. 135: 1085–97.

27. Kusumi, A., I. Koyama-honda, and K. Suzuiki. 2004. Molecular Dynamics and Interactions for Creation of Stimulation-Induced Stabilized Rafts from Small Unstable Steady-State Rafts. Traffic. 5: 213–230.

28. Baumgart, T., A.T. Hammond, P. Sengupta, S.T. Hess, D.A. Holowka, B.A. Baird, and W.W. Webb. 2007. Large-scale fluid/fluid phase separation of proteins and lipids in giant plasma membrane vesicles. Proc. Natl. Acad. Sci. U.S.A. 104: 3165–70.

29. Sengupta, P., A. Hammond, D. Holowka, and B. Baird. 2008. Structural determinants for partitioning of lipids and proteins between coexisting fluid phases in giant plasma membrane vesicles. Biochim. Biophys. Acta. 1778: 20–32.

30. Lingwood, D., J. Ries, P. Schwille, and K. Simons. 2008. Plasma membranes are poised for activation of raft phase coalescence at physiological temperature. Proc. Natl. Acad. Sci. U.S.A. 105: 10005–10010.

31. Kabouridis, P.S., J. Janzen, A.L. Magee, and S.C. Ley. 2000. Cholesterol depletion disrupts lipid rafts and modulates the activity of multiple signaling pathways in T lymphocytes. Eur. J. Immunol. 30: 954–963.

32. Dykstra, M., A. Cherukuri, H.W. Sohn, S.-J. Tzeng, and S.K. Pierce. 2003. Location is everything: lipid rafts and immune cell signaling. Annu. Rev. Immunol. 21: 457–481.

33. Allen, J.A., R.A. Halverson-Tamboli, and M.M. Rasenick. 2007. Lipid raft microdomains and neurotransmitter signalling. Nat. Rev. Neurosci. 8: 128–140.

34. Salaün, C., D.J. James, and L.H. Chamberlain. 2004. Lipid rafts and the regulation of exocytosis. Traffic. 5: 255–264.

35. Mayor, S., and R.E. Pagano. 2007. Pathways of clathrin-independent endocytosis. Nat. Rev. Mol. Cell Biol. 8: 603–612.

36. Ewers, H., W. Römer, A.E. Smith, K. Bacia, S. Dmitrieff, W. Chai, R. Mancini, J. Kartenbeck, V. Chambon, L. Berland, A. Oppenheim, G. Schwarzmann, T. Feizi, P. Schwille, P. Sens, A. Helenius, and L. Johannes. 2010. GM1 structure determines SV40-induced membrane invagination and infection. Nat. Cell Biol. 12: 11–18.

37. Pietiäinen, V.M., V. Marjomäki, J. Heino, and T. Hyypiä. 2005. Viral entry, lipid rafts and caveosomes. Ann. Med. 37: 394–403.

38. Rajendran, L., and K. Simons. 2005. Lipid rafts and membrane dynamics. J. Cell Sci. 118: 1099–1102.

39. Simons, K., and J.L. Sampaio. 2011. Membrane organization and lipid rafts. Cold Spring Harb. Perspect. Biol. 3: 1–17.

40. Dietrich, C., L.A. Bagatolli, Z.N. Volovyk, N.L. Thompson, M. Levi, K. Jacobson, and E. Gratton. 2001. Lipid rafts reconstituted in model membranes. Biophys. J. 80: 1417–1428.

41. Cheng, H.-T., Megha, and E. London. 2009. Preparation and properties of asymmetric vesicles that mimic cell membranes. Effect upon lipid raft formation and transmembrane helix orientation. J. Biol. Chem. 284: 6079–6092.

42. Crane, J.M., V. Kiessling, and L.K. Tamm. 2005. Measuring lipid asymmetry in planar supported bilayers by fluorescence interference contrast microscopy. Langmuir. 21: 1377–1388.

43. Marsh, D. 2009. Cholesterol-induced fluid membrane domains: A compendium of lipid-raft ternary phase diagrams. Biochim. Biophys. Acta - Biomembr. 1788: 2114–2123.

44. Wang, T.-Y.Y., and J.R. Silvius. 2001. Cholesterol does not induce segregation of liquid-ordered domains in bilayers modeling the inner leaflet of the plasma membrane. Biophys. J. 81: 2762–2773.

45. Harder, T., P. Scheiffele, P. Verkade, and K. Simons. 1998. Lipid domain structure of the plasma membrane revealed by patching of membrane components. J. Cell Biol. 141: 929–942.

46. Kiessling, V., J.M. Crane, and L.K. Tamm. 2006. Transbilayer effects of raft-like lipid domains in asymmetric planar bilayers measured by single molecule tracking. Biophys. J. 91: 3313–3326.

47. Lin, Q., and E. London. 2015. Ordered Raft Domains Induced by Outer Leaflet Sphingomyelin in Cholesterol-Rich Asymmetric Vesicles. Biophys. J. 108: 2212–2222.

48. Heberle, F.A., and G.W. Feigenson. 2011. Phase separation in lipid membranes. Cold Spring Harb. Perspect. Biol. 3: 1–13.

49. Feigenson, G.W. 2009. Phase diagrams and lipid domains in multicomponent lipid bilayer mixtures. Biochim. Biophys. Acta. 1788: 47–52.

50. Buboltz, J.T. 2007. Steady-state probe-partitioning fluorescence resonance energy transfer: A simple and robust tool for the study of membrane phase behavior. Phys. Rev. E. 76: 021903.

51. Heberle, F.A., J. Wu, S.L. Goh, R.S. Petruzielo, and G.W. Feigenson. 2010. Comparison of three ternary lipid bilayer mixtures: FRET and ESR reveal nanodomains. Biophys. J. 99: 3309–18.

52. Heberle, F.A., R.S. Petruzielo, J. Pan, P. Drazba, N. Kučerka, R.F. Standaert, G.W. Feigenson, and J. Katsaras. 2013. Bilayer thickness mismatch controls domain size in model membranes. J. Am. Chem. Soc. 135: 6853–9.

53. Petruzielo, R.S., F.A. Heberle, P. Drazba, J. Katsaras, and G.W. Feigenson. 2013. Phase behavior and domain size in sphingomyelin-containing lipid bilayers. Biochim. Biophys. Acta - Biomembr. 1828: 1302–1313.

54. Veatch, S.L., and S.L. Keller. 2002. Organization in lipid membranes containing cholesterol. Phys. Rev. Letters. 89: 268101.

55. Zhao, J., J. Wu, F.A. Heberle, T.T. Mills, P. Klawitter, G. Huang, G. Costanza, and G.W. Feigenson. 2007. Phase studies of model biomembranes: complex behavior of DSPC/DOPC/cholesterol. Biochim. Biophys. Acta. 1768: 2764–76.

56. Veatch, S.L., and S.L. Keller. 2005. Miscibility phase diagrams of giant vesicles containing sphingomyelin. Phys. Rev. Lett. 94: 148101.

57. Veatch, S.L., K. Gawrisch, and S.L. Keller. 2006. Closed-loop miscibility gap and quantitative tie-lines in ternary membranes containing diphytanoyl PC. Biophys. J. 90: 4428–4436.

58. Konyakhina, T.M., S.L. Goh, J. Amazon, F.A. Heberle, J. Wu, and G.W. Feigenson. 2011. Control of a nanoscopic-to-macroscopic transition: modulated phases in four-component DSPC/DOPC/POPC/Chol giant unilamellar vesicles. Biophys. J. 101: L08–10.

59. Seul, M., and D. Andelman. 1995. Domain Shapes and Patterns: The Phenomenology of Modulated Phases. Science. 267: 476–483.

60. Baumgart, T., S.T. Hess, and W.W. Webb. 2003. Imaging coexisting fluid domains in biomembrane models coupling curvature and line tension. Nature. 425: 821–824.

61. Kuzmin, P.I., S.A. Akimov, Y.A. Chizmadzhev, J. Zimmerberg, and F.S. Cohen. 2005. Line tension and interaction energies of membrane rafts calculated from lipid splay and tilt. Biophys. J. 88: 1120–33.

62. Amazon, J.J., S.L. Goh, and G.W. Feigenson. 2013. Competition between line tension and curvature stabilizes modulated phase patterns on the surface of giant unilamellar vesicles: a simulation study. Phys. Rev. E. 87: 022708.

63. Goh, S.L., J.J. Amazon, and G.W. Feigenson. 2013. Toward a better raft model: modulated phases in the four-component bilayer, DSPC/DOPC/POPC/CHOL. Biophys. J. 104: 853–62.

64. Amazon, J.J., and G.W. Feigenson. 2014. Lattice simulations of phase morphology on lipid bilayers: Renormalization, membrane shape, and electrostatic dipole interactions. Phys. Rev. E. 89: 022702.

65. Hassan-Zadeh, E., E. Baykal-Caglar, M. Alwarawrah, and J. Huang. 2014. Complex roles of hybrid lipids in the composition, order, and size of lipid membrane domains. Langmuir. 30: 1361–9.

66. Semrau, S., T. Idema, L. Holtzer, T. Schmidt, and C. Storm. 2008. Accurate Determination of Elastic Parameters for Multicomponent Membranes. Phys. Rev. Lett. 100: 088101.

67. Hofsäß, C., E. Lindahl, and O. Edholm. 2003. Molecular dynamics simulations of phospholipid bilayers with cholesterol. Biophys. J. 84: 2192–206.

68. Kaiser, H.-J., D. Lingwood, I. Levental, J.L. Sampaio, L. Kalvodova, L. Rajendran, and K. Simons. 2009. Order of lipid phases in model and plasma membranes. Proc. Natl. Acad. Sci. U.S.A. 106: 16645–16650.

69. Bacia, K., C.G. Schuette, N. Kahya, R. Jahn, and P. Schwille. 2004. SNAREs prefer liquid-disordered over "raft" (liquid-ordered) domains when reconstituted into giant unilamellar vesicles. J. Biol. Chem. 279: 37951–37955.

70. Schäfer, L. V, D.H. de Jong, A. Holt, A.J. Rzepiela, A.H. de Vries, B. Poolman, J.A. Killian, and S.J. Marrink. 2011. Lipid packing drives the segregation of transmembrane helices into disordered lipid domains in model membranes. Proc. Natl. Acad. Sci. U.S.A. 108: 1343–1348.

71. Shogomori, H., A.T. Hammond, A.G. Ostermeyer-Fay, D.J. Barr, G.W. Feigenson, E. London, and D.A. Brown. 2005. Palmitoylation and intracellular domain interactions both contribute to raft targeting of linker for activation of T cells. J. Biol. Chem. 280: 18931–18942.

72. Hammond, A.T., F.A. Heberle, T. Baumgart, D. Holowka, B. Baird, and G.W. Feigenson. 2005. Crosslinking a lipid raft component triggers liquid ordered-liquid disordered phase separation in model plasma membranes. Proc. Natl. Acad. Sci. U.S.A. 102: 6320–6325.

73. Rapaport, D.C. 2004. The art of molecular dynamics simulations [Online]. 2nd ed. Cambridge: Cambridge University Press.

74. Van der Spoel, D., E. Lindahl, B. Hess, C. Kutzner, A.R. van Buuren, E. Apol, P.J. Meulenhoff, D.P. Tieleman, A.L.T.M. Sijbers, K.A. Feenstra, R. van Drunen, and H.J.C. Berendsen. 2005. Gromacs User Manual Version 4.5. .

75. Klauda, J.B., R.M. Venable, J.A. Freites, J.W. O'Connor, D.J. Tobias, C. Mondragon-Ramirez, I. Vorobyov, A.D. MacKerell, and R.W. Pastor. 2010. Update of the CHARMM All-Atom Additive Force Field for Lipids: Validation on Six Lipid Types. J. Phys. Chem. B. 114: 7830–7843.

76. Best, R.B., X. Zhu, J. Shim, P.E.M. Lopes, J. Mittal, M. Feig, and A.D. MacKerell Jr. 2012. Optimization of the additive CHARMM all-atom protein force field targeting improved sampling of the backbone ϕ, ψ and side-chain $\chi 1$ and $\chi 2$ Dihedral Angles. J. Chem. Theory Comput. 8: 3257–3273.

77. Van Gunsteren, W.F., and H.J.C. Berendsen. 1987. Groningen Molecular Simulation (GROMOS) Library Manual. Groningen, The Netherlands: Biomos.

78. Berger, O., O. Edholm, F. Jähnig, and F. Jahnig. 1997. Molecular dynamics simulations of a fluid bilayer of dipalmitoylphosphatidylcholine at full hydration, constant pressure, and constant temperature. Biophys. J. 72: 2002–13.

79. Marrink, S.J., H.J. Risselada, S. Yefimov, D.P. Tieleman, and A.H. de Vries. 2007. The MARTINI force field: coarse grained model for biomolecular simulations. J. Phys. Chem. B. 111: 7812–24.

80. Polley, A., S. Vemparala, and M. Rao. 2012. Atomistic Simulations of a Multicomponent Asymmetric Lipid Bilayer. J. Phys. Chem. B. 116: 13403–13410.

81. Hakobyan, D., and A. Heuer. 2013. Phase separation in a lipid/cholesterol system: comparison of coarse-grained and united-atom simulations. J. Phys. Chem. B. 117: 3841–51.

82. Pandit, S.A., S. Vasudevan, S.W. Chiu, R.J. Mashl, E. Jakobsson, and H.L. Scott. 2004. Sphingomyelin-cholesterol domains in phospholipid membranes: atomistic simulation. Biophys. J. 87: 1092–1100.

83. Sodt, A.J., M.L. Sandar, K. Gawrisch, R.W. Pastor, and E. Lyman. 2014. The molecular structure of the liquid-ordered phase of lipid bilayers. J. Am. Chem. Soc. 136: 725–32.

84. Ackerman, D.G., and G.W. Feigenson. 2015. Multiscale Modeling of Four-Component Lipid Mixtures: Domain Composition, Size, Alignment, and Properties of the Phase Interface. J. Phys. Chem. B. 119: 4240–4250.

85. Bennett, W.F.D., and D.P. Tieleman. 2013. Computer simulations of lipid membrane domains. Biochim. Biophys. Acta. 1828: 1765–1776.

86. Stevens, M.J. 2005. Complementary matching in domain formation within lipid bilayers. J. Am. Chem. Soc. 127: 15330–1.

87. Risselada, H.J., and S.J. Marrink. 2008. The molecular face of lipid rafts in model membranes. Proc. Natl. Acad. Sci. U.S.A. 105: 17367–17372.

88. Ingólfsson, H.I., M.N. Melo, F.J. van Eerden, C. Arnarez, C.A. López, T.A. Wassenaar, X. Periole, A.H. de Vries, D.P. Tieleman, and S.J. Marrink. 2014. Lipid Organization of the Plasma Membrane. J. Am. Chem. Soc. 136: 14554–14559.

89. Schäfer, L. V., and S.J. Marrink. 2010. Partitioning of lipids at domain boundaries in model membranes. Biophys. J. 99: L91–3.

90. Hakobyan, D., and A. Heuer. 2014. Key molecular requirements for raft formation in lipid/cholesterol membranes. PLoS One. 9: e87369.

91. Rosetti, C., and C. Pastorino. 2012. Comparison of ternary bilayer mixtures with asymmetric or symmetric unsaturated phosphatidylcholine lipids by coarse grained molecular dynamics simulations. J. Phys. Chem. B. 116: 3525–37.

92. Domański, J., S.J. Marrink, and L. V. Schäfer. 2012. Transmembrane helices can induce domain formation in crowded model membranes. Biochim. Biophys. Acta. 1818: 984–94.

93. De Jong, D.H., C.A. Lopez, and S.J. Marrink. 2013. Molecular view on protein sorting into liquid-ordered membrane domains mediated by gangliosides and lipid anchors. Faraday Discuss. 161: 347–363.

94. Janosi, L., Z. Li, J.F. Hancock, and A.A. Gorfe. 2012. Organization, dynamics, and segregation of Ras nanoclusters in membrane domains. Proc. Natl. Acad. Sci. U.S.A. 109: 8097–8102.

95. Killian, J.A. 2003. Synthetic peptides as models for intrinsic membrane proteins. FEBS Lett. 555: 134–138.

96. Liang, Q., Q.-Y. Wu, and Z.-Y. Wang. 2014. Effect of hydrophobic mismatch on domain formation and peptide sorting in the multicomponent lipid bilayers in the presence of immobilized peptides. J. Chem. Phys. 141: 074702.

97. Castillo, N., L. Monticelli, J. Barnoud, and D.P. Tieleman. 2013. Free energy of WALP23 dimer association in DMPC, DPPC, and DOPC bilayers. Chem. Phys. Lipids. 169: 95–105.

98. Parton, D.L., A. Tek, M. Baaden, and M.S.P. Sansom. 2013. Formation of Raft-Like Assemblies within Clusters of Influenza Hemagglutinin Observed by MD Simulations. PLoS Comput. Biol. 9: e1003034.

CHAPTER 2
Limited perturbation of a DPPC bilayer by fluorescent lipid probes: A molecular dynamics study[‡]

2.1 Abstract

The properties of lipid bilayer nanometer-scale domains could be crucial for understanding cell membranes. Fluorescent probes are often used to study bilayers, yet their effects on host lipids are not well understood. We used molecular dynamics simulations to investigate perturbations in a fluid DPPC bilayer upon incorporation of three indocarbocyanine probes: DiI-C18:0, DiI-C18:2, or DiI-C12:0. We find a 10–12% decrease in chain order for DPPC in the solvation shell nearest the probe, but smaller effects in subsequent shells, indicating that the probes significantly alter only their local environment. We also observe order perturbations of lipids directly across from the probe in the opposite leaflet. Additionally, the DPPC headgroup phosphorus-to-nitrogen vector of lipids nearest the probe exhibits preferential orientation pointing away from the DiI. We show that while DiI probes perturb their local environment, they do not strongly influence the average properties of "nanoscopic" domains containing a few hundred lipids.

2.2 Introduction

Probe-based studies greatly aid our understanding of lipid membranes. Fluorescent probes in particular have proven useful, and bilayer properties studied with fluorescence techniques include order (1), hydration and polarity (2), electrostatic potential (3), lipid lateral diffusion (4), and phase state (5). In recent years, fluorescence spectroscopy (reviewed in

[‡] The following chapter is reproduced from: Ackerman, D.G., F. A. Heberle, and G.W. Feigenson. 2013. Limited Perturbation of a DPPC Bilayer by Fluorescent Lipid Probes: A Molecular Dynamics Study. J. Phys. Chem. B. 117: 4844–4852. It has been modified to fit the format of this thesis. DGA and FAH worked on developing the methodolgy and DGA performed the simulations and final analysis.

reference (6)) and microscopy (reviewed in references (7) and (8)) have played an important role in elucidating the lateral organization of model membranes. Fluorescence studies continue to drive the membrane raft field, including recent observations of Ising-like critical behavior (9) and stable nanoscopic phase domains (10).

Accurate fluorescence experiments, especially when concerning raft-sized domains, rely on the assumption that the probes do not alter the properties they are measuring. However, fluorescent probes report only on their local environment. Therefore, effects that are negligible in the bulk may still be significant in the smaller reporting region of the probe. For instance the local dielectric field near the probe—such as that produced by the charge-dense lipid headgroups—can affect probe fluorescence, while lipid order near the probe can affect partitioning of the probes and (for spin-labeled probes) can also alter their order and motion. If the probes themselves affect the headgroup orientation or order of nearby lipids, they may be reporting on altered environments.

Clearly, probe-induced perturbations must be assessed independently from the information reported by the probe, and several techniques have proven useful in this regard. In bilayers doped with fluorescent probes, differential scanning calorimetry (11) and ^{2}HNMR (12) have been used to detect changes in the bilayer gel/fluid transition temperature, X-ray diffraction has been employed to measure differences in average bilayer structure (13), and ^{1}HNMR has been used to measure changes in motional freedom of the host lipid (14). Each of these techniques reports on average properties of a large number of lipids. Typically, significant perturbations are not detected until the probe concentration exceeds several mole percent, although exceptions are reported (12). Bulk membrane properties are inherently insensitive to the very local perturbations induced by a probe at the dilute concentrations (< 0.1 mol%) typically

found in spectrophotometric experiments. Two different but related questions can be posed: To what extent does the probe report on a perturbed local environment? And, how far out from the probe is the lipid perturbed?

MD simulations can provide insight into bilayer structure and dynamics that might otherwise be impossible to obtain experimentally. Simulations offer a unique way of characterizing spatial dependence of perturbations induced by a probe, including local changes. MD studies of bilayers containing fluorescent probes have appeared in the literature, aimed at understanding the location and dynamics of the fluorophore and the distance dependence of their perturbative effects within the bilayer (15–18). Reviewing several of these studies, Loura and Ramalho emphasized the important distinction between first-shell lipids and the average properties of all lipids in the simulation (19). In a recent MD study, the indocarbocyanine probe DiI-C18:0 was found to increase the *average* order and thickness of a fluid DPPC bilayer, while changing *average* headgroup orientation as measured by the phosphorus-to-nitrogen (P-N) vector (20). Here, we used MD to examine the spatial dependence of such perturbations in a DPPC bilayer from three types of positively charged DiI: DiI-C18:0, DiI-C18:2, or DiI-C12:0.

We examined perturbations as a function of distance from the DiI molecules. This allowed us to analyze the length-scale over which the dye perturbs its environment. We saw that on a very small scale, the DiI molecules disorder their local environment and cause reorientation of the local lipid headgroups. However, these effects are short-range, and overall the dye has a negligible effect on a patch of a few hundred lipids.

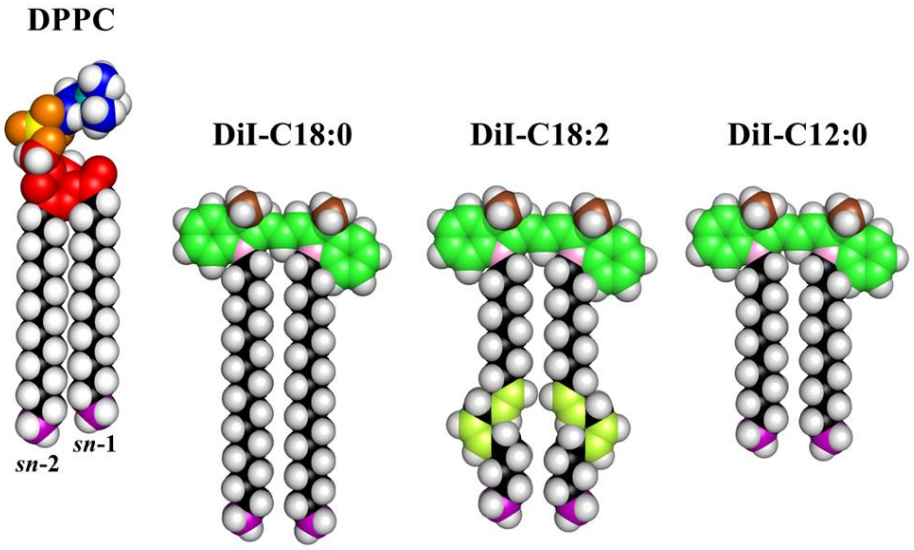

Figure 2.1 Molecular structures used in this study**.** DPPC: choline-$(CH_2)_2$ carbon (blue) and nitrogen (cyan), phosphate oxygen (orange) and phosphorus (yellow), glycerol-carbonyl (red), methylene carbon (black), terminal methyl (purple). DiI: chromophore (green), headgroup methyl (brown), nitrogen (pink), methylene carbon (black), alkene carbon (yellow-green), terminal methyl (purple). This color coding is used in Figures 2.3, 2.4, 2.5 and 2.10.

2.3 Simulation methods

All MD simulations were performed using version 4.5.3 of the Groningen Machine for Chemical Simulations (GROMACS) (21), using the ffg53a6 force field (22) with Berger lipid parameters (23).

2.3.1 Simulation setup

The molecular structures used in this study are shown in Figure 2.1. A DiI-C18:0 PDB file was constructed using the PRODRG2 server (http://davapc1.bioch.dundee.ac.uk/prodrg/), and its topology file (including charge distribution) was obtained from reference (24), with some atom types changed to match the force field. DiI-C12:0 was constructed by truncating the DiI-C18:0 alkyl chains. Similarly, DiI-C18:2 was constructed by replacing the appropriate single bonds in the alkyl chains of DiI-C18:0 with *cis* double bonds, using parameters from the oleoyl chain of POPC (http://moose.bio.ucalgary.ca/index.php?page=Structures_and_Topologies) (23). Topology files for the DiI probes are included in Appendix A.1. DPPC topology parameters were from Chiu et al. (25).

A total of 12 bilayer simulations were performed for each probe (DiI-C18:0, DiI-C18:2, or DiI-C12:0). The starting configurations of each lipid were identical for all 12 simulations with the exception of the inserted molecule, which was randomly rotated about its long axis. To ensure statistical independence of the 12 simulations, different random seeds were used to generate different initial velocities. The bilayer initially contained 512 DPPC molecules, constructed from an equilibrated DPPC bilayer with 128 total lipids (http://people.ucalgary.ca/~tieleman/download.html) (26). One DPPC molecule from each leaflet was then removed to provide space for insertion of a probe molecule. To minimize unfavorable interactions, all inserted molecules were initially placed so that they were slightly protruding out

of the bilayer. As a control, we also performed 12 simulations in which a DPPC molecule (rather than a probe) was reinserted to ensure that the insertion step did not itself cause perturbations. Additional information regarding the simulation setup is included in Appendix A.2.

2.3.2 Simulation conditions

After bilayer assembly, the systems were solvated using the simple point charge (SPC) water model (26), with ~ 29 waters per lipid. For the DiI-containing simulations, two chloride ions were added to cancel the net charge of the system. A 3 ns NVT temperature equilibration was performed at 323 K (i.e., fluid-phase DPPC) using the V-rescale thermostat with a time constant of 0.1 ps. During this time the inserted molecules were pulled into the bilayer. A 60 ns production run was then performed in the NPT ensemble at 323 K and 1 atm, using the Nosé-Hoover thermostat and Parrinello-Rahman semi-isotropic barostat with 0.5 ps and 2 ps time constants, respectively. The first 10 ns of these runs were considered as additional equilibration, and only the final 50 ns were analyzed. Data for the production run were saved every 10 ps.

Periodic boundary conditions were applied in all three spatial directions, with x and y corresponding to the bilayer plane and z to the bilayer normal. Bond lengths were constrained using the LINCS algorithm (27, 28) and the Particle-Mesh Ewald (PME) method (29, 30) was used for electrostatic interactions, with cubic interpolation order 4 and a Fourier transform grid spacing of 0.16 nm. A neighbor-list cutoff of 1.1 nm, short range interaction cutoff of 1.1 nm, and Lennard-Jones interaction cutoff of 1.1 nm were also applied. The equations of motion were integrated via the leap-frog algorithm with a timestep of 2 fs (27, 28).

2.3.3 Data analysis methodology: shell partitioning scheme

Our primary objective is to understand the magnitude and spatial extent of probe perturbations, and to this end we examined average properties of the host lipid (fluid phase

DPPC) as a function of distance from the probe molecule. Following the procedure of Kim (31) and Venturoli (32), we partitioned the simulation box into zones, each defined by a range of probe-lipid separation distances. The zones are considered to be "solvation shells" around the probe, each containing an integer number of DPPC lipids at any particular instant. We define the *n*th solvation shell as an annulus containing 6*n* lipids on average, as specified by the inner and outer radii that satisfy this condition.

A simple way to partition the molecules into shells is to consider only the projections of the molecular centers of mass $\boldsymbol{\rho}$ onto the 2D plane of the bilayer (Figure 2.2). Taking the reference molecule center of mass $\boldsymbol{\rho_R}$ as the origin of a 2D coordinate system, the reference-lipid separation distance *r* is defined as:

$$r = \|\boldsymbol{\rho_R} - \boldsymbol{\rho_L}\| \qquad (2.1)$$

where $\boldsymbol{\rho_L}$ is the lipid center of mass. Positional correlations in fluid phases are short range, and therefore the $\boldsymbol{\rho_L}$ are nearly randomly distributed. Under this assumption, shell *n* has an average area of $6nA_L$, where A_L is the average area of a host lipid calculated on a per frame basis (i.e., the total bilayer area divided by the number of lipids per leaflet). Assuming a circular lipid area, the average lipid radius is:

$$r_0 = \sqrt{A_L/\pi} \qquad (2.2)$$

The annular radii are then defined as:

$$r_n = r_0\left(1 + 6\sum_{i=1}^{n} i\right)^{1/2} = r_0\sqrt{1 + 3n(n+1)} \qquad (2.3)$$

At a given instant (i.e., a particular simulation snapshot), a lipid is considered to reside in shell *n* if $\boldsymbol{\rho_L}$ falls within the inner and outer radii of the shell—that is, if $r_{n-1} \leq r < r_n$ (with $r < r_0$ assigned to the first shell). An identical approach is used to partition lipids in the leaflet opposite the probe, with the modification that lipids with $r < r_0$ are considered to reside in shell 0. With

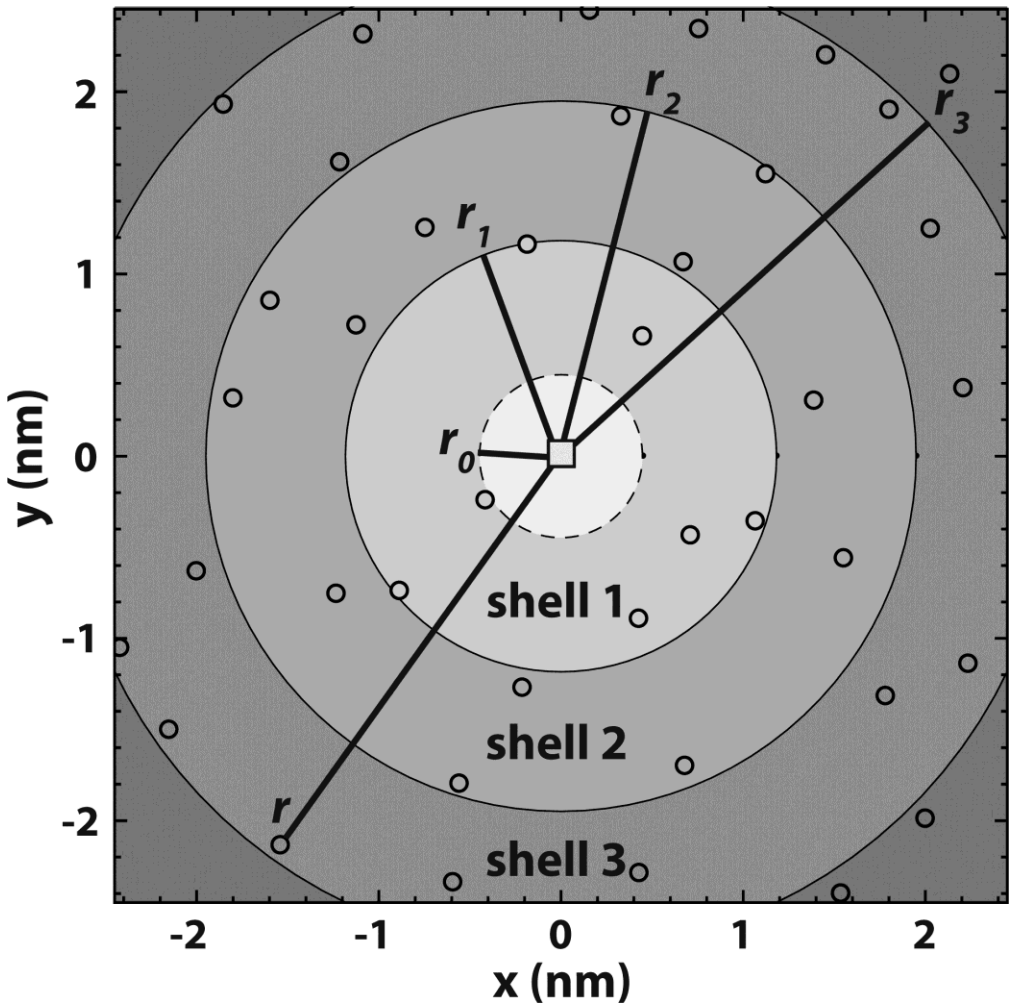

Figure 2.2 Partitioning of DPPC into solvation shells (shown for first 3 shells). Probe and lipid centers-of-mass (circles) are projected onto the plane of the bilayer. The reference center-of-mass (square) is taken to be the origin, and shell inner and outer radii are defined such that shell *n* contains on average 6*n* lipids (see Equation 2.3). A DPPC molecule is considered to be contained in shell *n* if $r_{n-1} \leq r < r_n$ (with $r < r_0$ assigned to the first shell for same leaflet lipids, and assigned to shell 0 for opposite leaflet lipids).

these definitions, lipids residing in shell $n > 0$ (both leaflets) are directly opposite each other in the bilayer, while shell 0 contains the probe and opposing DPPC molecule. The simulation box was divided into shells 0–10 using this scheme, with all remaining lipids considered to be in the 11^{th} shell. For DiI simulations, the reference molecule was in every case the probe itself. For simulations containing only DPPC, the reference DPPC was randomly chosen in each frame (rather than referencing to the inserted DPPC), which allows for better sampling of the system and so produces more accurate results. This method is justified, as the insertion of DPPC did not influence any aspect of the simulation (data not shown).

In addition to neglecting any short range positional order of the fluid bilayer, our definition of shells neglects the average area of the probe molecule (which will in general be different than that of the host lipid), as well as any distance-dependent perturbations of lipid areas. Though somewhat crude, the method nevertheless partitions the simulation box such that each shell contains an average of ~ 6*n* lipids (Table A.1). We note however that while this type of partitioning is often used, it results in a particularly interesting artifact: lipids with larger areas (and greater disorder) are preferentially "squeezed" into higher shell numbers for same-leaflet lipids (Figure A.1). This is likely because the total shell area increases with shell number, with the result that a lipid with a larger area is more likely to be assigned to a higher shell. A similar phenomenon (though with the opposite result) is seen when using a partitioning scheme based on the Voronoi tessellation (data not shown). In this case, lipids with smaller areas (and higher order) are preferentially squeezed into higher shell numbers. This phenomenon is known from theory and has been studied in 3D simulations of water hydration shells (33). Therefore, regardless of the partitioning scheme, care must be taken to account for such shell-dependent trends. For our partitioning methodology, we report our average shell measurements as a ratio:

we divide the shell *n* average for a DiI-containing bilayer by the corresponding shell *n* average for the pure DPPC bilayer.

Finally, we note that for the purposes of calculating error bars, each leaflet is considered to be an independent simulation (i.e., 12 bilayer simulations yield a total of 24 data sets). We performed a cross-correlation analysis of the parameters discussed in the text (i.e., $\langle S_{CD} \rangle$ and P-N vector orientation) to verify complete independence across simulations for the production run (data not shown). Ratios are reported with error bars corresponding to 95% confidence intervals. In all other cases, error bars correspond to one standard deviation.

2.4 Results

2.4.1 Systems equilibrate within the first 10 ns of production run

Simulation equilibration is essential to ensure accurate and realistic results. Area per lipid (APL) is one standard way to determine when a membrane simulation is equilibrated and can be used to check if the system is physically sensible (34). Figure 2.3*A* shows APL versus time for a representative production run of a pure DPPC bilayer. The APL for a given snapshot was calculated as the area of the simulation box divided by the number of lipids per leaflet. For the graph shown, the data were smoothed using boxcar averaging over 10 consecutive frames (black curve). The APL is equilibrated after the first 10 ns (dashed gray line), and indeed the APL over the last 50 ns never drifts far from the average APL of 63.9 ± 0.6 $Å^2$ (red line) calculated over the same time. This value is in good agreement with the experimentally measured APL of a pure DPPC bilayer of 63.0 $Å^2$ at 323 K (35).

To further confirm the complete equilibration within the first 10 ns of the production run, we looked at the transverse positions of various bilayer components over the full production run. Figure 2.3*B* shows the locations of the DPPC phosphorus and nitrogen, and the centers of mass

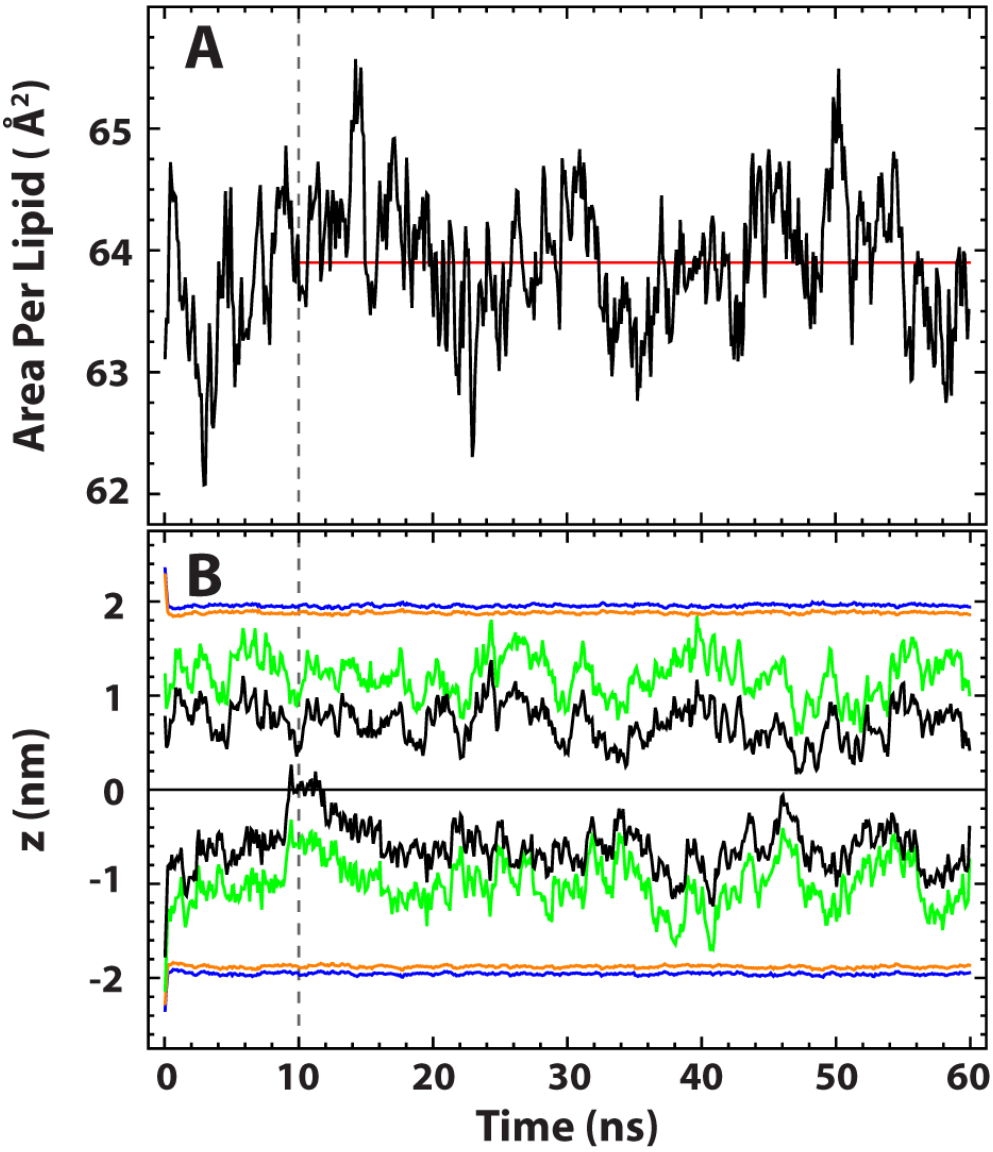

Figure 2.3 Representative data showing equilibration of simulations within 10 ns. A) APL during a representative 60 ns simulation of a pure DPPC bilayer. The average value over the final 50 ns (red line) is consistent with the experimentally measured value for DPPC (35). B) Transverse bilayer position with respect to bilayer midplane (z = 0 nm) of DPPC nitrogen (blue) and phosphate (orange), and center-of-mass of the DiI chromophore (green) and entire DiI molecule (black).

of the DiI-C18:0 chromophore and entire molecule, for a representative simulation. The bilayer center of mass is located at z = 0 nm. The initial thickness and rapid movement of bilayer components towards the bilayer center of mass is due to the system transitioning from the NVT to NPT ensemble. After 10 ns, the positions do not fluctuate significantly, nor do they drift. Additionally, as described in reference (20), the DiIs are fully buried within the bilayer by 10 ns and remain oriented with their chromophore close to the water. Similar equilibrations were seen in the systems containing DiI-C18:2 and DiI-C12:0 (Figure A.2). These results indicate that the simulations are fully equilibrated within the first 10 ns of the production run, and we therefore use only the last 50 ns for the following analysis.

2.4.2 DiI localization

A snapshot of the equilibrated bilayer at the end of a production run is shown in Figure 2.4, demonstrating the DiI location within the hydrocarbon-dense region of the bilayer. Average mass density profiles shown in Figure 2.5 further reveal trends for the DiI position within the bilayer, confirming the probe location and orientation with respect to the bilayer interface over the last 50 ns. These data are in agreement with previous simulations (20). Mass density profiles for DiI-C18:2 and DiI-C12:0 are included in Figure A.3.

Each simulation consists of two DiI molecules, one in each leaflet. The position of the two probes with respect to each other is an important aspect of our analysis: Since we wish to study the probe's effect on lipids in the same and opposing leaflets, it is important that the two DiI molecules remain well-separated to minimize competing effects on nearby lipids. Using the shell partitioning scheme described in Section 2.3, we find that the DiI molecules are located ~ 10 shells apart for most of the simulation, with an average separation distance of 7.4 ± 0.7 nm, 7.1 ± 0.7 nm, and 7.2 ± 0.9 nm (for DiI-C18:0, DiI-C18:2 and DiI-C12:0, respectively). We

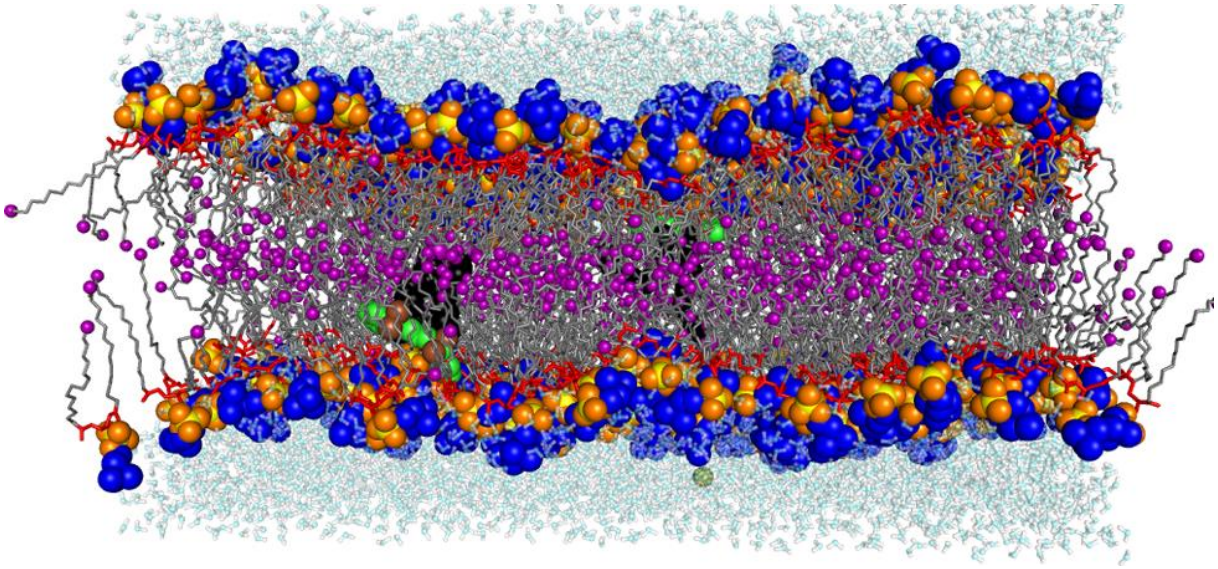

Figure 2.4 Representative simulation snapshot reveals DiI-C18:0 location in the bilayer (colors as in Figure 2.1). DPPC phosphate (orange/yellow) and choline-$(CH_2)_2$ (blue) are shown with space filling spheres, glycerol-carbonyl (red) and methylene groups (gray) are shown as sticks, and terminal methyls (purple) as small spheres. The DiI chromophore (green) is found beneath the DPPC headgroups, predominantly within the hydrophobic interior of the bilayer. Chloride ions (green spheres) were added to neutralize the positive charge of the DiI chromophore. Water (aqua and white) shown as ball-and-sticks.

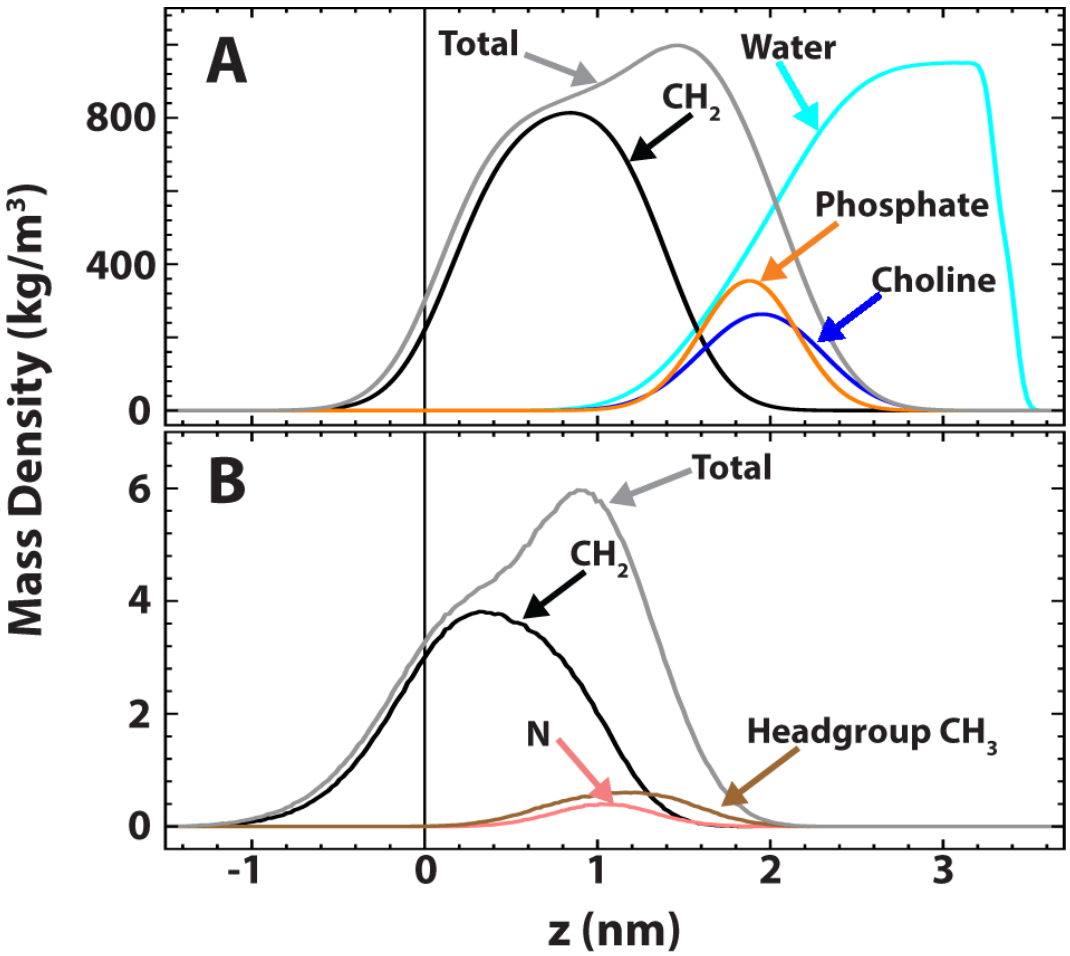

Figure 2.5 Average single-leaflet mass density profiles. A) Average densities of DPPC components and water for pure DPPC simulations. B) Average densities for DiI-C18:0 components reveal its location and orientation within the bilayer. Bilayer midplane at z = 0 nm.

conclude that probe effects seen in the first few solvation shells are unlikely to be influenced by the opposite-leaflet probe.

2.4.3 DiI is significantly more disordered than DPPC

To assess the differences between the DiI and DPPC molecules at an atomic level, we measured the order parameter of their hydrocarbon chains. We calculated carbon-deuterium order parameters for lipid chains as:

$$S_{CD} = \langle 3\cos^2\theta - 1 \rangle / 2 \qquad (2.4)$$

where θ is the angle between the C-D bond and the magnetic field (chosen to be parallel to the membrane normal); locations of the deuterium atoms were calculated based on ideal bond geometry.

The average segmental S_{CD} profiles for the reference molecule chains are shown in Figure 2.6. (N.B. Carbon numbering for a chain starts at the carbonyl carbon for DPPC and at the first methylene carbon for the probes; numbering then increases down the chain.) We find that all DiI chains are more disordered than DPPC chains. The saturated 12:0 and 18:0 chains have similar profiles, whereas the double bonds introduce significant disorder in the 18:2 chains. Both the substantial disorder of the probe chains and the location of the bulky chromophore among the DPPC chains raise the possibility of local perturbations of DPPC molecules.

2.4.4 DiI perturbs the order of nearby lipids in the same and opposing leaflets

We examined the effect of an inserted DiI molecule on the overall chain order of successive shells of DPPC. The order parameter for each shell was calculated as an average over all DPPC *sn*-1 and *sn*-2 methylene carbons. To quantify the order perturbation induced by the probe, we calculated an order ratio (*i.e.*, the order parameter of a DiI-containing bilayer was divided by the corresponding order parameter of a DPPC bilayer).

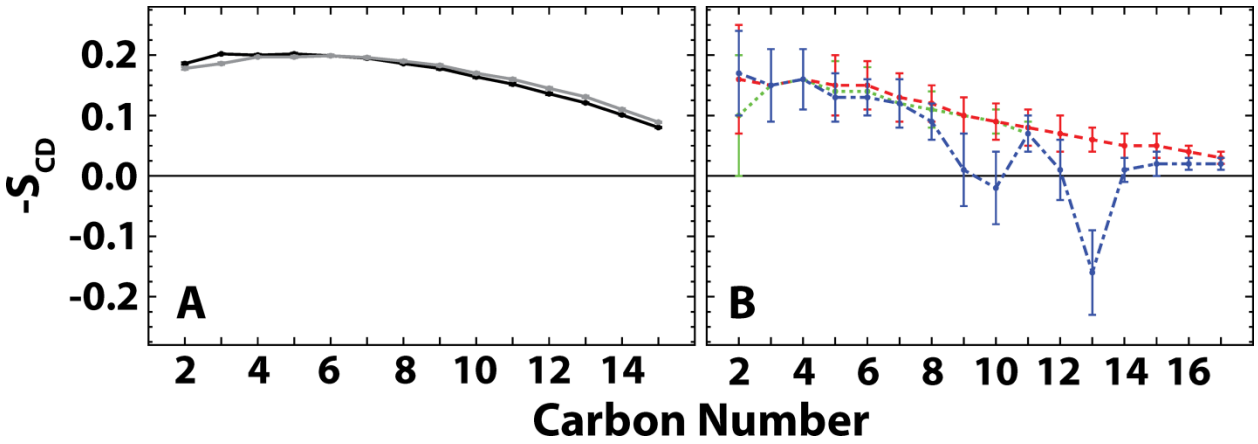

Figure 2.6 Segmental order parameter profiles for DPPC and DiI probes. A) DPPC *sn*-1 (black solid) and *sn*-2 (gray solid) profiles from a probe-free bilayer. B) DiI-C18:0 (red dashed) and DiI-C12:0 (green dotted) show similar order. Double bonds at carbon numbers 9–10 and 12–13 result in significant disordering of the DiI-C18:2 chains (blue dot-dashed). Error bars indicate the standard deviation.

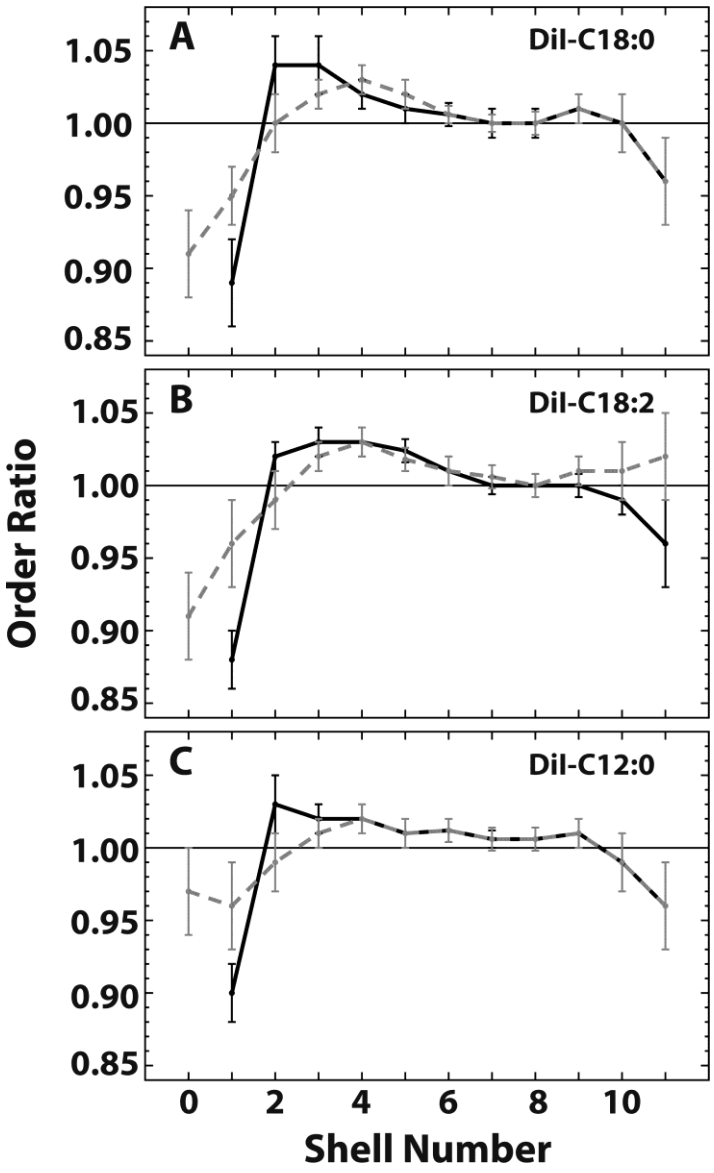

Figure 2.7 Order ratios reveal DiI-induced perturbations. DPPC order ratio by shell for bilayers containing A) DiI-C18:0, B) DiI-C18:2 and C) DiI-C12:0, for same-leaflet lipids (black solid) and opposite leaflet lipids (gray dashed). Error bars indicate 95% confidence intervals.

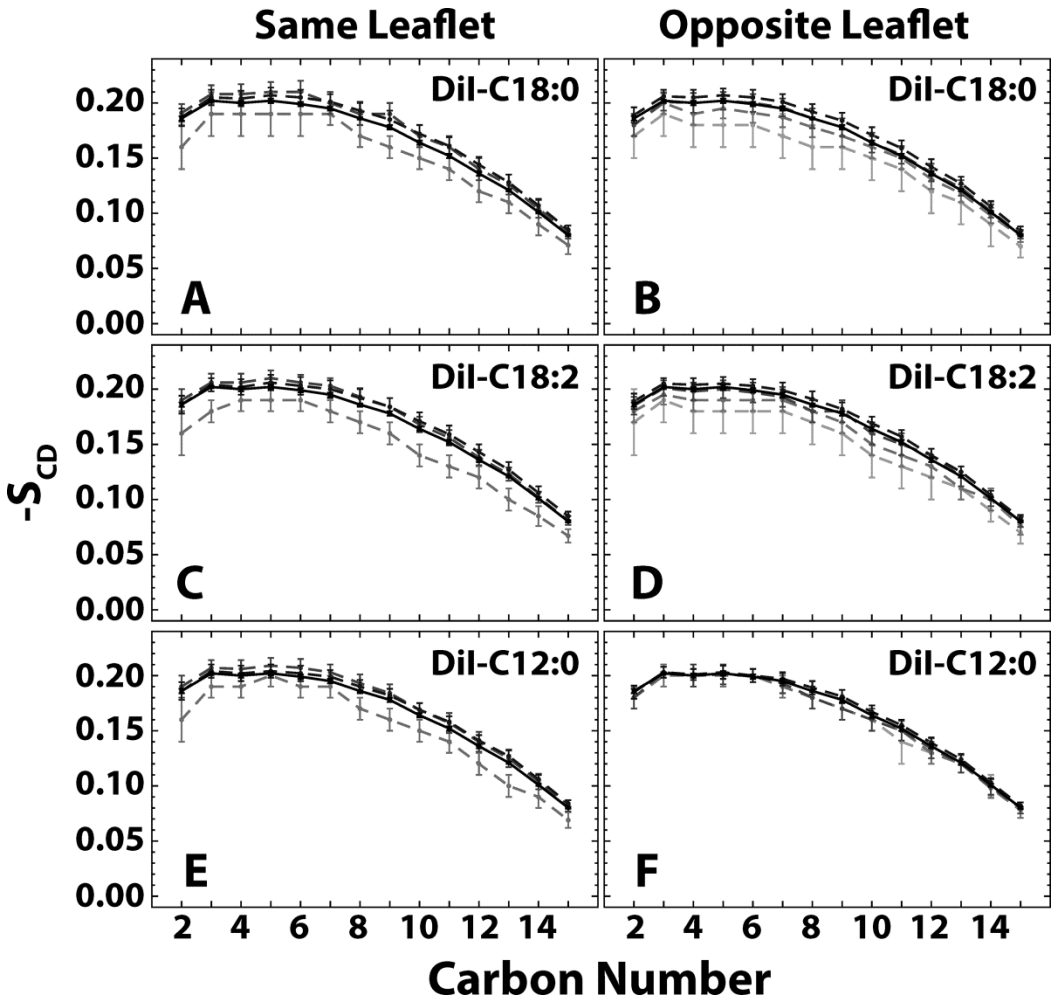

Figure 2.8 Order perturbations do not vary along chains. Order parameter of DPPC *sn*-1 carbons shown for same leaflet lipids (left) and opposite leaflet lipids (right) for bilayers containing A,B) DiI-C18:0, C,D) DiI-C18:2 and E,F) DiI-C12:0. Shells $n \leq 3$ are shown (gray dashed), with darker grays indicating increased shell number. Overall average *sn*-1 order of a pure DPPC bilayer (black solid) is shown for comparison. Error bars indicate the standard deviation.

Figure 2.7 shows the distance-dependent order ratio for the three DiI bilayer systems. DiI-C18:0, DiI-C18:2, and DiI-C12:0 (Figure 2.7*A*-*C*, respectively) each perturb same-leaflet lipids to a similar degree, inducing a ~ 10–12% *decrease* in chain order in first-shell lipids compared to the pure DPPC bilayer. Interestingly, second-shell lipids show a ~ 2–4% *increase* in order. Increased order persists for several shells and then gradually returns towards the unperturbed value.

In the opposite leaflet, DiI-C18:0 and DiI-C18:2 decrease the order of zeroth-shell lipids (i.e., located directly opposite the probe) by ~ 9%. Order gradually increases with increasing shell number, exceeds the order of unperturbed DPPC beginning at shell 4, and then gradually decreases towards the unperturbed value. Compared to long-chain DiIs, DiI-C12:0 causes only minor perturbations to zeroth-shell lipids in the opposite leaflet. Beyond the zeroth shell, perturbations are similar for all DiI regardless of chain length: order first increases, followed by a gradual decrease towards the unperturbed state. For all DiIs, the same and opposite leaflet order closely match in shells ~ 6–9. For shells 10–11, the observed decrease in order is likely due to the effect of the second (opposite leaflet) DiI. A complete listing of order parameters is included in Table A.2.

2.4.5 Carbon order perturbation depends on shell, not carbon number

To examine dye-induced order perturbations in more detail, we investigated how the segmental order of the DPPC chain varies by shell. Figure 2.8 shows the DPPC *sn*-1 segmental chain order as a function of shell for shells $n \leq 3$. Distance from the probe is indicated by grayscale dashed lines, with progressively darker gray indicating increasing shell number. The average segmental order profile of a pure DPPC bilayer (solid black line) is shown for comparison.

All three probes perturb the order of nearby, same-leaflet lipids. DiI-C18:0 and DiI-C18:2 also perturb opposite-leaflet lipids, while only minor changes are seen for DiI-C12:0. Despite the differences among the probe chains and between the probe chains and the host DPPC, no carbon appears to be significantly more perturbed than any other. This implies that the magnitude of chain order perturbations occur uniformly over the length of the DPPC chain, regardless of distance from the probe. These results are similar for the DPPC *sn*-2 chain (Figure A.4).

2.4.6 DiI causes reorientation of local lipid headgroups

We used the same distance-dependent analysis to study the DPPC P-N vector orientation, defined as the angle between the DPPC P-N vector and the bilayer normal (i.e., an angle of 0º (90º) indicates that the P-N vector is perpendicular (parallel) to the bilayer plane). For a pure DPPC bilayer, the average P-N vector orientation was 79.5 ± 0.2°. Figure 2.9 shows the P-N vector orientation ratio between DiI-containing and pure DPPC bilayers, for same-leaflet lipids. Compared to a pure DPPC bilayer, the P-N vector of first-shell lipids preferentially points away from the DiI. The P-N angle is ~ 11% smaller for shell 1 lipids near a DiI, compared to a pure DPPC bilayer. Significant perturbation also exists in shell 2, before returning to unperturbed values by shell 5. This result indicates that for DPPC close to a DiI, the P-N vector tends to reorient out of the plane of the bilayer, away from the DiI. In contrast, we did not observe any significant changes in orientation of the P-N vector for opposite leaflet lipids (Figure A.5). A complete listing of P-N vector angles by shell is included in Table A.3.

2.5 Discussion

Perturbation of DPPC by fluorescent probes within the same leaflet are nearly identical for all probes examined. Both acyl chain ordering as well as P-N vector reorientation are similar for same-leaflet DPPC, regardless of the DiI chain length or degree of unsaturation, whereas

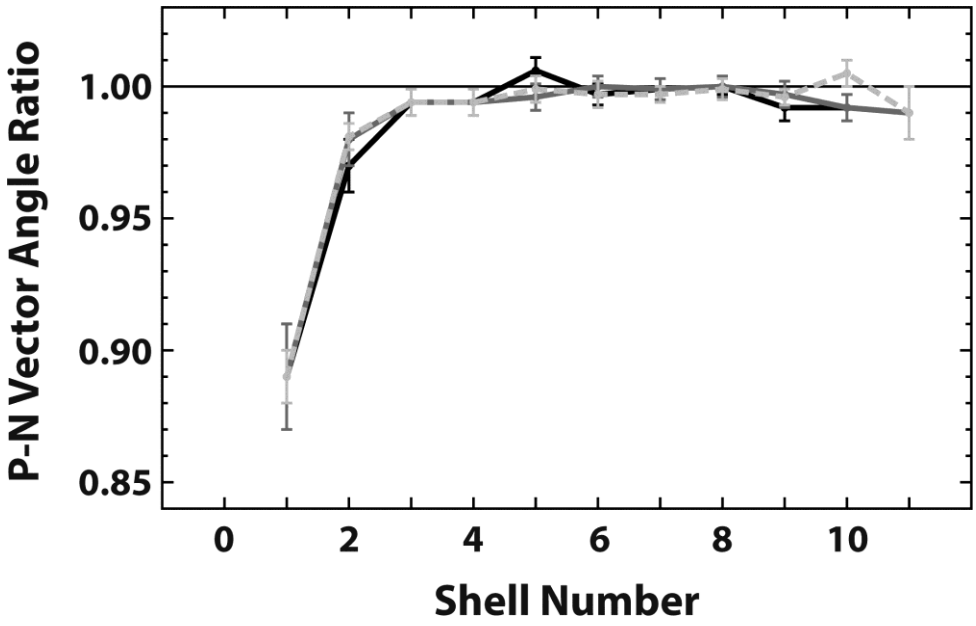

Figure 2.9 DPPC headgroups preferentially point away from the DiI within the same leaflet. P-N vector angle ratio by shell for same-leaflet lipids in bilayers containing DiI-C18:0 (black), DiI-C18:2 (dark gray), and DiI-C12:0 (light gray dashed), compared to a pure DPPC bilayer. Error bars indicate 95% confidence intervals.

differences in chain order were observed for DPPC in the opposite leaflet. Looking more closely at why these three different DiIs would have such similar influence on their nearest neighbor lipids but have different effects on opposite leaflet lipids, Figure 2.10 emphasizes similarities and differences of the DiI. The bulky, positively-charged DiI chromophore resides ~ 1.0–1.1 nm from the bilayer center, independent of probe chain length or degree of unsaturation. In contrast, the chains themselves, as shown by protrusion of terminal methyls into the opposing leaflet, differ significantly for the three probes. It is reasonable to conclude that these properties are responsible for the observed shell dependent effects.

For the three types of DiI we studied, the positively charged chromophore seems at first glance to be located surprisingly deep in the bilayer. It is likely that the strong delocalization of the charge over a large volume decreases the hydration energy (36, 37) and allows for a stable location beneath the lipid headgroups. For a similar chromophore, Krishna and Periasamy found that a variant with two-carbon chains does indeed create a more watery location, but a deep location was also observed (38), supporting the finding here that the bulky, charged DiI chromophore can be located within the bilayer. Though our simulations are not long enough to predict flip-flop rates, we believe that the chromophore position just beneath the lipid carbonyls is energetically favorable and stable due in part to the bilayer potential. As reviewed by Wang (39), all-atom membrane simulations show a dipole potential that peaks in the bilayer center. For UA simulations of a DPPC bilayer, Gullapalli et al. showed that the presence of charged DiI increases the potential difference between the carbonyl region and the bilayer center (20). Thus the hydrophobic nature of the DiI drives it into the bilayer, where it is energetically unfavorable for it to flip to the other leaflet.

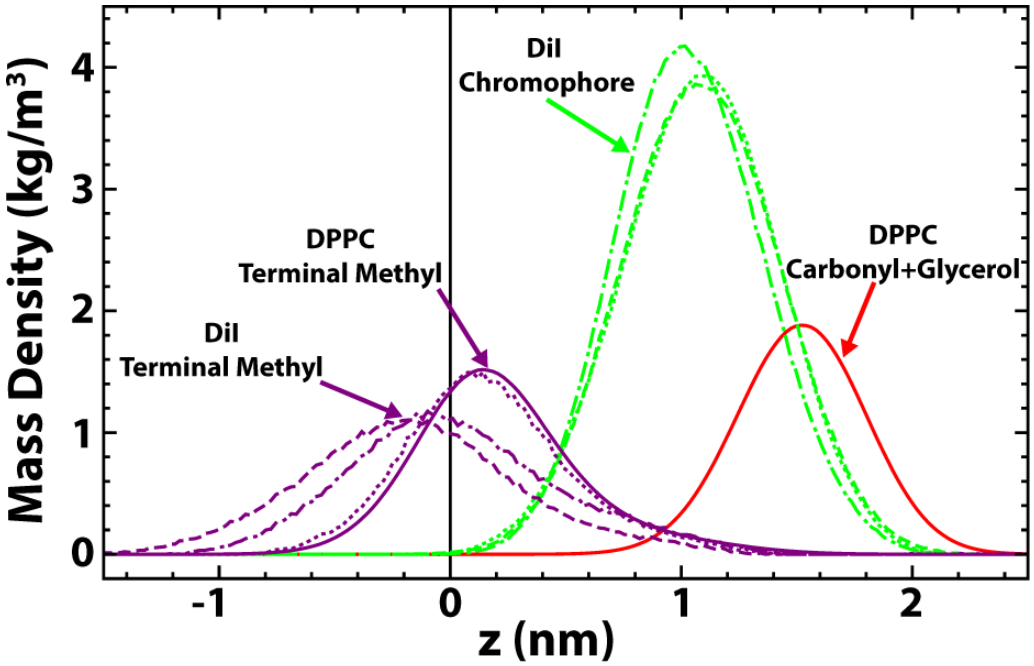

Figure 2.10 Mass densities show similarities and differences in reference molecule locations. The chromophore (green) of DiI-C18:0 (dashed), DiI-C18:2 (dot-dashed), and DiI-C12:0 (dotted) reside beneath the hydrophilic carbonyl-glycerol group of an average DPPC (red solid). The terminal methyl (purple) of DiI-C18:0 (dashed) and DiIC-18:2 (dot-dashed) show significant protrusion into the opposing leaflet, whereas DiI-C12:0 (dotted) protrudes to approximately the same extent as an average DPPC (solid). Terminal methyl densities are multiplied by a factor of 4 for visibility, and DPPC densities are reported as an average for a pure DPPC bilayer.

2.5.1 Chromophore location likely causes same-leaflet order perturbations

Despite significant differences in chain length, degree of unsaturation, and order between the DiI molecules tested, the order parameter effects on same-leaflet DPPC were similar for DiI-C18:0, DiIC-18:2, and DiI-C12:0. This implies that the probe chains cannot solely be responsible for the disordering of same-leaflet lipids. This is supported by the observation that all carbons along a DPPC chain are perturbed uniformly and independently of DiI chain structure. Therefore, it is more likely that the bulky headgroup of the DiI and its location within the bilayer have a significant disordering effect on neighboring lipid chains. One possible explanation could be that the DiI chromophore, residing among the hydrocarbon chains, causes the chains to kink. Another possibility is that free space under the DiI chromophore allows for more motional freedom and disordering of the lipids.

The increased order of same-leaflet lipids in shells ~ 2–6 reveal that bilayer perturbations do not decay monotonically to the unperturbed state with increasing distance from the probe, but instead have a gently oscillating perturbation profile. Damped oscillations in bilayer thickness near protein or lipid inclusions are predicted from theory (40–42), and arise from an interplay between the perturbing molecule and the mechanical properties of the unperturbed bilayer. The observed behavior may be a manifestation of such mechanical perturbations.

2.5.2 DiI charge changes local electrostatic environment

It was previously observed that in a 128 lipid system of fluid phase DPPC, the P-N vector angle points out of the bilayer to a greater extent in the presence of charged DiI, whereas no significant change is seen in the presence of uncharged DiI (20). The authors concluded that the positively charged DiI chromophore was responsible for the DPPC headgroup reorientation, due to electrostatic repulsion. Our results support this conclusion, since we find that DiI has a similar

chromophore localization beneath the charged DPPC headgroups, and induces similar DPPC headgroup reorientations, regardless of the probe's alkyl chain structure. Since the nitrogen of the P-N vector and the DiI chromophore are both positively charged, it is likely that electrostatic repulsion is at least in part responsible for the headgroup reorientation out of the bilayer plane and towards the solvent. The gradual decay of P-N reorientation with increasing distance from the chromophore is also consistent with electrostatic repulsion. Furthermore, the decreased order in first-shell lipids increases the area taken up by the hydrophobic chains. We would expect any increased chain area to be accompanied by increased shielding by the hydrophilic headgroup, similar to headgroup shielding of the largely hydrophobic cholesterol according to the umbrella model (43). However, we observe that in the presence of DiI, the P-N vector of neighboring DPPC points out of the bilayer to a greater extent, indicating decreased headgroup shielding. This implies that some other effect must be controlling headgroup orientation. We conclude that the location and charge of the chromophore are likely responsible for the observed lipid headgroup reorientations. This would also explain the lack of P-N vector reorientation in opposite leaflet lipids, as their headgroups are far from the charged chromophore.

2.5.3 Probe chain protrusion enables communication of information across the bilayer midplane

DiI can have a significant impact on lipids in the opposite leaflet, as was also seen in MD studies of PyrPC (16). DiI-C18:0 and DiI-C18:2 caused decreased order in DPPC chains directly across from the probes, whereas DiI-C12:0 did not. We are confident that such effects do not result from the presence of DiI in the opposite leaflet, since the two DiI molecules are separated by ~ 7 nm. Rather, this opposite leaflet effect is likely due to protrusion of the probe hydrocarbon chains into the opposite leaflet. As seen in Figure 2.10, there is substantial protrusion of DiI chains, which progressively decreases in the series 18:0 > 18:2 > 12:0 ≈ 16:0

(DPPC). This is consistent with the idea that the presence of these chains in the opposite leaflet causes order perturbations, rather than free space beneath the chromophore or other dye properties.

2.5.4 Small lipid domains are negligibly affected by DiI, but averages mask perturbation trends

When viewed as ensemble averages over all DPPC in a simulation, both acyl chain order and P-N vector orientation show only minimal perturbations. Compared to the ensemble order for a pure DPPC bilayer, changes of 0.6 ± 0.4%, 0.6 ± 0.4% and 0.8 ± 0.3% in ensemble order are seen for bilayers containing DiI-C18:0, DiI-C18:2, and DiI-C12:0, respectively. Compared to the ensemble P-N vector orientation in a pure DPPC bilayer, changes of -0.5 ± 0.1%, -0.6 ± 0.1% and -0.6 ± 0.1% are seen in ensemble P-N vector orientations for DiI-C18:0, DiI-C18:2, and DiI-C12:0, respectively. Thus, even in a patch of just a few hundred lipids per leaflet, less than a 1% change is seen in both order and P-N vector orientation. We conclude that the probes studied can effectively be used to examine the properties of nanodomains without significant perturbation of average bilayer properties so long as the probe concentrations within the nanodomains remain low.

We caution though that small changes in ensemble averages cannot always be used as a determination of probe fidelity. Some experiments rely on measuring small changes of probe fluorescence properties, and spin-labeled probes in particular report directly on the order of their local environment. Thus even if these types of probes have a minor effect on ensemble bilayer properties, they could still alter their local order or electrostatic environment and thereby distort measurements. Such significant effects in the same and opposite leaflet would have been masked in these simulations if only average ensemble properties were taken into account. Furthermore, the smaller the simulation size, the greater the extent to which local perturbations near the probe

can skew ensemble averages. Obtaining physically relevant and accurate results therefore requires distance-dependent analyses in large simulations which allow enough room for perturbations to both exist and decay. We emphasize that to gain statistically significant results in such systems, when measuring parameters in shells with fewer than 10 lipids, many long simulations are required.

2.6 Conclusions

MD simulations are a powerful tool for examining the spatial extent of bilayer perturbations of a fluorescent lipid analog. Using MD, we find significant perturbations of the local environment of DiI probes, even for lipids across from the probe in the opposite leaflet. For DPPC molecules near a DiI, we observe: 1) substantial localized disordering and minor persistent ordering caused by chromophore location and hydrocarbon protrusion, and 2) localized headgroup reorientation caused by chromophore location and charge. These small-scale ordering and electrostatic changes are inherently impossible to observe using conventional experimental techniques, especially those which rely on properties of the probe which may themselves be altered by the locally perturbed environment. When analysis is limited to only average bilayer properties, these local probe effects can be misunderstood or even masked altogether. Even though the DiI molecules may significantly perturb local DPPCs, these ensemble averages show that they *do not* significantly alter the properties of nanodomain patches containing a few hundred lipids. Our simulations indicate that at low local concentrations DiI will not alter membrane phase behavior (i.e., phase boundaries and tielines), and can therefore be used reliably to study nanodomains. However, while not a detriment for DiI molecules, the local perturbations caused by fluorescent probe molecules may be critical for other types of probes like spin-labels, which report directly on properties of their local environment. In the future, we plan to

investigate other probes to determine if such effects exist, and how large a role they would play in accurately interpreting information reported by the probe.

REFERENCES

1. Jähnig, F. 1979. Structural order of lipids and proteins in membranes: evaluation of fluorescence anisotropy data. Proc. Natl. Acad. Sci. U.S.A. 76: 6361–6365.

2. Klymchenko, A.S., Y. Mély, A.P. Demchenko, and G. Duportail. 2004. Simultaneous probing of hydration and polarity of lipid bilayers with 3-hydroxyflavone fluorescent dyes. Biochim. Biophys. Acta. 1665: 6–19.

3. Sims, P.J., A.S. Waggoner, C.-H. Wang, and J.F. Hoffman. 1974. Studies on the mechanism by which cyanine dyes measure membrane potential in red blood cells and phosphatidylcholine vesicles. Biochemistry. 13: 3315–3330.

4. Scherfeld, D., N. Kahya, and P. Schwille. 2003. Lipid dynamics and domain formation in model membranes composed of ternary mixtures of unsaturated and saturated phosphatidylcholines and cholesterol. Biophys. J. 85: 3758–68.

5. Parasassi, T., G. De Stasio, G. Ravagnan, R.M. Rusch, and E. Gratton. 1991. Quantitation of lipid phases in phospholipid vesicles by the generalized polarization of Laurdan fluorescence. Biophys. J. 60: 179–189.

6. Heberle, F.A., J.T. Buboltz, D. Stringer, and G.W. Feigenson. 2005. Fluorescence methods to detect phase boundaries in lipid bilayer mixtures. Biochim. Biophys. Acta - Mol. Cell Res. 1746: 186–192.

7. Veatch, S.L., and S.L. Keller. 2005. Seeing spots: Complex phase behavior in simple membranes. Biochim. Biophys. Acta - Mol. Cell Res. 1746: 172–185.

8. Bagatolli, L., and P.B.S. Kumar. 2009. Phase behavior of multicomponent membranes: Experimental and computational techniques. Soft Matter. 5: 3234–3248.

9. Honerkamp-Smith, A.R., P. Cicuta, M.D. Collins, S.L. Veatch, M. den Nijs, M. Schick, and S.L. Keller. 2008. Line tensions, correlation lengths, and critical exponents in lipid membranes near critical points. Biophys. J. 95: 236–246.

10. Heberle, F.A., J. Wu, S.L. Goh, R.S. Petruzielo, and G.W. Feigenson. 2010. Comparison of three ternary lipid bilayer mixtures: FRET and ESR reveal nanodomains. Biophys. J. 99: 3309–18.

11. Ethier, M.F., D.E. Wolf, and D.L. Melchiort. 1983. Calorimetric Investigation of the Phase Partitioning of the Fluorescent Carbocyanine Probes in Phosphatidylcholine Bilayers. Biochemistry. 22: 1178–1182.

12. Veatch, S.L., S.S.W. Leung, R.E.W. Hancock, and J.L. Thewalt. 2007. Fluorescent probes alter miscibility phase boundaries in ternary vesicles. J. Phys. Chem. B. 111: 502–4.

13. Lesslauer, W., J.E. Cain, and J.K. Blasie. 1972. X-ray diffraction studies of lecithin bimolecular leaflets with incorporated fluorescent probes. Proc. Natl. Acad. Sci. U.S.A. 69: 1499–1503.

14. Podo, F., and J.K. Blasie. 1977. Nuclear magnetic resonance studies of lecithin bimolecular leaflets with incorporated fluorescent probes. Proc. Natl. Acad. Sci. U.S.A. 74: 1032–6.

15. Repáková, J., J.M. Holopainen, M.R. Morrow, M.C. McDonald, P. Čapková, and I. Vattulainen. 2005. Influence of DPH on the structure and dynamics of a DPPC bilayer. Biophys. J. 88: 3398–3410.

16. Repáková, J., J.M. Holopainen, M. Karttunen, and I. Vattulainen. 2006. Influence of pyrene-labeling on fluid lipid membranes. J. Phys. Chem. B. 110: 15403–10.

17. Loura, L.M.S., and J.P.P. Ramalho. 2007. Location and dynamics of acyl chain NBD-labeled phosphatidylcholine (NBD-PC) in DPPC bilayers. A molecular dynamics and time-resolved fluorescence anisotropy study. Biochim. Biophys. Acta - Biomembr. 1768: 467–478.

18. Loura, L.M.S., F. Fernandes, A.C. Fernandes, and J.P.P. Ramalho. 2008. Effects of fluorescent probe NBD-PC on the structure, dynamics and phase transition of DPPC. A molecular dynamics and differential scanning calorimetry study. Biochim. Biophys. Acta. 1778: 491–501.

19. Loura, L.M.S., and J.P. Prates Ramalho. 2009. Fluorescent membrane probes' behavior in lipid bilayers: insights from molecular dynamics simulations. Biophys. Rev. 1: 141–148.

20. Gullapalli, R.R., M.C. Demirel, and P.J. Butler. 2008. Molecular dynamics simulations of DiI-C18(3) in a DPPC lipid bilayer. Phys. Chem. Chem. Phys. 10: 3548–60.

21. Hess, B., C. Kutzner, D. van Der Spoel, and E. Lindahl. 2008. GROMACS 4: Algorithms for highly efficient, load-balanced, and scalable molecular simulation. J. Chem. Theory Comput. 4: 435–447.

22. Oostenbrink, C., A. Villa, A.E. Mark, and W.F. Van Gunsteren. 2004. A biomolecular force field based on the free enthalpy of hydration and solvation: The GROMOS force-field parameter sets 53A5 and 53A6. J. Comput. Chem. 25: 1656–1676.

23. Berger, O., O. Edholm, F. Jähnig, and F. Jahnig. 1997. Molecular dynamics simulations of a fluid bilayer of dipalmitoylphosphatidylcholine at full hydration, constant pressure, and constant temperature. Biophys. J. 72: 2002–13.

24. Muddana, H.S., R.R. Gullapalli, E. Manias, and P.J. Butler. 2011. Atomistic simulation of lipid and DiI dynamics in membrane bilayers under tension. Phys. Chem. Chem. Phys. 13: 1368–78.

25. Chiu, S.-W., M. Clark, V. Balaji, S. Subramaniam, H.L. Scott, and E. Jakobsson. 1995. Incorporation of surface tension into molecular dynamics simulation of an interface: a fluid phase lipid bilayer membrane. Biophys. J. 69: 1230–1245.

26. Tieleman, D.P., and H.J.C. Berendsen. 1996. Molecular dynamics simulations of a fully hydrated dipalmitoylphosphatidylcholine bilayer with different macroscopic boundary conditions and parameters. J. Chem. Phys. 105: 4871–4880.

27. Van Der Spoel, D., E. Lindahl, B. Hess, G. Groenhof, A.E. Mark, and H.J.C. Berendsen. 2005. GROMACS: Fast, flexible, and free. J. Comput. Chem. 26: 1701–1718.

28. Lindahl, E., B. Hess, and D. van der Spoel. 2001. GROMACS 3.0: a package for molecular simulation and trajectory analysis. J Mol Model. 7: 306–317.

29. Essmann, U., L. Perera, M.L. Berkowitz, T. Darden, H. Lee, and L.G. Pedersen. 1995. A smooth particle mesh Ewald method. J. Chem. Phys. 103: 8577–8593.

30. Patra, M., M. Karttunen, M.T. Hyvönen, E. Falck, P. Lindqvist, and I. Vattulainen. 2003. Molecular dynamics simulations of lipid bilayers: major artifacts due to truncating electrostatic interactions. Biophys. J. 84: 3636–45.

31. Kim, T., K. Il Lee, P. Morris, R.W. Pastor, O.S. Andersen, and W. Im. 2012. Influence of hydrophobic mismatch on structures and dynamics of gramicidin A and lipid bilayers. Biophys. J. 102: 1551–60.

32. Venturoli, M., B. Smit, and M.M. Sperotto. 2005. Simulation studies of protein-induced bilayer deformations, and lipid-induced protein tilting, on a mesoscopic model for lipid bilayers with embedded proteins. Biophys. J. 88: 1778–98.

33. Voloshin, V.P.P., A.V. Anikeenko, N.N. Medvedev, A. Geiger, and D. Stoyan. 2010. Hydration Shells in Voronoi Tessellations. 2010 Int. Symp. Vor. Diagrams Sci. Eng. : 254–259.

34. Anézo, C., A.H. de Vries, H.-D. Höltje, D.P. Tieleman, and S.-J. Marrink. 2003. Methodological Issues in Lipid Bilayer Simulations. J. Phys. Chem. B. 107: 9424–9433.

35. Kučerka, N., J.F. Nagle, J.N. Sachs, S.E. Feller, J. Pencer, A. Jackson, and J. Katsaras. 2008. Lipid bilayer structure determined by the simultaneous analysis of neutron and X-ray scattering data. Biophys. J. 95: 2356–2367.

36. Severin, F.F., I.I. Severina, Y.N. Antonenko, T.I. Rokitskaya, D.A. Cherepanov, E.N. Mokhova, M.Y. Vyssokikh, A. V Pustovidko, O. V Markova, L.S. Yaguzhinsky, G.A. Korshunova, N. V Sumbatyan, M. V Skulachev, and V.P. Skulachev. 2010. Penetrating cation/fatty acid anion pair as a mitochondria-targeted protonophore. Proc. Natl. Acad. Sci. U.S.A. 107: 663–8.

37. Khuseynov, D., M.T. Fontana, and A. Sanov. 2012. Photoelectron spectroscopy and photochemistry of tetracyanoethylene radical anion in the gas phase. Chem. Phys. Lett. 550: 15–18.

38. Krishna, M.M.G., and N. Periasamy. 1999. Location and orientation of DODCI in lipid bilayer membranes : effects of lipid chain length and unsaturation. Biochim. Biophys. Acta. 1461: 58–68.

39. Wang, L. 2012. Measurements and implications of the membrane dipole potential. Annu. Rev. Biochem. 81: 615–35.

40. Dan, N., A. Berman, P. Pincus, and S. Safran. 1994. Membrane-induced interactions between inclusions. J. Phys. II. 4: 1713–1725.

41. Pata, V., and N. Dan. 2005. Effect of membrane characteristics on phase separation and domain formation in cholesterol-lipid mixtures. Biophys. J. 88: 916–924.

42. West, B., F.L.H. Brown, and F. Schmid. 2009. Membrane-protein interactions in a generic coarse-grained model for lipid bilayers. Biophys. J. 96: 101–115.

43. Huang, J., and G.W. Feigenson. 1999. A microscopic interaction model of maximum solubility of cholesterol in lipid bilayers. Biophys. J. 76: 2142–57.

CHAPTER 3
Multiscale modeling of four-component lipid mixtures: Domain composition, size, alignment, and properties of the phase interface[§]

3.1 Abstract

Simplified lipid mixtures are often used to model the complex behavior of the cell plasma membrane. Indeed, as few as four components — a high-Tm lipid, a nandomain-inducing low-Tm lipid, a macrodomain-inducing low-Tm lipid and cholesterol — can give rise to a wide range of domain sizes and patterns that are highly sensitive to lipid compositions. Though these systems are studied extensively with experiments, the molecular-level details governing their phase behavior are not yet known. We address this issue by using molecular dynamics simulations to analyze how phase separation evolves in a four-component system as it transitions from small domains to large domains. To do so, we fix concentrations of the high-Tm lipid DPPC and cholesterol, and incrementally replace the nanodomain-inducing low-Tm lipid 16:0,18:2-PC (PUPC) by the macrodomain-inducing low-melting lipid 18:2,18:2-PC (DUPC). CG simulations of this four-component system reveal that lipid demixing increases as the amount of DUPC increases. Additionally, we find that domain size and interleaflet alignment change sharply over a narrow range of replacement of PUPC by DUPC, indicating that intraleaflet and interleaflet behaviors are coupled. Corresponding UA simulations show that only lipids within ~ 2 nm of the phase interface are significantly perturbed regardless of domain composition or size. Thus, whereas the fraction of interface-perturbed lipids is negligible for large domains, it is significant for smaller ones. Together, these results reveal characteristic traits

[§] The following chapter is reproduced from: Ackerman, D.G., and G.W. Feigenson. 2015. Multiscale Modeling of Four-Component Lipid Mixtures: Domain Composition, Size, Alignment, and Properties of the Phase Interface. J. Phys. Chem. B. 119: 4240–4250. It has been modified to fit the format of this thesis.

of bilayer thermodynamic behavior in four-component mixtures, and provide a baseline for investigation of the effects of proteins and other lipids on membrane phase properties.

3.2 Introduction

The cell plasma membrane can exhibit nanoscopic mixing heterogeneities, or "rafts" (1, 2), thought to be involved in membrane trafficking, signaling, protein sequestration and virus budding (3, 4). Rafts are envisioned as distinct from the surrounding membrane, being enriched in high-Tm lipids and cholesterol (2). Although the mechanism that produces rafts is unclear in living cells, chemically defined mixtures that model the composition of the plasma membrane outer leaflet can give rise to raft-like coexistence of distinct phases (5). Of particular biological significance is the coexistence of an Lo phase, with fast translational diffusion and high chain order, and an Ld phase, with fast diffusion and low chain order. Like rafts in living cells, the Lo phase in model mixtures is enriched in high-Tm lipids and cholesterol, while the Ld phase is enriched in low-Tm lipids (5). Importantly, the properties, sizes, and even morphology of these two phases can vary greatly depending on lipid composition (5, 6) and bilayer curvature (7–10). Since cells can alter their membrane composition and shape, the complex functionality of a live cell's plasma membrane might be controlled in part by the same principles that influence Lo + Ld phase separation of model membranes.

Coexistence of Lo and Ld phases in lipid mixtures requires a minimum of three components: a high-Tm lipid (e.g. DSPC, DPPC, or sphingomyelin), a low-Tm lipid (e.g. POPC or DOPC) and cholesterol (5). Ternary model membranes containing three such components exhibit either nanoscopic Lo + Ld phase domains ("Type I" mixtures) or macroscopic Lo + Ld phase domains ("Type II" mixtures) (5). The type of mixture formed is strongly influenced by the nature of the low-Tm lipid. For example, DSPC/POPC/cholesterol is a Type I mixture (11)

whereas DSPC/DOPC/cholesterol is a Type II mixture (12). Four-component systems can exhibit a natural progression between Type I and Type II mixtures, providing a complex but biologically relevant model membrane mixture.

In a revealing quaternary mixture experiment, the fractions of DSPC and cholesterol are kept fixed while the nanodomain-inducing POPC is replaced by the macrodomain-inducing DOPC (6, 13). Using a replacement ratio defined as ρ = [DOPC]/[POPC + DOPC], a specific composition of DSPC/[POPC + DOPC]/cholesterol is chosen such that it lies within the Lo + Ld coexistence regions at both $\rho = 0$ (nanodomains) and $\rho = 1$ (macrodomains). In GUVs, compositional variation (a "trajectory") along ρ reveals stable macroscopic phase morphologies, termed "modulated phases", not seen in ternary systems (6, 13). Modulated phases have a characteristic size-scale and a variety of interesting morphologies including stripes, honeycomb and broken-up domains (6, 13). The ability to exert fine control over domain size and morphology through small changes in composition is a most useful capability of quaternary mixtures.

At a coarse level, Monte Carlo simulations and experiments have shown that the surprising range of phase morphologies observed in four-component GUVs can be explained by a competition between bending energies and line tension, the two-dimensional analog of surface tension (13, 14). The membrane curvature of GUVs makes large patches of the stiff Lo phase unfavorable compared with large domains of the pliant Ld phase; competing line tension favors the coalescence of small domains to minimize interfacial energy. In Monte Carlo simulations, high line tension that occurs at high ρ produces macroscopic domains, whereas low line tension that occurs at low ρ allows domains to break apart. Intermediate line tensions that occur at intermediate ρ yield energies comparable to bending energies, and the competition between the

two produces modulated phases (13, 14). While little is known about bending energies along a ρ-trajectory, that line tension increases with ρ is supported by both direct measurements of thermal fluctuations of domains (15), and calculations combining theoretical, simulation and experimental results (16). Together, Monte Carlo simulations and experiments suggest that line tension plays a dominant role in determining domain size and phase morphology in four-component systems.

MD simulations offer the unique capability to study the proposed or observed larger-scale behavior of quaternary mixtures with atomistic resolution. However, to our knowledge, there has yet to be a systematic MD study of such mixtures undergoing a "nano-to-macro" transition. And until recently, only two main ways existed to simulate phases in three- and four-component systems using MD: 1) predetermining initial lateral organization of atomistic lipids, or 2) using CG lipids. In 1), rather than waiting for phase separation to occur over an unattainably long computational time, the lateral organization of atomistic lipids is pre-defined to be phase-separated (17–20). This method enables high resolution and accurate analysis of the phases, at the cost of accuracy of equilibrium lateral organization. In 2), simplifications are made to the atomistic lipid and water models such that a lipid is represented by ~ 10 beads rather than ~ 100 atoms, as in the Martini model (21). CG lipid mixtures can phase separate in a reasonable amount of computational time, at the cost of atomic resolution (22–26). Neither 1) nor 2) alone is sufficient to fully understand quaternary systems, in which large-scale phase morphologies change, but also atomistic behavior of lipids is important. For phase separation studies, bridging the gap between the long timescale, low-resolution CG simulations and the short timescale, high-resolution atomistic simulations is now possible (27) with the advent of methods to convert CG models to atomistic representations (28–30).

In this report, we combine the capabilities of CG and UA simulations to investigate the phase behavior along a ρ-trajectory in a four-component lipid mixture. Our system contains cholesterol, the high-Tm lipid DPPC (4:0,4:0-PC in CG and 16:0,16:0-PC in UA), and the two low-Tm lipids PUPC (4:0,4:2-PC in CG and 16:0,18:2-PC in UA) and DUPC (4:2,4:2-PC in CG and 18:2,18:2-PC in UA). These lipids were chosen because, in the CG simulations, they reflect experimentally observed four-component phase behavior: PUPC, analogous to POPC, promotes clusters or small domains when mixed with DPPC and cholesterol, whereas DUPC, analogous to DOPC, promotes large-scale phase separation. In the simulations, we fix the overall composition such that DPPC/[PUPC + DUPC]/cholesterol ≈ 0.4/0.4/0.2. We then vary the relative fraction ρ = [DUPC]/[PUPC + DUPC] from ρ = 0 (small domains) to ρ = 1 (large domains) in ~ 0.1 increments. We first run these CG systems to equilibrium to study how domain composition, size, and alignment change over a ρ-trajectory. Then, using the program Backward (29), we convert the equilibrated CG structures to UA and run them further to measure phase properties at higher resolution, and to describe the phase interface along the ρ-trajectory. By providing a systematic analysis of the phase behavior of four-component lipid-only mixtures, this study can be used as a baseline to measure and understand how the addition of proteins affects the morphology, onset of phase separation and general phase properties of similar quaternary systems.

3.3 Computational methods

We studied lipid mixtures containing DPPC, PUPC, DUPC and cholesterol as a model four-component system, shown in Figure 3.1*A*. The bilayer patches were square with the plane of the bilayer in the xy plane and the z-axis normal to the bilayer. Each patch contained 4,608 lipids, with a total composition of DPPC/[PUPC + DUPC]/cholesterol ≈ 0.4/0.4/0.2. Eleven

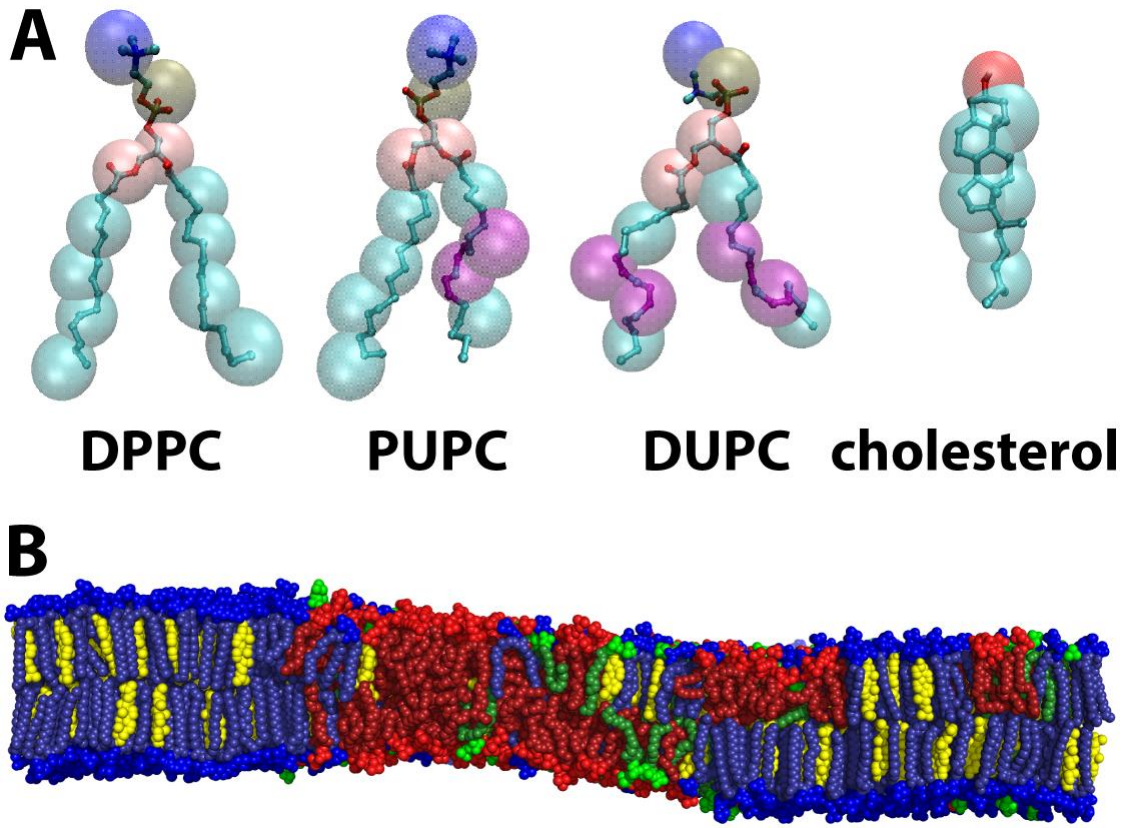

Figure 3.1 Molecules used in this study. A) CG (translucent spheres) and corresponding UA (ball-and-stick) representation of the four molecules used in this study. Purple denotes the location of double bonds. B) Snapshot of equilibrated UA bilayer for $\rho \sim 0.8$, with DPPC (blue), PUPC (green), DUPC (red) and cholesterol (yellow). Distinct regions of composition and order are observed. Molecule representations visualized in VMD version 1.9, snapshot visualized in PyMOL version 1.3.

different ρ conditions were simulated at this composition, from ρ = 0 to ρ = 1 in increments of ρ ~ 0.1. Each of the 11 simulation sets was comprised of one CG simulation and one corresponding UA simulation. Figure 3.1*B* shows a snapshot of an equilibrated UA bilayer for ρ ~ 0.8.

A complete description of bilayer construction is provided in Appendix B.1. All simulations were performed with GROMACS versions 4.0.5 and higher (31).

3.3.1 Force field and molecule parameters

CG simulations used version 2.1 of the Martini force field (21, 32), with all beads having the same mass. Lipid (33), cholesterol (34) and water parameters were from Martini version 2.0. PUPC parameters were not available in the Martini CG force field, and so were modeled by combining the *sn*-1 chain parameters of DPPC with the *sn*-2 chain parameters of DUPC.

UA simulations used the GROMOS 87 force field (35) with added Berger Lipid parameters (36), as described in reference (18). DPPC (36, 37), DUPC (18), and cholesterol (38) topologies were taken from existing parameterizations. UA parameters for PUPC were also not available, and were modeled by replacing the *sn*-2 chain parameters of DPPC with those of DUPC. The SPC model (39) was used for water.

3.3.2 Simulation conditions

The CG simulations were performed in the NPT ensemble with 20 fs timestep. The V-rescale thermostat (40) with a time constant of 1 ps and Berendsen semi-isotropic barostat (41) with a time constant of 4 ps were used to maintain a temperature of 295 K and a pressure of 1 atm. Each lipid type and the solvent were independently coupled to the temperature bath. Electrostatics and van der Waals interactions were cut off at 1.2 nm, and were shifted to zero

starting at 0 and 0.9 nm, respectively. Center of mass motion of the system was removed every 10 timesteps. The simulations were run for 25 μs.

Initial structures for the UA simulations were obtained by converting the final CG structures to UA representation using Backward (29); see Appendix B.1. The simulations were then performed in the NPT ensemble with 2 fs timesteps. The Nosé-Hoover thermostat (42, 43) with a time constant of 0.5 ps and Parrinello-Rahman semi-isotropic barostat (44) with a time constant of 2.0 ps were used to maintain a temperature of 300 K as in reference (18), and a pressure of 1 atm. Each lipid type and the solvent were independently coupled to the temperature bath. A 1.1 nm cutoff was employed for the electrostatics and van der Waals interactions. SETTLE (45) was used for rigid water constraints. PME (46, 47) was used for electrostatics, with a cubic interpolation order of 4 and Fourier grid spacing of 0.16. Center of mass motion of the bilayer and solvent were separately removed every 100 timesteps. The simulations were run for 200 ns.

All CG and UA simulations applied periodic boundary conditions in three dimensions, and employed the LINCS (31, 48) algorithm for bond constraints.

3.3.3 Phase determination algorithm

Determining phase patches in lipid simulations requires first deciding on a criterion for a phase. One possible choice is to use the order of lipid chains (49, 50), while another is to use local composition (20). We chose to use the latter, since it is independent of lipid-specific properties: order is dependent not only on phase, but also on lipid type (see e.g. Figures B.6–B.9) and phase of the apposed leaflet (51). Although hidden Markov models exist to determine phases based on lipid composition (20), we chose to use a single compositional cutoff for simplicity.

It is known from experiments that high-Tm lipids, in our case, DPPC, and cholesterol are enriched in the Lo phase compared to the Ld phase (12). This allows use of the local concentration of DPPC and cholesterol to determine phase domains (20). To do this, we first perform a Voronoi tessellation based on the centers of mass of each lipid within a leaflet. Next, the local environment of a particular lipid of interest (LOI) is defined to be those lipids that share a Voronoi edge with the LOI. Finally, the phase of the LOI is determined by its local concentration of DPPC + cholesterol. If the concentration of DPPC + cholesterol in the local environment is higher than that in the entire leaflet, the LOI is considered to be in the Lo phase; otherwise, the LOI is considered to be in the Ld phase. Continuous phase patches were determined using a connectivity matrix; patches containing fewer than 10 lipids were considered random compositional fluctuations and were included in their surrounding domain (49, 50). Voronoi edges between two phases are then phase boundaries. The phase boundaries are taken to lie within the xy plane, and for calculations involving the boundaries, only those within the leaflet being analyzed are considered. Example results of the phase determination algorithm (implemented in Matlab version R2010a) are shown in Figure 3.2.

We note here that at low ρ in these simulations, and in ternary mixture simulations of DPPC/PUPC/cholesterol (52, 53), small clusters reveal non-ideal mixing rather than nanoscopic phase domains. Regardless, the purpose of this work is to investigate trends in demixing as a low-Tm lipid that produces small domains is replaced by a low-Tm lipid that produces large domains. In this vein, we stick to Lo/Ld terminology for clarity and in a later section discuss the ρ value at which we believe true phase separation first appears in these simulations.

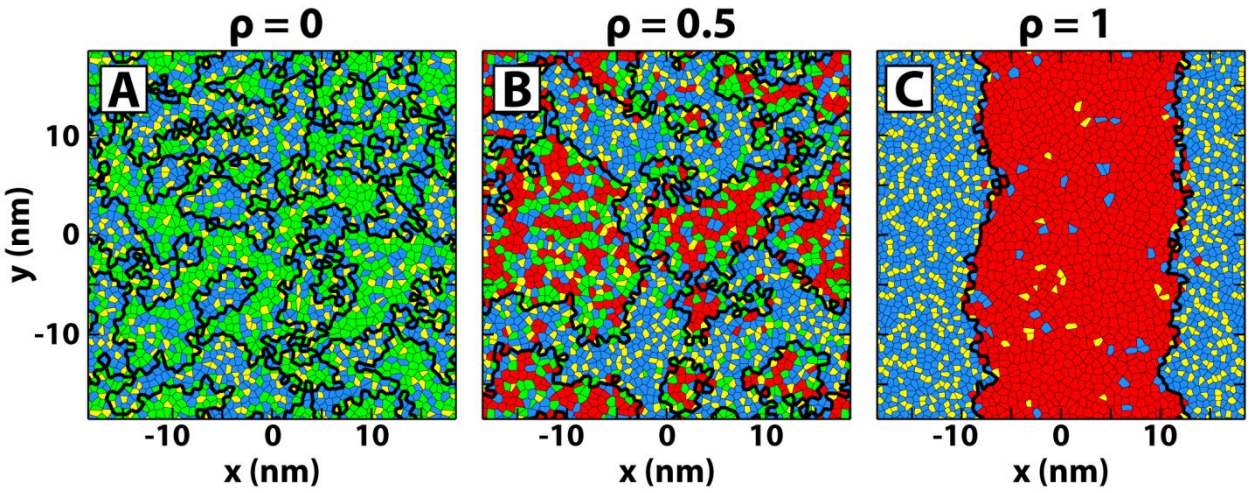

Figure 3.2 Phase determination algorithm reveals patches of Lo and Ld phases. Voronoi tessellation of one leaflet for A) ρ = 0, B) ρ = 0.5 and C) ρ = 1 with DPPC (blue), PUPC (green), DUPC (red) and cholesterol (yellow). Coexisting phase patches, demarcated by thick black lines, increase in size and compositional difference from ρ = 0 to ρ = 1.

3.3.4 Equilibration and data analysis

Based on equilibration of CG phase interface length and UA box size (Figure B.1), we determined that the CG and UA systems required 15 μs and 50 ns respectively to be sufficiently equilibrated. Consequently, data analysis for CG and UA simulations was performed only over the last 10 μs and last 150 ns of simulation time, respectively.

After equilibration, we calculated the time autocorrelations of several CG and UA properties — phase interface length, misaligned phase overlap fraction, order parameter, extent of lipid tilt and lipid tilt orientation — for the representative case of $\rho = 1$ (Figures B.2 and B.3). We chose $\rho = 1$ since it is expected to have the slowest correlation times due to its large domain size and high order in the Lo phase. All correlations are described in Appendix B.2, and the properties themselves are described throughout the text. Based on the correlation functions, we determined that the CG properties of interest became essentially uncorrelated by 250 ns and the UA properties became sufficiently uncorrelated by 25 ns. Thus, each 10 μs CG simulation could be split into 40 independent 250 ns traces and similarly, each 150 ns UA simulation into 6 independent 25 ns traces. For details on how averages and standard deviation error bars were calculated from these subsets, see Appendix B.2.

3.4 Results

In the following sections, CG results are in Sections 3.4.1-3.4.3, UA results in 3.4.4-3.4.5. Results plotted as a function of ρ are colored from green at $\rho = 0$ to red at $\rho = 1$ unless otherwise specified.

3.4.1 CG demixing of Lo lipids DPPC and cholesterol, and Ld lipids PUPC and DUPC, increases along the ρ-trajectory

We used the phase determination algorithm from Section 3.3.3 on our simulation results to define regions of similar phase (Figure 3.2). This algorithm ensures that Ld phases are enriched in the low-Tm lipids PUPC and DUPC, while Lo phases are enriched in DPPC and cholesterol. Once phases were determined, compositions of a given phase were calculated leaflet by leaflet based on all lipids in that phase. Figure 3.3 shows the coexisting Lo (circles) and Ld (squares) compositions throughout the ρ-trajectory, in terms of standard equilibrium ternary and quaternary phase diagrams at constant temperature. For each ρ value, coexisting phase compositions of Lo and Ld are connected by tielines. Triangles mark the *overall* composition of the bilayers simulated: DPPC/[PUPC + DUPC]/cholesterol ≈ 0.40/0.4/0.2.

The ternary and quaternary diagrams show that the compositions of coexisting Lo and Ld phases become increasingly different as ρ increases (from green to red). The differences between Lo and Ld compositions are measured by the lengths of tielines, which increase by ~ 400% from ρ = 0 to ρ = 1. Specifically, the amount of low-Tm lipid in the Lo phase decreases from 30.1 ± 0.4% at ρ = 0 to 2.3 ± 0.2 % at ρ = 1. Similarly, the amount of DPPC in the Ld phase decreases from 32.1 ± 0.3% at ρ = 0 to 6.6 ± 0.5% at ρ = 1. Thus, as DUPC replaces PUPC, the extent of demixing increases: DPPC and cholesterol become more enriched in the Lo phase and the low-Tm lipids become more enriched in the Ld phase.

3.4.2 CG domain size and interleaflet domain alignment increase with ρ

The phase domains of Figure 3.2 show that domain size increases with ρ. To analyze the dependence of size on ρ, we calculated an *intra*leaflet pair correlation function, $g(r)$, of Ld

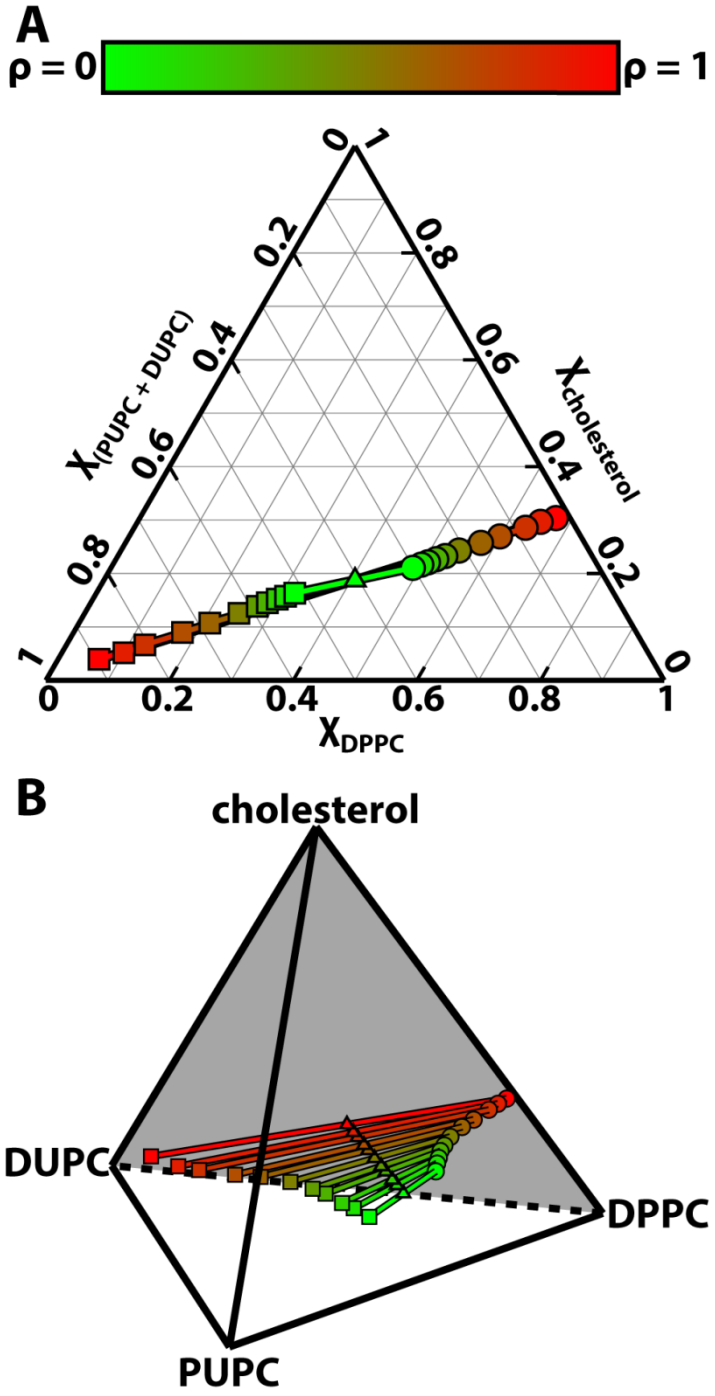

Figure 3.3 Lipid demixing increases with ρ. A) Ternary and B) quaternary phase diagrams for DPPC/[PUPC + DUPC]/cholesterol ≈ 0.4/0.4/0.2. Tielines connect the compositions of coexisting Lo phases (circles) and Ld phases (squares). Triangles mark the overall bilayer composition at each ρ. Results are shown from ρ = 0 (green) to ρ = 1 (red). Longer tielines at high ρ indicate increased compositional differences between coexisting phases.

lipids. $g(r)$ is the probability of finding two Ld lipids at a certain distance from each other in the same leaflet, normalized by the probability given a uniform random distribution:

$$g(r) = \frac{A}{\pi r \Delta r N^2} \sum_{i=1}^{N} \sum_{j>i}^{N} \boldsymbol{\delta}\left(r - \left|\vec{\boldsymbol{r}}_j - \vec{\boldsymbol{r}}_i\right|\right) \quad (3.1)$$

where A is the simulation area, N is the number of Ld lipids in a leaflet, $\vec{\boldsymbol{r}}$ are the coordinates of the lipid centers of mass, Δr = 0.25 nm is the bin size and $\boldsymbol{\delta}$ is the Kronecker delta. The pair correlation functions for all ρ-trajectory simulations are shown in Figure 3.4*A*. At low ρ, pair correlations have exponential-like decays indicating only short-range correlations. At higher ρ, pair correlations decay in a much slower, linear fashion, indicating large-scale phase patches that can be limited by the finite simulation size. The observed increase in pair correlations with increasing ρ means that the characteristic size-scale of domains grows with ρ.

In addition to using intraleaflet pair correlations to study domain size, we also measure *inter*leaflet correlations of phase patches to study domain alignment. Interleaflet correlations show the probability of finding two lipids in the same phase at a certain distance from each other in apposed leaflets, normalized by the probability given a uniform random distribution in the apposed leaflet. Similarly to Equation 3.1, we measure the interleaflet correlation, $g_{1,2}(r)$, of Ld lipids as:

$$g_{1,2}(r) = \frac{A}{2\pi r \Delta r N_1 N_2} \sum_{i=1}^{N_1} \sum_{j=1}^{N_2} \boldsymbol{\delta}\left(r - \left|\vec{\boldsymbol{r}}_j - \vec{\boldsymbol{r}}_i\right|\right) \quad (3.2)$$

where N_1 and N_2 are the number of Ld lipids in each of the two leaflets, and other terms are defined as in Equation 1. Interleaflet pair correlations for all ρ values are shown in Figure 3.4*B*. At low ρ, the interleaflet pair correlations remain near 1: there is no preferred alignment of phase domains between leaflets. Conversely, at high ρ, pair correlations grow significantly above 1: the phase domains in the two leaflets are more aligned.

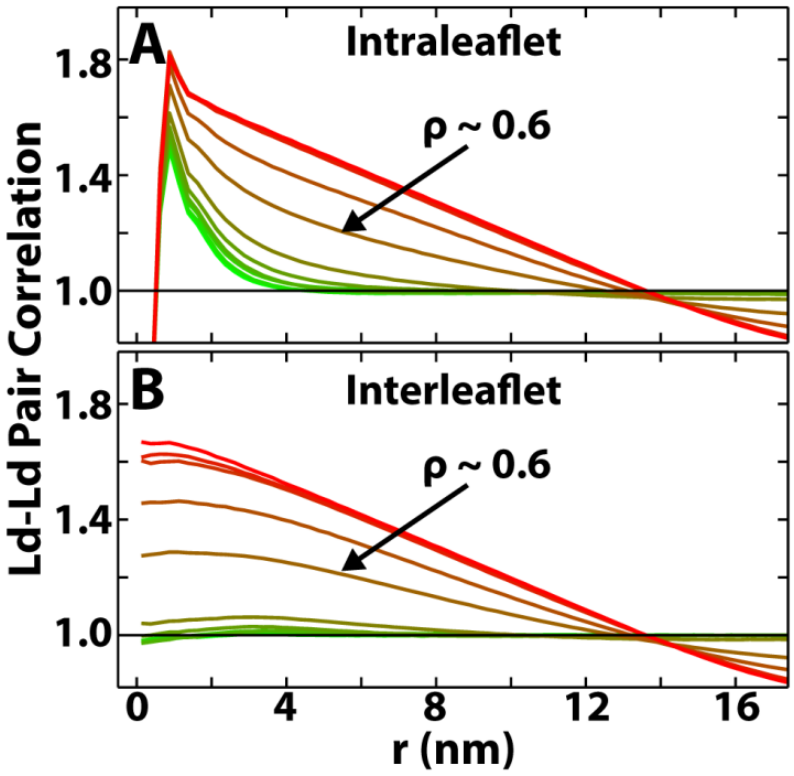

Figure 3.4 Ld-Ld pair correlations show that both domain size and alignment increase with ρ. A) Intraleaflet Ld-Ld pair correlation functions, $\boldsymbol{g(r)}$, plotted from ρ = 0 (green) to ρ = 1 (red). Longer correlations at higher ρ mean domain patches are larger. B) Interleaflet Ld-Ld pair correlation functions, $\boldsymbol{g_{1,2}(r)}$, plotted from ρ = 0 (green) to ρ = 1 (red). Larger correlations between leaflets at higher ρ mean that domain patches are more aligned between the two leaflets.

When measuring Lo-Lo correlations with a bin size of Δr = 0.025 nm, a simulation artifact becomes apparent. It is particularly noticeable in correlations between acyl chain and cholesterol centers of mass, as shown in Figure B.4*A*,*B*. At high ρ, the Lo phase has long-range periodicity in its correlations, revealing that it is gel-like. We discuss this apparent gelation artifact in Appendix B.3. We do not expect it to affect our simulations as it only appears in the Lo phase after phase separation has begun and is much less pronounced in the UA simulations (Figure B.5). A newly developed CG cholesterol available at http://md.chem.rug.nl/cgmartini/index.php/force-field-parameters/sterols prevents this gelation in the CG simulations.

3.4.3 A sharp transition in CG phase morphology occurs between ρ ~ 0.5 and ρ ~ 0.8

The intraleaflet pair correlation functions in Section 3.4.2 reveal two distinct regions of behavior: short-range correlations at low ρ and long-range correlations at high ρ. To better quantify the shift in intraleaflet phase behavior at intermediate ρ, we look at the amount of interface between Lo and Ld phases. As is often done (49, 50), we normalize the interface length, in this case by the x/y box length *L*. We plot the normalized interface lengths as a function of ρ in Figure 3.5*A*. The normalized interface length is large, greater than 20, at low ρ and decreases smoothly until ρ ~ 0.5. A steep drop-off then starts at ρ ~ 0.6, leveling off at ρ ~ 0.8. By ρ = 1, the normalized interface length is ~ 15% that at ρ = 0.

Changes in normalized interface length from one simulation to the next can arise from changes in either phase area fractions or domain size. To determine which factor was governing our results, we measured phase area fractions. Over the entire ρ-trajectory, normalized interface length decreases significantly, whereas the area fraction of Lo decreases from 48.3 +/- 0.4% to 44.3 +/- 0.2%, and the area fraction of Ld increases from 51.7 +/- 0.4% to 55.7 +/- 0.2 %. Since

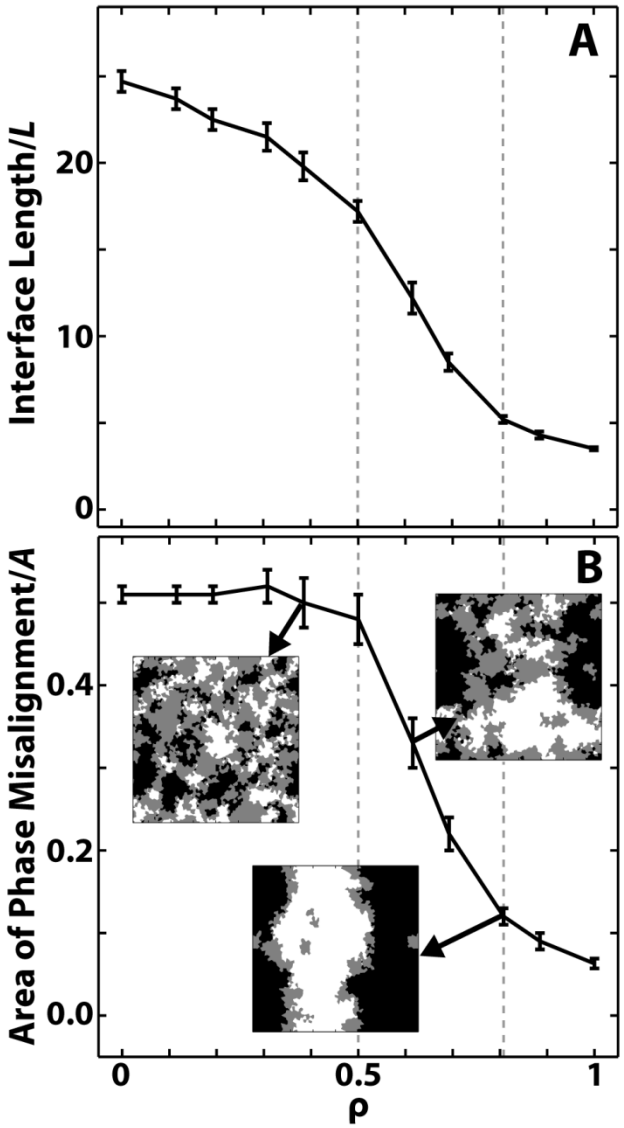

Figure 3.5 A transition in phase morphology occurs between ρ ~ 0.5 and ρ ~ 0.8 (dashed gray lines). A) Length of the phase interface along a ρ-trajectory, normalized by the bilayer length *L*. A significant decrease between ρ ~ 0.5 and ρ ~ 0.8 indicates an increase in domain coalescence. B) Area of misaligned phases along a ρ trajectory, normalized by the box area *A*. A significant decrease occurs between ρ ~ 0.5 and ρ ~ 0.8, indicating an increase in domain alignment. Also shown are overlayed phase plots of the two leaflets for ρ ~ 0.4, ρ ~ 0.6 and ρ ~ 0.8. Coloring: Lo across from Lo is white, Ld across from Ld is black, and Lo across from Ld is gray. Overlayed plots are 37 nm x 37 nm.

only small changes in phase area fractions occur, the decrease in interface length that occurs for $0.5 \leq \rho \leq 0.8$ must be due to increasing intraleaflet domain coalescence.

A change in phase behavior at intermediate ρ is also apparent in the interleaflet pair correlations: domains are uncorrelated at low ρ but are highly correlated at high ρ. A straightforward way to quantify this change in domain alignment is by measuring area fraction of domain overlap (25, 49, 54). In this case, we choose to measure the area of misaligned domains, i.e. Lo across from Ld (25), normalized by the simulation area *A*. Since the total area fraction of each phase is ~ 50%, in the three extreme cases of perfect domain anti-alignment, perfect domain alignment, and completely random domain alignment, the area fractions of misalignment would be ~ 1, ~ 0 and ~ 0.5 respectively.

Figure 3.5*B* shows snapshots of overlayed leaflets for ρ ~ 0.4, ρ ~ 0.6 and ρ ~ 0.8 (with white corresponding to aligned Lo phases, black to aligned Ld phases, and gray to misaligned phases), together with results of the misaligned fraction calculations. For $\rho \leq 0.5$, the area fraction of misaligned domains is ~ 0.5, showing domains are uncorrelated. For $\rho \geq 0.8$, misalignment drops to less than 0.15. The transition between these two extremes occurs over the relatively small ρ range between 0.5 and 0.8. This is similar to the transition region observed in Figure 3.5*A*, supporting the finding that a switch in phase behavior occurs between ρ ~ 0.5 and ρ ~ 0.8.

3.4.4 UA order parameter perturbations extend ~ 2 nm into each phase and are uniform along a chain

After running the converted UA simulations, we measure the order of UA lipid chains using the carbon deuterium order parameter:

$$S_{CD} = \langle 3\cos^2\alpha - 1\rangle/2 \qquad (3.3)$$

where α is the angle between the calculated CH bond and the bilayer normal, taken to be along the z-axis. Figure 3.6 shows $-S_{CD}$ averaged over all methylenes in the hydrocarbon chains of DPPC as a function of distance from the phase interface. As expected, equilibrium DPPC order in the Ld phase is substantially lower than equilibrium DPPC order in the Lo phase. As ρ increases, the Lo phase becomes more ordered and the Ld phase becomes less ordered. The changes in equilibrium order coincide with an increase (decrease) of cholesterol in the Lo (Ld) phase as ρ increases (Figure 3.3), consistent with the so-called ordering effect of cholesterol (55). Whatever the differences in equilibrium order along the ρ-trajectory, DPPCs in each phase always reach bulk values within ~ 2 nm of the interface. The same is true for PUPC and DUPC (Figure B.6).

The perturbed lipids near the interface adjust to the different phase equilibria through nearly uniform changes along their acyl chains, despite there being significantly more double bonds in the Ld phase than in the Lo phase. In Figure 3.7, $-S_{CD}$ is plotted for all carbons in the DPPC *sn*-1 chain as a function of distance to the interface for ρ = 0.5. No part of the DPPC acyl chains is significantly more perturbed than any other. Again, changes in order do not extend far from the interface. Similar behavior is observed for the *sn*-2 chain of DPPC, and the *sn*-1 and *sn*-2 chains of PUPC and DUPC (Figure B.7). The uniform change in order of the high-Tm lipid agrees with a previous study of a sphingomyelin/chol-enriched Lo phase surrounded by a DOPC-enriched Ld phase; whether the same was true for the low-Tm lipid is less clear (19).

For corresponding CG order plots, see Figures B.8 and B.9.

3.4.5 UA lipid phase determines the extent and orientation of lipid tilt

To measure lipid tilts, we assume the bilayer lies in the xy plane, and take the normal to be along the z-axis. We then define the tilt of a lipid (Figure 3.8*A*) as in reference (56): the tilt

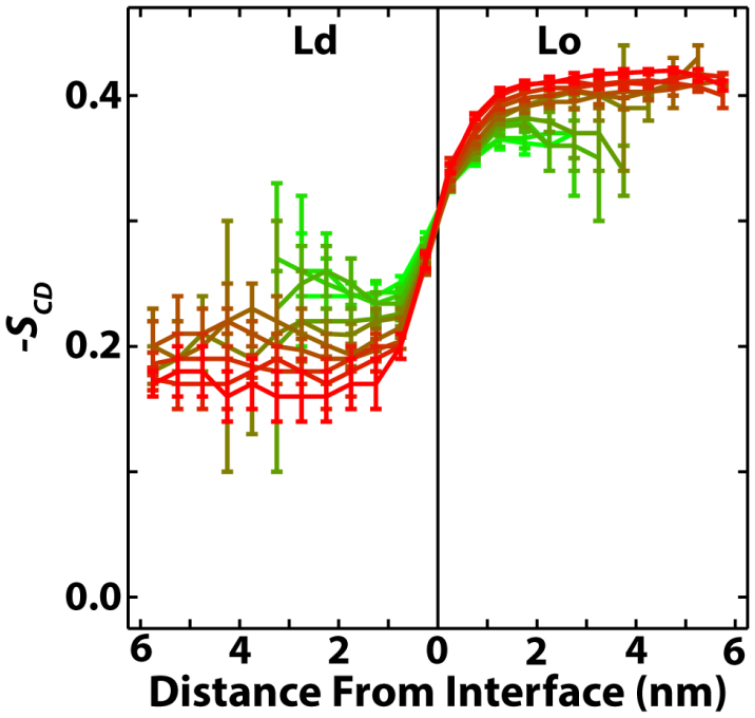

Figure 3.6 DPPC order parameter $-\boldsymbol{S_{CD}}$ is only perturbed ~ 2 nm from the interface into each phase. $-\boldsymbol{S_{CD}}$ is averaged over all methylenes in both chains of DPPC, as a function of distance from the phase interface. Results shown from ρ = 0 (green) to ρ = 1 (red). DPPC order in both phases reaches equilibrium within ~ 2 nm of the phase interface, regardless of ρ.

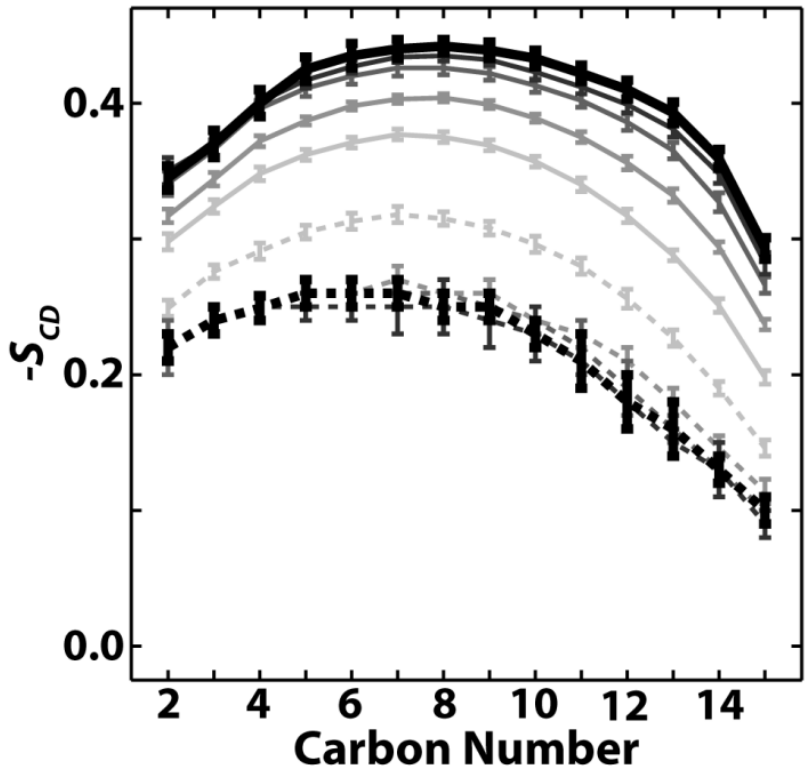

Figure 3.7 DPPC carbons are nearly uniformly perturbed regardless of phase or distance from the phase interface. Order parameters are plotted for DPPC *sn*-1 carbons for Ld lipids (dashed) and Lo lipids (solid), with increasing darkness indicating increasing distance from the interface in increments of 0.5 nm. Thicker black curves are averaged over all DPPCs greater than or equal to 2 nm from the interface. Results shown for $\rho = 0.5$.

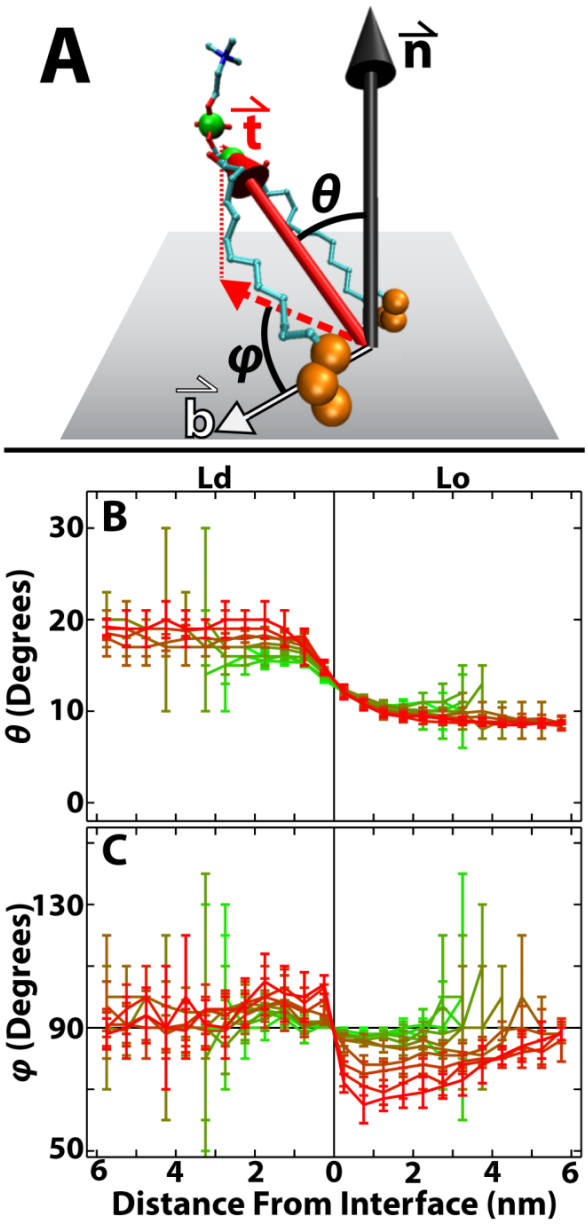

Figure 3.8 Lipid tilt is affected by phase and distance to interface. A) Lipid tilt vector ($\vec{t}$) connects the combined center of mass of the last three carbons on each acyl chain (large orange spheres) to the combined center of mass of the CD atom and phosphorus of the headgroup (large green spheres). The local bilayer midplane, which is assumed to lie along the xy plane, is shown as a gray rectangle. $\vec{n}$ is the bilayer normal, and $\vec{b}$ is the vector joining the lipid center of mass to the nearest phase interface. θ and φ are, respectively, the polar and azimuthal angles of $\vec{t}$: θ is the angle between $\vec{t}$ and $\vec{n}$, and φ is the angle between $\vec{t}$ (projected onto the xy plane) and $\vec{b}$. B) θ is larger, i.e. lipids tilt more, in the Ld phase compared to the Lo phase. C) Near the interface, lipids tilt away from the interface in Ld ($\varphi > 90°$) but towards the interface in Lo ($\varphi < 90°$). Results shown from $\rho = 0$ (green) to $\rho = 1$ (red). Molecule representation visualized in VMD version 1.9.

vector ($\vec{t}$) of a PC lipid joins the combined center of mass of the last three carbons of the acyl chains to the combined center of mass of the CD atom and phosphorus of the headgroup. The polar angle (θ) of $\vec{t}$ with the bilayer normal ($\vec{n}$) indicates the extent of lipid tilt.

Figure 3.8*B* shows θ versus distance from the interface for DPPC. Throughout the ρ trajectory, DPPCs in the Ld phase tilt on average ~ 10° more than those in the Lo phase. Whereas DPPC in the Ld phase tilts more at low ρ than at high ρ, DPPC tilt in the Lo phase does not change much along the ρ-trajectory. Just as with order, tilt perturbations are gone less than 2 nm from the phase interface, regardless of ρ. Similar, but not identical, tilt behavior is seen for PUPC and DUPC, whereas cholesterol tilts more than other lipids in the Ld phase (Figure B.10). A larger cholesterol tilt and a tendency of lipids to tilt less as cholesterol fraction increases is consistent with previous simulations (57).

While θ quantifies the magnitude of tilts, we used another angle (φ) to determine if the tilts have any preferential orientation. φ is the azimuthal angle of $\vec{t}$, defined to be the angle between $\vec{t}$ (projected onto the xy plane) and the vector ($\vec{b}$) connecting the lipid center of mass to the nearest phase interface (Figure 3.8*A*). Average values of φ equal to 90° indicate random orientation, while averages greater than 90° indicate that lipids tilt away from the phase interface and averages less than 90° indicate that lipids tilt toward the interface. As an example, consider a lipid in the Ld phase. If φ is less than 90°, it is tilting toward the phase interface and so tilts toward the Lo phase. Conversely, if φ is greater than 90°, it tilts away from the interface and so tilts towards the bulk Ld phase.

In Figure 8*C*, φ is plotted as a function of distance to the phase interface for DPPC. For large ρ, DPPCs, especially those near the interface, tilt towards the bulk Ld phase: lipids in Lo tilt towards Ld (φ < 90°), and lipids in Ld tilt towards Ld (φ > 90°). This preferential orientation

of tilts tends to increase with ρ. At higher ρ values, the preferential orientation persists for several nanometers in the Lo phase, but extends a much shorter distance in Ld. φ for PUPC, DUPC and cholesterol show similar, but not identical, trends of preferential orientation (Figure B.11). Though surprising, long range preferential orientation of tilts has been observed in other bilayer simulations (17).

To ensure that local curvature was not dramatically altering our tilt results, we recalculated θ and φ using the local normals and the local tangent planes (data not shown). Indeed, trends in θ and the significant preferential orientation of φ at high ρ were not significantly altered using this technique.

For corresponding CG tilt plots, see Figures B.12 and B.13.

3.5. Discussion

In the following sections, CG results are discussed in Sections 3.5.1-3.5.2, UA results in 3.5.3-3.5.4.

3.5.1 Comparison of CG phase separation to experiments

The CG simulations are able to qualitatively capture four important traits of quaternary phase separation. First, both experiments (58–60) and the simulations reported here show an increase in domain size as ρ increases. Second, the transition from small domains to large domains is relatively sharp in both experiments on GUVs (6, 60) and in simulations. Third, the simulations reveal that compositional differences between coexisting Lo and Ld phases increase with ρ which has also been observed experimentally (59). And fourth, we see that along the ρ-trajectory, increased demixing and an increased fraction of DUPC result in a predictable increase in thickness mismatch between Lo and Ld phases (Figures B.14 and B.15*A*). A similar increase

in thickness mismatch between coexisting phases along a ρ-trajectory has been detected with SANS (58).

Disparities between simulation results and experiments are also revealing. Perhaps most noticeable is that the simulations do not capture the experimentally observed modulated phase patterns. This is simply because the limited size-scale and relatively flat nature of the simulations means that they are unable to sustain modulated patterns which are microns in size and likely require curvature to form (13, 14). Another discrepancy, as mentioned in Section 3.3.3, is that the low ρ simulations are more properly termed non-ideal mixing rather than the phase domains measured experimentally. The simulations also exhibit a much larger compositional change of Lo and Ld phases along a ρ-trajectory compared to experiments (59), meaning that CG demixing is too strong. A final distinction between the simulations and experiments is that the CG Lo phase undergoes gelation at high ρ, but we emphasize this to be an artifact of the CG cholesterol which does not occur with a newer cholesterol model.

Some differences between experiments and the simulations may simply be due to the fact that the Martini model was parameterized to enable large size-scale and long time-scale simulations. The coarse-grained nature of the model means that while entropy may play some role in phase separation (61), it is not necessarily a dominant effect (62), and likely does not play as large a role in phase separation as it would *in vitro*. Similarly, the simplified treatment of electrostatics in the Martini model (21, 32) would affect phase behavior differently than would electrostatics *in vitro* and *in vivo*. The simplifications inherent in the Martini model are not a hindrance, but are instead essential to its success; by cutting down the computational costs, the simplifications allow for phase separation to take place in systems that would otherwise require unreasonable amounts of computational time. Thus, while our simulations involve somewhat

different interactions than experimentally studied quaternary systems, we have shown that they are able to capture much of the essential experimentally observed phase behavior. Furthermore, by capturing the trends in phase separation, the CG simulations allow for conversion to a more accurate atomistic force field for more detailed analysis of phase properties.

3.5.2 CG intraleaflet phase separation and interleaflet domain alignment are coupled and highly dependent on the fraction of the low-Tm lipid

An abrupt transition from small, non-aligned domains to large, aligned phase patches occurs between $\rho \sim 0.5$ and $\rho \sim 0.8$ in the CG simulations. The transition window location and narrow size indicates that intraleaflet and interleaflet effects are sensitive to the fractions of PUPC and DUPC at intermediate ρ. That the intraleaflet and interleaflet transition windows are the same hints that the two effects are coupled. These observed morphological changes along the ρ-trajectory can be explained in terms of enthalpies.

Liquid-liquid phase coexistence in Martini ternary mixtures of DPPC/DUPC/cholesterol is largely driven by enthalpy (61, 62). This likely governs the quaternary system behavior as well. The unsaturated beads of DUPC and PUPC mix unfavorably with cholesterol and with the saturated beads of DPPC (21). Since DUPC has four unsaturated beads compared to PUPC's two, DUPC is expected to segregate from DPPC and cholesterol more readily than is PUPC. At low ρ, PUPC is the dominant low-Tm lipid and demixing is weak. When DUPC begins to outnumber PUPC at $\rho > 0.5$, the unfavorable interactions dominate and phase domains enlarge to minimize the interfacial penalty. This is in agreement with previous Martini studies showing that more unsaturation of the low-Tm lipid enhances demixing (52). An increase in lipid and monolayer thickness mismatch between the Lo and Ld phases as ρ increases (Figures B.14 and

B.15*A*) may further drive intraleaflet phase separation (53, 63–65) as a way to minimize the amount of unfavorable conformational adjustments and interactions at the interface.

Coincident with the abrupt increase in domain size near $\rho \sim 0.6$ is the alignment of phase domains. For $\rho > 0.5$, the free energy contribution of aligned phases must outweigh the energetically unfavorable increasing thickness mismatch (51, 66). While electrostatics, cholesterol flip-flop, interdigitation (66, 67), and curvature (51, 54) can play a role in alignment, another influential factor is a surface tension at the bilayer midplane between the leaflet phases (68). In the Martini model, a surface tension between domains (25) could arise from the unfavorable interleaflet interaction between the unsaturated beads of the Ld phase and the saturated beads and cholesterol of the Lo phase (69). From the phase diagram, the fraction of DUPC — and in turn unsaturated beads — in the Ld phase *increases* with ρ, while the fraction of unsaturated beads in the Lo phase *decreases* with ρ. This results in a higher density of unsaturated beads near the bilayer center in the Ld phase compared to the Lo phase (Figure S.15*B*), likely increasing the penalty for phase mismatch at higher ρ. Furthermore, the penalty for interleaflet phase mismatch grows with area of the domains (25, 66). The large change in domain size near $\rho \sim 0.6$ is therefore expected to result in a correspondingly large increase in mismatch penalty per domain, favoring domain alignment. Since alignment only increases significantly for $\rho > 0.5$, it seems as though domain size, more so than just the increased surface tension between Lo and Ld phases, drives interleaflet domain alignment. This is in agreement with previous studies of bilayer mixtures that show domain alignment is greater for larger domains (25, 54, 61). We therefore conclude that interleaflet domain alignment in the quaternary system DPPC/PUPC/DUPC/cholesterol is significantly affected by intraleaflet domain size, and in turn ρ.

It is interesting that the phase morphology transition window in the simulations occurs when domains reach the approximate size-scale of nanodomains measured *in vitro* (~ 7 nm radius for DSPC/POPC/chol) (58). This can be seen in Figure 3.4 and Figure B.4, where the intraleaflet correlations at r = 7.5 nm are much larger for $\rho \geq 0.6$ compared to $\rho < 0.6$. As $\rho \sim 0.6$ is also the composition when alignment begins, it is possible that $\rho \sim 0.6$ marks the beginning of true phase behavior for this particular mixture and in turn most closely reflects the behavior of nanodomains measured experimentally. Larger simulations, beyond the scope of this project, could indicate if the $\rho \sim 0.6$ composition does indeed produce many, separate, nanodomains that are not simply limited by the simulation size.

Experimentally, the transition window from nanoscopic to macroscopic domains can vary substantially depending on the mixture used. In some systems, this transition window is narrow and low, and in other cases it is high and broad (13). Thus, there is nothing universal about the region $0.5 \leq \rho \leq 0.8$. Instead, the transition window simply represents a regime *in this particular four-component mixture* where the interfacial penalty in the simulation becomes large enough to induce the formation of large domains. We expect that the location and width of such a transition window *in vitro* are likely affected by water entropy, electrostatics of the different lipid moieties, and other atomistic properties that are outside the scope of the Martini model. Regardless, differences between the high-Tm lipid and the low-Tm lipid are expected to strongly affect the location of the transition window in both experiments and simulations: larger differences, e.g. in thickness, unsaturation, branching, result in larger interfacial penalties and in turn, lower transition windows. Whether or not the experimentally observed intraleaflet transition window is also in general an interleaflet transition window is not currently known. In all experimental quaternary systems to date, macroscopic phase domains are aligned between the two leaflets,

consistent with the simulations. However, the simulations indicate that alignment is likely lower for nanodomains than for macrodomains, which has yet to be tested experimentally.

3.5.3 Energy penalty of the UA phase interface is spread out over only a few lipid shells

Line tension plays a crucial role in phase separation of lipid mixtures and acts as a competing interaction producing modulated phases (14, 70). The atomistic underpinnings of line tension are not well understood, though it is hypothesized to be a function of the bending moduli, tilt moduli, spontaneous curvatures and thickness mismatch of the two phases (64). Here, we determine how lipids adjust to the interface in the UA systems and thus the width of lipid layers whose perturbed energy contributes to line tension.

As shown in Figures 3.6 and 3.8*B*, the Ld/Lo phase interface — in terms of order and extent of lipid tilt — extends ~ 2 nm into each phase, with the largest changes occurring within 1 nm of the interface, consistent with other simulations and mesoscopic modeling of phase separated bilayers (51, 71). Perhaps as a manifestation of order and tilt perturbations, we also find that lipid thicknesses of the UA PC lipids in the Lo and Ld phases reach equilibrium within ~ 1.5 nm of the interface (Figure B.16). The interfacial width of 1-2 nm in each phase is relatively constant along the ρ-trajectory despite increasing equilibrium differences in order, tilt and thickness between Lo and Ld phases. Therefore, lipids within ~ 2 nm of the phase interface must bear the brunt of the energetic cost of the interface regardless of domain size, alignment, composition or equilibrium phase properties.

Assuming an interface width of just 2 nm into each phase, a circular 7 nm radius nanodomain (58) (similar to that observed at ρ ~ 0.6) would have ~ 50% of its lipids within the interfacial environment. The fraction of lipids at the interface drops off with domain size, reaching 1% at a domain radius of ~ 400 nm. These interface percentages are inherently

overestimates as they do not account for the magnitude of perturbations, which are most significant within 1 nm of the interface. Nevertheless, they demonstrate that while the width of the interface might only be one or two lipids in each phase, it can make up a large fraction of small domains. This could be crucial for interpreting experiments, such as those involving ESR and SANS, that assume homogeneity of the phases. It may also affect the partitioning of molecules, some of which may prefer the environment of the interface (72).

3.5.4 The Ld phase alters molecule behavior deep within the Lo phase in UA simulations

One might naively assume that all phase properties change to their bulk values through an intermediate transition at the interface. Indeed, we saw that this was the case for order and the magnitude of lipid tilts, which reach bulk values within ~ 2 nm of the interface. However, an interesting property of the UA lipids, which is distinct from bulk phase properties and persists beyond the interfacial length of ~ 2 nm, is the orientation of lipid tilt with respect to the boundaries. Rather than being randomly oriented, lipids several nanometers from the phase interface preferentially tilt towards the Ld phase at high ρ. This spatially extended preferred orientation could be explained by the nature of the Ld phase, which is more disordered and fluid-like than the Lo phase. As ρ increases, the Ld phase becomes even more disordered and the Lo phase becomes even more ordered. The Ld phase can then more easily accommodate lipid tilts compared to the Lo phase, and preferential orientation of lipid tilts towards the Ld phase increases. By $\rho = 1$, lipids in the Lo phase as far as 6 nm from the interface significantly preferentially tilt towards the Ld phase.

There is some uncertainty as to whether the extended tilt orientation observed here represents the true behavior of lipids *in vitro* or is instead an artifact of the UA simulation. If the preferential orientation is an artifact, it is important for other researchers to be aware of it.

However, recent findings of long-range tilt orientations in simulations of bilayers (17) provide support that the effect may be real, though such correlations were only observed in asymmetric bilayers and were not detected in corresponding symmetric bilayers as in our present study. If the observed long-range interaction is not an artifact, then it may affect membrane shape (17, 73), allow for transmission of information beyond nearest neighbors, and alter the behavior of molecules deep within the bulk phases. So while the interface itself may only be 3-4 nm wide in total, its presence may have more far-reaching effects.

3.6 Conclusion

We found several interesting behaviors of a four-component lipid bilayer through use of a series of CG and UA simulations that take the mixture from nanoscopic to macroscopic phase separation. The CG simulations show that domain size and interleaflet alignment are coupled, and that domain alignment is especially sensitive to the fractions of low-Tm lipids. They also indicate that compositions of the coexisting Lo and Ld phases become more distinct as DUPC replaces PUPC. The UA simulations show that the phase interface, in terms of perturbed order and extent of lipid tilt, does not extend very far into either phase. However, the interface is not negligible, and can make up a significant fraction of smaller domains.

The UA simulations also revealed two surprising aspects of lipids in the coexisting phases. First, the UA lipids were shown to adjust to the different phase orders through uniform changes in their acyl chains, despite the high fraction of double bonds in the Ld phase compared to the Lo phase. Second, the UA simulations showed a long-range preferential tilt of lipids toward the Ld phase, meaning that lipids in a phase far from the interface can be affected by a distant, coexisting phase.

Though no experiments have been performed on the DPPC/PUPC/DUPC/cholesterol system simulated here, direct comparison of such experiments to the simulations could be very informative. Fluorescence microscopy, FRET and SANS could provide information about domain composition, size and thickness along an experimental ρ-trajectory (6, 13, 58, 59). One could also find the ρ value where an abrupt transition in domain morphology occurs. ESR analysis of a spin-labeled lipid could be used to study equilibrium phase properties, and could provide an estimate for the fraction of phase interface by determining the amount of lipids with order between the equilibrium orders of the Lo and Ld phases. These results could all be directly compared to the results reported here in order to learn both how to improve force fields and molecular parameterizations, and in what ways the limitations of box size and coarse-graining affect simulation results. Such a comparison would have implications for the reliability of simulation properties that are not amenable to experimental measurements, such as pressure profiles and atomistic-level details of lipid behavior.

By providing a thorough analysis of a four-component mixture, CG and UA simulations reported here will be useful as a control for future studies addressing how addition of other molecules, membrane proteins in particular, affect the phase behavior in similar complex mixtures. They also form a basis for comparison to complementary experiments.

REFERENCES

1. Simons, K., and J.L. Sampaio. 2011. Membrane organization and lipid rafts. Cold Spring Harb. Perspect. Biol. 3: 1–17.

2. Lingwood, D., and K. Simons. 2010. Lipid Rafts as a Membrane-organizing Principle. Science. 327: 46–50.

3. Rajendran, L., and K. Simons. 2005. Lipid rafts and membrane dynamics. J. Cell Sci. 118: 1099–1102.

4. Simons, K., and M.J. Gerl. 2010. Revitalizing membrane rafts: new tools and insights. Nat. Rev. Mol. Cell Biol. 11: 688–99.

5. Feigenson, G.W. 2009. Phase diagrams and lipid domains in multicomponent lipid bilayer mixtures. Biochim. Biophys. Acta. 1788: 47–52.

6. Konyakhina, T.M., S.L. Goh, J. Amazon, F.A. Heberle, J. Wu, and G.W. Feigenson. 2011. Control of a nanoscopic-to-macroscopic transition: modulated phases in four-component DSPC/DOPC/POPC/Chol giant unilamellar vesicles. Biophys. J. 101: L08–10.

7. Heinrich, M., A. Tian, C. Esposito, and T. Baumgart. 2010. Dynamic sorting of lipids and proteins in membrane tubes with a moving phase boundary. Proc. Natl. Acad. Sci. U.S.A. 107: 7208–13.

8. Amazon, J.J., and G.W. Feigenson. 2014. Lattice simulations of phase morphology on lipid bilayers: Renormalization, membrane shape, and electrostatic dipole interactions. Phys. Rev. E. 89: 022702.

9. Hu, J., T. Weikl, and R. Lipowsky. 2011. Vesicles with multiple membrane domains. Soft Matter. 7: 6092–6102.

10. Parthasarathy, R., C. Yu, and J.T. Groves. 2006. Curvature-modulated phase separation in lipid bilayer membranes. Langmuir. 22: 5095–9.

11. Heberle, F.A., J. Wu, S.L. Goh, R.S. Petruzielo, and G.W. Feigenson. 2010. Comparison of three ternary lipid bilayer mixtures: FRET and ESR reveal nanodomains. Biophys. J. 99: 3309–18.

12. Zhao, J., J. Wu, F.A. Heberle, T.T. Mills, P. Klawitter, G. Huang, G. Costanza, and G.W. Feigenson. 2007. Phase studies of model biomembranes: complex behavior of DSPC/DOPC/cholesterol. Biochim. Biophys. Acta. 1768: 2764–76.

13. Goh, S.L., J.J. Amazon, and G.W. Feigenson. 2013. Toward a better raft model: modulated phases in the four-component bilayer, DSPC/DOPC/POPC/CHOL. Biophys. J. 104: 853–62.

14. Amazon, J.J., S.L. Goh, and G.W. Feigenson. 2013. Competition between line tension and curvature stabilizes modulated phase patterns on the surface of giant unilamellar vesicles: a simulation study. Phys. Rev. E. 87: 022708.

15. Hassan-Zadeh, E., E. Baykal-Caglar, M. Alwarawrah, and J. Huang. 2014. Complex roles of hybrid lipids in the composition, order, and size of lipid membrane domains. Langmuir. 30: 1361–9.

16. Kollmitzer, B., P. Heftberger, M. Rappolt, and G. Pabst. 2013. Monolayer spontaneous curvature of raft-forming membrane lipids. Soft Matter. 9: 10877–10884.

17. Polley, A., S. Vemparala, and M. Rao. 2012. Atomistic Simulations of a Multicomponent Asymmetric Lipid Bilayer. J. Phys. Chem. B. 116: 13403–13410.

18. Hakobyan, D., and A. Heuer. 2013. Phase separation in a lipid/cholesterol system: comparison of coarse-grained and united-atom simulations. J. Phys. Chem. B. 117: 3841–51.

19. Pandit, S.A., S. Vasudevan, S.W. Chiu, R.J. Mashl, E. Jakobsson, and H.L. Scott. 2004. Sphingomyelin-cholesterol domains in phospholipid membranes: atomistic simulation. Biophys. J. 87: 1092–100.

20. Sodt, A.J., M.L. Sandar, K. Gawrisch, R.W. Pastor, and E. Lyman. 2014. The molecular structure of the liquid-ordered phase of lipid bilayers. J. Am. Chem. Soc. 136: 725–32.

21. Marrink, S.J., H.J. Risselada, S. Yefimov, D.P. Tieleman, and A.H. de Vries. 2007. The MARTINI force field: coarse grained model for biomolecular simulations. J. Phys. Chem. B. 111: 7812–24.

22. Bennett, W.F.D., and D.P. Tieleman. 2013. Computer simulations of lipid membrane domains. Biochim. Biophys. Acta. 1828: 1765–1776.

23. Meinhardt, S., R.L.C. Vink, and F. Schmid. 2013. Monolayer curvature stabilizes nanoscale raft domains in mixed lipid bilayers. Proc. Natl. Acad. Sci. U.S.A. 110: 4476–81.

24. Stevens, M.J. 2005. Complementary matching in domain formation within lipid bilayers. J. Am. Chem. Soc. 127: 15330–1.

25. Risselada, H.J., and S.J. Marrink. 2008. The molecular face of lipid rafts in model membranes. Proc. Natl. Acad. Sci. U.S.A. 105: 17367–72.

26. Ingólfsson, H.I., M.N. Melo, F.J. van Eerden, C. Arnarez, C.A. López, T.A. Wassenaar, X. Periole, A.H. De Vries, D.P. Tieleman, and S.J. Marrink. 2014. Lipid Organization of the Plasma Membrane. J. Am. Chem. Soc. .

27. Schäfer, L. V, D.H. de Jong, A. Holt, A.J. Rzepiela, A.H. de Vries, B. Poolman, J.A. Killian, and S.J. Marrink. 2011. Lipid packing drives the segregation of transmembrane helices into disordered lipid domains in model membranes. Proc. Natl. Acad. Sci. U.S.A. 108: 1343–8.

28. Rzepiela, A.J., L. V Schäfer, N. Goga, H.J. Risselada, A.H. de Vries, and S.J. Marrink. 2010. Reconstruction of Atomistic Details from Coarse-Grained Structures. J. Comput. Chem. 31: 1333–1343.

29. Wassenaar, T.A., K. Pluhackova, R.A. Böckmann, S.J. Marrink, and D.P. Tieleman. 2013. Going Backward : A Flexible Geometric Approach to Reverse Transformation from Coarse Grained to Atomistic Models. J. Chem. Theory Comput. 10: 676–690.

30. Stansfeld, P.J., and M.S.P. Sansom. 2011. From Coarse Grained to Atomistic: A Serial Multiscale Approach to Membrane Protein Simulations. J. Chem. Theory Comput. 7: 1157–1166.

31. Hess, B., C. Kutzner, D. van der Spoel, and E. Lindahl. 2008. GROMACS 4 : Algorithms for Highly Efficient , Load-Balanced , and Scalable Molecular Simulation. J. Chem. Theory Comput. 4: 435–447.

32. Monticelli, L., S.K. Kandasamy, X. Periole, R.G. Larson, D.P. Tieleman, and S.-J. Marrink. 2008. The MARTINI Coarse-Grained Force Field: Extension to Proteins. J. Chem. Theory Comput. 4: 819–834.

33. Marrink, S.J., A.H. de Vries, and A.E. Mark. 2004. Coarse Grained Model for Semiquantitative Lipid Simulations. J. Phys. Chem. B. 108: 750–760.

34. Marrink, S.J., A.H. de Vries, T.A. Harroun, J. Katsaras, and S.R. Wassall. 2008. Cholesterol shows preference for the interior of polyunsaturated lipid membranes. J. Am. Chem. Soc. 130: 10–1.

35. Van Gunsteren, W.F., and H.J.C. Berendsen. 1987. Groningen Molecular Simulation (GROMOS) Library Manual. Groningen, The Netherlands: Biomos.

36. Berger, O., O. Edholm, and F. Jähnig. 1997. Molecular dynamics simulations of a fluid bilayer of dipalmitoylphosphatidylcholine at full hydration, constant pressure, and constant temperature. Biophys. J. 72: 2002–13.

37. Tieleman, D.P., and H.J.C. Berendsen. 1996. Molecular dynamics simulations of a fully hydrated dipalmitoylphosphatidylcholine bilayer with different macroscopic boundary conditions and parameters. J. Chem. Phys. 105: 4871–4880.

38. Höltje, M., T. Förster, B. Brandt, T. Engels, W. von Rybinski, and H.-D. Höltje. 2001. Molecular dynamics simulations of stratum corneum lipid models: fatty acids and cholesterol. Biochim. Biophys. Acta. 1511: 156–67.

39. Berendsen, H.J.C., J.P.M. Postma, W.F. van Gunsteren, and J. Hermans. 1981. Interaction Models for Water in Relation to Protein Hydration. In: Pullman B, editor. Intermolecular Forces. Dordrecht, The Netherlands: D. Reidel Publishing Company. pp. 331–342.

40. Bussi, G., D. Donadio, and M. Parrinello. 2007. Canonical sampling through velocity rescaling. J. Chem. Phys. 126: 014101.

41. Berendsen, H.J.C., J.P.M. Postma, W.F. van Gunsteren, A. DiNola, and J.R. Haak. 1984. Molecular dynamics with coupling to an external bath. J. Chem. Phys. 81: 3684–3690.

42. Nosé, S. 1984. A molecular dynamics method for simulations in the canonical ensemble. Mol. Phys. 55: 255–268.

43. Hoover, W.G. 1985. Canonical dynamics: Equilibrium phase-space distributions. Phys. Rev. A. 31: 1695–1697.

44. Parrinello, M., and A. Rahman. 1981. Polymorphic transitions in single crystals: A new molecular dynamics method. J. Appl. Phys. 52: 7182–7190.

45. Miyamoto, S., and P.A. Kollman. 1992. Settle: An analytical version of the SHAKE and RATTLE algorithm for rigid water models. J. Comput. Chem. 13: 952–962.

46. Essmann, U., L. Perera, M.L. Berkowitz, T. Darden, H. Lee, and L.G. Pedersen. 1995. A smooth particle mesh Ewald method. J. Chem. Phys. 103: 8577–8593.

47. Darden, T., D. York, and L. Pedersen. 1993. Particle mesh Ewald: An Nlog(N) method for Ewald sums in large systems. J. Chem. Phys. 98: 10089–10092.

48. Hess, B., H. Bekker, H.J.C. Berendsen, and J.G.E.M. Fraaije. 1997. LINCS: A linear constraint solver for molecular simulations. J. Comput. Chem. 18: 1463–1472.

49. Baoukina, S., E. Mendez-Villuendas, W.F.D. Bennett, and D.P. Tieleman. 2013. Computer simulations of the phase separation in model membranes. Faraday Discuss. 161: 63–75.

50. Baoukina, S., E. Mendez-Villuendas, and D.P. Tieleman. 2012. Molecular view of phase coexistence in lipid monolayers. J. Am. Chem. Soc. 134: 17543–53.

51. Perlmutter, J.D., and J.N. Sachs. 2011. Interleaflet interaction and asymmetry in phase separated lipid bilayers: molecular dynamics simulations. J. Am. Chem. Soc. 133: 6563–77.

52. Rosetti, C., and C. Pastorino. 2012. Comparison of ternary bilayer mixtures with asymmetric or symmetric unsaturated phosphatidylcholine lipids by coarse grained molecular dynamics simulations. J. Phys. Chem. B. 116: 3525–37.

53. Domański, J., S.J. Marrink, and L. V Schäfer. 2012. Transmembrane helices can induce domain formation in crowded model membranes. Biochim. Biophys. Acta. 1818: 984–94.

54. Pantano, D.A., P.B. Moore, M.L. Klein, and D.E. Discher. 2011. Raft registration across bilayers in a molecularly detailed model. Soft Matter. 7: 8182–8191.

55. Róg, T., M. Pasenkiewicz-Gierula, I. Vattulainen, and M. Karttunen. 2009. Ordering effects of cholesterol and its analogues. Biochim. Biophys. Acta. 1788: 97–121.

56. Khelashvili, G., B. Kollmitzer, P. Heftberger, G. Pabst, and D. Harries. 2013. Calculating the Bending Modulus for Multicomponent Lipid Membranes in Different Thermodynamic Phases. J. Chem. Theory Comput. 9: 3866–3871.

57. Hofsäß, C., E. Lindahl, and O. Edholm. 2003. Molecular dynamics simulations of phospholipid bilayers with cholesterol. Biophys. J. 84: 2192–206.

58. Heberle, F.A., R.S. Petruzielo, J. Pan, P. Drazba, N. Kučerka, R.F. Standaert, G.W. Feigenson, and J. Katsaras. 2013. Bilayer thickness mismatch controls domain size in model membranes. J. Am. Chem. Soc. 135: 6853–9.

59. Konyakhina, T.M., J. Wu, J.D. Mastroianni, F.A. Heberle, and G.W. Feigenson. 2013. Phase diagram of a 4-component lipid mixture: DSPC/DOPC/POPC/chol. Biochim. Biophys. Acta. 1828: 2204–14.

60. Heberle, F.A., M. Doktorova, S.L. Goh, R.F. Standaert, J. Katsaras, and G.W. Feigenson. 2013. Hybrid and Nonhybrid Lipids Exert Common E ff ects on Membrane Raft Size and Morphology. J. Am. Chem. Soc. 135: 14932–14935.

61. Hakobyan, D., and A. Heuer. 2014. Key molecular requirements for raft formation in lipid/cholesterol membranes. PLoS One. 9: e87369.

62. Davis, R.S., P.B. Sunil Kumar, M.M. Sperotto, and M. Laradji. 2013. Predictions of phase separation in three-component lipid membranes by the MARTINI force field. J. Phys. Chem. B. 117: 4072–80.

63. García-Sáez, A.J., S. Chiantia, and P. Schwille. 2007. Effect of line tension on the lateral organization of lipid membranes. J. Biol. Chem. 282: 33537–44.

64. Kuzmin, P.I., S.A. Akimov, Y.A. Chizmadzhev, J. Zimmerberg, and F.S. Cohen. 2005. Line tension and interaction energies of membrane rafts calculated from lipid splay and tilt. Biophys. J. 88: 1120–33.

65. Muddana, H.S., H.H. Chiang, and P.J. Butler. 2012. Tuning membrane phase separation using nonlipid amphiphiles. Biophys. J. 102: 489–97.

66. May, S. 2009. Trans-monolayer coupling of fluid domains in lipid bilayers. Soft Matter. 5: 3148–3156.

67. Chiantia, S., and E. London. 2012. Acyl Chain Length and Saturation Modulate Interleaflet Coupling in Asymmetric Bilayers: Effects on Dynamics and Structural Order. Biophys. J. 103: 2311–2319.

68. Collins, M.D. 2008. Interleaflet coupling mechanisms in bilayers of lipids and cholesterol. Biophys. J. 94: L32–4.

69. Rosetti, C., and C. Pastorino. 2010. Polyunsaturated and saturated phospholipids in mixed bilayers: a study from the molecular scale to the lateral lipid organization. J. Phys. Chem. B. 115: 1002–13.

70. Seul, M., and D. Andelman. 1995. Domain Shapes and Patterns: The Phenomenology of Modulated Phases. Science. 267: 476–483.

71. Shi, Q., and G.A. Voth. 2005. Multi-scale modeling of phase separation in mixed lipid bilayers. Biophys. J. 89: 2385–94.

72. Palmieri, B., T. Yamamoto, R.C. Brewster, and S.A. Safran. 2014. Line active molecules promote inhomogeneous structures in membranes: theory, simulations and experiments. Adv. Colloid Interface Sci. 208: 58–65.

73. Sarasij, R.C., S. Mayor, and M. Rao. 2007. Chirality-induced budding: a raft-mediated mechanism for endocytosis and morphology of caveolae? Biophys. J. 92: 3140–58.

CHAPTER 4
The effects of WALP length and concentration on phase behavior in quaternary lipid mixtures: A molecular dynamics study

4.1 Abstract

Four-component lipid mixtures containing a high-Tm lipid, a nanodomain-inducing low-Tm lipid, a macrodomain-inducing low-Tm lipid and cholesterol have become increasingly popular for modeling the cell plasma membrane. In these mixtures, domain size can be controlled by varying the relative amounts of the two low-Tm lipids. Previously, we used CG and atomistic simulations to study phase properties in the four-component mixture DPPC/[PUPC + DUPC]/cholesterol = 0.4/0.4/0.2, where the nanodomain-inducing low-Tm lipid PUPC was incrementally replaced by the macrodomain-inducing low-Tm lipid DUPC. Here, we expand this study by adding transmembrane α-helical WALP peptides to the CG four-component lipid mixtures. We examine three lengths of WALP (WALP-17, WALP-23 and WALP-29) and five concentrations of WALP (0 mol%, 0.5 mol%, 1 mol%, 2 mol% and 4 mol%) to study how they affect the behavior of the four-component mixture as PUPC is replaced by DUPC. Regardless of the relative amounts of the low-Tm lipids, we find that WALPs always increase phase domain size and alignment compared to the corresponding lipid-only mixtures. These effects are smallest for the longest WALP, and increase with increasing WALP concentration. Thus WALPs could potentially induce macroscopic domain formation in otherwise nanodomain-forming lipid-only mixtures. Since the cell plasma membrane contains a large fraction of transmembrane proteins, our findings help to link the behavior of lipid-only model membranes to phase behavior *in vivo*.

4.2 Introduction

The cell plasma membrane is comprised of hundreds of different lipid and protein species giving rise to distinct nanoscale environments known as rafts (1, 2). The properties and lipid

compositions of the raft and non-raft environments suggest that they may be nanoscopic phase domains. Indeed, simplified lipid mixtures representing the plasma membrane can give rise to coexisting Lo and Ld phases, similar to the raft and non-raft environments, respectively (1, 3). Modeling the complexity of the plasma membrane using these simplified lipid mixtures has helped elucidate many of the fundamental features of phase separation that may underlie raft formation. However, a key feature commonly left out of experimental model membranes is the presence of proteins. Since transmembrane protein domains make up 15-20% of the volume of the plasma membrane (4, 5), a complete understanding of phase behavior and raft formation requires inclusion of proteins in the well-established, but more simplistic, lipid-only model membranes.

The simplest biologically relevant model membrane mixtures giving rise to coexisting Lo and Ld domains contain three representative lipid types found in the plasma membrane: a high-Tm lipid, a low-Tm lipid and cholesterol (6–9). Depending on the particular mixture, the Lo + Ld domains will either be nanoscopic or macroscopic (3). In both cases, the more disordered and fluid-like Ld phase is enriched in the low-Tm lipid whereas the Lo phase has high chain order and is enriched in the high-Tm lipid and cholesterol (3, 10). Rafts are also enriched in high-Tm lipids and cholesterol compared to the rest of the membrane (1), indicating that the simplistic lipid-only membrane models capture the general nature of coexisting plasma membrane domains. However, the behavior of the plasma membrane is complicated by the presence of proteins.

Proteins within the plasma membrane affect raft behavior, and are affected by it. In cells, rafts must be on the order of tens of nanometers as they are below the optical resolution limit (1), but cooled plasma membrane vesicles (blebs) that are separated from the proteins of the

cytoskeleton can exhibit coexisting micron-scale fluid domains (11, 12). This has been supported by theoretical models showing that pinning from the cytoskeleton can prevent large-scale domains while also stabilizing small-scale critical fluctuations (13). In this way, proteins can play an active role in altering domain size and morphology within the plasma membrane. Proteins also respond to the underlying phase behavior of the plasma membrane, with peripheral and integral membrane proteins preferentially partitioning into certain phases of blebs (11, 12). The ability of proteins to alter and respond to phase behavior is perhaps best captured by experiments in which crosslinking of gangliosides by proteins induces phase separation, which in turn alters the partitioning of transmembrane peptides (14, 15). The molecular underpinnings of this two-way relationship are beyond the resolution of experiments, but they have been elucidated through CG MD simulations of ternary model membranes with proteins.

By simplifying the representation of molecules, CG models allow access to the size-scales and time-scales necessary for studying membrane phase separation and protein-phase interactions (16–19). Simulations of phase-separated model membranes show that protein-anchors, such as the H-Ras anchor, and protein binding molecules, such as gangliosides, can exhibit preferential phase partitioning and even interfacial partitioning lowering the line tension between phases (20, 21). Interactions of the anchors with the surrounding membrane in turn influence overall protein behavior, with the peripheral membrane proteins Hedgehog, H-Ras and N-Ras partitioning based on the nature of their cholesterol-like (Hedgehog) or lipid-like (H- and N-Ras) anchors (20). Simple α-helical peptides have also been useful at elucidating protein-membrane interactions as they represent the ubiquitous transmembrane α-helical domains of integral membrane proteins (22). CG simulations of phase separated bilayers with these α-helices have provided insight into peptide partitioning (23), the effect of peptide-phase hydrophobic

mismatch (23–25), and the ability of the helices to alter domain patterning either through helix fixation (24), interactions of the helices' extracellular domains (26), or by large concentrations of the helices crowding the membrane (27). Further control and evaluation of domain properties and peptide effects requires expanding beyond the minimum ternary lipid mixtures commonly used to achieve phase separation in CG simulations. This can be accomplished by adding just one more lipid component.

Recent work with four-component lipid mixtures has taken advantage of the fact that the difference between a nanoscopic ternary mixture (eg. DSPC/POPC/cholesterol (28)) and macroscopic ternary mixture (eg. DSPC/DOPC/cholesterol (29)) can be as simple as the type of low-Tm lipid (30–32). The size of domains can then be controlled in four-component mixtures by fixing the overall concentration of high-Tm lipid/[nanodomain-forming low-Tm lipid + macrodomain-forming low-Tm lipid]/cholesterol (eg. (DSPC/[POPC + DOPC]/cholesterol), and incrementally replacing the nanoscopic low-Tm lipid with the macroscopic low-Tm lipid. As replacement increases, domains grow from nanoscopic, up several orders of magnitude to macroscopic (30). Specifics of the phases can then be measured throughout this replacement, with properties such as phase thickness mismatch found to be correlated with domain size (33). Since cells may similarly be able to use composition to control raft behavior and size, four-component systems are the next logical step for modeling protein-phase interactions that may occur *in vivo*.

In this paper, we study the effects of simple transmembrane α-helical peptides (WALPs) on phase behavior in four-component lipid mixtures using CG molecular dynamics. To reflect experimental four-component mixtures, we use the same system as described in our previous work (34): the high-Tm lipid DPPC, the macrodomain-forming low-Tm lipid DUPC, the

nanodomain-forming low-Tm lipid PUPC, and cholesterol at a composition of DPPC/[PUPC + DUPC]/cholesterol = 0.4/0.4/0.2 (Figure 4.1). We define a replacement ratio as ρ = [DUPC]/[PUPC + DUPC] and simulate along a compositional trajectory (ρ-trajectory) of increasing ρ. Thus, low ρ simulations have large fractions of PUPC and small domains, and high ρ simulations have large fractions of DUPC and large domains. As a function of ρ, we investigate how domain properties are affected by WALP length and concentration. A main result is that all WALPS tested, regardless of length and concentration, increase domain size and alignment for all ρ values tested.

4.3 Computational Methods

All simulations were performed at a lipid composition of DPPC/[PUPC + DUPC]/cholesterol = 0.4/0.4/0.2. While the DPPC/PUPC/cholesterol mixture is more properly termed non-ideal mixing rather than nanoscopic phase separation (27, 35), it does lead to small domain formation and so allows us to study the transition of domain behavior from small clusters at low ρ to large phase separated patches at high ρ.

We chose which WALPs to add to the quaternary lipid mixtures based on their ability to span the possible range of phase thicknesses in the simulations. The thicknesses (measured as the distance between phosphate beads, see Section 4.4.4) of a pure DUPC Ld phase, a pure PUPC Ld phase and a DPPC/cholesterol = 0.68/0.32 Lo phase are ~ 3.53 nm, ~ 3.76 nm and ~ 4.47 nm, respectively. We therefore chose to use WALP-17, WALP-23 and WALP-29 which have thicknesses (measured as the distance from one end bead to the other) of ~ 2.6 nm, ~ 3.6 nm and ~ 4.5 nm, respectively.

Based on our previous work (34), we found that the largest change in phase behavior for the peptide-free mixture DPPC/[PUPC + DUPC]/cholesterol = 0.4/0.4/0.2 occurred between ρ =

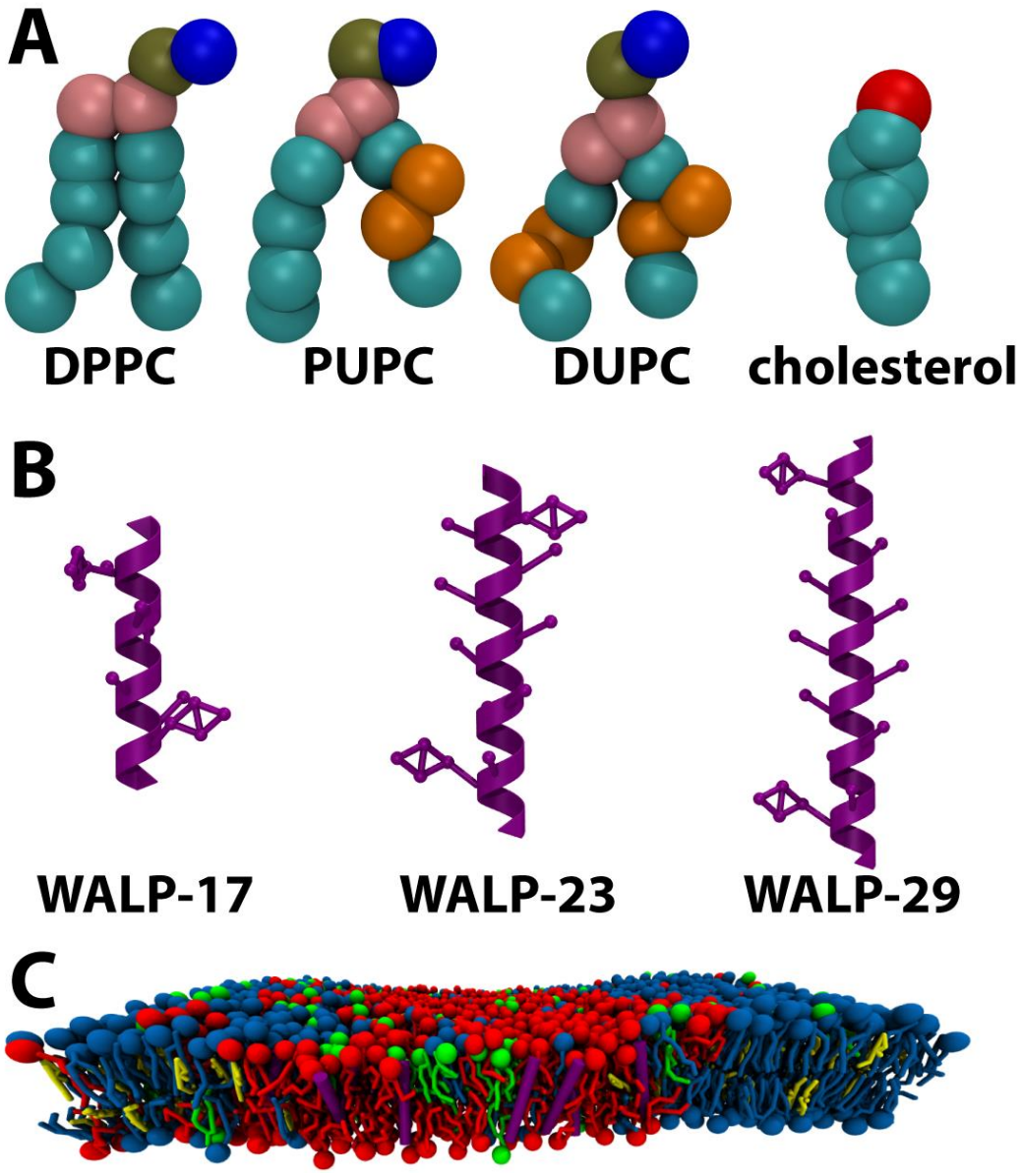

Figure 4.1 Molecules used in this study. A) Lipids, with unsaturated beads colored orange, and B) WALPs used in the simulations. C) Snapshot of bilayer at $\rho = 0.8$ with 2 mol% WALP23, with DPPC (blue), PUPC (green), DUPC (red), cholesterol (yellow) and WALP-23 (purple cylinders).

Table 4.1 Simulation information. Number of lipids, number of WALPs, ρ values and run times for the 7 different systems discussed in the Chapter 4.

	No WALP	**2 mol% WALP-17**	**2 mol% WALP-23**	**2 mol% WALP-29**	**0.5 mol% WALP-23**	**1 mol% WALP-23**	**4 mol% WALP-23**
Num. Lipids	4,608	4,608	4,608	4,608	4,608	4,608	4,608
Num. WALPs	0	90	90	90	18	54	180
ρ	0.4 - 0.8	0.4 - 0.8	0.4 - 0.8	0.4 - 0.8	0.6	0.6	0.6
Run time (μs)	25	10	10	10	10	10	10

0.6 and ρ = 0.8. To fully capture this transition in our current work, we decided to simulate from ρ = 0.4 to ρ = 0.8 in increments of ρ ~ 0.1. Four ρ-trajectories were simulated in this way: one ρ-trajectory each with either 2 mol% WALP-17, 2 mol% WALP-23 or 2 mol% WALP-29, and one ρ-trajectory without WALP (Table 4.1). Three additional simulations were performed at ρ = 0.6, with WALP-23 concentrations of either 0.5 mol%, 1 mol% or 4 mol% (Table 4.1). All simulations contained 4,608 lipids and were fully solvated with ~ 11 water beads per molecule.

4.3.1 Molecular parameters

All simulations were performed with Gromacs (36) version 4.6 and the Martini 2.1 CG force field (37, 38). The standard water and lipid parameters (39) were used, in addition to the newest cholesterol model (40).

All WALPs had the amino acid sequence AGAW$(LA)_n$LWAGA, where n = 4, 7 and 10 for WALP-17, WALP-23 and WALP-29 respectively. Atomistic structures of WALP were first built using PyMol (41), followed by conversion to the Martini 2.1 force field using martinize.py (42).

Note: We initially ran simulations using these standard parameters, but found that all WALPs clustered excessively compared with experimental findings (43), with many clusters containing tens of tightly packed WALPs (data not shown). To prevent overclustering, we changed the amino acid AC1-AC1 bead interactions from "intermediate" to "super-repulsive". This change in parameterization is very mild since it only affects WALP-WALP and internal WALP interactions (no lipid interactions are modified), but it still successfully prevented large-scale clusters. We further note that our main conclusions – that WALPs increase domain size and alignment – were observed both with and without the super-repulsive AC1-AC1 beads.

4.3.2 Simulation parameters

Simulations were run in the NPT ensemble with 20 fs time steps. A temperature of 295 K was maintained using the V-rescale thermostat (44) with a time constant of 1 ps. All molecule types were individually coupled to the temperature bath. The Berendsen semi-isotropic barostat (45) was used to maintain a pressure of 1 bar with a time constant of 4 ps. van der Waals interactions were shifted to zero from 0.9 to 1.2 nm. Electrostatics interactions were shifted to zero from 0 to 1.2 nm. Every 10 timesteps, the center of mass motion of the system was removed. Periodic boundary conditions were used in all three dimensions, and the LINCS (36, 46) algorithm was used to constrain bonds.

The WALP-free systems were run for 25 μs. The WALP-containing simulations were also initially run for 25 μs, but after finding that clustering occurred (see Section 4.3.1), they were rerun with the new super repulsive interaction for 10 μs. The shorter time was necessary due to limited computational resources. However this was still sufficient time for equilibration and data analysis, as discussed in Section 4.3.5.

4.3.3 Bilayer assembly

Initial template bilayers containing 512 lipids and proteins at the desired concentrations were built along the xy plane using in-house code. To ensure complete solvation, ~ 11 water beads were added per molecule. During an initial 3 ns equilibration step at 295 K and 1 bar, the GL1 bead of the lipids, the R2 bead of cholesterols, and the two end beads of the WALPs were weakly position-restrained in the z-dimension (force constant = 20 kJ mol^{-1} nm^{-2}) to prevent excessive bilayer deformation. Position restraints were then removed and the system was further equilibrated for 3 ns at 295 K and 1 bar. The resultant bilayer was tiled 3 x 3 times, yielding the final bilayer sizes (Table 4.1).

Concentrations mentioned throughout the paper are the desired concentrations, but are only approximate due to the limited number of molecules during bilayer assembly. For instance, the desired 0.5 mol% WALP-23 concentration is actually 18/4,608 ≈ 0.39%.

4.3.4 Phase determination

To determine phases, we start by partitioning the molecules into leaflets. If a lipid center of mass is above (below) the local bilayer center of mass, then it is considered in the top (bottom) leaflet. If a WALP's first *and* last beads are above (below) the local bilayer center of mass, then it is considered in the top (bottom) leaflet; if the first *and* last beads are in opposite leaflets, then the WALP is considered in both leaflets. Phases are then determined as in reference (34). First, we project the centers of mass of all molecules in a given leaflet onto the xy plane. Next, a Voronoi tessellation is performed on the centers of mass. A molecule's local environment is then defined to be all molecules that share a Voronoi edge with it. If the local environment is enriched in DPPC and cholesterol compared to the rest of the leaflet, the molecule of interest is considered Lo. Otherwise it is considered Ld. Large-scale phases are then determined based on connectivity of like-phase molecules, where two molecules are connected if they share a Voronoi edge. Clusters fewer than 10 molecules are considered part of the surrounding phase. Boundaries between phases are then the phase interface. This methodology was implemented in Matlab version 2014b.

4.3.5 Equilibration and data analysis

Based on equilibration of box area, phase interface length and phase alignment (Figure C.1), we determined that the simulations were sufficiently equilibrated by 5 μs. Therefore, we only used the last 5 μs for data analysis for the peptide-containing mixtures. For the peptide-free

mixtures, which were run for 25 μs, we allowed for an extended equilibration of 15 μs before data was acquired over the final 10 μs.

For the purposes of calculating standard errors, each simulation data set was split into 250 ns subsets, with each subset considered independent. To confirm that each subset is sufficiently independent, we looked at the autocorrelations of two main parameters of interest: normalized phase interface length, and normalized alignment fraction (discussed below). The autocorrelations are plotted in Figure C.2, which shows that the data becomes sufficiently uncorrelated by 250 ns, and so each 250 ns subset can be considered independent. Where applicable, each subset was further split into two for the two leaflets. Means and standard errors were calculated from these subsets.

4.4 Results

In the following sections we describe the main findings of WALP-induced changes on overall phase behavior (Section 4.4.1), the behavior of the WALPs themselves (Section 4.4.2), and the effect of WALPs on specific lipid and phase properties (Sections 4.4.3 and 4.4.4).

4.4.1 WALPs increase domain size and alignment

To help visualize changes in domain morphology we plot snapshots of the WALP-free and WALP-23 simulations for the representative case of $\rho = 0.6$ (Figure 4.2). Figure 4.2*A-D* are snapshots of individual leaflets with phase boundaries in black, and Figure 4.2*E-H* shows alignment of phase domains between leaflets, with white corresponding to aligned Lo phases, black corresponding to aligned Ld phases and grey corresponding to an Lo phase across from an Ld phase. Even in these one-frame snapshots, there is a clear decrease in perimeter and an increase in domain size and alignment as WALP concentration increases. We quantify these effects in Figure 4.3.

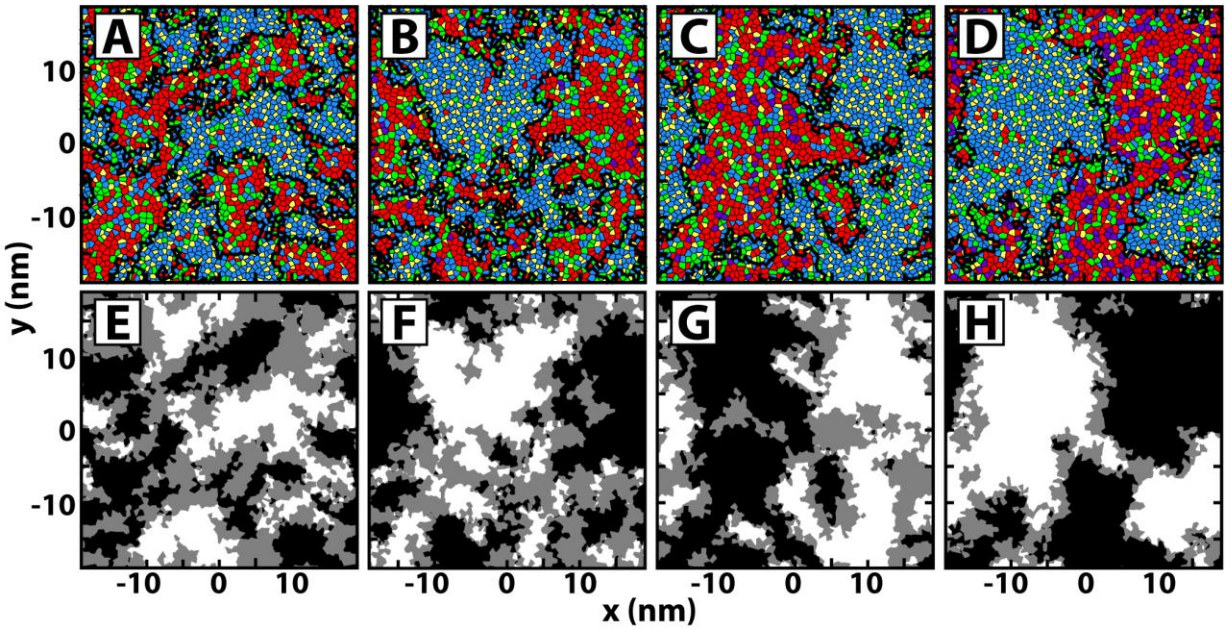

Figure 4.2 Domain size and phase alignment change in the presence of WALP, shown for ρ = 0.6. A-D) Voronoi tesselation for one leaflet of the bilayer with DPPC (blue), PUPC (green), DUPC (red), cholesterol (yellow) and WALP-23 (purple) for A) the peptide-free system, B) 0.5 mol% WALP-23, C) 1 mol% WALP-23 and D) 4 mol% WALP-23. Phase boundaries demarcated by thick black lines. E-H) Corresponding plots overlaying the bilayer leaflets, with Lo-Lo overlap white, Ld-Ld overlap black, and Lo-Ld overlap gray, shown for E) the peptide-free system, F) 0.5 mol% WALP-23 G) 1 mol% WALP-23 and H) 4 mol% WALP-23.

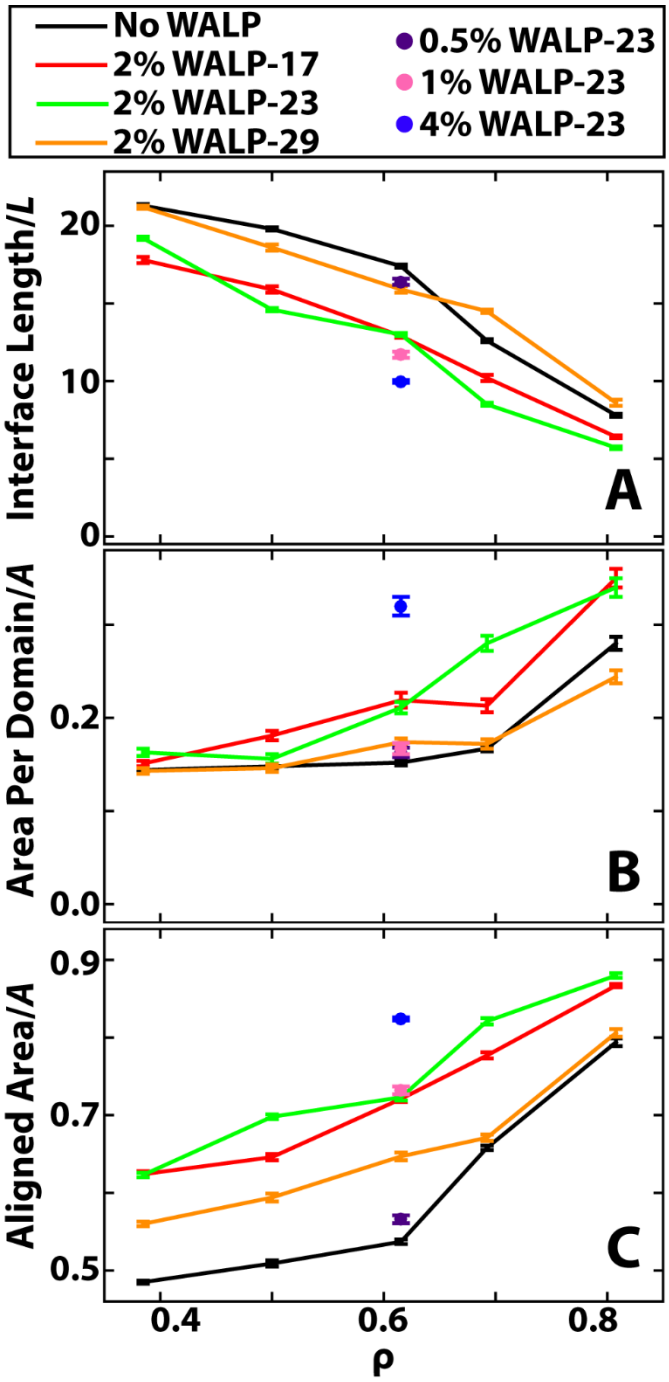

Figure 4.3 Domains grow and phase alignment increases with ρ. A) Interface length, normalized by the box length *L*, decreases along the ρ-trajectories and is smaller in the presence of WALP. B) Area per domain, normalized by the box area *A*, increases along the ρ-trajectories and is larger in the presence of WALPs. C) Aligned area of like-phases, normalized by the box area *A*, increases along the ρ-trajectories and is larger in the presence of WALPs. The color scheme used here is used for other Figures in this Chapter, unless otherwise specified.

Figure 4.3*A* shows the interface length between coexisting phases (normalized by the box length *L*) for all simulations. Since the area fractions of each phase are ~ 50 ± 5% for all simulations (data not shown), changes in boundary length can be predominantly attributed to coalesced domains rather than changes in phase fractions. Consistent with the expected domain coalescence as DUPC fraction increases, all bilayers exhibit a decreasing interface length along the ρ-trajectory. Compared to the WALP-free systems, 2 mol% WALP-17 and 2 mol% WALP-23 dramatically decrease the interface length. 2 mol% WALP-29 has the smallest effect on morphology compared to the other WALPs, only slightly decreasing the interface length at low ρ and slightly increasing it at higher ρ. Of all systems studied, the largest effect is due to 4 mol% WALP-23, which decreases the interface length by ~ 40% compared to the corresponding WALP-free system. Lowering the concentration of WALP-23 generally decreases this effect, but detectable changes are still observed at 0.5 mol% WALP.

The changes in domain coalescence are also visible in Figure 4.3*B*, which shows the average domain area, normalized by the box area *A*. The trends in Figure 4.3*B* are slightly different from those in Figure 4.3*A*, which may be due to sporadic fracturing and fusing of domains having a larger impact on average domain size than perimeter. Still, Figure 4.3*B* shows that domains grow along a ρ-trajectory and in the presence of WALP. Other simulations have shown similar WALP-induced domain size growth in a ternary mixture of DPPC/PUPC/cholesterol (27).

The trends in WALP effects on domain coalescence are mirrored in their effects on domain alignment. In Figure 4.3*C*, we plot the area fraction of aligned domains (i.e. the area fraction of white or black in Figure 4.2*E-H*) for all simulations. Given that phase area fractions are ~ 50%, alignment fractions of ~ 0, ~ 0.5 and ~ 1 correspond respectively to complete

antialignment of domains, random alignment of domains, and complete alignment of domains. For each ρ-trajectory, domain alignment increases as ρ increases. The WALP-free systems exhibit nearly random alignment at low ρ, with alignment increasing beyond ρ = 0.6. The addition of 2 mol% WALP-17 and 2 mol% WALP-23 significantly increases the alignment, regardless of ρ. 2 mol% WALP-29 also causes increased alignment as ρ increases, but the effect is smaller compared to the other WALPs, and is negligible at higher ρ. Again, we find that higher WALP concentrations have more pronounced effects, and that 4 mol% WALP-23 induces the largest alignment of any system at ρ = 0.6.

We compare the size-scales of domains and alignment using pair correlation functions. In Figure 4.4, we plot the interleaflet and intraleaflet pair correlations for the centers of mass of Lo phase molecules for the example case of ρ = 0.6. Even at concentrations as low as 0.5 mol% WALP-23, there is a discernible increase in both domain size and alignment compared to the WALP-free bilayer. Increasing concentration beyond 0.5 mol% generally drives the formation of larger, more aligned domains with a uniquely large effect at 1 mol% WALP. While the three different 2 mol% systems all increase the size-scale of domain size and alignment, as before we see that the effects of WALP-17 and WALP-23 are more significant than those of WALP-29.

4.4.2 WALP behavior: Partitioning, local environment, clustering and tilts

In Figure 4.5*A*, we plot the concentration of WALP as a function of distance from the phase interface, for the representative case of ρ = 0.6. WALPs are almost entirely found in the Ld phase, consistent with previous MD and experimental work (23). Their concentration increases as distance from the interface increases. The unique behavior of WALP-17 is likely due to clustering, as discussed in the next section. Similar trends are observed for all ρ values (data not shown).

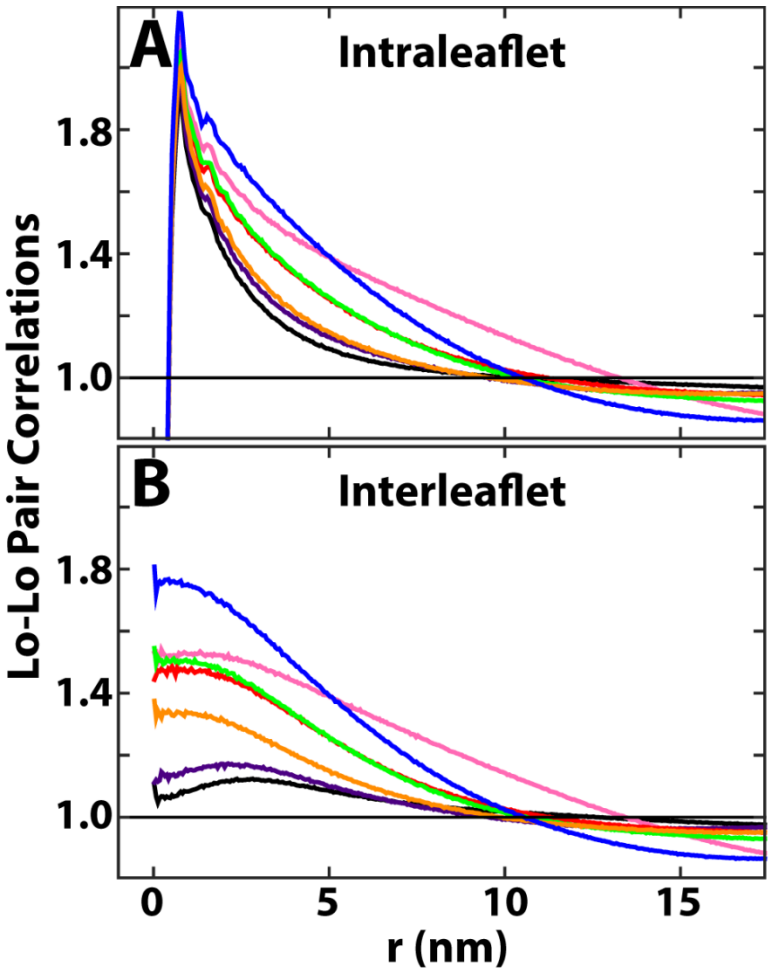

Figure 4.4 Pair correlations can be used to detect changes in domain size and alignment, shown for the example case of $\rho = 0.6$. Centers of mass of Lo phase molecules were used to calculate A) intraleaflet pair correlations which provide information on the characteristic size of Lo domains, and B) interleaflet pair correlations which provide information on the characteristic size of Lo domain alignment. In general, WALPs increase the size-scale of phases and alignment. Results colored as follows: peptide-free (black), 2 mol% WALP-17 (red), 2 mol% WALP-23 (green), 2 mol% WALP-29 (orange), 0.5 mol% WALP-23 (purple), 1 mol% WALP-23 (pink) and 4 mol% WALP-23 (blue).

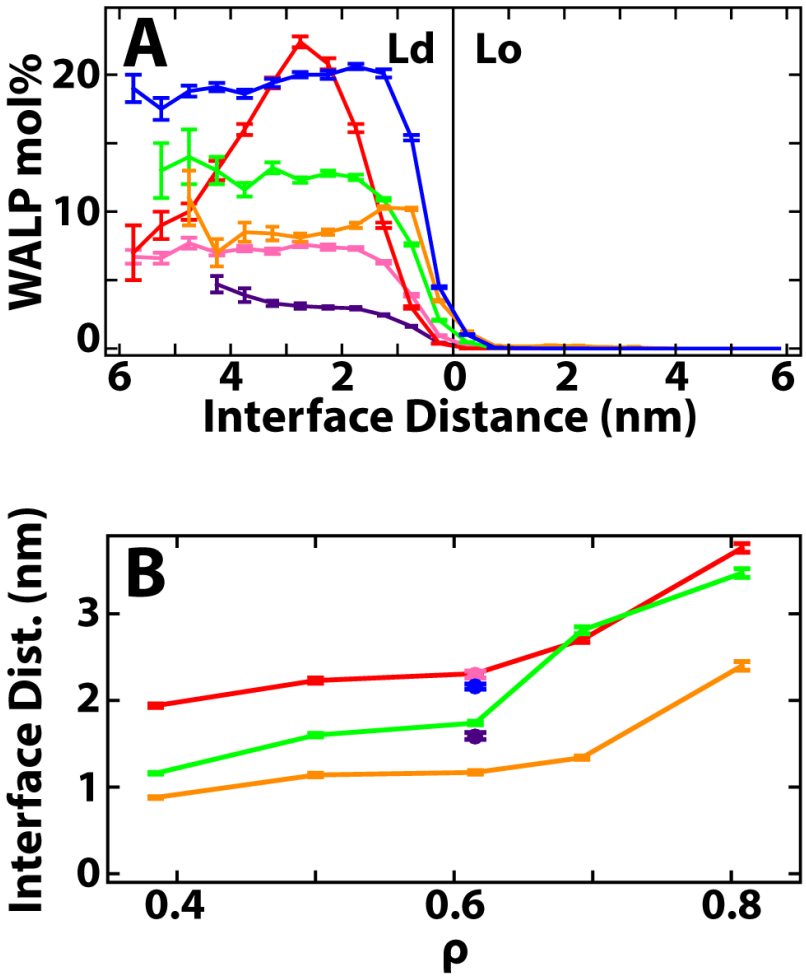

Figure 4.5 Shorter WALPs are found furthest from the phase interface. A) Percentage of lipids that are WALP as a function of distance from the phase interface, shown for the example case of ρ = 0.6. All molecules further than 5.5 nm from the interface were included in the same bin, centered at 5.75 nm. B) Average distance between WALPs and the phase interface shows that shorter WALPs tend to be further from the interface. Results colored as follows: 2 mol% WALP-17 (red), 2 mol% WALP-23 (green), 2 mol% WALP-29 (orange), 0.5 mol% WALP-23 (purple), 1 mol% WALP-23 (pink) and 4 mol% WALP-23 (blue).

We plot the average distance of WALPs from the interface in Figure 4.5*B*. In general, as domains grow with ρ, WALPs are found further from the interface. This implies they prefer being deep within the Ld phases. Figure 4.5*B* also shows that shorter WALPs are further from the interface than longer WALPs.

To study WALP behavior more closely, we can look at their local environments; the local environment of a WALP is defined to be all molecules that share a Voronoi edge with it. In Figure 4.6, we plot the fraction of these Voronoi contacts corresponding to each molecule type. Regardless of ρ value or WALP-type, WALPs tend to predominantly neighbor DUPCs. This is true even at ρ = 0.4, where the amount of PUPC in the simulation exceeds that of DUPC. In all cases, there is preference of WALPs for the low-Tm lipids (27), in agreement with their favorable partitioning into the Ld phase. However, as WALP length increases and WALPs partition closer to the interface, there is an increase in the fraction of contacts between WALP and the Lo lipids DPPC and cholesterol. For all WALPs, there is a significant fraction of WALP-WALP contacts, implying clustering.

The clustering of WALPs seen in Figure 4.6 is further quantified in Figure 4.7, where we plot the average WALP cluster size. As done elsewhere (23), we consider two WALPs to be in the same cluster if any of their beads are within 0.7 nm of each other. At 2 mol%, WALP-23 and WALP-29 clusters remain small, with an average size of ~ 2-4 WALPs per cluster. The size of clusters increases with increasing WALP concentration. Interestingly, 2 mol% WALP-17 simulations have the largest clusters of any simulation, and they decrease as ρ increases. We note that while peptide clustering in a response to bilayer phase and hydrophobic mismatch has been explored extensively (23, 43, 47–54), due to our implementation of a super repulsive interaction to prevent clustering, we cannot draw any conclusions as to why WALP-17 clusters more than

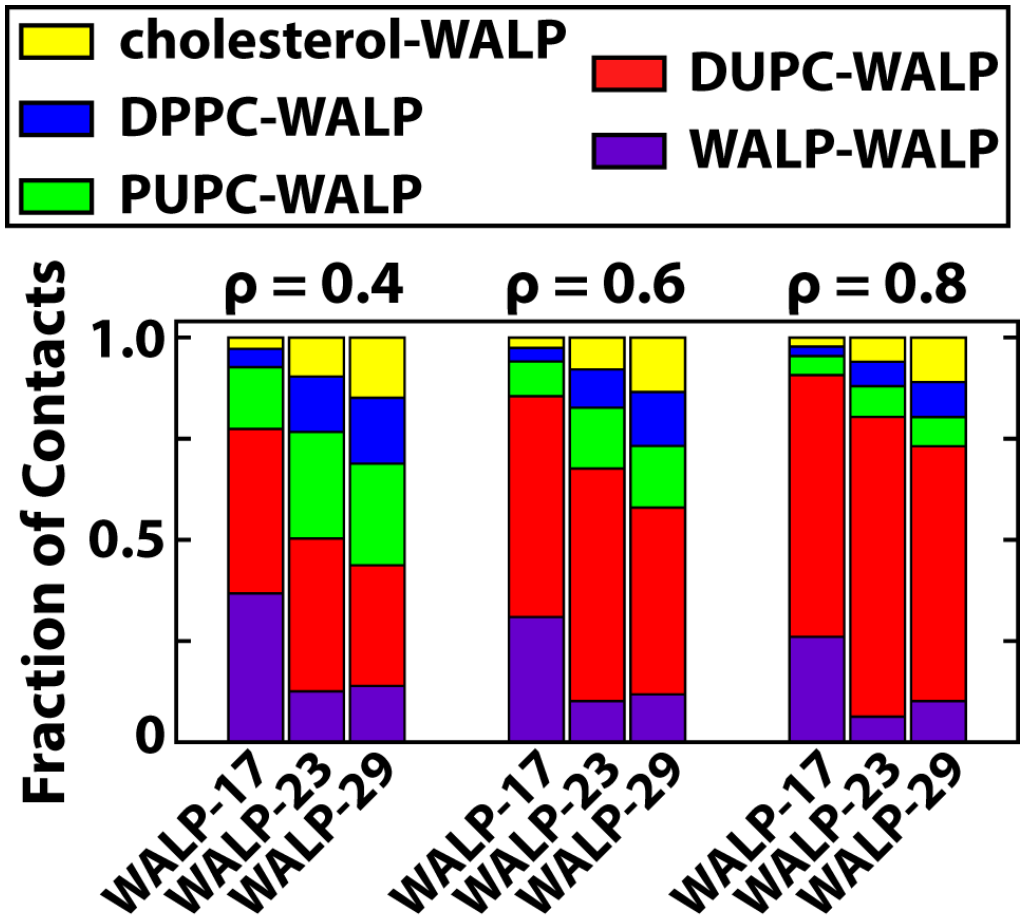

Figure 4.6 WALPs are predominantly surrounded by DUPC, with longer WALPS having a higher fraction of contacts with Lo lipids. Fraction of Voronoi contacts between WALP and other molecules shown for 2 mol% WALP-17, 2 mol% WALP-23 and 2 mol% WALP-29 at ρ = 0.4, ρ = 0.6 and ρ = 0.8.

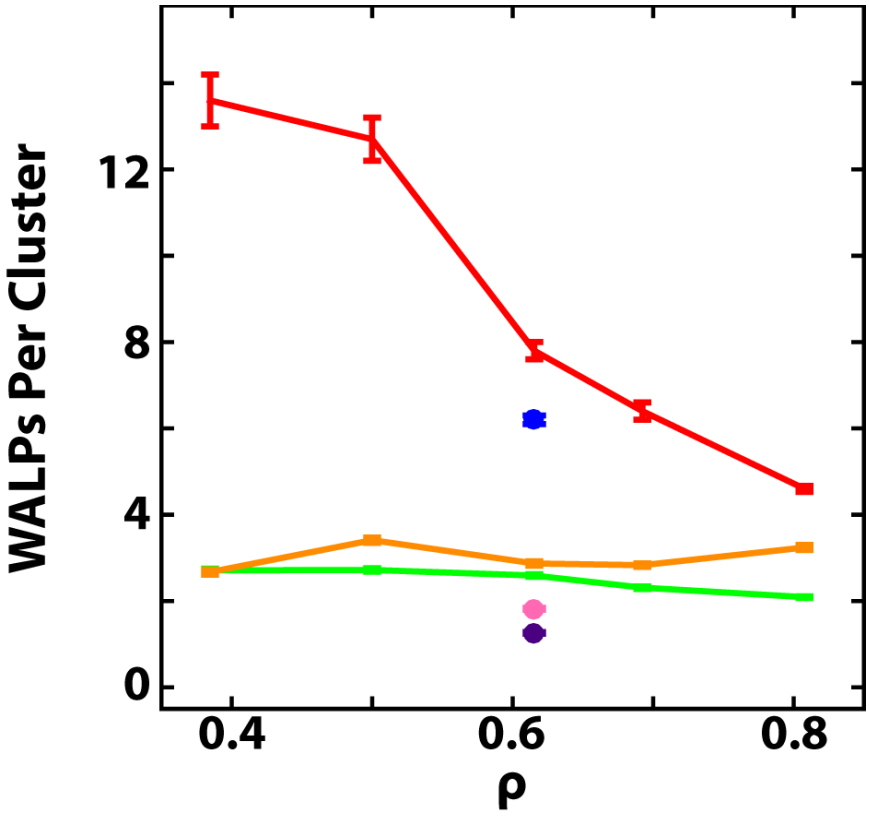

Figure 4.7 Large-scale WALP clustering only occurs for high WALP concentrations or short WALPs. Average number of WALPs per cluster, where two WALPs are considered in the same cluster if two of their beads are within 0.7 nm of eachother. Clustering increases with WALP concentration, but 2 mol% WALP-17 exhibits the most clustering. Results colored as follows: 2 mol% WALP-17 (red), 2 mol% WALP-23 (green), 2 mol% WALP-29 (orange), 0.5 mol% WALP-23 (purple), 1 mol% WALP-23 (pink) and 4 mol% WALP-23 (blue).

the other WALPs. What Figure 4.7 shows is that we were generally successful at preventing the extremely large, tight WALP clusters that are not observed experimentally (43).

In addition to their clustering to adjust to different bilayers, another important characteristic of the WALP molecules is their ability to tilt. In Figure 4.8*A* we plot the tilts of WALP molecules with respect to the bilayer normal. WALP-17 and WALP-23 exhibit similar distributions, but WALP-29 tilts more substantially. WALP-17 also has a peak at high tilt angles, corresponding to the small fraction of WALP-17 that orient perpendicular to the bilayer normal.

Figure 4.8*B* shows the average tilt angle for all the WALP simulations. Aside from the large tilts for WALP-17 at low ρ, WALP-17 and WALP-23 tilt approximately the same amount. This is independent of WALP concentration. WALP-29 tilts the most at every ρ value, and shows a trend of increasing tilt as ρ increases. A similar, but much smaller trend seems to occur for WALP-23. As the thickness of the peptide increases above the thickness of the surrounding membrane, tilting is expected to increase (55). This is consistent with our finding that WALP-29, thicker than the Ld phase, tilts significantly more than either WALP-17 or WALP-23, and that it tilts more in the thinner Ld phases at high ρ (see Section 4.4.4 for phase thicknesses). A nonzero tilt for WALPs thinner than the surrounding bilayer, as we find for WALP-17, has also been observed in other simulations (48, 56).

4.4.3 WALPs increase lipid demixing

Although a small mole fraction of the bilayer, the WALPs promote demixing and change the compositions of coexisting Lo and Ld phases. Figure 4.9*A*-*D* show the mol% of DPPC, PUPC, DUPC and cholesterol in Lo and Ld phases. In order to compare to the WALP-free case, we do not include WALPs in the concentration calculations. Along the WALP-free ρ-trajectory, we see an increase in demixing between the Lo phase lipids (DPPC and cholesterol) and the Ld

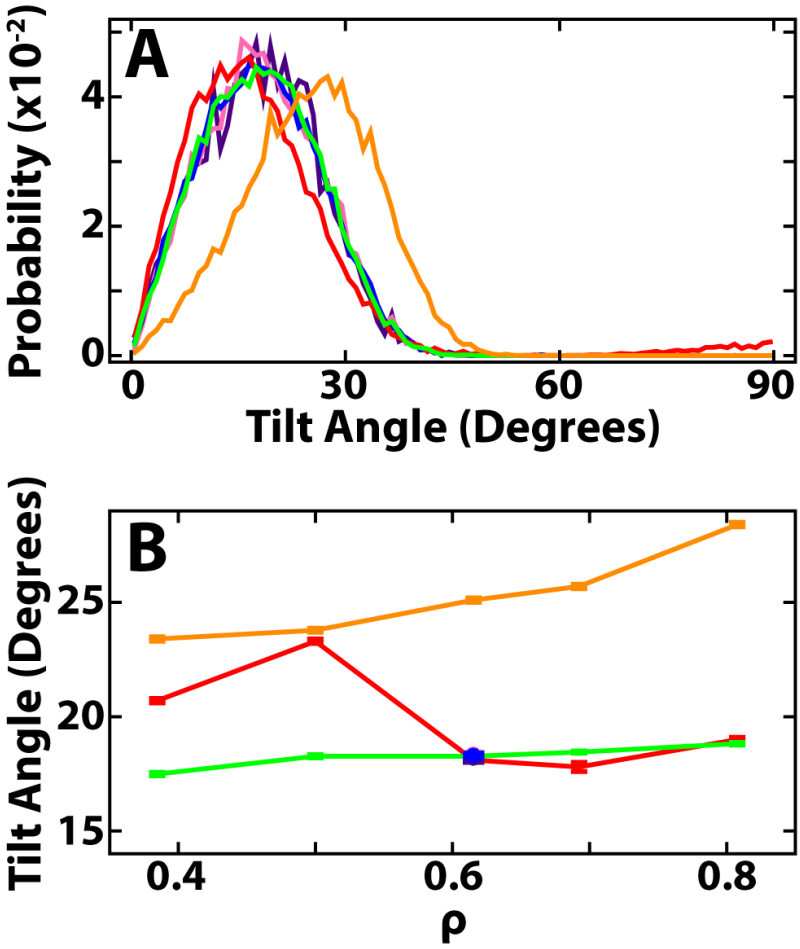

Figure 4.8 Longer WALPs tilt more than shorter WALPs. A) Tilt angle distributions for different WALPs at ρ = 0.6. The high tilt angles for WALP-17 are due to WALPs aligning with the bilayer plane. B) Average tilt angles for WALPs as a function of ρ show that WALP-29 tilts more than WALP-17 or WALP-23. Results colored as follows: 2 mol% WALP-17 (red), 2 mol% WALP-23 (green), 2 mol% WALP-29 (orange), 0.5 mol% WALP-23 (purple), 1 mol% WALP-23 (pink) and 4 mol% WALP-23 (blue).

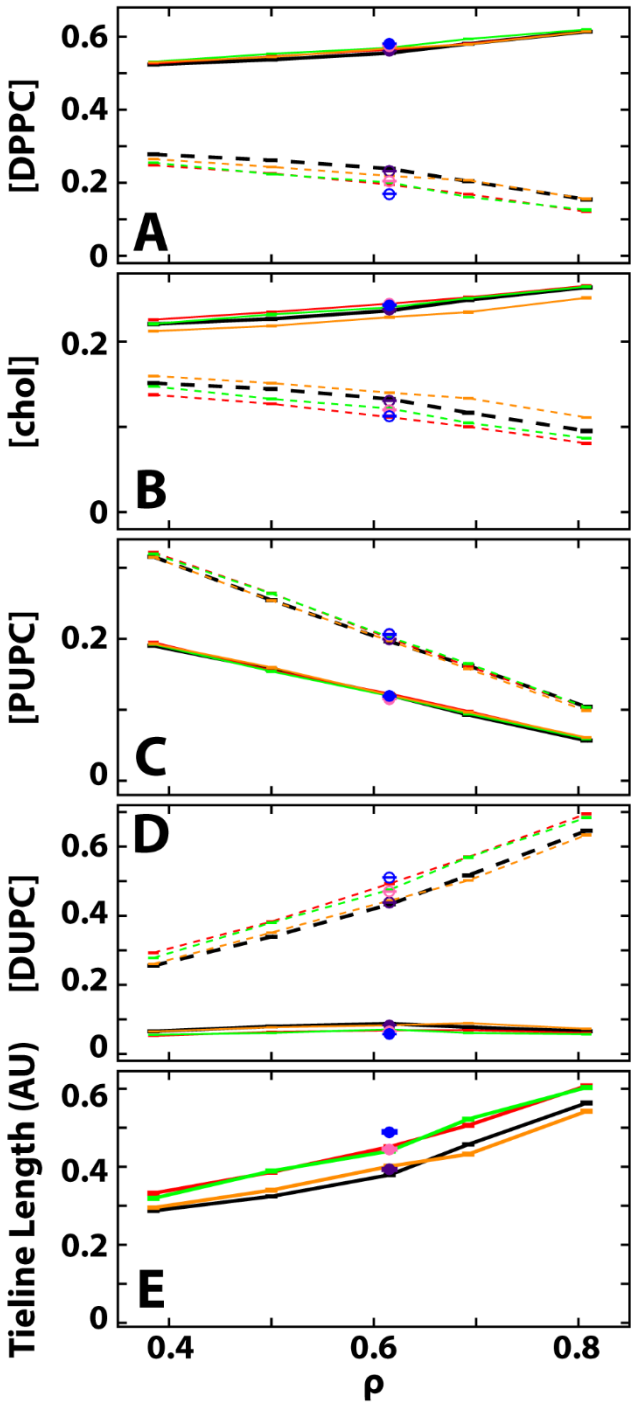

Figure 4.9 WALPs increase demixing. Mol% of A) DPPC, B) cholesterol, C) PUPC and D) DUPC for the Lo phases (solid line or filled circles) and Ld phases (dashed line or empty circles). E) Length of tieline connecting Lo and Ld compositions, in arbitrary units. Tieline length calculated based on pseudo 3-component phase diagram of DPPC/[PUPC + DUPC]/cholesterol where the two low-Tm lipids are grouped together. Results colored as follows: peptide-free (black), 2 mol% WALP-17 (red), 2 mol% WALP-23 (green), 2 mol% WALP-29 (orange), 0.5 mol% WALP-23 (purple), 1 mol% WALP-23 (pink) and 4 mol% WALP-23 (blue).

phase lipids (PUPC and DUPC). In the presence of WALP, there is a further depletion of DPPC in the Ld phases and a less noticeable change in the Lo phase. Similarly, WALPs tend to further decrease cholesterol concentration in the Ld phase and increase cholesterol concentration in the Lo phase. An exception is the 2 mol% WALP-29 ρ-trajectory which has the opposite behavior. For the low-Tm lipids, we find that WALPs deplete DUPC from the Lo phase and enrich it in the Ld phase, whereas WALP-induced compositional changes for PUPC are fairly negligible. For all lipids, the demixing increases as WALP concentration increases.

We summarize these findings by measuring the lengths of tielines between coexisting phases; i.e, measuring the distance between compositions of the coexisting phases as they would appear on the pseudo 3-component phase diagram of DPPC/[PUPC + DUPC]/cholesterol where the two low-Tm lipids are grouped together. Larger compositional differences between coexisting phases are then reflected in longer tielines. In Figure 4.9*E*, we plot the length of the tielines for all systems studied. In nearly every case, WALPs increase the compositional differences between coexisting Lo and Ld phases. The extent of demixing is largest for WALP-17 and WALP-23, and it increases with WALP concentration. Our findings are in agreement with CG simulations of similar mixtures showing WALP-enhanced demixing that increases with WALP concentration (27).

4.4.4 WALPs alter lipid order and phase thickness

We calculate the average order of a lipid using the equation

$$S_z = \frac{1}{8}\sum_{n=1}^{8} \langle 3\cos^2 \alpha_n - 1\rangle/2 \qquad (4.1)$$

where α is the angle between a bond in the lipid acyl chain and the bilayer normal, and the sum is over the four bonds in each acyl chain. In Figure 4.10 we plot the average order of each lipid in WALP-free bilayers as a function of distance to the phase interface from ρ = 0.4 (gray) to ρ =

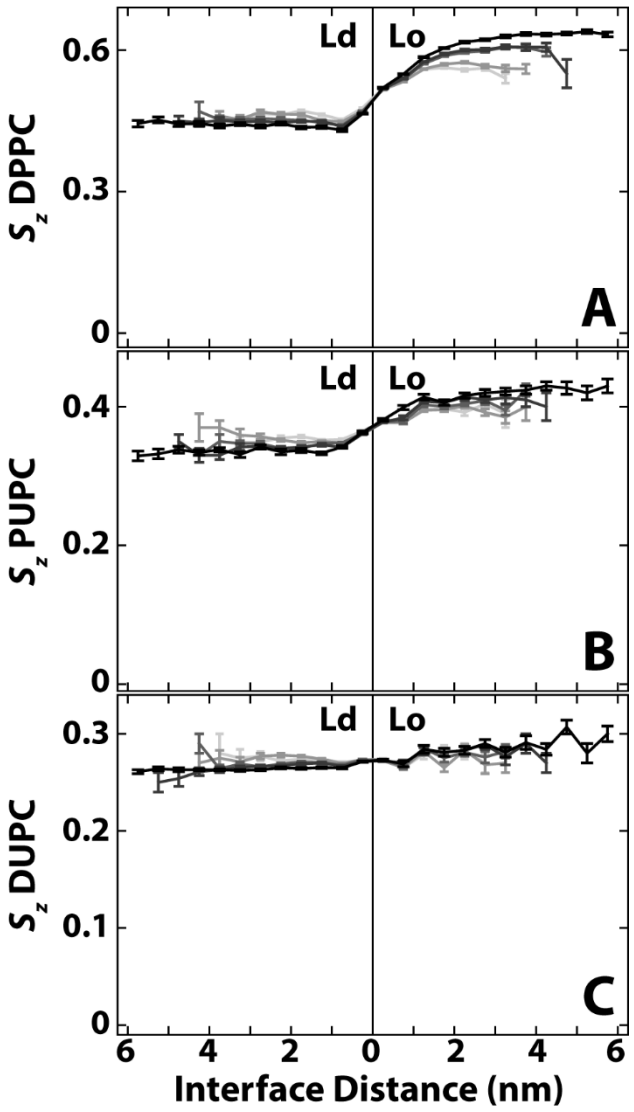

Figure 4.10 Lipid order is perturbed near the interface. Average lipid order, S_z, for A) DPPC, B) PUPC and C) DUPC as a function of distance from the phase interface. Darkness increases with ρ, from ρ = 0.4 (light gray) to ρ = 0.8 (black). All molecules further than 5.5 nm from the interface were included in the same bin, centered at 5.75 nm.

0.8 (black). As we have shown previously (34), the order increases across the interface from the Ld phase to the Lo over the span of only a few nanometers.

To measure the effects of WALP on lipid order, we normalized for the distance-dependent effects near the phase interface shown in Figure 4.10. In Figure 4.11, we plot the average order of Ld phase DUPCs for the WALP-containing mixtures at $\rho = 0.8$, divided by the corresponding WALP-free results. Using this ratio, we find that WALP-17 decreases the order of nearby lipids by ~ 30% compared to the WALP-free mixtures. WALP-23 has a smaller effect, slightly raising the order in some places, but there is no significant dependence on WALP-23 distance. WALP-29 raises the overall average order of nearby lipids by ~ 15%, and slightly raises the average order at further distances. We find similar behavior for DPPC and PUPC (data not shown). Such WALP-induced local perturbations that die off within a couple of nanometers has also been observed in previous simulations (25) and is predicted by theoretical models (53).

As expected with changes in order, bilayer thickness is also altered in the presence of WALP. To measure thickness, we first pair each top leaflet PC lipid with the nearest bottom leaflet PC lipid. We consider the pair of lipids to be "valid" if both lipids are in the same phase, and if they are both more than 2 nm from the phase interface (to avoid interfacial influence). Phase thickness is then defined to be the average phosphate-phosphate distance of all such valid lipid pairs in that phase. We plot the coexisting phase thicknesses, and difference in thickness between the phases, in Figure 4.12. For all systems, the Lo phase thickness is ~ 4.3 nm, and only slightly increases from $\rho = 0.4$ to $\rho = 0.8$. Changes in Ld thickness are much more pronounced. WALP-17 Ld phases are always the thinnest (thinner than ~ 3.5 nm), WALP-29 Ld phases are always the thickest (thicker than ~ 3.75 nm) and WALP-23 and the WALP-free Ld phases are of comparable moderate thickness (~ 3.75 nm).

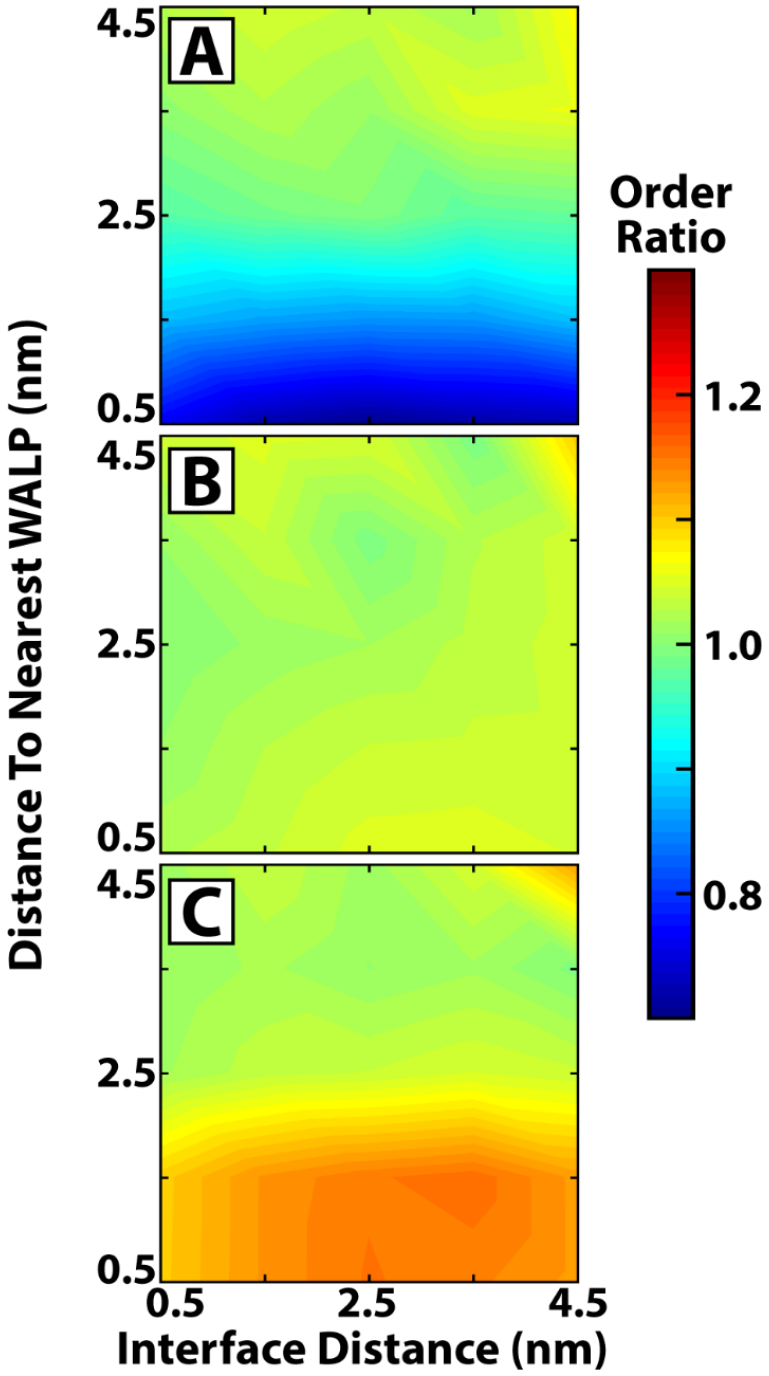

Figure 4.11 WALPs at 2 mol% perturb nearby lipids, shown for the representative case of ρ = 0.8. Average Ld phase DUPC order ratio as a function of distance to the interface and distance to the nearest WALP for A) WALP-17, B) WALP-23 and C) WALP-29. Ratio is taken by dividing DUPC order at a given interface distance by the corresponding DUPC order from the peptide-free simulation. All DUPCs further than 4 nm from the interface were included in the same bin, centered at 4.5 nm.

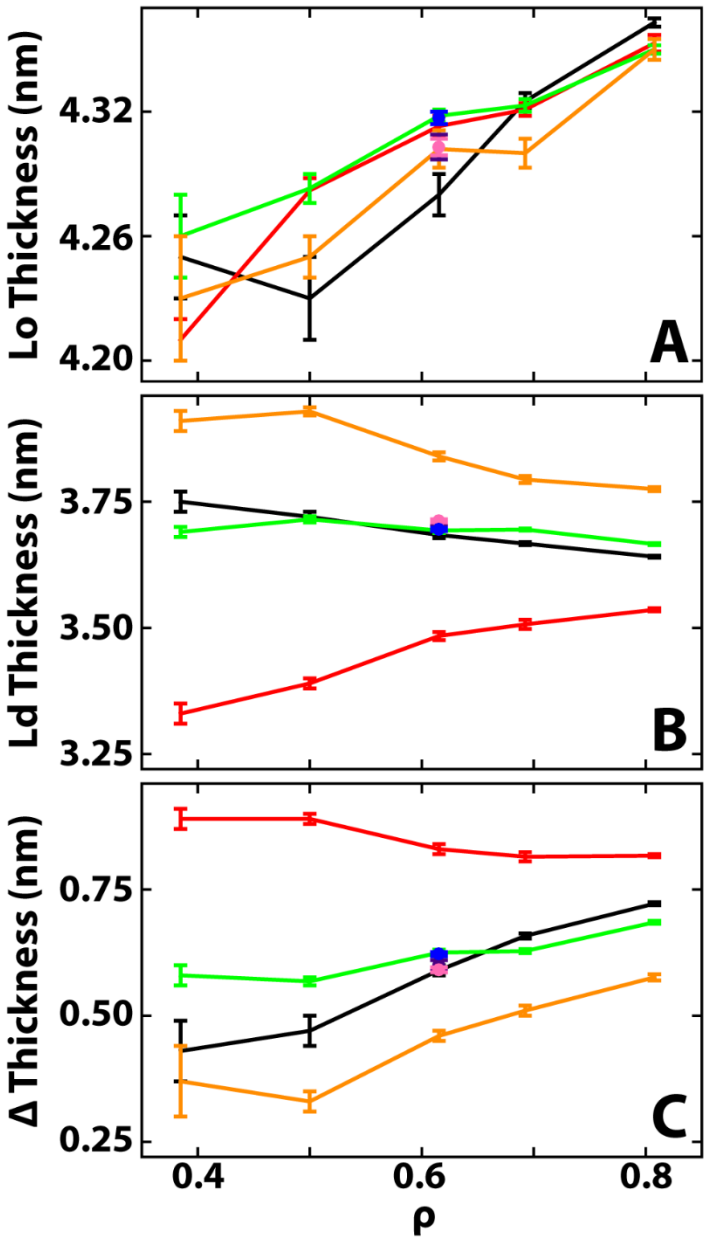

Figure 4.12 WALPs change the thickness mismatch between phases**.** Thicknesses of A) the Lo phase and B) the Ld phase for all simulations. Thickness was measured as the average phosphate-phosphate distance between pairs of "valid" PC lipids in opposite leaflets, as defined in the main text. C) The thickness difference between coexisting phases differs for the different WALPs and different ρ values. Results colored as follows: peptide-free (black), 2 mol% WALP-17 (red), 2 mol% WALP-23 (green), 2 mol% WALP-29 (orange), 0.5 mol% WALP-23 (purple), 1 mol% WALP-23 (pink) and 4 mol% WALP-23 (blue).

In Figure 4.12*C*, we show the thickness mismatch between coexisting phases. Thickness mismatch increases as WALP length decreases, with WALP-23 and WALP-free simulations exhibiting similar thickness mismatches. At low ρ values, the difference in thickness between coexisting phases can vary dramatically. For example, the thickness mismatch for the WALP-17 simulation at ρ = 0.4 is nearly three times the corresponding WALP-29 simulation thickness mismatch. The differences in thickness mismatches decrease as ρ increases.

Supporting our findings, peptide-induced order and thickness changes have been predicted theoretically (53, 57, 58), and measured in simulations (23, 25, 48, 52) and experiments (59, 60).

4.5 Discussion

Our main findings from Section 4.4 are that WALPs induce both an increase in domain size and an increase in domain alignment. In Sections 4.5.1 and 4.5.2 we discuss how the other results from Section 4 help to explain these findings. In Section 4.5.3, we discuss the implications our findings have for experiments on similar systems, and for the life of a cell.

4.5.1 WALPs increase intraleaflet line tension

Line tension is the energy per unit length of the phase interface. It has been measured both experimentally (61–63), and in simulations (18, 27, 64) using a variety of techniques. Typically, large stable domains are required for such measurements. However many of our simulations exhibit small transient domains that are not easily accommodated by existing methods. Instead, we use boundary length as an analog for line tension. An increase in line tension would drive domains to coalesce, reducing the amount of interface. Since the area fractions of the phases remain at ~ 50%, changes in the normalized boundary length of Figure 4.3*A* and area per domain of Figure 4.3*B* are directly correlated to changes in line tension. Our

results showed a pronounced decrease in boundary length and increase in domain size in the presence of WALP. We can therefore conclude that all WALPs, regardless of concentration, raise the line tension compared to corresponding WALP-free simulations. This has been supported by other CG MD simulations which indicate higher line tensions in systems with WALP (27).

The increase in line tension is in part driven by WALP partitioning. Even at small concentrations, molecules can alter phase behavior based on how they partition. Those that preferentially partition to the phase interface lower line tension (21, 64, 65), while those that partition away from the phase interface raise line tension. In Figure 4.5 we showed that not only do WALPs partition into the Ld phase, in agreement with other work (23), but that they avoid the interface, tending to be deep within the Ld phase. This implies that WALPs raise line tension, and that higher concentrations of the interface-avoiding WALPs further increases line tension. Additionally, we found that WALP-29 was always closest to the interface for all ρ values, which implies it should raise line tension the least. Indeed, this simple partitioning-driven line tension reasoning is in agreement with our boundary length and domain size results, as well as previous simulations (27) and experiments showing WALPs and other peptides can raise line tension in lipid systems (66).

Another contribution to line tension is the WALP-induced demixing of the coexisting phases. In Figure 4.9 we showed that the addition of WALPs to the simulations increases the fraction of DPPC and cholesterol in the Lo phase and increases the fraction of the low-Tm lipids in the Ld phase. Such an increase in compositional differences between coexisting phases raises the line tension, as has been measured experimentally for lipid only systems (62). This is consistent with our findings of increased demixing, and increased line tension, for WALP-17 and

WALP-23 compared to WALP-29 and the lipid-only mixtures. It is also consistent with our observation that higher WALP concentrations increase demixing and line tension. Other simulations have even shown that high WALP concentrations increase demixing to the point where domains are stabilized in otherwise mixed systems (27).

In addition to partitioning and demixing, one of the key factors often attributed to raising line tension is the thickness mismatch between coexisting phases (27, 67–69). Thickness mismatch forces the phases to adjust at the interface, which is energetically more unfavorable for larger mismatches. In the WALP-free simulations studied here, there is always a thickness mismatch between the phases (Figure 4.12). This thickness mismatch increases along the ρ-trajectory, contributing to the higher line tension observed at higher ρ. In the presence of WALP, thickness mismatches change. Compared to the peptide-free simulations, WALP-17 increases the mismatch by thinning the Ld phase, WALP-23 barely changes the thickness mismatch since it does not significantly perturb either phase, and WALP-29 decreases the thickness mismatch by thickening the Ld phase. If line tension in the WALP-containing systems were solely determined by thickness mismatch of the coexisting phases, then compared to the peptide-free simulations we would expect a very large increase in line tension for WALP-17, a negligible change in line tension for WALP-23 and a decrease in line tension for WALP-29. We would also expect that different WALP-23 concentrations would not significantly affect line tension since they do not significantly change thickness mismatch. This is not the case. Instead, all WALPs increase the line tension compared to the WALP-free systems, with higher WALP-23 concentrations leading to increased line tensions. The only case where we do not see an increase in line tension is for high ρ values for WALP-29. There, the decreased thickness difference may play a role in preventing large line tensions.

4.5.2 WALPs increase interleaflet surface tension

As reported in Section 4.4.1, all WALPs at all concentrations increase alignment. Since alignment is caused by a surface tension between phases in apposed leaflets, the presence of WALPs must be increasing this surface tension. This likely occurs through both intraleaflet and interleaflet effects.

The increase in intraleaflet demixing and domain growth in the presence of WALP is one mechanism that can raise surface tension and contribute to the dramatic increase in alignment. As we have shown previously (34), the increase of both DUPC fraction and demixing along the WALP-free ρ-trajectory results in a higher fraction of unsaturated beads at the bilayer midplane in the Ld phase. These beads interact unfavorably with the saturated beads in the bilayer midplane in the Lo phase, driving like-phase domains to align. The fact that domains are larger at higher ρ in the WALP-free systems further drives alignment due to the increased energy penalty that accompanies large, misaligned, domains (70–72). The addition of WALPs is thus able to increase interleaflet alignment by increasing both demixing *and* domain size. This two-fold effect also helps explain why the small increase in demixing and domain size for WALP-29 only results in a small increase in alignment.

Along with intraleaflet effects, the interleaflet nature of the transmembrane WALPs contributes significantly to alignment. Since the WALPs span the bilayer and partition into the Ld phase, it is reasonable that they would increase domain alignment by "anchoring" the Ld domains from one leaflet to another. This is consistent with our finding that alignment increases with WALP concentration, since more WALPs mean more interleaflet anchors. Not surprisingly, simulations have shown that this effect can be lessened by palmitoylating one end of α-helical transmembrane domains, which promotes clustering of Ld lipids to the non-palmitoylated end

and clustering of Lo lipids to the palmitoylated end (20, 26). Therefore the ability of the WALP to partition into the Ld phase in *both* leaflets is essential to alignment of domains.

To a lesser extent, alignment might also be affected by the line tension of phases. Systems with higher line tension fluctuate less, and have fewer domains, than systems with lower line tensions. Lower line tension, as is the case for WALP-29, may then contribute to decreased alignment due to larger domain fluctuations.

Note that some phase properties are proposed to favor antialignment of domains. For instance, thickness mismatch between coexisting phases is thought to hamper alignment as a way to minimize the exposure of hydrocarbon to water at the phase interface (72, 73). However, we find alignment is largest for the 4 mol% WALP-23 simulation which has a relatively large thickness mismatch. Compared to the WALP-free mixtures, there is also a significant increase in alignment for all the 2 mol% WALP-17 simulations which have the largest thickness mismatches. Evidently, thickness mismatch is not a major factor in alignment for these simulations.

4.5.3 Implication of WALP effects for experiments and cells

Experiments measuring ρ-trajectories are useful for finding the compositional crossover point between nanodomains and macrodomains (30, 31). The transition can be modeled as a competition between line tension, which favors large domains, and some competing interaction that favors broken-up domains (74, 75). When line tension exceeds this competing interaction, nanodomains give way to macrodomains. Line tension has been measured along ρ-trajectories (76, and unpublished) but they are limited to measurements in the macroscopic regime. Nevertheless, they have shown that macroscopic domains first form along the ρ-trajectory when line tension reaches a value of ~ 0.4 pN, regardless of the lipid mixture (unpublished). Based on

our findings, we predict that WALPs *in vitro* raise the line tension and increase domain size, and so should shift the nano-to-macro transition to lower ρ values compared to the corresponding lipid-only mixtures. This effect should be least pronounced for WALPs thicker than the bilayer, and should increase with increasing WALP concentration.

WALPs *in vitro* should also increase the registry of domains. This property is harder to measure experimentally as lipid bilayer domains are always observed to be in registry within the resolution of optical microscopy, likely due to a high surface tension (77). However, antiregistration has been observed in simulations exhibiting large thickness mismatch between coexisting phases (73). If observed experimentally, such a system would be useful to test for WALP-induced alignment.

Our findings in model membranes suggest that transmembrane α-helical peptides in the cell plasma membrane can help stabilize rafts and interleaflet alignment. However, the cell plasma membrane differs from most model membranes since it has different lipid compositions in its two leaflets (78), each with distinct properties. For instance, symmetric membranes modeling the outer leaflet composition (enriched in sphingomyelins, PC and cholesterol) do phase separate, but those modeling inner leaflet compositions (enriched in PE or PS and cholesterol) do not (79). The effects of asymmetry have been studied with MD (73, 80, 81) and experiments (82, 83), in some cases showing that a phase-separated leaflet can induce phase separation in the otherwise uniform leaflet (81–83). Though these studies were in lipid-only systems, it is possible that transmembrane proteins can further enhance interleaflet interactions (84). We have begun to measure the effect of WALP on domain stabilization and registration in asymmetric bilayers, and describe our preliminary work in Appendix C.2. The ability of transmembrane domains to affect raft size and registration *in vivo* could be an essential

mechanism by which cells alter localization and interaction of molecules in the two asymmetric leaflets.

4.6 Conclusions

Transmembrane proteins make up a significant fraction of cell plasma membrane volume. We used the model transmembrane α-helical WALP peptides to show that transmembrane domains can influence phase domain size and alignment within the membrane by increasing line tension and surface tension, respectively.

With regard to domain size, we conclude that: 1) phase thickness mismatch plays a smaller role in determining line tension compared to WALP partitioning and WALP-induced demixing; 2) WALPs that are longer than the Ld phase raise line tension the least; 3) increased WALP concentration increases line tension; and 4) these changes are generally independent of domain size and occur for all ρ.

With regard to domain alignment, we conclude that: 1) surface tension increases in WALP-containing systems due to a combination of increased demixing, domain growth and transmembrane anchoring, 2) WALPS longer than the Ld phase increase surface tension the least, 3) increased concentrations of WALP lead to increases in surface tension and 4) increases in surface tension occurs for all WALPs at all ρ.

Additionally, we have shown that WALPs can significantly change lipid order and phase thicknesses. Thus raft properties, sizes and alignment within a cell plasma membrane are likely affected by the presence and properties of transmembrane proteins, which may in turn affect the partitioning and functionality of other membrane proteins.

REFERENCES

1. Lingwood, D., and K. Simons. 2010. Lipid Rafts as a Membrane-organizing Principle. Science. 327: 46–50.

2. Simons, K., and J.L. Sampaio. 2011. Membrane organization and lipid rafts. Cold Spring Harb. Perspect. Biol. 3: 1–17.

3. Feigenson, G.W. 2009. Phase diagrams and lipid domains in multicomponent lipid bilayer mixtures. Biochim. Biophys. Acta. 1788: 47–52.

4. Sheetz, M.P. 1993. Glycoprotein motility and dynamic domains in fluid plasma membranes. Annu. Rev. Biophys. Biomol. Struct. 22: 417–431.

5. Golan, D.E., M.R. Alecio, W.R. Veatch, and R.R. Rando. 1984. Lateral mobility of phospholipid and cholesterol in the human erythrocyte membrane: effects of protein-lipid interactions. Biochemistry. 23: 332–339.

6. Dietrich, C., L.A. Bagatolli, Z.N. Volovyk, N.L. Thompson, M. Levi, K. Jacobson, and E. Gratton. 2001. Lipid rafts reconstituted in model membranes. Biophys. J. 80: 1417–1428.

7. Samsonov, A. V, I. Mihalyov, and F.S.C. Cohen. 2001. Characterization of cholesterol-sphingomyelin domains and their dynamics in bilayer membranes. Biophys. J. 81: 1486–1500.

8. Veatch, S.L., and S.L. Keller. 2003. Separation of liquid phases in giant vesicles of ternary mixtures of phospholipids and cholesterol. Biophys. J. 85: 3074–3083.

9. Veatch, S.L., and S.L. Keller. 2002. Organization in lipid membranes containing cholesterol. Phys. Rev. Letters. 89: 268101.

10. Marsh, D. 2009. Cholesterol-induced fluid membrane domains: A compendium of lipid-raft ternary phase diagrams. Biochim. Biophys. Acta - Biomembr. 1788: 2114–2123.

11. Baumgart, T., A.T. Hammond, P. Sengupta, S.T. Hess, D.A. Holowka, B.A. Baird, and W.W. Webb. 2007. Large-scale fluid/fluid phase separation of proteins and lipids in giant plasma membrane vesicles. Proc. Natl. Acad. Sci. U.S.A. 104: 3165–70.

12. Sengupta, P., A. Hammond, D. Holowka, and B. Baird. 2008. Structural determinants for partitioning of lipids and proteins between coexisting fluid phases in giant plasma membrane vesicles. Biochim. Biophys. Acta - Biomembr. 1778: 20–32.

13. Machta, B.B., S. Papanikolaou, J.P. Sethna, and S.L. Veatch. 2011. Minimal model of plasma membrane heterogeneity requires coupling cortical actin to criticality. Biophys. J. 100: 1668–1677.

14. Hammond, A.T., F.A. Heberle, T. Baumgart, D. Holowka, B. Baird, and G.W. Feigenson. 2005. Crosslinking a lipid raft component triggers liquid ordered-liquid disordered phase separation in model plasma membranes. Proc. Natl. Acad. Sci. U.S.A. 102: 6320–6325.

15. Lingwood, D., J. Ries, P. Schwille, and K. Simons. 2008. Plasma membranes are poised for activation of raft phase coalescence at physiological temperature. Proc. Natl. Acad. Sci. U.S.A. 105: 10005–10010.

16. Meinhardt, S., R.L.C. Vink, and F. Schmid. 2013. Monolayer curvature stabilizes nanoscale raft domains in mixed lipid bilayers. Proc. Natl. Acad. Sci. U.S.A. 110: 4476–81.

17. Stevens, M.J. 2005. Complementary matching in domain formation within lipid bilayers. J. Am. Chem. Soc. 127: 15330–1.

18. Risselada, H.J., and S.J. Marrink. 2008. The molecular face of lipid rafts in model membranes. Proc. Natl. Acad. Sci. U.S.A. 105: 17367–17372.

19. Bennett, W.F.D., and D.P. Tieleman. 2013. Computer simulations of lipid membrane domains. Biochim. Biophys. Acta. 1828: 1765–1776.

20. De Jong, D.H., C.A. Lopez, and S.J. Marrink. 2013. Molecular view on protein sorting into liquid-ordered membrane domains mediated by gangliosides and lipid anchors. Faraday Discuss. 161: 347–363.

21. Janosi, L., Z. Li, J.F. Hancock, and A.A. Gorfe. 2012. Organization, dynamics, and segregation of Ras nanoclusters in membrane domains. Proc. Natl. Acad. Sci. U.S.A. 109: 8097–8102.

22. Killian, J.A. 2003. Synthetic peptides as models for intrinsic membrane proteins. FEBS Lett. 555: 134–138.

23. Schäfer, L. V, D.H. de Jong, A. Holt, A.J. Rzepiela, A.H. de Vries, B. Poolman, J.A. Killian, and S.J. Marrink. 2011. Lipid packing drives the segregation of transmembrane helices into disordered lipid domains in model membranes. Proc. Natl. Acad. Sci. U.S.A. 108: 1343–1348.

24. Liang, Q., Q.-Y. Wu, and Z.-Y. Wang. 2014. Effect of hydrophobic mismatch on domain formation and peptide sorting in the multicomponent lipid bilayers in the presence of immobilized peptides. J. Chem. Phys. 141: 074702.

25. Castillo, N., L. Monticelli, J. Barnoud, and D.P. Tieleman. 2013. Free energy of WALP23 dimer association in DMPC, DPPC, and DOPC bilayers. Chem. Phys. Lipids. 169: 95–105.

26. Parton, D.L., A. Tek, M. Baaden, and M.S.P. Sansom. 2013. Formation of Raft-Like Assemblies within Clusters of Influenza Hemagglutinin Observed by MD Simulations. PLoS Comput. Biol. 9: e1003034.

27. Domański, J., S.J. Marrink, and L. V. Schäfer. 2012. Transmembrane helices can induce domain formation in crowded model membranes. Biochim. Biophys. Acta. 1818: 984–94.

28. Heberle, F.A., J. Wu, S.L. Goh, R.S. Petruzielo, and G.W. Feigenson. 2010. Comparison of three ternary lipid bilayer mixtures: FRET and ESR reveal nanodomains. Biophys. J. 99: 3309–18.

29. Zhao, J., J. Wu, F.A. Heberle, T.T. Mills, P. Klawitter, G. Huang, G. Costanza, and G.W. Feigenson. 2007. Phase studies of model biomembranes: complex behavior of DSPC/DOPC/cholesterol. Biochim. Biophys. Acta. 1768: 2764–76.

30. Konyakhina, T.M., S.L. Goh, J. Amazon, F.A. Heberle, J. Wu, and G.W. Feigenson. 2011. Control of a nanoscopic-to-macroscopic transition: modulated phases in four-component DSPC/DOPC/POPC/Chol giant unilamellar vesicles. Biophys. J. 101: L08–10.

31. Goh, S.L., J.J. Amazon, and G.W. Feigenson. 2013. Toward a better raft model: modulated phases in the four-component bilayer, DSPC/DOPC/POPC/CHOL. Biophys. J. 104: 853–62.

32. Konyakhina, T.M., J. Wu, J.D. Mastroianni, F.A. Heberle, and G.W. Feigenson. 2013. Phase diagram of a 4-component lipid mixture: DSPC/DOPC/POPC/chol. Biochim. Biophys. Acta. 1828: 2204–14.

33. Heberle, F.A., R.S. Petruzielo, J. Pan, P. Drazba, N. Kučerka, R.F. Standaert, G.W. Feigenson, and J. Katsaras. 2013. Bilayer thickness mismatch controls domain size in model membranes. J. Am. Chem. Soc. 135: 6853–9.

34. Ackerman, D.G., and G.W. Feigenson. 2015. Multiscale Modeling of Four-Component Lipid Mixtures: Domain Composition, Size, Alignment, and Properties of the Phase Interface. J. Phys. Chem. B. 119: 4240–4250.

35. Rosetti, C., and C. Pastorino. 2012. Comparison of ternary bilayer mixtures with asymmetric or symmetric unsaturated phosphatidylcholine lipids by coarse grained molecular dynamics simulations. J. Phys. Chem. B. 116: 3525–37.

36. Hess, B., C. Kutzner, D. van Der Spoel, and E. Lindahl. 2008. GROMACS 4: Algorithms for highly efficient, load-balanced, and scalable molecular simulation. J. Chem. Theory Comput. 4: 435–447.

37. Marrink, S.J., H.J. Risselada, S. Yefimov, D.P. Tieleman, and A.H. de Vries. 2007. The MARTINI force field: coarse grained model for biomolecular simulations. J. Phys. Chem. B. 111: 7812–24.

38. Monticelli, L., S.K. Kandasamy, X. Periole, R.G. Larson, D.P. Tieleman, and S.-J. Marrink. 2008. The MARTINI Coarse-Grained Force Field: Extension to Proteins. J. Chem. Theory Comput. 4: 819–834.

39. Marrink, S.J., A.H. de Vries, and A.E. Mark. 2004. Coarse Grained Model for Semiquantitative Lipid Simulations. J. Phys. Chem. B. 108: 750–760.

40. Ingólfsson, H.I., M.N. Melo, F.J. van Eerden, C. Arnarez, C.A. López, T.A. Wassenaar, X. Periole, A.H. de Vries, D.P. Tieleman, and S.J. Marrink. 2014. Lipid Organization of the Plasma Membrane. J. Am. Chem. Soc. 136: 14554–14559.

41. The PyMOL Molecular Graphics System, Version 1.7.4 Schrödinger, LLC. .

42. De Jong, D.H., G. Singh, W.F.D. Bennett, C. Arnarez, T.A. Wassenaar, L. V. Schäfer, X. Periole, D.P. Tieleman, and S.J. Marrink. 2013. Improved parameters for the martini coarse-grained protein force field. J. Chem. Theory Comput. 9: 687–697.

43. Sparr, E., W.L. Ash, P. V. Nazarov, D.T.S. Rijkers, M.A. Hemminga, D.P. Tieleman, and J.A. Killian. 2005. Self-association of transmembrane α-helices in model membranes: Importance of helix orientation and role of hydrophobic mismatch. J. Biol. Chem. 280: 39324–39331.

44. Bussi, G., D. Donadio, and M. Parrinello. 2007. Canonical sampling through velocity rescaling. J. Chem. Phys. 126: 014101.

45. Berendsen, H.J.C., J.P.M. Postma, W.F. van Gunsteren, A. DiNola, and J.R. Haak. 1984. Molecular dynamics with coupling to an external bath. J. Chem. Phys. 81: 3684–3690.

46. Hess, B., H. Bekker, H.J.C. Berendsen, and J.G.E.M. Fraaije. 1997. LINCS: A linear constraint solver for molecular simulations. J. Comput. Chem. 18: 1463–1472.

47. Parton, D.L., J.W. Klingelhoefer, and M.S.P. Sansom. 2011. Aggregation of model membrane proteins, modulated by hydrophobic mismatch, membrane curvature, and protein class. Biophys. J. 101: 691–699.

48. Kaiser, H.-J., A. Orlowski, T. Róg, T.K.M. Nyholm, W. Chai, T. Feizi, D. Lingwood, I. Vattulainen, and K. Simons. 2011. Lateral sorting in model membranes by cholesterol-mediated hydrophobic matching. Proc. Natl. Acad. Sci. U.S.A. 108: 16628–16633.

49. Schmidt, U., and M. Weiss. 2010. Hydrophobic mismatch-induced clustering as a primer for protein sorting in the secretory pathway. Biophys. Chem. 151: 34–38.

50. De Meyer, F.J.-M., M. Venturoli, and B. Smit. 2008. Molecular simulations of lipid-mediated protein-protein interactions. Biophys. J. 95: 1851–1865.

51. Scarpelli, F., M. Drescher, T. Rutters-Meijneke, A. Holt, D.T.S. Rijkers, J.A. Killian, and M. Huber. 2009. Aggregation of transmembrane peptides studied by spin-label EPR. J. Phys. Chem. B. 113: 12257–12264.

52. Schmidt, U., G. Guigas, and M. Weiss. 2008. Cluster formation of transmembrane proteins due to hydrophobic mismatching. Phys. Rev. Lett. 101: 128104.

53. Marčelja, S. 1976. Lipid-mediated protein interaction in membranes. Biochim. Biophys. Acta. 455: 1–7.

54. Dan, N., A. Berman, P. Pincus, and S. Safran. 1994. Membrane-induced interactions between inclusions. J. Phys. II. 4: 1713–1725.

55. Strandberg, E., S. Esteban-Martín, A.S. Ulrich, and J. Salgado. 2012. Hydrophobic mismatch of mobile transmembrane helices: Merging theory and experiments. Biochim. Biophys. Acta - Biomembr. 1818: 1242–1249.

56. Kim, T., and W. Im. 2010. Revisiting hydrophobic mismatch with free energy simulation studies of transmembrane helix tilt and rotation. Biophys. J. 99: 175–183.

57. Mouritsen, O.G., and M. Bloom. 1984. Mattress model of lipid-protein interactions in membranes. Biophys. J. 46: 141–153.

58. Dan, N., P. Pincus, and S.A. Safran. 1993. Membrane-induced interactions between inclusions. Langmuir. 4: 2768–2771.

59. De Planque, M.R.R., D. V. Greathouse, R.E. Koeppe, H. Schäfer, D. Marsh, and J.A. Killian. 1998. Influence of lipid/peptide hydrophobic mismatch on the thickness of diacylphosphatidylcholine bilayers. A 2H NMR and ESR study using designed transmembrane α-helical peptides and gramicidin A. Biochemistry. 37: 9333–9345.

60. Nezil, F.A., and M. Bloom. 1992. Combined influence of cholesterol and synthetic amphiphillic peptides upon bilayer thickness in model membranes. Biophys. J. 61: 1176–1183.

61. Esposito, C., A. Tian, S. Melamed, C. Johnson, S.-Y. Tee, and T. Baumgart. 2007. Flicker spectroscopy of thermal lipid bilayer domain boundary fluctuations. Biophys. J. 93: 3169–81.

62. Tian, A., C. Johnson, W. Wang, and T. Baumgart. 2007. Line tension at fluid membrane domain boundaries measured by micropipette aspiration. Phys. Rev. Lett. 98: 208102.

63. Baumgart, T., S.T. Hess, and W.W. Webb. 2003. Imaging coexisting fluid domains in biomembrane models coupling curvature and line tension. Nature. 425: 821–824.

64. Schäfer, L. V., and S.J. Marrink. 2010. Partitioning of lipids at domain boundaries in model membranes. Biophys. J. 99: L91–3.

65. Palmieri, B., T. Yamamoto, R.C. Brewster, and S.A. Safran. 2014. Line active molecules promote inhomogeneous structures in membranes: theory, simulations and experiments. Adv. Colloid Interface Sci. 208: 58–65.

66. Dhar, P., E. Eck, J.N. Israelachvili, D.W. Lee, Y. Min, A. Ramachandran, A.J. Waring, and J.A. Zasadzinski. 2012. Lipid-protein interactions alter line tensions and domain size distributions in lung surfactant monolayers. Biophys. J. 102: 56–65.

67. García-Sáez, A.J., S. Chiantia, and P. Schwille. 2007. Effect of line tension on the lateral organization of lipid membranes. J. Biol. Chem. 282: 33537–44.

68. Kuzmin, P.I., S.A. Akimov, Y.A. Chizmadzhev, J. Zimmerberg, and F.S. Cohen. 2005. Line tension and interaction energies of membrane rafts calculated from lipid splay and tilt. Biophys. J. 88: 1120–33.

69. Muddana, H.S., H.H. Chiang, and P.J. Butler. 2012. Tuning membrane phase separation using nonlipid amphiphiles. Biophys. J. 102: 489–97.

70. Hakobyan, D., and A. Heuer. 2014. Key molecular requirements for raft formation in lipid/cholesterol membranes. PLoS One. 9: e87369.

71. Pantano, D.A., P.B. Moore, M.L. Klein, and D.E. Discher. 2011. Raft registration across bilayers in a molecularly detailed model. Soft Matter. 7: 8182–8191.

72. May, S. 2009. Trans-monolayer coupling of fluid domains in lipid bilayers. Soft Matter. 5: 3148–3156.

73. Perlmutter, J.D., and J.N. Sachs. 2011. Interleaflet interaction and asymmetry in phase separated lipid bilayers: molecular dynamics simulations. J. Am. Chem. Soc. 133: 6563–77.

74. Amazon, J.J., S.L. Goh, and G.W. Feigenson. 2013. Competition between line tension and curvature stabilizes modulated phase patterns on the surface of giant unilamellar vesicles: a simulation study. Phys. Rev. E. 87: 022708.

75. Amazon, J.J., and G.W. Feigenson. 2014. Lattice simulations of phase morphology on lipid bilayers: Renormalization, membrane shape, and electrostatic dipole interactions. Phys. Rev. E. 89: 022702.

76. Hassan-Zadeh, E., E. Baykal-Caglar, M. Alwarawrah, and J. Huang. 2014. Complex roles of hybrid lipids in the composition, order, and size of lipid membrane domains. Langmuir. 30: 1361–9.

77. Collins, M.D. 2008. Interleaflet coupling mechanisms in bilayers of lipids and cholesterol. Biophys. J. 94: L32–4.

78. Van Meer, G. 2005. Cellular lipidomics. EMBO J. 24: 3159–65.

79. Van Meer, G., D.R. Voelker, and G.W. Feigenson. 2008. Membrane lipids: where they are and how they behave. Nat. Rev. Mol. Cell Biol. 9: 112–124.

80. Polley, A., S. Vemparala, and M. Rao. 2012. Atomistic Simulations of a Multicomponent Asymmetric Lipid Bilayer. J. Phys. Chem. B. 116: 13403–13410.

81. Polley, A., S. Mayor, and M. Rao. 2014. Bilayer registry in a multicomponent asymmetric membrane : dependence on lipid composition and chain length. J. Chem. Phys. 141: 1–17.

82. Kiessling, V., J.M. Crane, and L.K. Tamm. 2006. Transbilayer effects of raft-like lipid domains in asymmetric planar bilayers measured by single molecule tracking. Biophys. J. 91: 3313–3326.

83. Lin, Q., and E. London. 2015. Ordered Raft Domains Induced by Outer Leaflet Sphingomyelin in Cholesterol-Rich Asymmetric Vesicles. Biophys. J. 108: 2212–2222.

84. Devaux, P.F., and R. Morris. 2004. Transmembrane asymmetry and lateral domains in biological membranes. Traffic. 5: 241–246.

CHAPTER 5
Conclusion

5.1 Summary of findings

5.1.1 Overall framework

Phase separation in simplified lipid mixtures is frequently used to model functional heterogeneities, known as rafts, within cell plasma membranes. Throughout this work, we sought to better understand model membrane behavior at a molecular level through MD simulations. Our simulations spanned different levels of resolution, sizes and time-scales, each with their own advantages and each chosen to answer a specific set of questions. Whereas the more atomistic simulations were limited to shorter time-scales, they were useful for addressing nuanced molecular behavior. CG simulations sacrifice this resolution for the benefits of larger sizes and longer times required to model changes in phase behavior. MD simulations enabled measurements in an unperturbed manner inherently impossible with experiments.

5.1.2 Probe-induced perturbations in model membranes

Fluorescent probes are ubiquitous in studies of model membranes and lipid rafts (1). Such probes are especially useful for detecting coexisting phases since the probes often preferentially partition into one phase. Based on this preferential partitioning, fluorescence microscopy and FRET measurements can indicate if multiple phases are present (2, 3). However, these techniques rely on the assumption that the probes are not altering the bilayer and phase behavior. Experimentally confirming that the probe does not affect its local environment is difficult without further perturbing the system with additional, extrinsic probes. Atomistic molecular dynamics simulations provide a way to measure local probe-induced perturbations without any additional probes.

In Chapter 2, we examined three different fluorescent lipid analogs commonly used to study lipid bilayers: DiI-C12:0, DiI-C18:0 and DiI-C18:2. We found that all probes significantly perturb their local environments. Within the same leaflet as the probe, lipids near the probe were disordered and their headgroups pointed away from the probe. We determined that disordering was caused by the free volume under the large probe headgroup, and that lipid headgroup reorientation was due to the positive charge of the probe headgroup. Surprisingly, we also found that lipids across from the two longer probes were also significantly disordered compared to bulk lipids. We concluded that this disordering was due to the two longer probes' hydrocarbon chains protruding into the apposed leaflet. Importantly, significant inter- and intraleaflet perturbations were only short-ranged, dying off within nanometers of the probes. This means that these fluorescent probes can reliably be used to study membrane behavior even for nanodomains. However, this also implies that other probes that report directly on their local environment might be providing skewed results. This possibility is discussed in Section 5.2.1.

5.1.3 Phase behavior of quaternary lipid mixtures

In Chapter 3 we examined phase behavior in quaternary lipid mixtures by combining the advantages of short time-scale atomistic simulations and long time-scale CG simulations. We first ran the systems to equilibrium with CG and then converted them to an atomistic representation. Each type of simulation provided valuable information that was not possible with the other method.

We were particularly interested in a four-component CG mixture that mimicked experimental systems (4), and so chose DPPC/[PUPC + DUPC]/cholesterol which produces nanodomains when the low-Tm lipid is all PUPC and macrodomains when the low-Tm lipid is all DUPC. To further mimic experiments, we incrementally replaced the nanodomain-inducing

PUPC with the macrodomain-inducing DUPC. The CG simulations revealed that domain size and alignment remain small until a critical replacement is reached, at which point both size and alignment increase dramatically. This matched well with experimental findings showing domain size abruptly changes from nanoscopic to macroscopic over a small replacement window (4).

Conversion of the equilibrated CG simulations to atomistic representation allowed for detailed evaluation of lipid properties near the phase interface. We found that regardless of composition and equilibrium order of the phases, the interface between Lo + Ld phases is only a couple of nanometers wide. Thus the interface is a negligible fraction of large domains, but it can make up a more significant fraction of smaller domains. Since the interface has distinct properties compared to the surrounding phases, it may be important for SANS and ESR experiments which often assume that the two bulk phases are the only distinct environments.

5.1.4 The role of peptides in quaternary lipid mixtures

Protein transmembrane domains are abundant in the cell plasma membrane and are frequently modeled by simple transmembrane α-helical peptides (5, 6). Key questions regarding their effects on membrane behavior include how the transmembrane domains interact with lipids, how they can affect domain size and alignment, and how these behaviors are affected by transmembrane domain length and concentration. Quaternary lipid mixtures are the ideal system for testing these questions since they provide a standard of domain size and alignment at various lipid compositions.

In Chapter 4, we used CG MD to study the effects of three α-helical WALP peptides (WALP-17, WALP-23 and WALP-29) on phase behavior in the quaternary mixture DPPC/[PUPC + DUPC]/cholesterol of Chapter 3. As expected, all WALPs partitioned into the Ld phase in the coexisting membranes (7). We also found that all WALPs increase domain size

and alignment compared to corresponding lipid-only mixtures. The effects were largest for WALP-17 and WALP-23, smallest for WALP-29, and generally increased with increasing WALP concentration. The increase in domain size that we observed was likely due to increased demixing of lipids in the presence of the peptides and the increase in line tension that accompanies the peptides' preferential partitioning away from the phase interface. The increase in domain alignment was driven by the ability of the transmembrane helices to anchor together Ld phases in apposed leaflets. Together, these results indicate that if a cell can alter the concentration and localization of its integral membrane proteins, it can control the size and alignment of rafts.

5.2 Ongoing work and future directions

5.2.1 ESR probes in model membranes

ESR probes report directly on the order of their local environment and are useful for characterizing different lipid phases (8). An ongoing project in our lab is to use MD to quantify the ESR probe-induced perturbations of model membranes. We can then use these results to determine if any corrections need to be made to ESR experiments. This will be essential to ESR studies of model membranes and cell plasma membranes which rely on the accuracy of ESR probes to measure order parameters of different phases. Our preliminary work indicates that the perturbations due to ESR probes are not as significant as those from the DiI probes. However, because ESR probes report on their local environment, even small perturbations may affect results.

5.2.2 Asymmetric bilayer simulations of quaternary lipid mixtures with protein

Asymmetry is a property of the plasma membrane which is often overlooked when making model membranes, in large part due to the difficulty of preparing asymmetric

membranes (9). However, asymmetry may be crucial to raft behavior. As mentioned in Appendix C.2, we have begun some preliminary simulations of asymmetric quaternary mixtures with peptide to see if large-scale phase separation in one leaflet can induce large-scale phase separation in the apposed, otherwise nanodomain-forming leaflet. Future simulations should be performed which more thoroughly address this issue of asymmetry.

5.2.3 All-atom simulations of phase separation

In the not-so distant future, it may become feasible to run large-scale all-atom simulations for the hundreds of microseconds required for phase separation to take place starting from an initially mixed state. The additional information that accompanies increased resolution will be necessary for a complete understanding of phase separation and rafts in model and plasma membranes. Such simulations will more clearly show how electrostatics, hydrophobicity, and atom-atom interactions help drive lipid demixing and phase separation. Currently Anton, a purpose-built supercomputer for optimizing all-atom MD, seems to have the best chance of achieving such a lofty goal of watching phase separation with atomic resolution.

5.2.4 Experiments to test MD predictions

Though they are used to study details inaccessible via experimental methods, MD simulations still provide experimentally testable results. For instance, the bilayer thickness change that accompanies probe-induced disordering could be measured by SANS. For quaternary mixture simulations, domain size can be measured with SANS (10) and the transition from nanodomains to macrodomains can be determined via fluorescence microscopy (4). The effect of different lipid compositions and/or the addition of proteins to the quaternary mixtures can also be tested in similar manners (11). Indeed, recent experiments have shown that GWALP23 addition to a DSPC/[POPC + DOPC]/cholesterol quaternary mixture increases

domain size (unpublished), in agreement with our MD simulations. Confirmation of MD results by experiments will help to validate the MD models, increasing their believability in the regimes that experiments cannot access. Conversely, invalidation of MD results by experiments will lead to improved MD models.

REFERENCES

1. Sezgin, E., and P. Schwille. 2011. Lipid Dynamics. Cold Spring Harb. Perspect. Biol. 3: 1–32.

2. Buboltz, J.T. 2007. Steady-state probe-partitioning fluorescence resonance energy transfer: A simple and robust tool for the study of membrane phase behavior. Phys. Rev. E. 76: 021903.

3. Feigenson, G.W. 2009. Phase diagrams and lipid domains in multicomponent lipid bilayer mixtures. Biochim. Biophys. Acta. 1788: 47–52.

4. Konyakhina, T.M., S.L. Goh, J. Amazon, F.A. Heberle, J. Wu, and G.W. Feigenson. 2011. Control of a nanoscopic-to-macroscopic transition: modulated phases in four-component DSPC/DOPC/POPC/Chol giant unilamellar vesicles. Biophys. J. 101: L08–10.

5. Sheetz, M.P. 1993. Glycoprotein motility and dynamic domains in fluid plasma membranes. Annu. Rev. Biophys. Biomol. Struct. 22: 417–431.

6. Killian, J.A. 2003. Synthetic peptides as models for intrinsic membrane proteins. FEBS Lett. 555: 134–138.

7. Schäfer, L. V, D.H. de Jong, A. Holt, A.J. Rzepiela, A.H. de Vries, B. Poolman, J.A. Killian, and S.J. Marrink. 2011. Lipid packing drives the segregation of transmembrane helices into disordered lipid domains in model membranes. Proc. Natl. Acad. Sci. U.S.A. 108: 1343–1348.

8. Borbat, P.P., A.J. Costa-Filho, K.A. Earle, J.K. Moscicki, and J.H. Freed. 2001. Electron spin resonance in studies of membranes and proteins. Science. 291: 266–269.

9. Feigenson, G.W. 2007. Phase boundaries and biological membranes. Annu. Rev. Biophys. Biomol. Struct. 36: 63–77.

10. Heberle, F.A., R.S. Petruzielo, J. Pan, P. Drazba, N. Kučerka, R.F. Standaert, G.W. Feigenson, and J. Katsaras. 2013. Bilayer thickness mismatch controls domain size in model membranes. J. Am. Chem. Soc. 135: 6853–9.

11. Goh, S.L., J.J. Amazon, and G.W. Feigenson. 2013. Toward a better raft model: modulated phases in the four-component bilayer, DSPC/DOPC/POPC/CHOL. Biophys. J. 104: 853–62.

APPENDIX A
Supporting information for Chapter 1

A.1 DiI topology files

The topology files for DiI-C18:0, DiI-C18:2 and DiI-C12:0 are listed below:

A1.1 DiI-C18:0

```
[ moleculetype ]
; Name nrexcl
DII      3

[ atoms ]
;   nr       type  resnr resid  atom  cgnr    charge      mass
     1        LP3      1  DII      C1     1     0.000  15.0350
     2        LP2      1  DII      C2     2     0.000  14.0270
     3        LP2      1  DII      C3     3     0.000  14.0270
     4        LP2      1  DII      C4     4     0.000  14.0270
     5        LP2      1  DII      C5     5     0.000  14.0270
     6        LP2      1  DII      C6     6     0.000  14.0270
     7        LP2      1  DII      C7     7     0.000  14.0270
     8        LP2      1  DII      C8     8     0.000  14.0270
     9        LP2      1  DII      C9     9     0.000  14.0270
    10        LP2      1  DII     C10    10     0.000  14.0270
    11        LP2      1  DII     C11    11     0.000  14.0270
    12        LP2      1  DII     C12    12     0.000  14.0270
    13        LP2      1  DII     C13    13     0.000  14.0270
    14        LP2      1  DII     C14    14     0.000  14.0270
    15        LP2      1  DII     C15    15     0.000  14.0270
    16        LP2      1  DII     C16    16     0.000  14.0270
    17        LP2      1  DII     C17    17     0.000  14.0270
    18        LP2      1  DII     C18    18     0.150  14.0270
    19         NR      1  DII     N19    19    -0.010  14.0067
    20          C      1  DII     C20    20     0.100  12.0110
    21        CR1      1  DII     C21    21    -0.040  13.0190
    22        CR1      1  DII     C22    22     0.040  13.0190
    23        CR1      1  DII     C23    23     0.010  13.0190
    24        CR1      1  DII     C24    24     0.010  13.0190
    25          C      1  DII     C25    25    -0.100  12.0110
    26        CH1      1  DII     C26    26     0.400  12.0110
    27        CH3      1  DII     C27    27    -0.060  15.0350
    28        CH3      1  DII     C28    28    -0.070  15.0350
    29          C      1  DII     C29    29     0.300  12.0110
    30        CR1      1  DII     C30    30    -0.430  13.0190
    31        CR1      1  DII     C31    31     0.370  13.0190
    32        CR1      1  DII     C32    32    -0.340  13.0190
    33          C      1  DII     C33    33     0.410  12.0110
    34        CH1      1  DII     C34    34     0.140  12.0110
    35        CH3      1  DII     C35    35    -0.030  15.0350
    36        CH3      1  DII     C36    36    -0.040  15.0350
    37          C      1  DII     C37    37     0.030  12.0110
    38        CR1      1  DII     C38    38    -0.020  13.0190
    39        CR1      1  DII     C39    39     0.010  13.0190
    40        CR1      1  DII     C40    40     0.040  13.0190
    41        CR1      1  DII     C41    41    -0.060  13.0190
    42          C      1  DII     C42    42     0.140  12.0110
    43          N      1  DII     N43    43    -0.100  14.0067
    44        LP2      1  DII     C44    44     0.150  14.0270
    45        LP2      1  DII     C45    45     0.000  14.0270
    46        LP2      1  DII     C46    46     0.000  14.0270
    47        LP2      1  DII     C47    47     0.000  14.0270
    48        LP2      1  DII     C48    48     0.000  14.0270
    49        LP2      1  DII     C49    49     0.000  14.0270
    50        LP2      1  DII     C50    50     0.000  14.0270
```

```
    51       LP2     1  DII     C51    51    0.000  14.0270
    52       LP2     1  DII     C52    52    0.000  14.0270
    53       LP2     1  DII     C53    53    0.000  14.0270
    54       LP2     1  DII     C54    54    0.000  14.0270
    55       LP2     1  DII     C55    55    0.000  14.0270
    56       LP2     1  DII     C56    56    0.000  14.0270
    57       LP2     1  DII     C57    57    0.000  14.0270
    58       LP2     1  DII     C58    58    0.000  14.0270
    59       LP2     1  DII     C59    59    0.000  14.0270
    60       LP2     1  DII     C60    60    0.000  14.0270
    61       LP3     1  DII     C61    61    0.000  15.0350

[ bonds ]
; ai   aj  fu    c0, c1, ...
   1    2   1    0.153    334720.0    0.153    334720.0 ;   CAA  CAR
   2    3   1    0.153    334720.0    0.153    334720.0 ;   CAR  CAT
   3    4   1    0.153    334720.0    0.153    334720.0 ;   CAT  CAV
   4    5   1    0.153    334720.0    0.153    334720.0 ;   CAV  CAX
   5    6   1    0.153    334720.0    0.153    334720.0 ;   CAX  CAZ
   6    7   1    0.153    334720.0    0.153    334720.0 ;   CAZ  CBB
   7    8   1    0.153    334720.0    0.153    334720.0 ;   CBB  CBD
   8    9   1    0.153    334720.0    0.153    334720.0 ;   CBD  CBF
   9   10   1    0.153    334720.0    0.153    334720.0 ;   CBF  CBH
  10   11   1    0.153    334720.0    0.153    334720.0 ;   CBH  CBJ
  11   12   1    0.153    334720.0    0.153    334720.0 ;   CBJ  CBL
  12   13   1    0.153    334720.0    0.153    334720.0 ;   CBL  CBN
  13   14   1    0.153    334720.0    0.153    334720.0 ;   CBN  CBP
  14   15   1    0.153    334720.0    0.153    334720.0 ;   CBP  CBR
  15   16   1    0.153    334720.0    0.153    334720.0 ;   CBR  CBT
  16   17   1    0.153    334720.0    0.153    334720.0 ;   CBT  CBV
  17   18   1    0.153    334720.0    0.153    334720.0 ;   CBV  CBX
  18   19   1    0.147    376560.0    0.147    376560.0 ;   CBX  NCF
  19   20   1    0.141    418400.0    0.133    418400.0 ;   NCF  CCB
  19   29   1    0.133    418400.0    0.133    418400.0 ;   NCF  CBZ
  20   21   1    0.139    418400.0    0.139    418400.0 ;   CCB  CAN
  20   25   1    0.139    418400.0    0.139    418400.0 ;   CCB  CCD
  21   22   1    0.139    418400.0    0.139    418400.0 ;   CAN  CAJ
  22   23   1    0.139    418400.0    0.139    418400.0 ;   CAJ  CAL
  23   24   1    0.139    418400.0    0.139    418400.0 ;   CAL  CAP
  24   25   1    0.139    418400.0    0.139    418400.0 ;   CAP  CCD
  25   26   1    0.153    334720.0    0.153    334720.0 ;   CCD  CCH
  26   27   1    0.153    334720.0    0.153    334720.0 ;   CCH  CAC
  26   28   1    0.153    334720.0    0.153    334720.0 ;   CCH  CAD
  26   29   1    0.153    334720.0    0.153    334720.0 ;   CCH  CBZ
  29   30   1    0.139    418400.0    0.139    418400.0 ;   CBZ  CAH
  30   31   1    0.139    418400.0    0.139    418400.0 ;   CAH  CAG
  31   32   1    0.139    418400.0    0.139    418400.0 ;   CAG  CAI
  32   33   1    0.139    418400.0    0.139    418400.0 ;   CAI  CCA
  33   34   1    0.153    334720.0    0.153    334720.0 ;   CCA  CCI
  33   43   1    0.133    418400.0    0.133    418400.0 ;   CCA  NCG
  34   35   1    0.153    334720.0    0.153    334720.0 ;   CCI  CAE
  34   36   1    0.153    334720.0    0.153    334720.0 ;   CCI  CAF
  34   37   1    0.153    334720.0    0.153    334720.0 ;   CCI  CCE
  37   38   1    0.139    418400.0    0.139    418400.0 ;   CCE  CAQ
  37   42   1    0.139    418400.0    0.139    418400.0 ;   CCE  CCC
  38   39   1    0.139    418400.0    0.139    418400.0 ;   CAQ  CAM
  39   40   1    0.139    418400.0    0.139    418400.0 ;   CAM  CAK
  40   41   1    0.139    418400.0    0.139    418400.0 ;   CAK  CAO
  41   42   1    0.139    418400.0    0.139    418400.0 ;   CAO  CCC
  42   43   1    0.141    418400.0    0.133    418400.0 ;   CCC  NCG
  43   44   1    0.147    376560.0    0.147    376560.0 ;   NCG  CBY
  44   45   1    0.153    334720.0    0.153    334720.0 ;   CBY  CBW
  45   46   1    0.153    334720.0    0.153    334720.0 ;   CBW  CBU
  46   47   1    0.153    334720.0    0.153    334720.0 ;   CBU  CBS
  47   48   1    0.153    334720.0    0.153    334720.0 ;   CBS  CBQ
  48   49   1    0.153    334720.0    0.153    334720.0 ;   CBQ  CBO
  49   50   1    0.153    334720.0    0.153    334720.0 ;   CBO  CBM
  50   51   1    0.153    334720.0    0.153    334720.0 ;   CBM  CBK
  51   52   1    0.153    334720.0    0.153    334720.0 ;   CBK  CBI
  52   53   1    0.153    334720.0    0.153    334720.0 ;   CBI  CBG
  53   54   1    0.153    334720.0    0.153    334720.0 ;   CBG  CBE
```

```
  54  55   1    0.153    334720.0    0.153    334720.0 ;   CBE  CBC
  55  56   1    0.153    334720.0    0.153    334720.0 ;   CBC  CBA
  56  57   1    0.153    334720.0    0.153    334720.0 ;   CBA  CAY
  57  58   1    0.153    334720.0    0.153    334720.0 ;   CAY  CAW
  58  59   1    0.153    334720.0    0.153    334720.0 ;   CAW  CAU
  59  60   1    0.153    334720.0    0.153    334720.0 ;   CAU  CAS
  60  61   1    0.153    334720.0    0.153    334720.0 ;   CAS  CAB

[ pairs ]
; ai  aj  fu    c0, c1, ...
  19  22   1                                            ;   NCF  CAJ
  19  24   1                                            ;   NCF  CAP
  19  27   1                                            ;   NCF  CAC
  19  28   1                                            ;   NCF  CAD
  19  31   1                                            ;   NCF  CAG
  20  23   1                                            ;   CCB  CAL
  20  27   1                                            ;   CCB  CAC
  20  28   1                                            ;   CCB  CAD
  20  30   1                                            ;   CCB  CAH
  21  24   1                                            ;   CAN  CAP
  21  26   1                                            ;   CAN  CCH
  21  29   1                                            ;   CAN  CBZ
  22  25   1                                            ;   CAJ  CCD
  23  26   1                                            ;   CAL  CCH
  24  27   1                                            ;   CAP  CAC
  24  28   1                                            ;   CAP  CAD
  24  29   1                                            ;   CAP  CBZ
  25  30   1                                            ;   CCD  CAH
  26  31   1                                            ;   CCH  CAG
  27  30   1                                            ;   CAC  CAH
  28  30   1                                            ;   CAD  CAH
  29  32   1                                            ;   CBZ  CAI
  30  33   1                                            ;   CAH  CCA
  31  34   1                                            ;   CAG  CCI
  31  43   1                                            ;   CAG  NCG
  32  35   1                                            ;   CAI  CAE
  32  36   1                                            ;   CAI  CAF
  32  37   1                                            ;   CAI  CCE
  32  42   1                                            ;   CAI  CCC
  33  38   1                                            ;   CCA  CAQ
  33  41   1                                            ;   CCA  CAO
  34  39   1                                            ;   CCI  CAM
  34  41   1                                            ;   CCI  CAO
  35  38   1                                            ;   CAE  CAQ
  35  42   1                                            ;   CAE  CCC
  35  43   1                                            ;   CAE  NCG
  36  38   1                                            ;   CAF  CAQ
  36  42   1                                            ;   CAF  CCC
  36  43   1                                            ;   CAF  NCG
  37  40   1                                            ;   CCE  CAK
  38  41   1                                            ;   CAQ  CAO
  38  43   1                                            ;   CAQ  NCG
  39  42   1                                            ;   CAM  CCC
  40  43   1                                            ;   CAK  NCG


[ angles ]
; ai  aj  ak  fu    c0, c1, ...
   1   2   3   1    111.0       460.2    111.0       460.2 ;   CAA  CAR  CAT
   2   3   4   1    111.0       460.2    111.0       460.2 ;   CAR  CAT  CAV
   3   4   5   1    111.0       460.2    111.0       460.2 ;   CAT  CAV  CAX
   4   5   6   1    111.0       460.2    111.0       460.2 ;   CAV  CAX  CAZ
   5   6   7   1    111.0       460.2    111.0       460.2 ;   CAX  CAZ  CBB
   6   7   8   1    111.0       460.2    111.0       460.2 ;   CAZ  CBB  CBD
   7   8   9   1    111.0       460.2    111.0       460.2 ;   CBB  CBD  CBF
   8   9  10   1    111.0       460.2    111.0       460.2 ;   CBD  CBF  CBH
   9  10  11   1    111.0       460.2    111.0       460.2 ;   CBF  CBH  CBJ
  10  11  12   1    111.0       460.2    111.0       460.2 ;   CBH  CBJ  CBL
  11  12  13   1    111.0       460.2    111.0       460.2 ;   CBJ  CBL  CBN
  12  13  14   1    111.0       460.2    111.0       460.2 ;   CBL  CBN  CBP
```

```
 13  14  15   1    111.0       460.2    111.0       460.2 ;   CBN  CBP  CBR
 14  15  16   1    111.0       460.2    111.0       460.2 ;   CBP  CBR  CBT
 15  16  17   1    111.0       460.2    111.0       460.2 ;   CBR  CBT  CBV
 16  17  18   1    111.0       460.2    111.0       460.2 ;   CBT  CBV  CBX
 17  18  19   1    109.5       460.2    109.5       460.2 ;   CBV  CBX  NCF
 18  19  20   1    120.0       418.4    120.0       418.4 ;   CBX  NCF  CCB
 18  19  29   1    120.0       418.4    120.0       418.4 ;   CBX  NCF  CBZ
 20  19  29   1    108.0       418.4    108.0       418.4 ;   CCB  NCF  CBZ
 19  20  21   1    120.0       418.4    120.0       418.4 ;   NCF  CCB  CAN
 19  20  25   1    108.0       418.4    108.0       418.4 ;   NCF  CCB  CCD
 21  20  25   1    120.0       418.4    120.0       418.4 ;   CAN  CCB  CCD
 20  21  22   1    120.0       418.4    120.0       418.4 ;   CCB  CAN  CAJ
 21  22  23   1    120.0       418.4    120.0       418.4 ;   CAN  CAJ  CAL
 22  23  24   1    120.0       418.4    120.0       418.4 ;   CAJ  CAL  CAP
 23  24  25   1    120.0       418.4    120.0       418.4 ;   CAL  CAP  CCD
 20  25  24   1    120.0       418.4    120.0       418.4 ;   CCB  CCD  CAP
 20  25  26   1    108.0       418.4    108.0       418.4 ;   CCB  CCD  CCH
 24  25  26   1    132.0       418.4    132.0       418.4 ;   CAP  CCD  CCH
 25  26  27   1    109.5       397.5    109.5       397.5 ;   CCD  CCH  CAC
 25  26  28   1    109.5       397.5    109.5       397.5 ;   CCD  CCH  CAD
 25  26  29   1    104.0       460.2    104.0       460.2 ;   CCD  CCH  CBZ
 27  26  28   1    111.0       460.2    111.0       460.2 ;   CAC  CCH  CAD
 27  26  29   1    109.5       397.5    109.5       397.5 ;   CAC  CCH  CBZ
 28  26  29   1    109.5       397.5    109.5       397.5 ;   CAD  CCH  CBZ
 19  29  26   1    108.0       418.4    108.0       418.4 ;   NCF  CBZ  CCH
 19  29  30   1    132.0       418.4    132.0       418.4 ;   NCF  CBZ  CAH
 26  29  30   1    132.0       418.4    132.0       418.4 ;   CCH  CBZ  CAH
 29  30  31   1    120.0       418.4    120.0       418.4 ;   CBZ  CAH  CAG
 30  31  32   1    135.0       418.4    135.0       418.4 ;   CAH  CAG  CAI
 31  32  33   1    125.0       418.4    125.0       418.4 ;   CAG  CAI  CCA
 32  33  34   1    120.0       418.4    120.0       418.4 ;   CAI  CCA  CCI
 32  33  43   1    132.0       418.4    132.0       418.4 ;   CAI  CCA  NCG
 34  33  43   1    108.0       418.4    108.0       418.4 ;   CCI  CCA  NCG
 33  34  35   1    109.5       397.5    109.5       397.5 ;   CCA  CCI  CAE
 33  34  36   1    109.5       397.5    109.5       397.5 ;   CCA  CCI  CAF
 33  34  37   1    104.0       460.2    104.0       460.2 ;   CCA  CCI  CCE
 35  34  36   1    111.0       460.2    111.0       460.2 ;   CAE  CCI  CAF
 35  34  37   1    109.5       397.5    109.5       397.5 ;   CAE  CCI  CCE
 36  34  37   1    109.5       397.5    109.5       397.5 ;   CAF  CCI  CCE
 34  37  38   1    132.0       418.4    132.0       418.4 ;   CCI  CCE  CAQ
 34  37  42   1    108.0       418.4    108.0       418.4 ;   CCI  CCE  CCC
 38  37  42   1    120.0       418.4    120.0       418.4 ;   CAQ  CCE  CCC
 37  38  39   1    120.0       418.4    120.0       418.4 ;   CCE  CAQ  CAM
 38  39  40   1    120.0       418.4    120.0       418.4 ;   CAQ  CAM  CAK
 39  40  41   1    120.0       418.4    120.0       418.4 ;   CAM  CAK  CAO
 40  41  42   1    120.0       418.4    120.0       418.4 ;   CAK  CAO  CCC
 37  42  41   1    120.0       418.4    120.0       418.4 ;   CCE  CCC  CAO
 37  42  43   1    108.0       418.4    108.0       418.4 ;   CCE  CCC  NCG
 41  42  43   1    132.0       418.4    132.0       418.4 ;   CAO  CCC  NCG
 33  43  42   1    108.0       418.4    108.0       418.4 ;   CCA  NCG  CCC
 33  43  44   1    120.0       418.4    120.0       418.4 ;   CCA  NCG  CBY
 42  43  44   1    120.0       418.4    120.0       418.4 ;   CCC  NCG  CBY
 43  44  45   1    109.5       460.2    109.5       460.2 ;   NCG  CBY  CBW
 44  45  46   1    111.0       460.2    111.0       460.2 ;   CBY  CBW  CBU
 45  46  47   1    111.0       460.2    111.0       460.2 ;   CBW  CBU  CBS
 46  47  48   1    111.0       460.2    111.0       460.2 ;   CBU  CBS  CBQ
 47  48  49   1    111.0       460.2    111.0       460.2 ;   CBS  CBQ  CBO
 48  49  50   1    111.0       460.2    111.0       460.2 ;   CBQ  CBO  CBM
 49  50  51   1    111.0       460.2    111.0       460.2 ;   CBO  CBM  CBK
 50  51  52   1    111.0       460.2    111.0       460.2 ;   CBM  CBK  CBI
 51  52  53   1    111.0       460.2    111.0       460.2 ;   CBK  CBI  CBG
 52  53  54   1    111.0       460.2    111.0       460.2 ;   CBI  CBG  CBE
 53  54  55   1    111.0       460.2    111.0       460.2 ;   CBG  CBE  CBC
 54  55  56   1    111.0       460.2    111.0       460.2 ;   CBE  CBC  CBA
 55  56  57   1    111.0       460.2    111.0       460.2 ;   CBC  CBA  CAY
 56  57  58   1    111.0       460.2    111.0       460.2 ;   CBA  CAY  CAW
 57  58  59   1    111.0       460.2    111.0       460.2 ;   CAY  CAW  CAU
 58  59  60   1    111.0       460.2    111.0       460.2 ;   CAW  CAU  CAS
 59  60  61   1    111.0       460.2    111.0       460.2 ;   CAU  CAS  CAB

[ dihedrals ]
```

```
; ai  aj  ak  al  fu    c0, c1, m, ...
  19  18  20  29   2      0.0 1673.6       0.0 1673.6  ; imp   NCF  CBX  CCB  CBZ
  20  25  21  19   2      0.0 1673.6       0.0 1673.6  ; imp   CCB  CCD  CAN  NCF
  25  20  26  24   2      0.0 1673.6       0.0 1673.6  ; imp   CCD  CCB  CCH  CAP
  29  30  26  19   2      0.0 1673.6       0.0 1673.6  ; imp   CBZ  CAH  CCH  NCF
  33  32  34  43   2      0.0 1673.6       0.0 1673.6  ; imp   CCA  CAI  CCI  NCG
  37  34  42  38   2      0.0 1673.6       0.0 1673.6  ; imp   CCE  CCI  CCC  CAQ
  42  37  41  43   2      0.0 1673.6       0.0 1673.6  ; imp   CCC  CCE  CAO  NCG
  43  33  42  44   2      0.0 1673.6       0.0 1673.6  ; imp   NCG  CCA  CCC  CBY
  26  25  28  27   2     35.3  836.8      35.3  836.8  ; imp   CCH  CCD  CAD  CAC
  34  33  35  36   2     35.3  836.8      35.3  836.8  ; imp   CCI  CCA  CAE  CAF
  37  38  39  40   2      0.0 1673.6       0.0 1673.6  ; imp   CCE  CAQ  CAM  CAK
  38  39  40  41   2      0.0 1673.6       0.0 1673.6  ; imp   CAQ  CAM  CAK  CAO
  39  40  41  42   2      0.0 1673.6       0.0 1673.6  ; imp   CAM  CAK  CAO  CCC
  40  41  42  37   2      0.0 1673.6       0.0 1673.6  ; imp   CAK  CAO  CCC  CCE
  41  42  37  38   2      0.0 1673.6       0.0 1673.6  ; imp   CAO  CCC  CCE  CAQ
  42  37  38  39   2      0.0 1673.6       0.0 1673.6  ; imp   CCC  CCE  CAQ  CAM
  20  21  22  23   2      0.0 1673.6       0.0 1673.6  ; imp   CCB  CAN  CAJ  CAL
  21  22  23  24   2      0.0 1673.6       0.0 1673.6  ; imp   CAN  CAJ  CAL  CAP
  22  23  24  25   2      0.0 1673.6       0.0 1673.6  ; imp   CAJ  CAL  CAP  CCD
  23  24  25  20   2      0.0 1673.6       0.0 1673.6  ; imp   CAL  CAP  CCD  CCB
  24  25  20  21   2      0.0 1673.6       0.0 1673.6  ; imp   CAP  CCD  CCB  CAN
  25  20  21  22   2      0.0 1673.6       0.0 1673.6  ; imp   CCD  CCB  CAN  CAJ
   4   3   2   1   3
   5   4   3   2   3
   6   5   4   3   3
   7   6   5   4   3
   8   7   6   5   3
   9   8   7   6   3
  10   9   8   7   3
  11  10   9   8   3
  12  11  10   9   3
  13  12  11  10   3
  14  13  12  11   3
  15  14  13  12   3
  16  15  14  13   3
  17  16  15  14   3
  18  17  16  15   3
  19  18  17  16   1      0.0    5.9 3      0.0    5.9 3 ; dih   NCF  CBX  CBV  CBT
  17  18  19  29   1      0.0    3.8 6      0.0    3.8 6 ; dih   CBV  CBX  NCF  CBZ
  18  19  20  25   1    180.0   33.5 2    180.0   33.5 2 ; dih   CBX  NCF  CCB  CCD
  18  19  29  30   1    180.0   33.5 2    180.0   33.5 2 ; dih   CBX  NCF  CBZ  CAH
  20  25  26  29   1      0.0    0.4 6      0.0    0.4 6 ; dih   CCB  CCD  CCH  CBZ
  25  26  29  30   1      0.0    0.4 6      0.0    0.4 6 ; dih   CCD  CCH  CBZ  CAH
  19  29  30  31   1    180.0   41.8 2    180.0   41.8 2 ; dih   NCF  CBZ  CAH  CAG
  29  30  31  32   1    180.0   41.8 2    180.0   41.8 2 ; dih   CBZ  CAH  CAG  CAI
  30  31  32  33   1    180.0   41.8 2    180.0   41.8 2 ; dih   CAH  CAG  CAI  CCA
  43  33  32  31   1    180.0   41.8 2    180.0   41.8 2 ; dih   NCG  CCA  CAI  CAG
  32  33  34  37   1      0.0    0.4 6      0.0    0.4 6 ; dih   CAI  CCA  CCI  CCE
  32  33  43  44   1    180.0   33.5 2    180.0   33.5 2 ; dih   CAI  CCA  NCG  CBY
  33  34  37  42   1      0.0    0.4 6      0.0    0.4 6 ; dih   CCA  CCI  CCE  CCC
  37  42  43  44   1    180.0   33.5 2    180.0   33.5 2 ; dih   CCE  CCC  NCG  CBY
  33  43  44  45   1      0.0    3.8 6      0.0    3.8 6 ; dih   CCA  NCG  CBY  CBW
  46  45  44  43   1      0.0    5.9 3      0.0    5.9 3 ; dih   CBU  CBW  CBY  NCG
  47  46  45  44   3
  48  47  46  45   3
  49  48  47  46   3
  50  49  48  47   3
  51  50  49  48   3
  52  51  50  49   3
  53  52  51  50   3
  54  53  52  51   3
  55  54  53  52   3
  56  55  54  53   3
  57  56  55  54   3
  58  57  56  55   3
  59  58  57  56   3
  60  59  58  57   3
  61  60  59  58   3

; Strong position restraints for InflateGRO
```

```
;#ifdef STRONG_POSRES
;#include "strong_posre.itp"
;#endif
```

A.1.2 DiI-C18:2

```
[ moleculetype ]
; Name nrexcl
DII      3

[ atoms ]
;   nr       type  resnr resid  atom  cgnr   charge     mass
     1        LP3     1  DII      C1     1    0.000  15.0350
     2        LP2     1  DII      C2     2    0.000  14.0270
     3        LP2     1  DII      C3     3    0.000  14.0270
     4        LP2     1  DII      C4     4    0.000  14.0270
     5        LP2     1  DII      C5     5    0.000  14.0270
     6        LH1     1  DII      C6     6    0.000  13.0190
     7        LH1     1  DII      C7     7    0.000  13.0190
     8        LP2     1  DII      C8     8    0.000  14.0270
     9        LH1     1  DII      C9     9    0.000  13.0190
    10        LH1     1  DII     C10    10    0.000  13.0190
    11        LP2     1  DII     C11    11    0.000  14.0270
    12        LP2     1  DII     C12    12    0.000  14.0270
    13        LP2     1  DII     C13    13    0.000  14.0270
    14        LP2     1  DII     C14    14    0.000  14.0270
    15        LP2     1  DII     C15    15    0.000  14.0270
    16        LP2     1  DII     C16    16    0.000  14.0270
    17        LP2     1  DII     C17    17    0.000  14.0270
    18        LP2     1  DII     C18    18    0.150  14.0270
    19         NR     1  DII     N19    19   -0.010  14.0067
    20          C     1  DII     C20    20    0.100  12.0110
    21        CR1     1  DII     C21    21   -0.040  13.0190
    22        CR1     1  DII     C22    22    0.040  13.0190
    23        CR1     1  DII     C23    23    0.010  13.0190
    24        CR1     1  DII     C24    24    0.010  13.0190
    25          C     1  DII     C25    25   -0.100  12.0110
    26        CH1     1  DII     C26    26    0.400  12.0110
    27        CH3     1  DII     C27    27   -0.060  15.0350
    28        CH3     1  DII     C28    28   -0.070  15.0350
    29          C     1  DII     C29    29    0.300  12.0110
    30        CR1     1  DII     C30    30   -0.430  13.0190
    31        CR1     1  DII     C31    31    0.370  13.0190
    32        CR1     1  DII     C32    32   -0.340  13.0190
    33          C     1  DII     C33    33    0.410  12.0110
    34        CH1     1  DII     C34    34    0.140  12.0110
    35        CH3     1  DII     C35    35   -0.030  15.0350
    36        CH3     1  DII     C36    36   -0.040  15.0350
    37          C     1  DII     C37    37    0.030  12.0110
    38        CR1     1  DII     C38    38   -0.020  13.0190
    39        CR1     1  DII     C39    39    0.010  13.0190
    40        CR1     1  DII     C40    40    0.040  13.0190
    41        CR1     1  DII     C41    41   -0.060  13.0190
    42          C     1  DII     C42    42    0.140  12.0110
    43          N     1  DII     N43    43   -0.100  14.0067
    44        LP2     1  DII     C44    44    0.150  14.0270
    45        LP2     1  DII     C45    45    0.000  14.0270
    46        LP2     1  DII     C46    46    0.000  14.0270
    47        LP2     1  DII     C47    47    0.000  14.0270
    48        LP2     1  DII     C48    48    0.000  14.0270
    49        LP2     1  DII     C49    49    0.000  14.0270
    50        LP2     1  DII     C50    50    0.000  14.0270
    51        LP2     1  DII     C51    51    0.000  14.0270
    52        LH1     1  DII     C52    52    0.000  13.0190
    53        LH1     1  DII     C53    53    0.000  13.0190
    54        LP2     1  DII     C54    54    0.000  14.0270
    55        LH1     1  DII     C55    55    0.000  13.0190
    56        LH1     1  DII     C56    56    0.000  13.0190
    57        LP2     1  DII     C57    57    0.000  14.0270
    58        LP2     1  DII     C58    58    0.000  14.0270
    59        LP2     1  DII     C59    59    0.000  14.0270
    60        LP2     1  DII     C60    60    0.000  14.0270
    61        LP3     1  DII     C61    61    0.000  15.0350
```

```
[ bonds ]
; ai   aj   fu    c0, c1, ...
   1    2    1    0.153    334720.0    0.153    334720.0 ;   CAA  CAR
   2    3    1    0.153    334720.0    0.153    334720.0 ;   CAR  CAT
   3    4    1    0.153    334720.0    0.153    334720.0 ;   CAT  CAV
   4    5    1    0.153    334720.0    0.153    334720.0 ;   CAV  CAX
   5    6    1    0.153    334720.0    0.153    334720.0 ;   CAX  CAZ

   6    7    1    0.139    418400.0    0.139    418400.0 ;   CAZ  CBB

   7    8    1    0.153    334720.0    0.153    334720.0 ;   CBB  CBD
   8    9    1    0.153    334720.0    0.153    334720.0 ;   CBD  CBF

   9   10    1    0.139    418400.0    0.139    418400.0 ;   CBF  CBH

  10   11    1    0.153    334720.0    0.153    334720.0 ;   CBH  CBJ
  11   12    1    0.153    334720.0    0.153    334720.0 ;   CBJ  CBL
  12   13    1    0.153    334720.0    0.153    334720.0 ;   CBL  CBN
  13   14    1    0.153    334720.0    0.153    334720.0 ;   CBN  CBP
  14   15    1    0.153    334720.0    0.153    334720.0 ;   CBP  CBR
  15   16    1    0.153    334720.0    0.153    334720.0 ;   CBR  CBT
  16   17    1    0.153    334720.0    0.153    334720.0 ;   CBT  CBV
  17   18    1    0.153    334720.0    0.153    334720.0 ;   CBV  CBX
  18   19    1    0.147    376560.0    0.147    376560.0 ;   CBX  NCF
  19   20    1    0.141    418400.0    0.133    418400.0 ;   NCF  CCB
  19   29    1    0.133    418400.0    0.133    418400.0 ;   NCF  CBZ
  20   21    1    0.139    418400.0    0.139    418400.0 ;   CCB  CAN
  20   25    1    0.139    418400.0    0.139    418400.0 ;   CCB  CCD
  21   22    1    0.139    418400.0    0.139    418400.0 ;   CAN  CAJ
  22   23    1    0.139    418400.0    0.139    418400.0 ;   CAJ  CAL
  23   24    1    0.139    418400.0    0.139    418400.0 ;   CAL  CAP
  24   25    1    0.139    418400.0    0.139    418400.0 ;   CAP  CCD
  25   26    1    0.153    334720.0    0.153    334720.0 ;   CCD  CCH
  26   27    1    0.153    334720.0    0.153    334720.0 ;   CCH  CAC
  26   28    1    0.153    334720.0    0.153    334720.0 ;   CCH  CAD
  26   29    1    0.153    334720.0    0.153    334720.0 ;   CCH  CBZ
  29   30    1    0.139    418400.0    0.139    418400.0 ;   CBZ  CAH
  30   31    1    0.139    418400.0    0.139    418400.0 ;   CAH  CAG
  31   32    1    0.139    418400.0    0.139    418400.0 ;   CAG  CAI
  32   33    1    0.139    418400.0    0.139    418400.0 ;   CAI  CCA
  33   34    1    0.153    334720.0    0.153    334720.0 ;   CCA  CCI
  33   43    1    0.133    418400.0    0.133    418400.0 ;   CCA  NCG
  34   35    1    0.153    334720.0    0.153    334720.0 ;   CCI  CAE
  34   36    1    0.153    334720.0    0.153    334720.0 ;   CCI  CAF
  34   37    1    0.153    334720.0    0.153    334720.0 ;   CCI  CCE
  37   38    1    0.139    418400.0    0.139    418400.0 ;   CCE  CAQ
  37   42    1    0.139    418400.0    0.139    418400.0 ;   CCE  CCC
  38   39    1    0.139    418400.0    0.139    418400.0 ;   CAQ  CAM
  39   40    1    0.139    418400.0    0.139    418400.0 ;   CAM  CAK
  40   41    1    0.139    418400.0    0.139    418400.0 ;   CAK  CAO
  41   42    1    0.139    418400.0    0.139    418400.0 ;   CAO  CCC
  42   43    1    0.141    418400.0    0.133    418400.0 ;   CCC  NCG
  43   44    1    0.147    376560.0    0.147    376560.0 ;   NCG  CBY
  44   45    1    0.153    334720.0    0.153    334720.0 ;   CBY  CBW
  45   46    1    0.153    334720.0    0.153    334720.0 ;   CBW  CBU
  46   47    1    0.153    334720.0    0.153    334720.0 ;   CBU  CBS
  47   48    1    0.153    334720.0    0.153    334720.0 ;   CBS  CBQ
  48   49    1    0.153    334720.0    0.153    334720.0 ;   CBQ  CBO
  49   50    1    0.153    334720.0    0.153    334720.0 ;   CBO  CBM
  50   51    1    0.153    334720.0    0.153    334720.0 ;   CBM  CBK
  51   52    1    0.153    334720.0    0.153    334720.0 ;   CBK  CBI

  52   53    1    0.139    418400.0    0.139    418400.0 ;   CBI  CBG

  53   54    1    0.153    334720.0    0.153    334720.0 ;   CBG  CBE
  54   55    1    0.153    334720.0    0.153    334720.0 ;   CBE  CBC

  55   56    1    0.139    418400.0    0.139    418400.0 ;   CBC  CBA

  56   57    1    0.153    334720.0    0.153    334720.0 ;   CBA  CAY
  57   58    1    0.153    334720.0    0.153    334720.0 ;   CAY  CAW
```

```
  58  59   1    0.153    334720.0    0.153    334720.0 ;   CAW  CAU
  59  60   1    0.153    334720.0    0.153    334720.0 ;   CAU  CAS
  60  61   1    0.153    334720.0    0.153    334720.0 ;   CAS  CAB

[ pairs ]
; ai  aj  fu    c0, c1, ...
  19  22   1                                             ;   NCF  CAJ
  19  24   1                                             ;   NCF  CAP
  19  27   1                                             ;   NCF  CAC
  19  28   1                                             ;   NCF  CAD
  19  31   1                                             ;   NCF  CAG
  20  23   1                                             ;   CCB  CAL
  20  27   1                                             ;   CCB  CAC
  20  28   1                                             ;   CCB  CAD
  20  30   1                                             ;   CCB  CAH
  21  24   1                                             ;   CAN  CAP
  21  26   1                                             ;   CAN  CCH
  21  29   1                                             ;   CAN  CBZ
  22  25   1                                             ;   CAJ  CCD
  23  26   1                                             ;   CAL  CCH
  24  27   1                                             ;   CAP  CAC
  24  28   1                                             ;   CAP  CAD
  24  29   1                                             ;   CAP  CBZ
  25  30   1                                             ;   CCD  CAH
  26  31   1                                             ;   CCH  CAG
  27  30   1                                             ;   CAC  CAH
  28  30   1                                             ;   CAD  CAH
  29  32   1                                             ;   CBZ  CAI
  30  33   1                                             ;   CAH  CCA
  31  34   1                                             ;   CAG  CCI
  31  43   1                                             ;   CAG  NCG
  32  35   1                                             ;   CAI  CAE
  32  36   1                                             ;   CAI  CAF
  32  37   1                                             ;   CAI  CCE
  32  42   1                                             ;   CAI  CCC
  33  38   1                                             ;   CCA  CAQ
  33  41   1                                             ;   CCA  CAO
  34  39   1                                             ;   CCI  CAM
  34  41   1                                             ;   CCI  CAO
  35  38   1                                             ;   CAE  CAQ
  35  42   1                                             ;   CAE  CCC
  35  43   1                                             ;   CAE  NCG
  36  38   1                                             ;   CAF  CAQ
  36  42   1                                             ;   CAF  CCC
  36  43   1                                             ;   CAF  NCG
  37  40   1                                             ;   CCE  CAK
  38  41   1                                             ;   CAQ  CAO
  38  43   1                                             ;   CAQ  NCG
  39  42   1                                             ;   CAM  CCC
  40  43   1                                             ;   CAK  NCG


[ angles ]
; ai  aj  ak  fu    c0, c1, ...
   1   2   3   1    111.0       460.2    111.0       460.2 ;   CAA  CAR  CAT
   2   3   4   1    111.0       460.2    111.0       460.2 ;   CAR  CAT  CAV
   3   4   5   1    111.0       460.2    111.0       460.2 ;   CAT  CAV  CAX
   4   5   6   1    111.0       460.2    111.0       460.2 ;   CAV  CAX  CAZ

   5   6   7   1    120.0       502.08    120.0       502.08 ;   CAX  CAZ  CBB
   6   7   8   1    120.0       502.08    120.0       502.08 ;   CAZ  CBB  CBD

   7   8   9   1    111.0       460.2    111.0       460.2 ;   CBB  CBD  CBF

   8   9  10   1    120.0       502.08    120.0       502.08 ;   CBD  CBF  CBH
   9  10  11   1    120.0       502.08    120.0       502.08 ;   CBF  CBH  CBJ

  10  11  12   1    111.0       460.2    111.0       460.2 ;   CBH  CBJ  CBL
  11  12  13   1    111.0       460.2    111.0       460.2 ;   CBJ  CBL  CBN
  12  13  14   1    111.0       460.2    111.0       460.2 ;   CBL  CBN  CBP
```

```
13  14  15   1    111.0       460.2    111.0       460.2 ;   CBN  CBP  CBR
14  15  16   1    111.0       460.2    111.0       460.2 ;   CBP  CBR  CBT
15  16  17   1    111.0       460.2    111.0       460.2 ;   CBR  CBT  CBV
16  17  18   1    111.0       460.2    111.0       460.2 ;   CBT  CBV  CBX
17  18  19   1    109.5       460.2    109.5       460.2 ;   CBV  CBX  NCF
18  19  20   1    120.0       418.4    120.0       418.4 ;   CBX  NCF  CCB
18  19  29   1    120.0       418.4    120.0       418.4 ;   CBX  NCF  CBZ
20  19  29   1    108.0       418.4    108.0       418.4 ;   CCB  NCF  CBZ
19  20  21   1    120.0       418.4    120.0       418.4 ;   NCF  CCB  CAN
19  20  25   1    108.0       418.4    108.0       418.4 ;   NCF  CCB  CCD
21  20  25   1    120.0       418.4    120.0       418.4 ;   CAN  CCB  CCD
20  21  22   1    120.0       418.4    120.0       418.4 ;   CCB  CAN  CAJ
21  22  23   1    120.0       418.4    120.0       418.4 ;   CAN  CAJ  CAL
22  23  24   1    120.0       418.4    120.0       418.4 ;   CAJ  CAL  CAP
23  24  25   1    120.0       418.4    120.0       418.4 ;   CAL  CAP  CCD
20  25  24   1    120.0       418.4    120.0       418.4 ;   CCB  CCD  CAP
20  25  26   1    108.0       418.4    108.0       418.4 ;   CCB  CCD  CCH
24  25  26   1    132.0       418.4    132.0       418.4 ;   CAP  CCD  CCH
25  26  27   1    109.5       397.5    109.5       397.5 ;   CCD  CCH  CAC
25  26  28   1    109.5       397.5    109.5       397.5 ;   CCD  CCH  CAD
25  26  29   1    104.0       460.2    104.0       460.2 ;   CCD  CCH  CBZ
27  26  28   1    111.0       460.2    111.0       460.2 ;   CAC  CCH  CAD
27  26  29   1    109.5       397.5    109.5       397.5 ;   CAC  CCH  CBZ
28  26  29   1    109.5       397.5    109.5       397.5 ;   CAD  CCH  CBZ
19  29  26   1    108.0       418.4    108.0       418.4 ;   NCF  CBZ  CCH
19  29  30   1    132.0       418.4    132.0       418.4 ;   NCF  CBZ  CAH
26  29  30   1    132.0       418.4    132.0       418.4 ;   CCH  CBZ  CAH
29  30  31   1    120.0       418.4    120.0       418.4 ;   CBZ  CAH  CAG
30  31  32   1    135.0       418.4    135.0       418.4 ;   CAH  CAG  CAI
31  32  33   1    125.0       418.4    125.0       418.4 ;   CAG  CAI  CCA
32  33  34   1    120.0       418.4    120.0       418.4 ;   CAI  CCA  CCI
32  33  43   1    132.0       418.4    132.0       418.4 ;   CAI  CCA  NCG
34  33  43   1    108.0       418.4    108.0       418.4 ;   CCI  CCA  NCG
33  34  35   1    109.5       397.5    109.5       397.5 ;   CCA  CCI  CAE
33  34  36   1    109.5       397.5    109.5       397.5 ;   CCA  CCI  CAF
33  34  37   1    104.0       460.2    104.0       460.2 ;   CCA  CCI  CCE
35  34  36   1    111.0       460.2    111.0       460.2 ;   CAE  CCI  CAF
35  34  37   1    109.5       397.5    109.5       397.5 ;   CAE  CCI  CCE
36  34  37   1    109.5       397.5    109.5       397.5 ;   CAF  CCI  CCE
34  37  38   1    132.0       418.4    132.0       418.4 ;   CCI  CCE  CAQ
34  37  42   1    108.0       418.4    108.0       418.4 ;   CCI  CCE  CCC
38  37  42   1    120.0       418.4    120.0       418.4 ;   CAQ  CCE  CCC
37  38  39   1    120.0       418.4    120.0       418.4 ;   CCE  CAQ  CAM
38  39  40   1    120.0       418.4    120.0       418.4 ;   CAQ  CAM  CAK
39  40  41   1    120.0       418.4    120.0       418.4 ;   CAM  CAK  CAO
40  41  42   1    120.0       418.4    120.0       418.4 ;   CAK  CAO  CCC
37  42  41   1    120.0       418.4    120.0       418.4 ;   CCE  CCC  CAO
37  42  43   1    108.0       418.4    108.0       418.4 ;   CCE  CCC  NCG
41  42  43   1    132.0       418.4    132.0       418.4 ;   CAO  CCC  NCG
33  43  42   1    108.0       418.4    108.0       418.4 ;   CCA  NCG  CCC
33  43  44   1    120.0       418.4    120.0       418.4 ;   CCA  NCG  CBY
42  43  44   1    120.0       418.4    120.0       418.4 ;   CCC  NCG  CBY
43  44  45   1    109.5       460.2    109.5       460.2 ;   NCG  CBY  CBW
44  45  46   1    111.0       460.2    111.0       460.2 ;   CBY  CBW  CBU
45  46  47   1    111.0       460.2    111.0       460.2 ;   CBW  CBU  CBS
46  47  48   1    111.0       460.2    111.0       460.2 ;   CBU  CBS  CBQ
47  48  49   1    111.0       460.2    111.0       460.2 ;   CBS  CBQ  CBO
48  49  50   1    111.0       460.2    111.0       460.2 ;   CBQ  CBO  CBM
49  50  51   1    111.0       460.2    111.0       460.2 ;   CBO  CBM  CBK
50  51  52   1    111.0       460.2    111.0       460.2 ;   CBM  CBK  CBI

51  52  53   1    111.0       460.2    111.0       460.2 ;   CBK  CBI  CBG
52  53  54   1    111.0       460.2    111.0       460.2 ;   CBI  CBG  CBE

53  54  55   1    111.0       460.2    111.0       460.2 ;   CBG  CBE  CBC

54  55  56   1    120.0       502.08    120.0       502.08 ;   CBE  CBC  CBA
55  56  57   1    120.0       502.08    120.0       502.08 ;   CBC  CBA  CAY
56  57  58   1    111.0       460.2    111.0       460.2 ;   CBA  CAY  CAW
57  58  59   1    111.0       460.2    111.0       460.2 ;   CAY  CAW  CAU
58  59  60   1    111.0       460.2    111.0       460.2 ;   CAW  CAU  CAS
```

```
  59  60  61   1    111.0       460.2    111.0       460.2 ;   CAU  CAS  CAB

[ dihedrals ]
; ai  aj  ak  al  fu    c0, c1, m, ...
  19  18  20  29   2      0.0 1673.6       0.0 1673.6  ; imp   NCF  CBX  CCB  CBZ
  20  25  21  19   2      0.0 1673.6       0.0 1673.6  ; imp   CCB  CCD  CAN  NCF
  25  20  26  24   2      0.0 1673.6       0.0 1673.6  ; imp   CCD  CCB  CCH  CAP
  29  30  26  19   2      0.0 1673.6       0.0 1673.6  ; imp   CBZ  CAH  CCH  NCF
  33  32  34  43   2      0.0 1673.6       0.0 1673.6  ; imp   CCA  CAI  CCI  NCG
  37  34  42  38   2      0.0 1673.6       0.0 1673.6  ; imp   CCE  CCI  CCC  CAQ
  42  37  41  43   2      0.0 1673.6       0.0 1673.6  ; imp   CCC  CCE  CAO  NCG
  43  33  42  44   2      0.0 1673.6       0.0 1673.6  ; imp   NCG  CCA  CCC  CBY
  26  25  28  27   2     35.3  836.8      35.3  836.8  ; imp   CCH  CCD  CAD  CAC
  34  33  35  36   2     35.3  836.8      35.3  836.8  ; imp   CCI  CCA  CAE  CAF
  37  38  39  40   2      0.0 1673.6       0.0 1673.6  ; imp   CCE  CAQ  CAM  CAK
  38  39  40  41   2      0.0 1673.6       0.0 1673.6  ; imp   CAQ  CAM  CAK  CAO
  39  40  41  42   2      0.0 1673.6       0.0 1673.6  ; imp   CAM  CAK  CAO  CCC
  40  41  42  37   2      0.0 1673.6       0.0 1673.6  ; imp   CAK  CAO  CCC  CCE
  41  42  37  38   2      0.0 1673.6       0.0 1673.6  ; imp   CAO  CCC  CCE  CAQ
  42  37  38  39   2      0.0 1673.6       0.0 1673.6  ; imp   CCC  CCE  CAQ  CAM
  20  21  22  23   2      0.0 1673.6       0.0 1673.6  ; imp   CCB  CAN  CAJ  CAL
  21  22  23  24   2      0.0 1673.6       0.0 1673.6  ; imp   CAN  CAJ  CAL  CAP
  22  23  24  25   2      0.0 1673.6       0.0 1673.6  ; imp   CAJ  CAL  CAP  CCD
  23  24  25  20   2      0.0 1673.6       0.0 1673.6  ; imp   CAL  CAP  CCD  CCB
  24  25  20  21   2      0.0 1673.6       0.0 1673.6  ; imp   CAP  CCD  CCB  CAN
  25  20  21  22   2      0.0 1673.6       0.0 1673.6  ; imp   CCD  CCB  CAN  CAJ
   4   3   2   1   3
   5   4   3   2   3
   6   5   4   3   3
   7   6   5   4   1      0.0    5.858 3      0.0    5.858 3
;   8   7   6   5   3
   9   8   7   6   1      0.0    5.858 3      0.0    5.858 3
  10   9   8   7   1      0.0    5.858 3      0.0    5.858 3
;  11  10   9   8   3
  12  11  10   9   1      0.0    5.858 3      0.0    5.858 3
  13  12  11  10   3
  14  13  12  11   3
  15  14  13  12   3
  16  15  14  13   3
  17  16  15  14   3
  18  17  16  15   3
  19  18  17  16   1      0.0    5.9 3        0.0    5.9 3 ; dih   NCF  CBX  CBV  CBT
  17  18  19  29   1      0.0    3.8 6        0.0    3.8 6 ; dih   CBV  CBX  NCF  CBZ
  18  19  20  25   1    180.0   33.5 2     180.0   33.5 2 ; dih   CBX  NCF  CCB  CCD
  18  19  29  30   1    180.0   33.5 2     180.0   33.5 2 ; dih   CBX  NCF  CBZ  CAH
  20  25  26  29   1      0.0    0.4 6        0.0    0.4 6 ; dih   CCB  CCD  CCH  CBZ
  25  26  29  30   1      0.0    0.4 6        0.0    0.4 6 ; dih   CCD  CCH  CBZ  CAH
  19  29  30  31   1    180.0   41.8 2     180.0   41.8 2 ; dih   NCF  CBZ  CAH  CAG
  29  30  31  32   1    180.0   41.8 2     180.0   41.8 2 ; dih   CBZ  CAH  CAG  CAI
  30  31  32  33   1    180.0   41.8 2     180.0   41.8 2 ; dih   CAH  CAG  CAI  CCA
  43  33  32  31   1    180.0   41.8 2     180.0   41.8 2 ; dih   NCG  CCA  CAI  CAG
  32  33  34  37   1      0.0    0.4 6        0.0    0.4 6 ; dih   CAI  CCA  CCI  CCE
  32  33  43  44   1    180.0   33.5 2     180.0   33.5 2 ; dih   CAI  CCA  NCG  CBY
  33  34  37  42   1      0.0    0.4 6        0.0    0.4 6 ; dih   CCA  CCI  CCE  CCC
  37  42  43  44   1    180.0   33.5 2     180.0   33.5 2 ; dih   CCE  CCC  NCG  CBY
  33  43  44  45   1      0.0    3.8 6        0.0    3.8 6 ; dih   CCA  NCG  CBY  CBW
  46  45  44  43   1      0.0    5.9 3        0.0    5.9 3 ; dih   CBU  CBW  CBY  NCG
  47  46  45  44   3
  48  47  46  45   3
  49  48  47  46   3
  50  49  48  47   3
  51  50  49  48   3
  52  51  50  49   3
  53  52  51  50   1      0.0    5.858 3      0.0    5.858 3
 ; 54  53  52  51   3
  55  54  53  52   1      0.0    5.858 3      0.0    5.858 3
  56  55  54  53   1      0.0    5.858 3      0.0    5.858 3
;  57  56  55  54   3
  58  57  56  55   1      0.0    5.858 3      0.0    5.858 3
  59  58  57  56   3
  60  59  58  57   3
```

```
  61   60   59   58    3

[ dihedrals ]
;  ai    aj    ak    al funct
      11       10        9        8        2 0.000       167.360
       8        7        6        5        2 0.000       167.360
      54       53       52       51        2 0.000       167.360
      57       56       55       54        2 0.000       167.360

; Strong position restraints for InflateGRO
#ifdef STRONG_POSRES
#include "strong_posre.itp"
#endif
```

A.1.3 DiI-C12:0

```
[ moleculetype ]
; Name nrexcl
DII      3

[ atoms ]
;   nr       type  resnr resid  atom  cgnr   charge     mass
     1        LP3     1  DII      C1     1    0.000  15.0350
     2        LP2     1  DII      C2     2    0.000  14.0270
     3        LP2     1  DII      C3     3    0.000  14.0270
     4        LP2     1  DII      C4     4    0.000  14.0270
     5        LP2     1  DII      C5     5    0.000  14.0270
     6        LP2     1  DII      C6     6    0.000  14.0270
     7        LP2     1  DII      C7     7    0.000  14.0270
     8        LP2     1  DII      C8     8    0.000  14.0270
     9        LP2     1  DII      C9     9    0.000  14.0270
    10        LP2     1  DII     C10    10    0.000  14.0270
    11        LP2     1  DII     C11    11    0.000  14.0270
    12        LP2     1  DII     C12    12    0.150  14.0270
    13         NR     1  DII     N13    13   -0.010  14.0067
    14          C     1  DII     C14    14    0.100  12.0110
    15        CR1     1  DII     C15    15   -0.040  13.0190
    16        CR1     1  DII     C16    16    0.040  13.0190
    17        CR1     1  DII     C17    17    0.010  13.0190
    18        CR1     1  DII     C18    18    0.010  13.0190
    19          C     1  DII     C19    19   -0.100  12.0110
    20        CH1     1  DII     C20    20    0.400  12.0110
    21        CH3     1  DII     C21    21   -0.060  15.0350
    22        CH3     1  DII     C22    22   -0.070  15.0350
    23          C     1  DII     C23    23    0.300  12.0110
    24        CR1     1  DII     C24    24   -0.430  13.0190
    25        CR1     1  DII     C25    25    0.370  13.0190
    26        CR1     1  DII     C26    26   -0.340  13.0190
    27          C     1  DII     C27    27    0.410  12.0110
    28        CH1     1  DII     C28    28    0.140  12.0110
    29        CH3     1  DII     C29    29   -0.030  15.0350
    30        CH3     1  DII     C30    30   -0.040  15.0350
    31          C     1  DII     C31    31    0.030  12.0110
    32        CR1     1  DII     C32    32   -0.020  13.0190
    33        CR1     1  DII     C33    33    0.010  13.0190
    34        CR1     1  DII     C34    34    0.040  13.0190
    35        CR1     1  DII     C35    35   -0.060  13.0190
    36          C     1  DII     C36    36    0.140  12.0110
    37          N     1  DII     N37    37   -0.100  14.0067
    38        LP2     1  DII     C38    38    0.150  14.0270
    39        LP2     1  DII     C39    39    0.000  14.0270
    40        LP2     1  DII     C40    40    0.000  14.0270
    41        LP2     1  DII     C41    41    0.000  14.0270
    42        LP2     1  DII     C42    42    0.000  14.0270
    43        LP2     1  DII     C43    43    0.000  14.0270
    44        LP2     1  DII     C44    44    0.000  14.0270
    45        LP2     1  DII     C45    45    0.000  14.0270
    46        LP2     1  DII     C46    46    0.000  14.0270
    47        LP2     1  DII     C47    47    0.000  14.0270
    48        LP2     1  DII     C48    48    0.000  14.0270
    49        LP3     1  DII     C49    49    0.000  15.0350

[ bonds ]
; ai  aj  fu    c0, c1, ...
   1   2   1    0.153    334720.0    0.153    334720.0 ;   CBB  CBD
   2   3   1    0.153    334720.0    0.153    334720.0 ;   CBD  CBF
   3   4   1    0.153    334720.0    0.153    334720.0 ;   CBF  CBH
   4   5   1    0.153    334720.0    0.153    334720.0 ;   CBH  CBJ
   5   6   1    0.153    334720.0    0.153    334720.0 ;   CBJ  CBL
   6   7   1    0.153    334720.0    0.153    334720.0 ;   CBL  CBN
   7   8   1    0.153    334720.0    0.153    334720.0 ;   CBN  CBP
   8   9   1    0.153    334720.0    0.153    334720.0 ;   CBP  CBR
   9  10   1    0.153    334720.0    0.153    334720.0 ;   CBR  CBT
  10  11   1    0.153    334720.0    0.153    334720.0 ;   CBT  CBV
```

```
  11  12   1    0.153    334720.0    0.153    334720.0 ;   CBV  CBX
  12  13   1    0.147    376560.0    0.147    376560.0 ;   CBX  NCF
  13  14   1    0.141    418400.0    0.133    418400.0 ;   NCF  CCB
  13  23   1    0.133    418400.0    0.133    418400.0 ;   NCF  CBZ
  14  15   1    0.139    418400.0    0.139    418400.0 ;   CCB  CAN
  14  19   1    0.139    418400.0    0.139    418400.0 ;   CCB  CCD
  15  16   1    0.139    418400.0    0.139    418400.0 ;   CAN  CAJ
  16  17   1    0.139    418400.0    0.139    418400.0 ;   CAJ  CAL
  17  18   1    0.139    418400.0    0.139    418400.0 ;   CAL  CAP
  18  19   1    0.139    418400.0    0.139    418400.0 ;   CAP  CCD
  19  20   1    0.153    334720.0    0.153    334720.0 ;   CCD  CCH
  20  21   1    0.153    334720.0    0.153    334720.0 ;   CCH  CAC
  20  22   1    0.153    334720.0    0.153    334720.0 ;   CCH  CAD
  20  23   1    0.153    334720.0    0.153    334720.0 ;   CCH  CBZ
  23  24   1    0.139    418400.0    0.139    418400.0 ;   CBZ  CAH
  24  25   1    0.139    418400.0    0.139    418400.0 ;   CAH  CAG
  25  26   1    0.139    418400.0    0.139    418400.0 ;   CAG  CAI
  26  27   1    0.139    418400.0    0.139    418400.0 ;   CAI  CCA
  27  28   1    0.153    334720.0    0.153    334720.0 ;   CCA  CCI
  27  37   1    0.133    418400.0    0.133    418400.0 ;   CCA  NCG
  28  29   1    0.153    334720.0    0.153    334720.0 ;   CCI  CAE
  28  30   1    0.153    334720.0    0.153    334720.0 ;   CCI  CAF
  28  31   1    0.153    334720.0    0.153    334720.0 ;   CCI  CCE
  31  32   1    0.139    418400.0    0.139    418400.0 ;   CCE  CAQ
  31  36   1    0.139    418400.0    0.139    418400.0 ;   CCE  CCC
  32  33   1    0.139    418400.0    0.139    418400.0 ;   CAQ  CAM
  33  34   1    0.139    418400.0    0.139    418400.0 ;   CAM  CAK
  34  35   1    0.139    418400.0    0.139    418400.0 ;   CAK  CAO
  35  36   1    0.139    418400.0    0.139    418400.0 ;   CAO  CCC
  36  37   1    0.141    418400.0    0.133    418400.0 ;   CCC  NCG
  37  38   1    0.147    376560.0    0.147    376560.0 ;   NCG  CBY
  38  39   1    0.153    334720.0    0.153    334720.0 ;   CBY  CBW
  39  40   1    0.153    334720.0    0.153    334720.0 ;   CBW  CBU
  40  41   1    0.153    334720.0    0.153    334720.0 ;   CBU  CBS
  41  42   1    0.153    334720.0    0.153    334720.0 ;   CBS  CBQ
  42  43   1    0.153    334720.0    0.153    334720.0 ;   CBQ  CBO
  43  44   1    0.153    334720.0    0.153    334720.0 ;   CBO  CBM
  44  45   1    0.153    334720.0    0.153    334720.0 ;   CBM  CBK
  45  46   1    0.153    334720.0    0.153    334720.0 ;   CBK  CBI
  46  47   1    0.153    334720.0    0.153    334720.0 ;   CBI  CBG
  47  48   1    0.153    334720.0    0.153    334720.0 ;   CBG  CBE
  48  49   1    0.153    334720.0    0.153    334720.0 ;   CBE  CBC

[ pairs ]
; ai  aj  fu    c0, c1, ...
  13  16   1                                          ;   NCF  CAJ
  13  18   1                                          ;   NCF  CAP
  13  21   1                                          ;   NCF  CAC
  13  22   1                                          ;   NCF  CAD
  13  25   1                                          ;   NCF  CAG
  14  17   1                                          ;   CCB  CAL
  14  21   1                                          ;   CCB  CAC
  14  22   1                                          ;   CCB  CAD
  14  24   1                                          ;   CCB  CAH
  15  18   1                                          ;   CAN  CAP
  15  20   1                                          ;   CAN  CCH
  15  23   1                                          ;   CAN  CBZ
  16  19   1                                          ;   CAJ  CCD
  17  20   1                                          ;   CAL  CCH
  18  21   1                                          ;   CAP  CAC
  18  22   1                                          ;   CAP  CAD
  18  23   1                                          ;   CAP  CBZ
  19  24   1                                          ;   CCD  CAH
  20  25   1                                          ;   CCH  CAG
  21  24   1                                          ;   CAC  CAH
  22  24   1                                          ;   CAD  CAH
  23  26   1                                          ;   CBZ  CAI
  24  27   1                                          ;   CAH  CCA
  25  28   1                                          ;   CAG  CCI
  25  37   1                                          ;   CAG  NCG
  26  29   1                                          ;   CAI  CAE
```

```
  26  30   1                                          ;   CAI  CAF
  26  31   1                                          ;   CAI  CCE
  26  36   1                                          ;   CAI  CCC
  27  32   1                                          ;   CCA  CAQ
  27  35   1                                          ;   CCA  CAO
  28  33   1                                          ;   CCI  CAM
  28  35   1                                          ;   CCI  CAO
  29  32   1                                          ;   CAE  CAQ
  29  36   1                                          ;   CAE  CCC
  29  37   1                                          ;   CAE  NCG
  30  32   1                                          ;   CAF  CAQ
  30  36   1                                          ;   CAF  CCC
  30  37   1                                          ;   CAF  NCG
  31  34   1                                          ;   CCE  CAK
  32  35   1                                          ;   CAQ  CAO
  32  37   1                                          ;   CAQ  NCG
  33  36   1                                          ;   CAM  CCC
  34  37   1                                          ;   CAK  NCG


[ angles ]
; ai   aj   ak   fu    c0, c1, ...
    1    2    3    1    111.0       460.2    111.0       460.2 ;   CBB  CBD  CBF
    2    3    4    1    111.0       460.2    111.0       460.2 ;   CBD  CBF  CBH
    3    4    5    1    111.0       460.2    111.0       460.2 ;   CBF  CBH  CBJ
    4    5    6    1    111.0       460.2    111.0       460.2 ;   CBH  CBJ  CBL
    5    6    7    1    111.0       460.2    111.0       460.2 ;   CBJ  CBL  CBN
    6    7    8    1    111.0       460.2    111.0       460.2 ;   CBL  CBN  CBP
    7    8    9    1    111.0       460.2    111.0       460.2 ;   CBN  CBP  CBR
    8    9   10    1    111.0       460.2    111.0       460.2 ;   CBP  CBR  CBT
    9   10   11    1    111.0       460.2    111.0       460.2 ;   CBR  CBT  CBV
   10   11   12    1    111.0       460.2    111.0       460.2 ;   CBT  CBV  CBX
   11   12   13    1    109.5       460.2    109.5       460.2 ;   CBV  CBX  NCF
   12   13   14    1    120.0       418.4    120.0       418.4 ;   CBX  NCF  CCB
   12   13   23    1    120.0       418.4    120.0       418.4 ;   CBX  NCF  CBZ
   14   13   23    1    108.0       418.4    108.0       418.4 ;   CCB  NCF  CBZ
   13   14   15    1    120.0       418.4    120.0       418.4 ;   NCF  CCB  CAN
   13   14   19    1    108.0       418.4    108.0       418.4 ;   NCF  CCB  CCD
   15   14   19    1    120.0       418.4    120.0       418.4 ;   CAN  CCB  CCD
   14   15   16    1    120.0       418.4    120.0       418.4 ;   CCB  CAN  CAJ
   15   16   17    1    120.0       418.4    120.0       418.4 ;   CAN  CAJ  CAL
   16   17   18    1    120.0       418.4    120.0       418.4 ;   CAJ  CAL  CAP
   17   18   19    1    120.0       418.4    120.0       418.4 ;   CAL  CAP  CCD
   14   19   18    1    120.0       418.4    120.0       418.4 ;   CCB  CCD  CAP
   14   19   20    1    108.0       418.4    108.0       418.4 ;   CCB  CCD  CCH
   18   19   20    1    132.0       418.4    132.0       418.4 ;   CAP  CCD  CCH
   19   20   21    1    109.5       397.5    109.5       397.5 ;   CCD  CCH  CAC
   19   20   22    1    109.5       397.5    109.5       397.5 ;   CCD  CCH  CAD
   19   20   23    1    104.0       460.2    104.0       460.2 ;   CCD  CCH  CBZ
   21   20   22    1    111.0       460.2    111.0       460.2 ;   CAC  CCH  CAD
   21   20   23    1    109.5       397.5    109.5       397.5 ;   CAC  CCH  CBZ
   22   20   23    1    109.5       397.5    109.5       397.5 ;   CAD  CCH  CBZ
   13   23   20    1    108.0       418.4    108.0       418.4 ;   NCF  CBZ  CCH
   13   23   24    1    132.0       418.4    132.0       418.4 ;   NCF  CBZ  CAH
   20   23   24    1    132.0       418.4    132.0       418.4 ;   CCH  CBZ  CAH
   23   24   25    1    120.0       418.4    120.0       418.4 ;   CBZ  CAH  CAG
   24   25   26    1    135.0       418.4    135.0       418.4 ;   CAH  CAG  CAI
   25   26   27    1    125.0       418.4    125.0       418.4 ;   CAG  CAI  CCA
   26   27   28    1    120.0       418.4    120.0       418.4 ;   CAI  CCA  CCI
   26   27   37    1    132.0       418.4    132.0       418.4 ;   CAI  CCA  NCG
   28   27   37    1    108.0       418.4    108.0       418.4 ;   CCI  CCA  NCG
   27   28   29    1    109.5       397.5    109.5       397.5 ;   CCA  CCI  CAE
   27   28   30    1    109.5       397.5    109.5       397.5 ;   CCA  CCI  CAF
   27   28   31    1    104.0       460.2    104.0       460.2 ;   CCA  CCI  CCE
   29   28   30    1    111.0       460.2    111.0       460.2 ;   CAE  CCI  CAF
   29   28   31    1    109.5       397.5    109.5       397.5 ;   CAE  CCI  CCE
   30   28   31    1    109.5       397.5    109.5       397.5 ;   CAF  CCI  CCE
   28   31   32    1    132.0       418.4    132.0       418.4 ;   CCI  CCE  CAQ
   28   31   36    1    108.0       418.4    108.0       418.4 ;   CCI  CCE  CCC
   32   31   36    1    120.0       418.4    120.0       418.4 ;   CAQ  CCE  CCC
```

```
  31   32   33    1     120.0       418.4     120.0       418.4 ;   CCE  CAQ  CAM
  32   33   34    1     120.0       418.4     120.0       418.4 ;   CAQ  CAM  CAK
  33   34   35    1     120.0       418.4     120.0       418.4 ;   CAM  CAK  CAO
  34   35   36    1     120.0       418.4     120.0       418.4 ;   CAK  CAO  CCC
  31   36   35    1     120.0       418.4     120.0       418.4 ;   CCE  CCC  CAO
  31   36   37    1     108.0       418.4     108.0       418.4 ;   CCE  CCC  NCG
  35   36   37    1     132.0       418.4     132.0       418.4 ;   CAO  CCC  NCG
  27   37   36    1     108.0       418.4     108.0       418.4 ;   CCA  NCG  CCC
  27   37   38    1     120.0       418.4     120.0       418.4 ;   CCA  NCG  CBY
  36   37   38    1     120.0       418.4     120.0       418.4 ;   CCC  NCG  CBY
  37   38   39    1     109.5       460.2     109.5       460.2 ;   NCG  CBY  CBW
  38   39   40    1     111.0       460.2     111.0       460.2 ;   CBY  CBW  CBU
  39   40   41    1     111.0       460.2     111.0       460.2 ;   CBW  CBU  CBS
  40   41   42    1     111.0       460.2     111.0       460.2 ;   CBU  CBS  CBQ
  41   42   43    1     111.0       460.2     111.0       460.2 ;   CBS  CBQ  CBO
  42   43   44    1     111.0       460.2     111.0       460.2 ;   CBQ  CBO  CBM
  43   44   45    1     111.0       460.2     111.0       460.2 ;   CBO  CBM  CBK
  44   45   46    1     111.0       460.2     111.0       460.2 ;   CBM  CBK  CBI
  45   46   47    1     111.0       460.2     111.0       460.2 ;   CBK  CBI  CBG
  46   47   48    1     111.0       460.2     111.0       460.2 ;   CBI  CBG  CBE
  47   48   49    1     111.0       460.2     111.0       460.2 ;   CBG  CBE  CBC

[ dihedrals ]
; ai   aj   ak   al   fu    c0, c1, m, ... FIXED
  13   12   14   23    2       0.0 1673.6       0.0 1673.6  ; imp   NCF  CBX  CCB  CBZ
  14   19   15   13    2       0.0 1673.6       0.0 1673.6  ; imp   CCB  CCD  CAN  NCF
  19   14   20   18    2       0.0 1673.6       0.0 1673.6  ; imp   CCD  CCB  CCH  CAP
  23   24   20   13    2       0.0 1673.6       0.0 1673.6  ; imp   CBZ  CAH  CCH  NCF
  27   26   28   37    2       0.0 1673.6       0.0 1673.6  ; imp   CCA  CAI  CCI  NCG
  31   28   36   32    2       0.0 1673.6       0.0 1673.6  ; imp   CCE  CCI  CCC  CAQ
  36   31   35   37    2       0.0 1673.6       0.0 1673.6  ; imp   CCC  CCE  CAO  NCG
  37   27   36   38    2       0.0 1673.6       0.0 1673.6  ; imp   NCG  CCA  CCC  CBY
  20   19   22   21    2      35.3  836.8      35.3  836.8  ; imp   CCH  CCD  CAD  CAC
  28   27   29   30    2      35.3  836.8      35.3  836.8  ; imp   CCI  CCA  CAE  CAF
  31   32   33   34    2       0.0 1673.6       0.0 1673.6  ; imp   CCE  CAQ  CAM  CAK
  32   33   34   35    2       0.0 1673.6       0.0 1673.6  ; imp   CAQ  CAM  CAK  CAO
  33   34   35   36    2       0.0 1673.6       0.0 1673.6  ; imp   CAM  CAK  CAO  CCC
  34   35   36   31    2       0.0 1673.6       0.0 1673.6  ; imp   CAK  CAO  CCC  CCE
  35   36   31   32    2       0.0 1673.6       0.0 1673.6  ; imp   CAO  CCC  CCE  CAQ
  36   31   32   33    2       0.0 1673.6       0.0 1673.6  ; imp   CCC  CCE  CAQ  CAM
  14   15   16   17    2       0.0 1673.6       0.0 1673.6  ; imp   CCB  CAN  CAJ  CAL
  15   16   17   18    2       0.0 1673.6       0.0 1673.6  ; imp   CAN  CAJ  CAL  CAP
  16   17   18   19    2       0.0 1673.6       0.0 1673.6  ; imp   CAJ  CAL  CAP  CCD
  17   18   19   14    2       0.0 1673.6       0.0 1673.6  ; imp   CAL  CAP  CCD  CCB
  18   19   14   15    2       0.0 1673.6       0.0 1673.6  ; imp   CAP  CCD  CCB  CAN
  19   14   15   16    2       0.0 1673.6       0.0 1673.6  ; imp   CCD  CCB  CAN  CAJ
   4    3    2    1    3
   5    4    3    2    3
   6    5    4    3    3
   7    6    5    4    3
   8    7    6    5    3
   9    8    7    6    3
  10    9    8    7    3
  11   10    9    8    3
  12   11   10    9    3
  13   12   11   10    1       0.0     5.9 3       0.0     5.9 3 ; dih   NCF  CBX  CBV  CBT
  11   12   13   23    1       0.0     3.8 6       0.0     3.8 6 ; dih   CBV  CBX  NCF  CBZ
  12   13   14   19    1     180.0    33.5 2     180.0    33.5 2 ; dih   CBX  NCF  CCB  CCD
  12   13   23   24    1     180.0    33.5 2     180.0    33.5 2 ; dih   CBX  NCF  CBZ  CAH
  14   19   20   23    1       0.0     0.4 6       0.0     0.4 6 ; dih   CCB  CCD  CCH  CBZ
  19   20   23   24    1       0.0     0.4 6       0.0     0.4 6 ; dih   CCD  CCH  CBZ  CAH
  13   23   24   25    1     180.0    41.8 2     180.0    41.8 2 ; dih   NCF  CBZ  CAH  CAG
  23   24   25   26    1     180.0    41.8 2     180.0    41.8 2 ; dih   CBZ  CAH  CAG  CAI
  24   25   26   27    1     180.0    41.8 2     180.0    41.8 2 ; dih   CAH  CAG  CAI  CCA
  37   27   26   25    1     180.0    41.8 2     180.0    41.8 2 ; dih   NCG  CCA  CAI  CAG
  26   27   28   31    1       0.0     0.4 6       0.0     0.4 6 ; dih   CAI  CCA  CCI  CCE
  26   27   37   38    1     180.0    33.5 2     180.0    33.5 2 ; dih   CAI  CCA  NCG  CBY
  27   28   31   36    1       0.0     0.4 6       0.0     0.4 6 ; dih   CCA  CCI  CCE  CCC
  31   36   37   38    1     180.0    33.5 2     180.0    33.5 2 ; dih   CCE  CCC  NCG  CBY
  26   37   38   39    1       0.0     3.8 6       0.0     3.8 6 ; dih   CCA  NCG  CBY  CBW
  40   39   38   37    1       0.0     5.9 3       0.0     5.9 3 ; dih   CBU  CBW  CBY  NCG
```

```
  41   40   39   38    3
  42   41   40   39    3
  43   42   41   40    3
  44   43   42   41    3
  45   44   43   42    3
  46   45   44   43    3
  47   46   45   44    3
  48   47   46   45    3
  49   48   47   46    3

; Strong position restraints for InflateGRO
#ifdef STRONG_POSRES
#include "strong_posre.itp"
#endif
```

A.2 Simulation setup

Construction of the desired bilayers was a multi-step process. First, the PDB file of a template bilayer consisting of 128 DPPC molecules and water was obtained from the Tieleman website [http://people.ucalgary.ca/~tieleman/download.html]. Water was then removed and the system was tiled 2 times in both the x and y dimensions to create a bilayer with 512 DPPC molecules, with the z-axis being normal to the bilayer. One DPPC per leaflet was chosen so that their separation distance, including periodic copies, was maximized. These two DPPC molecules were then removed from the template bilayer and replaced with either two identical probe molecules (DiI-C18:0, DiI-C18:2, DiI-C12:0) or two DPPC (as a control). These inserted molecules were randomly rotated about their z-axis, and placed at the (x,y) position of the removed DPPC molecule. To minimize the possibility of atomic overlap, the inserted molecules were initially placed so that they were protruding from the bilayer, with only the ends of their hydrocarbon chains within the bilayer, and energy minimization was performed to reduce unfavorable interactions or overlaps. The inserted molecules were then moved 1 nm into the bilayer in 0.05 nm increments along the bilayer normal, with energy minimization performed at each step.

We tested a variety of simulation parameters, choosing particular values based on their ability to reproduce experimentally measured parameters. Importantly, we found that our results are robust even under different conditions including a lower hydration level or lower pressure (results not shown). We also saw that for the pure DPPC control simulations, insertion of the DPPC molecule did not cause bilayer perturbations.

Table A.1 Number of lipids per shell after partitioning. The shell assignments described in Equation 2.3 partition the leaflets such that there are ~ 6*n* lipids in shell *n*, for all systems studied. For shell $n > 7$ the shell diameters exceed the (x,y) box dimensions, leading to a decrease in the number of lipids per shell for the remaining shells.

inserted molecule	leaf	shell 0	shell 1	shell 2	shell 3	shell 4	shell 5	shell 6	shell 7	shell 8	shell 9	shell 10	shell 11
DPPC	same		6.01±0.02	12.00±0.03	18.04±0.03	23.99±0.03	30.00±0.04	35.99±0.04	42.00±0.04	44.23±0.05	24.86±0.04	13.32±0.03	4.56±0.01
DPPC	opp.	1.000±0.007	6.00±0.02	12.00±0.03	18.00±0.04	23.99±0.05	30.01±0.03	35.99±0.03	42.01±0.05	44.23±0.04	24.88±0.04	13.32±0.03	4.56±0.01
DiI-C18:0	same		6.0±0.1	12.1±0.3	18.1±0.4	24.0±0.4	30.1±0.6	36.0±0.5	41.8±0.5	44.3±0.6	24.8±0.5	13.3±0.4	4.5±0.1
DiI-C18:0	opp.	0.97±0.09	5.8±0.2	12.0±0.3	18.2±0.3	24.2±0.3	30.0±0.4	36.1±0.5	41.9±0.5	44.0±0.6	24.6±0.3	12.9±0.3	4.4±0.2
DiI-C18:2	same		5.9±0.2	12.0±0.3	18.1±0.3	24.1±0.4	30.1±0.4	36.2±0.4	41.7±0.4	44.3±0.4	24.7±0.3	13.3±0.2	4.6±0.2
DiI-C18:2	opp.	0.97±0.09	5.8±0.1	12.0±0.3	18.2±0.3	24.0±0.4	30.1±0.6	36.1±0.5	41.8±0.4	44.1±0.4	24.6±0.3	12.9±0.2	4.4±0.2
DiI-C12:0	same		5.9±0.2	12.2±0.4	17.9±0.4	24.0±0.5	29.9±0.4	36.4±0.5	41.8±0.5	44.3±0.4	24.7±0.5	13.2±0.3	4.5±0.1
DiI-C12:0	opp.	0.98±0.09	5.9±0.2	12.0±0.2	17.9±0.4	24.2±0.4	30.1±0.4	35.9±0.5	42.0±0.6	44.2±0.6	24.5±0.4	12.9±0.3	4.4±0.2

Table A.2 DPPC chain order by shell. The average acyl chain order parameter S_{CD} (Equation 2.4) for DPPC partitioned into shells, for each leaflet. Overall average for each system is shown in the last column.

inserted molecule	leaf	shell 0	shell 1	shell 2	shell 3	shell 4	shell 5	shell 6	shell 7	shell 8	shell 9	shell 10	shell 11	Avg.
DPPC	same		0.169 ±0.001	0.166 ±0.001	0.165 ±0.001	0.165 ±0.001	0.165 ±0.001	0.165 ±0.001	0.165± 0.001	0.165± 0.001	0.165± 0.001	0.166± 0.001	0.166± 0.001	**0.165±0.001**
DPPC	opp.	0.165 ±0.002	0.166 ±0.002	0.166 ±0.002	0.166 ±0.001	0.165 ±0.001	0.165 ±0.001	0.165 ±0.001	0.165 ±0.001	0.165 ±0.001	0.166 ±0.001	0.165 ±0.001	0.166 ±0.001	
DiI-C18:0	same		0.15±0.01	0.172 ±0.009	0.171 ±0.006	0.169 ±0.004	0.167 ±0.004	0.166 ±0.003	0.165 ±0.004	0.165 ±0.004	0.167 ±0.004	0.166 ±0.006	0.16 ±0.01	**0.166±0.001**
DiI-C18:0	opp.	0.15±0.01	0.158 ±0.008	0.166 ±0.006	0.170 ±0.005	0.170 ±0.004	0.168 ±0.004	0.166 ±0.002	0.165 ±0.002	0.165 ±0.003	0.166 ±0.004	0.165 ±0.007	0.16±0.01	
DiI-C18:2	same		0.148 ±0.009	0.169 ±0.005	0.170 ±0.005	0.170 ±0.005	0.169 ±0.003	0.167 ±0.004	0.165 ±0.002	0.165 ±0.003	0.165 ±0.003	0.165 ±0.005	0.16±0.01	**0.166±0.001**
DiI-C18:2	opp.	0.15±0.01	0.16±0.01	0.164 ±0.007	0.170 ±0.004	0.170 ±0.004	0.168 ±0.003	0.167 ±0.004	0.166 ±0.003	0.165 ±0.003	0.166 ±0.005	0.166 ±0.006	0.17±0.01	
DiI-C12:0	same		0.152 ±0.009	0.171 ±0.006	0.169 ±0.005	0.168 ±0.004	0.167 ±0.004	0.167 ±0.003	0.166 ±0.002	0.166 ±0.003	0.166 ±0.004	0.164 ±0.006	0.16±0.01	**0.1664±0.0008**
DiI-C12:0	opp.	0.16±0.01	0.16±0.01	0.164 ±0.008	0.168 ±0.004	0.168 ±0.004	0.167 ±0.004	0.167 ±0.003	0.166 ±0.003	0.166 ±0.003	0.166 ±0.004	0.164 ±0.007	0.16±0.01	

Table A.3 P-N vector angle by shell with respect to the bilayer normal. The average P-N vector angle of all shells in each leaflet for each system is shown. Overall average for each system is shown in the last column.

inserted molecule	leaf	shell 0	shell 1	shell 2	shell 3	shell 4	shell 5	shell 6	shell 7	shell 8	shell 9	shell 10	shell 11	Avg
DPPC	same		79.6±0.2	79.5±0.2	79.5±0.2	79.5±0.2	79.5±0.2	79.5±0.2	79.5±0.2	79.5±0.2	79.5±0.2	79.6±0.2	79.5±0.2	**79.5±0.2**
DPPC	opp.	79.6±0.4	79.5±0.2	79.5±0.2	79.5±0.2	79.5±0.2	79.5±0.2	79.5±0.2	79.5±0.2	79.5±0.2	79.5±0.2	79.5±0.2	79.5±0.2	
DiI-C18:0	same		71±2	77±2	79±1	79±1	80±1	79.3±0.7	79.4±0.7	79.5±0.6	78.9±0.9	79±1	79±2	**79.1±0.2**
DiI-C18:0	opp.	79±4	79±2	79±1	79±1	79.4±0.9	79.4±0.7	79.3±0.8	79.2±0.6	79±1	78.4±0.8	77±1	77±3	
DiI-C18:2	same		71±3	78±2	79±1	79±1	79.2±0.9	79.5±0.7	79.4±0.8	79.5±0.8	79.3±0.9	79±1	79±2	**79.0±0.2**
DiI-C18:2	opp.	80±4	79±2	79±1	79±1	79.0±0.9	79.5±0.7	79.2±0.6	79.4±0.7	79.0±0.7	78.6±0.8	78±2	77±3	
DiI-C12:0	same		71±2	78±1	79±1	79±1	79.4±0.9	79.4±0.9	79.3±0.6	79.4±0.7	79.2±0.6	80±1	79±2	**79.0±0.1**
DiI-C12:0	opp.	80±5	79±1	79±2	79±1	79±1	79.5±0.7	79.4±0.6	79.3±0.7	79.0±0.8	79.5±0.9	78±1	77±4	

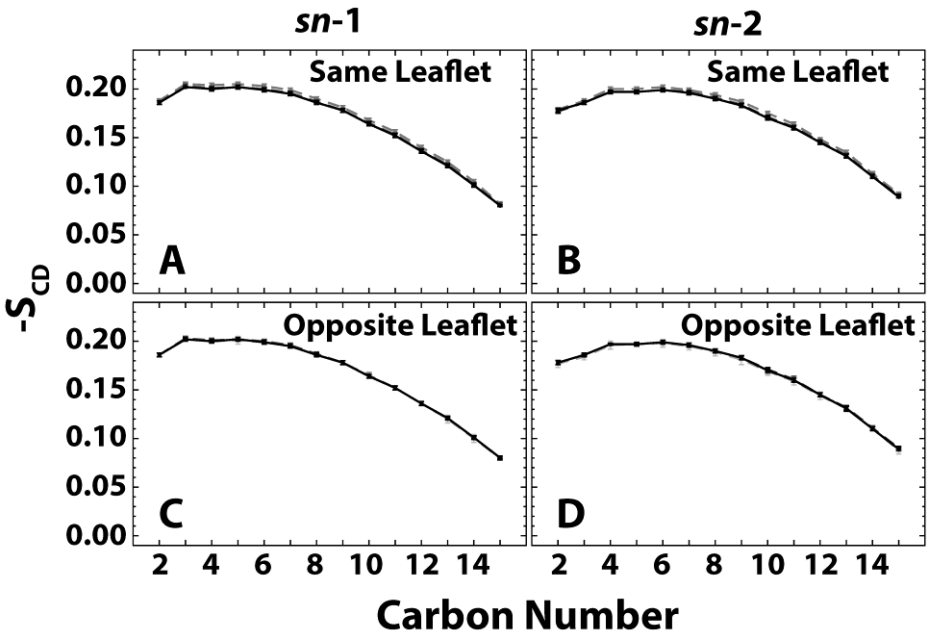

Figure A.1 Order parameter by shell for a pure DPPC bilayer reveals a partitioning artifact. Order parameter of DPPC carbons shown for A,B) same leaflet lipids and C,D) opposite leaflet lipids for a pure DPPC bilayer. Shells $n \leq 3$ are shown (gray dashed) with darker grays indicating increasing shell number. Overall average order for the pure DPPC bilayers (black solid) is shown for comparison. For same leaflet lipids, first shell order is marginally increased due to the partitioning scheme, while opposite leaflet lipids are unaffected.

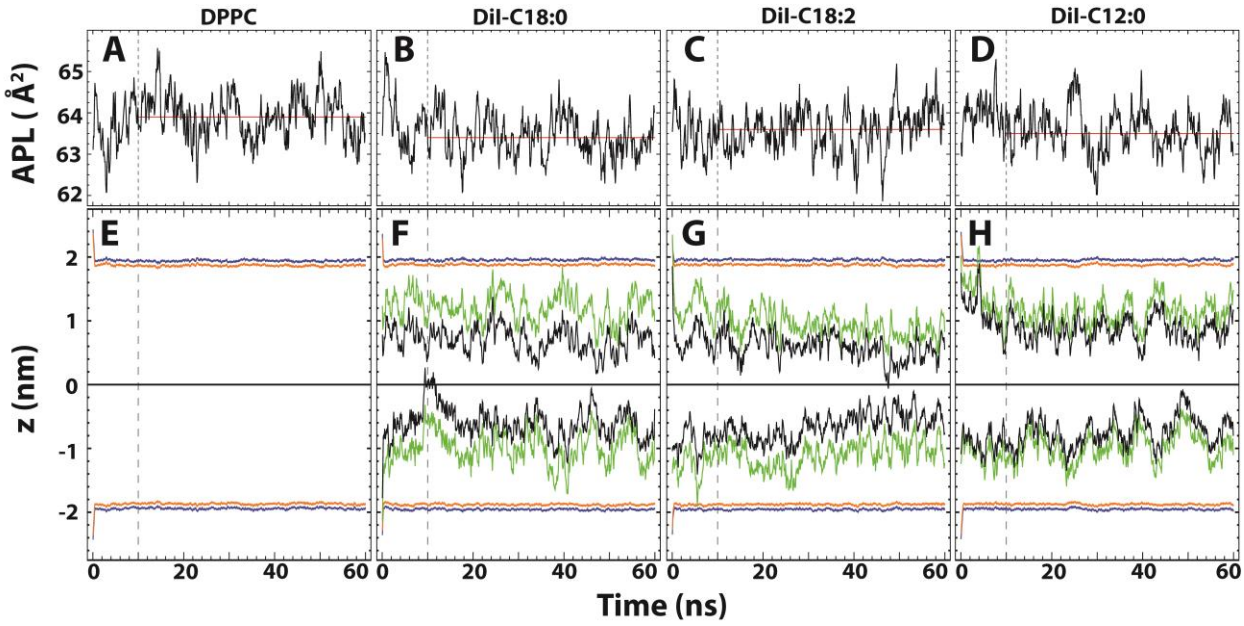

Figure A.2 Representative data showing equilibration of pure DPPC and DiI-containing, simulations. A-D) APL during a representative 60 ns simulation of the systems studied. The average value over the final 50 ns is shown (red line). E-H) transverse bilayer position with respect to the bilayer midplane (z = 0 nm) of DPPC nitrogen (blue) and phosphate (yellow), and center-of-mass of the DiI chromophore (green) and entire DiI molecule (black).

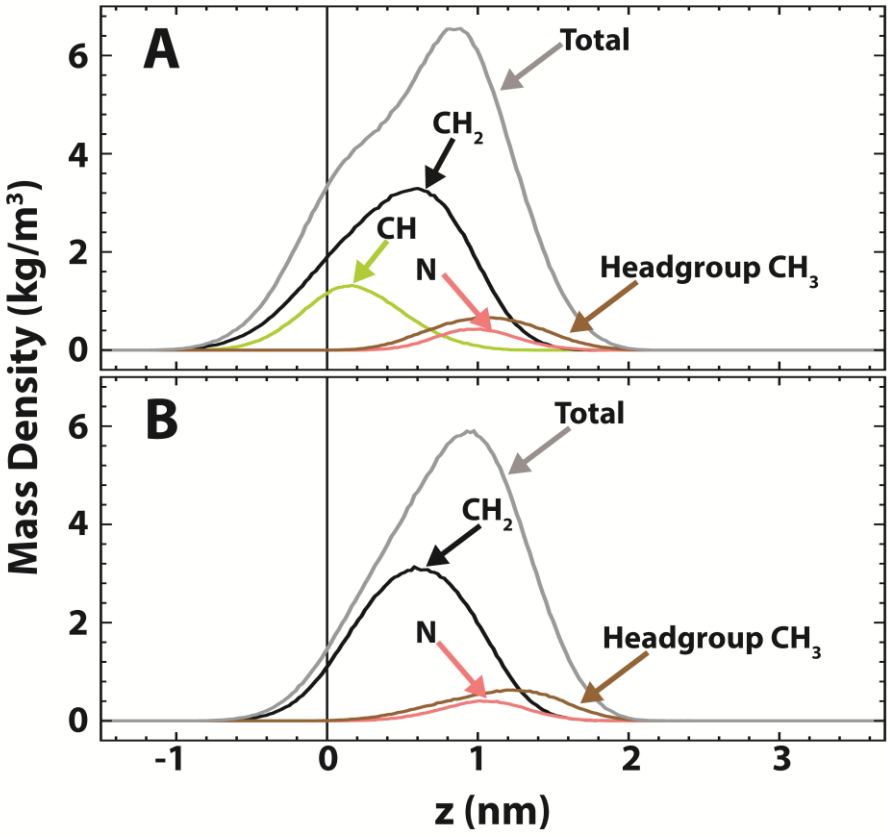

Figure A.3 Average single-leaflet mass density profiles for simulations. A) Average densities of DiI-C18:2 components. B) Average densities for DiI-C12:0 components. Bilayer midplane at z = 0 nm.

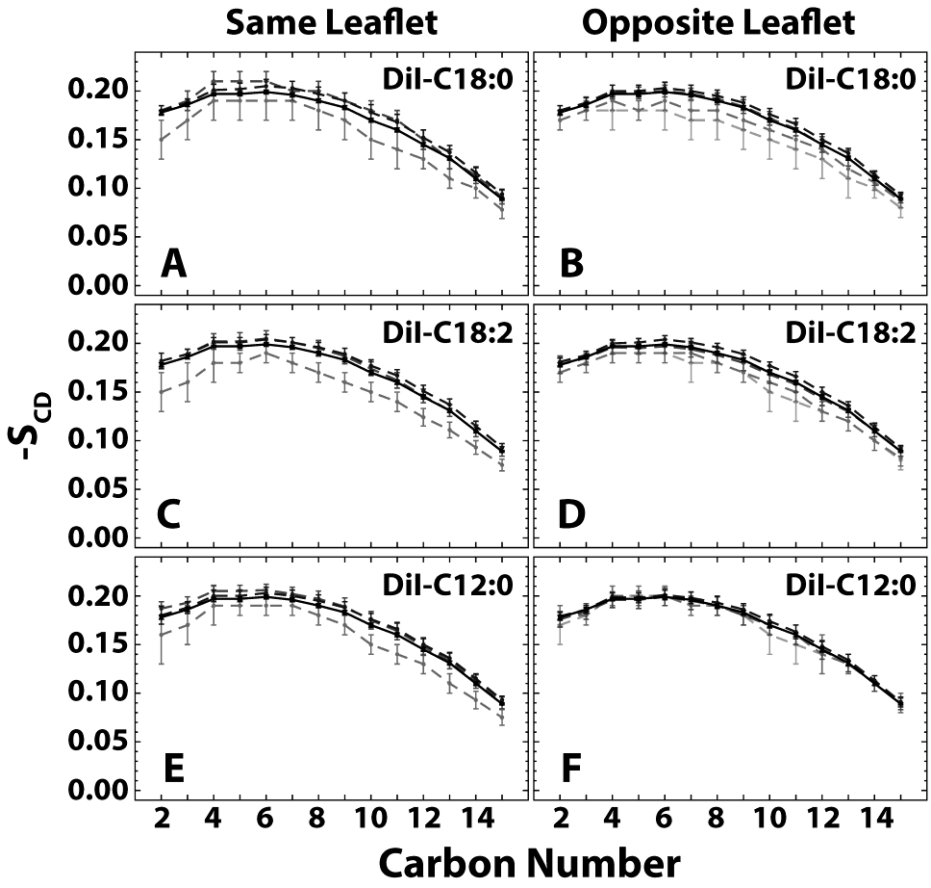

Figure A.4 DPPC *sn*-2 carbon order perturbation depends on shell, not carbon number. Order parameter of DPPC *sn*-2 carbons shown for same leaflet lipids (left) and opposite leaflet lipids (right) for bilayers containing A,B) DiI-C18:0, C,D) DiI-C18:2 and E,F) DiI-C12:0. Shells $n \leq 3$ are shown (gray dashed), with darker grays indicating increased shell number. Overall average *sn*-2 order for pure DPPC bilayers (black solid) is shown for comparison. Error bars indicate the standard deviation.

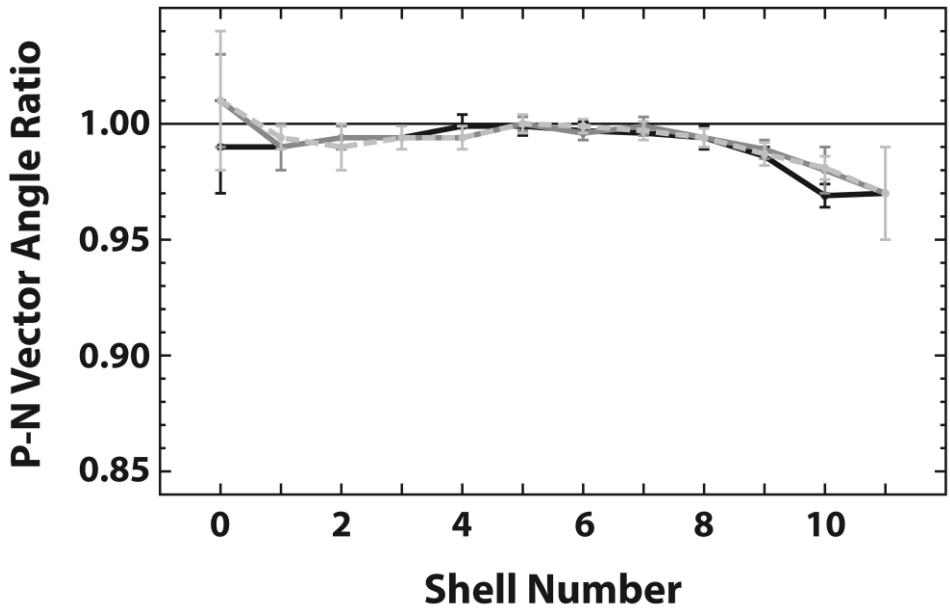

Figure A.5 DPPC headgroups show no preferential orientation in the leaflet opposite the probe. P-N vector angle ratio by shell for opposite leaflet lipids in bilayers containing DiI-C18:0 (black), DiI-C18:2 (dark gray) and DiI-C12:0 (light gray dashed) compared to the pure DPPC simulations. Error bars indicate 95% confidence intervals.

APPENDIX B
Supporting information for Chapter 3

B.1 Bilayer construction

For each value of ρ, a template CG bilayer was created in the xy plane by randomly distributing 128 lipids (64 per leaflet) at the chosen concentrations. 1,024 CG waters (8 per lipid) were placed outside the bilayer to ensure full hydration of the system. Energy minimization was then performed, followed by a series of equilibration steps at 295 K and 1 atm. During the first equilibration step of 5 ns, one bead per lipid was position-restrained in the z-dimension. This prevented lipid flip-flop and preserved leaflet compositional symmetry. Position restraints were then removed, and the system was further equilibrated for 20 ns. The bilayer patch was then tiled 6 x 6 times in the xy plane to produce the final system size. The resultant 4,608-lipid membrane underwent a final equilibration for 20 ns. The equilibrated, full-size CG system was then run at 295 K and 1 atm for 25 μs, allowing sufficient time for phase separation to occur, as discussed in Section 3.3.4.

The final CG states at 25 μs were then converted to UA using Backward (1), which maintains lipid lateral organization and replaces each CG bead with the united atoms it represents. It also replaces each CG water with 4 UA waters. Mappings of PUPC and DUPC (required for the conversion) were not available and were created by combining and modifying appropriate parts of the available DPPC and DOPC mappings. After conversion, the UA systems were run for 200 ns at 300 K and 1 atm (as done in reference (2)).

For force fields and general simulation parameters, see Sections 3.3.1 and 3.3.2.

B.2 Data aquisition

To determine when the systems became equilibrated, we tracked the CG phase interface length and UA box size over the course of the simulations, for all 11 ρ values (Figure B.1). All CG and UA systems were essentially equilibrated by 15 μs and 50 ns, respectively. Analysis was only performed after systems were equilibrated.

To acquire meaningful statistics we split the simulations into independent subsets in time. The minimum length of time for a subset should be longer than the autocorrelation times of the properties of interest. We plot the time autocorrelations of various properties discussed throughout Chapter 3 for both CG systems (Figure B.2) and UA systems (Figure B.3) for $\rho = 1$. We used $\rho = 1$ as the test case for correlation as it is expected to have the slowest correlations due to the large domain sizes and high order in the $\rho = 1$ simulations.

For $\rho = 1$, the CG interface length and misaligned phase overlap fraction become sufficiently uncorrelated by 250 ns. The UA order and tilts become sufficiently uncorrelated by 25 ns. Thus each CG simulation could be split into independent subsets of 250 ns each, and likewise the UA simulations could be split into independent subsets of 25 ns each.

Averages and error bars as standard deviations were calculated from these independent traces, with each leaflet considered an independent set of data where applicable. In figures where error bars are not shown, averages were simply calculated over every 25 ns for CG simulations and every 1 ns for UA simulations.

Where properties are binned as a function of distance to the phase interface (Figures 3.6, 3.8, B.6, B.8, B.10-14 and B.16), bins are only included if they contain data from each of the independent subsets. Additionally, lipids farther than or equal to 5.5 nm from the interface are

included in the 5.5 nm bins. Large error bars for low-Tm lipids in the Lo phases — and DPPC and cholesterol in the Ld phase — are in part due to the paucity of those lipids in those phases.

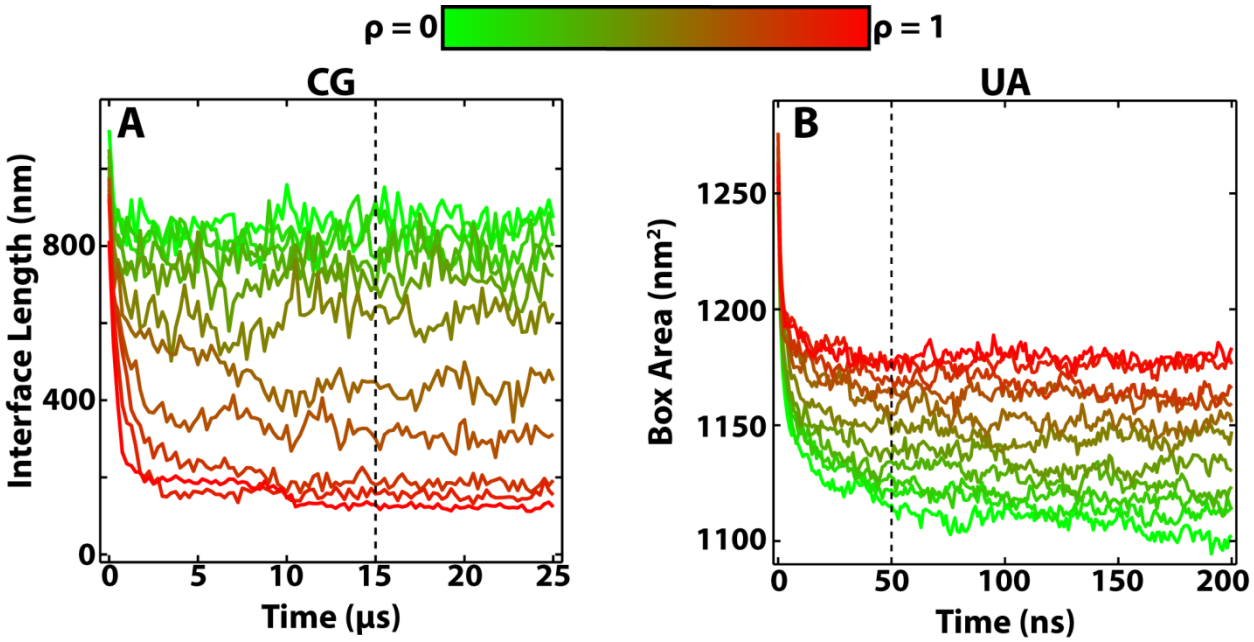

Figure B.1 Equilibration of simulations was determined using leaflet phase interface length for CG systems and box area for UA systems. A) The phase interface length from ρ = 0 (green) to ρ = 1 (red) for the CG systems reached equilibrium within 15 μs (vertical dashed line). B) The box area from ρ = 0 (green) to ρ = 1 (red) for the UA simulations reached equilibrium within 50 ns (vertical dashed line).

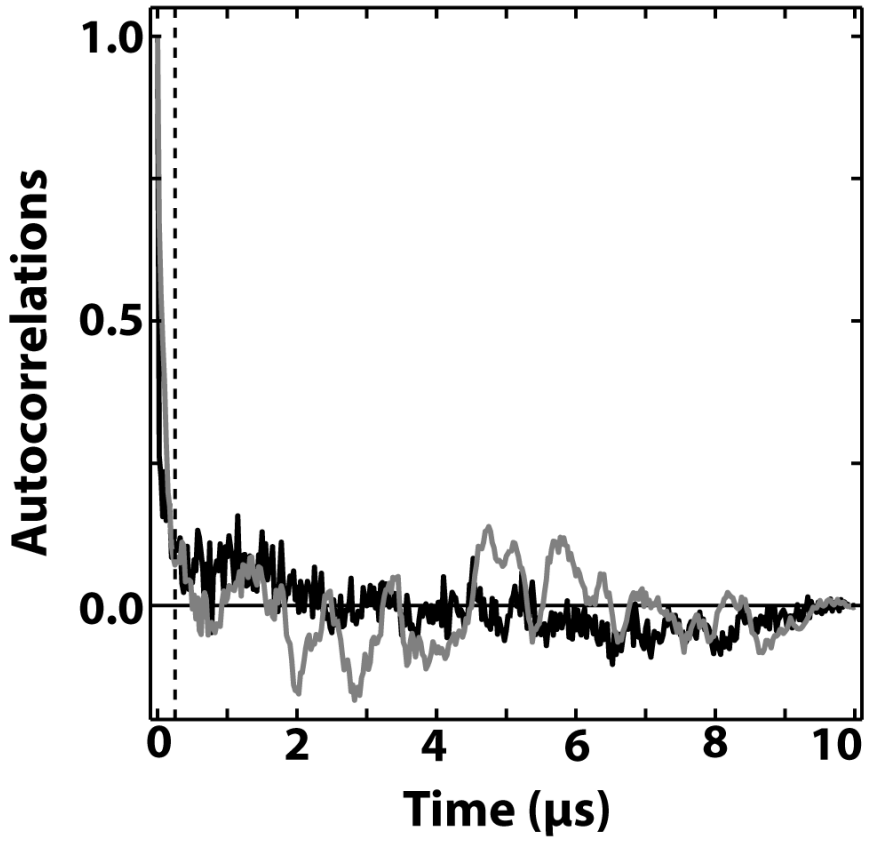

Figure B.2 Bulk CG phase properties become uncorrelated after 250 ns. The time autocorrelation for normalized interface length (black) and normalized misaligned phase overlap fraction (gray) for $\rho = 1$, calculated over the last 10 μs of run time. They are essentially uncorrelated by 250 ns (vertical dashed line).

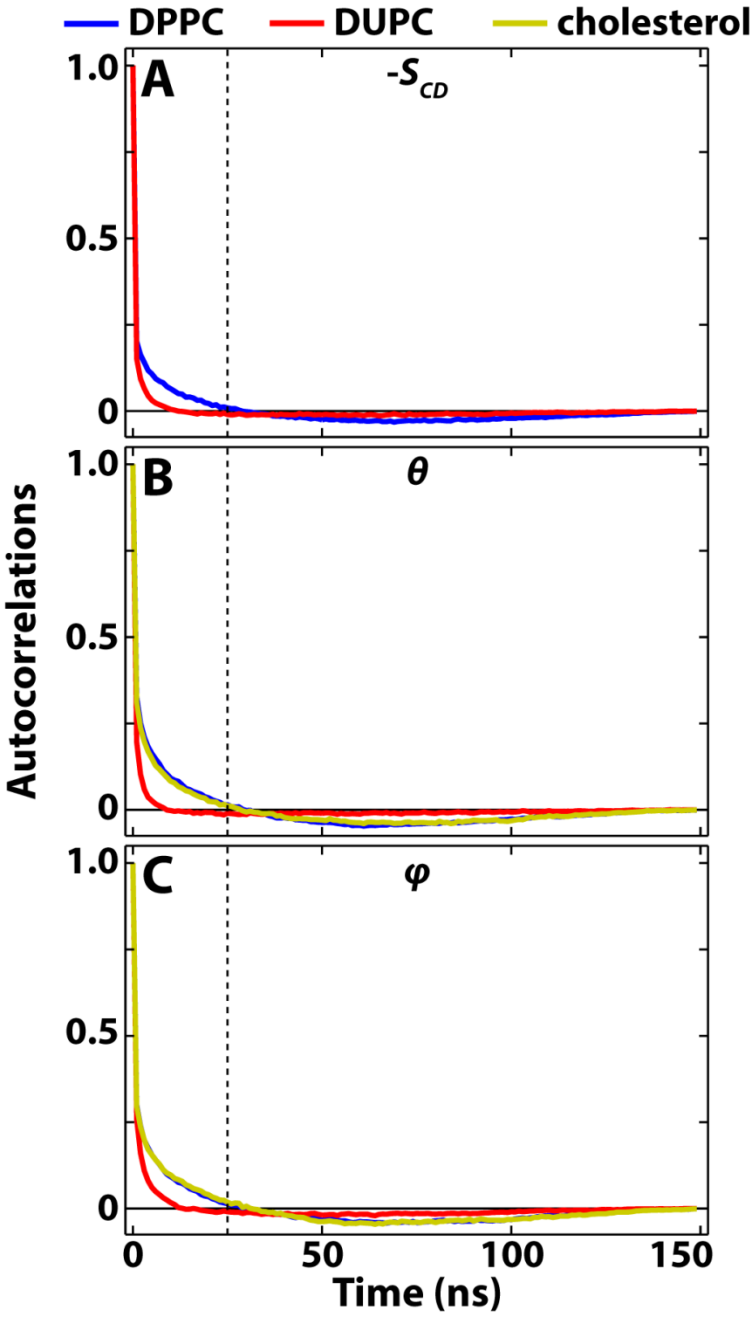

Figure B.3 Autocorrelations for different UA lipid parameters decrease significantly by 25 ns. All curves are averages over the autocorrelations of individual lipids for ρ = 1, calculated over the last 150 ns of runtime. Results shown for DPPC (blue), DUPC (red) and cholesterol (yellow). A) $-\boldsymbol{S_{CD}}$, and the tilt angles B) $\boldsymbol{\theta}$ and C) $\boldsymbol{\varphi}$ as defined in Figure 3.8A are each essentially uncorrelated by 25 ns (vertical dashed line) for all lipids. However, the Lo lipids DPPC and cholesterol take longer to become uncorrelated as compared to DUPC. All show some indication of anticorrelation at longer times.

B.3 Cholesterol artifact

For ρ ~ 0.9 and 1, $g(r)$ and $g_{1,2}(r)$ of Lo chains and cholesterol show a persistent periodicity that extends for more than 10 nm, apparent in Figure B.4*A,B*. This appears after large domains begin to form. Additionally, we find that at high ρ, the CG Lo phase has slow and concerted diffusion (data not shown). These properties are characteristic of a gel, not a liquid. It is therefore appropriate for the high ρ "Lo phases" to be considered gel. We have seen this gelation with various versions of the Martini force field (data not shown); it is a known issue and is currently being fixed by the developers (Siewart-Jan Marrink, personal communication). In fact, a newly developed CG cholesterol available at http://md.chem.rug.nl/cgmartini/index.php/force-field-parameters/sterols seems to prevent this gelation. Even with the current cholesterol, no such gelation is observed in the Ld phase (Figure B.4*C,D*).

In this study we are interested in trends in phase separation, so distinction between a gel and a liquid that appear only after large-scale phase separation has begun is inconsequential to the CG results. Importantly, strong persistent correlations are not present after conversion to UA (Figure B.5), likely due to the extra equilibration that allows lipids to move and disrupt long-range correlations. Thus the UA results are also unlikely to be affected by the CG artifact, aside from any effect of the artifact on equilibrium lipid distributions, which we do not expect to significantly alter results.

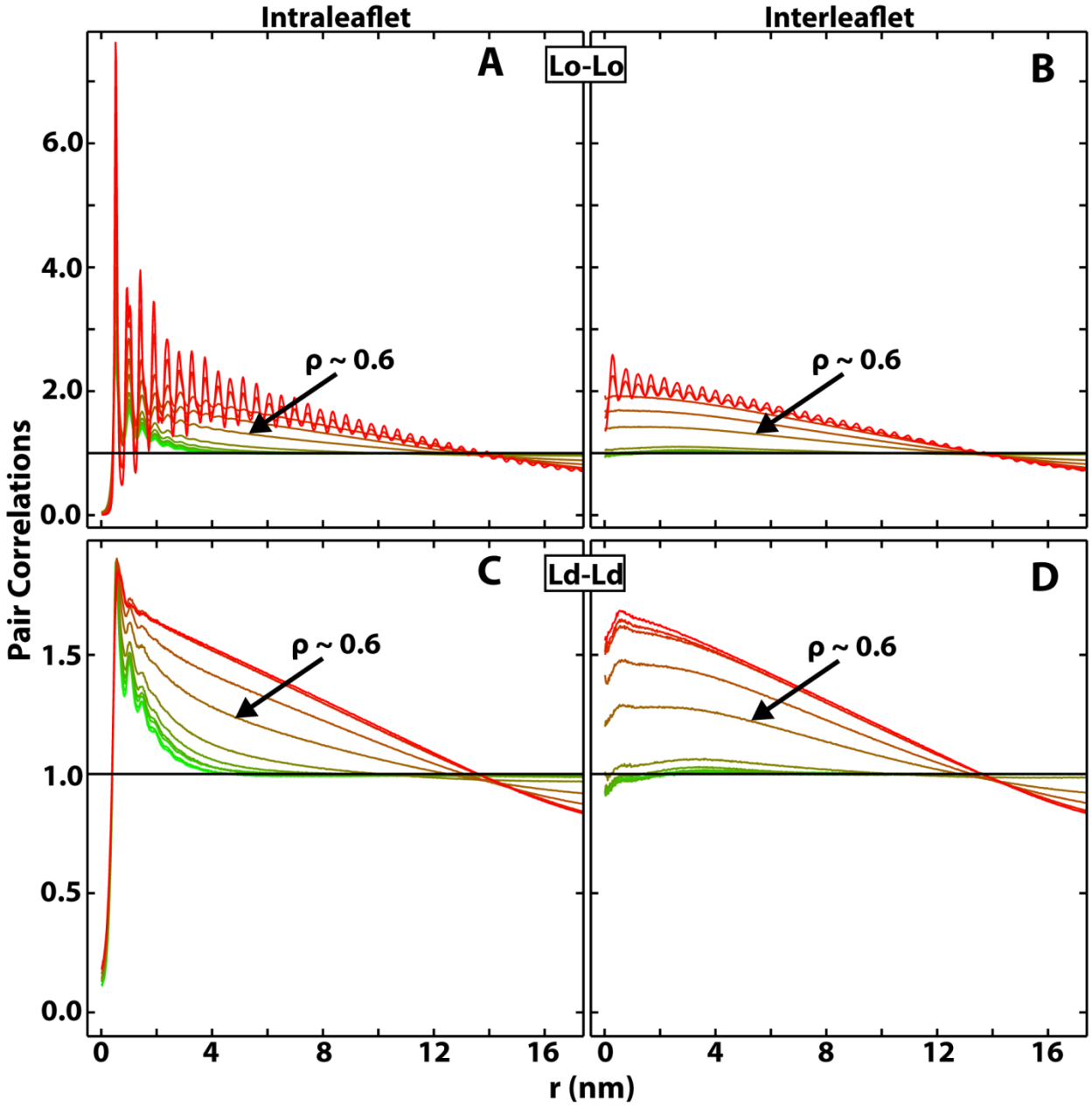

Figure B.4 CG pair correlation functions describe size and alignment of domains. Pair correlation functions were calculated using chain centers of mass for PCs, and molecular centers of maass for cholesterol, with $\Delta \boldsymbol{r}$ = 0.025 nm. Data shown for ρ = 0 (green) to ρ = 1 (red). A,C) Intraleaflet correlations and B,D) interleaflet correlations increase significantly for ρ > 0.5, indicating increased domain size and alignment as ρ increases. Note that Lo-Lo correlations for large ρ show a periodicity that persists for more than 10 nm, both A) within a leaflet and B) between leaflets. These correlations are artifacts of the Martini model Lo phase due to the cholesterol used. (Bottom) Ld-Ld correlations show no persistent correlations C) within leaflets or D) between leaflets.

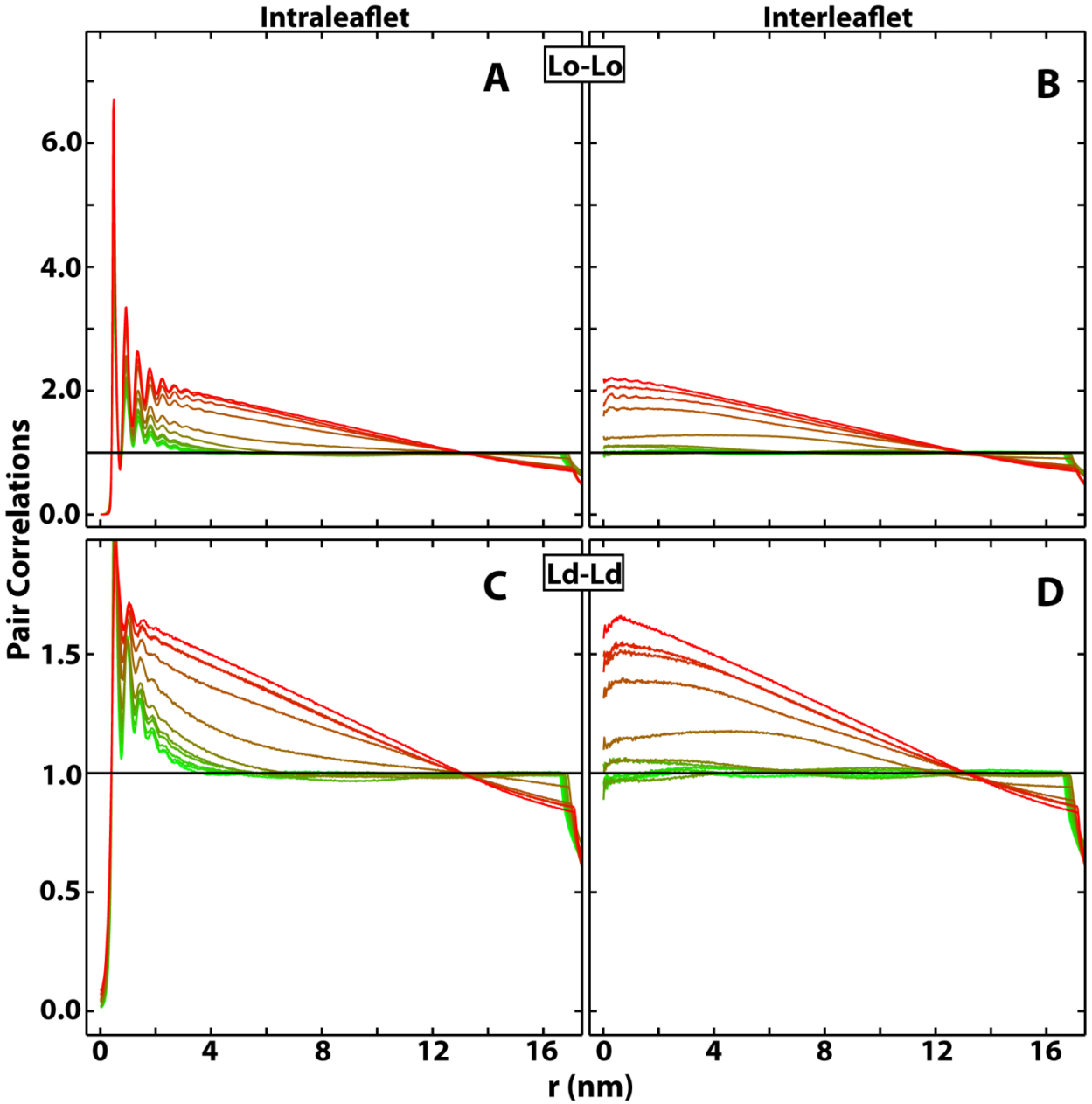

Figure B.5 Correlation functions for UA simulations are consistent with liquid phases. Correlation functions were calculated using chain centers of mass for PCs, and molecular centers of mass for chol, with $\Delta \boldsymbol{r}$ = 0.025 nm. A-B) Lo-Lo correlations and C-D) Ld-Ld correlations do not have significant extended periodicity.

B.3 Order parameter

In Figure B.6, we plot the UA order parameter $-S_{CD}$ averaged over all methylenes in the acyl chains of the PC lipids, as a function of distance to the interface. While the PCs have different equilibrium orders, they all reach equilibrium within ~ 2 nm of the phase interface. This is true throughout the ρ-trajectory, even though the difference in equilibrium order between the Lo and Ld phases increases with ρ.

We also see that no particular location on the acyl chains of the PC lipids is significantly more perturbed than any other (Figure B.7). Indeed, on average, lipids adjust to the difference in equilibrium order between Lo and Ld phases through a nearly uniform change in order along their acyl chains.

For comparison, we plot the corresponding CG order parameters in Figures B.8 and B.9. CG order parameter, S_z, is calculated as in reference (3):

$$S_z = \langle 3\cos^2\alpha - 1\rangle/2 \qquad \text{(B.1)}$$

where α is the angle between a bond in the acyl chain of a lipid and the bilayer normal, taken to be along the z-axis. This was calculated for the last three bonds in the acyl chains. Changes in CG order are qualitatively very similar to those in UA order.

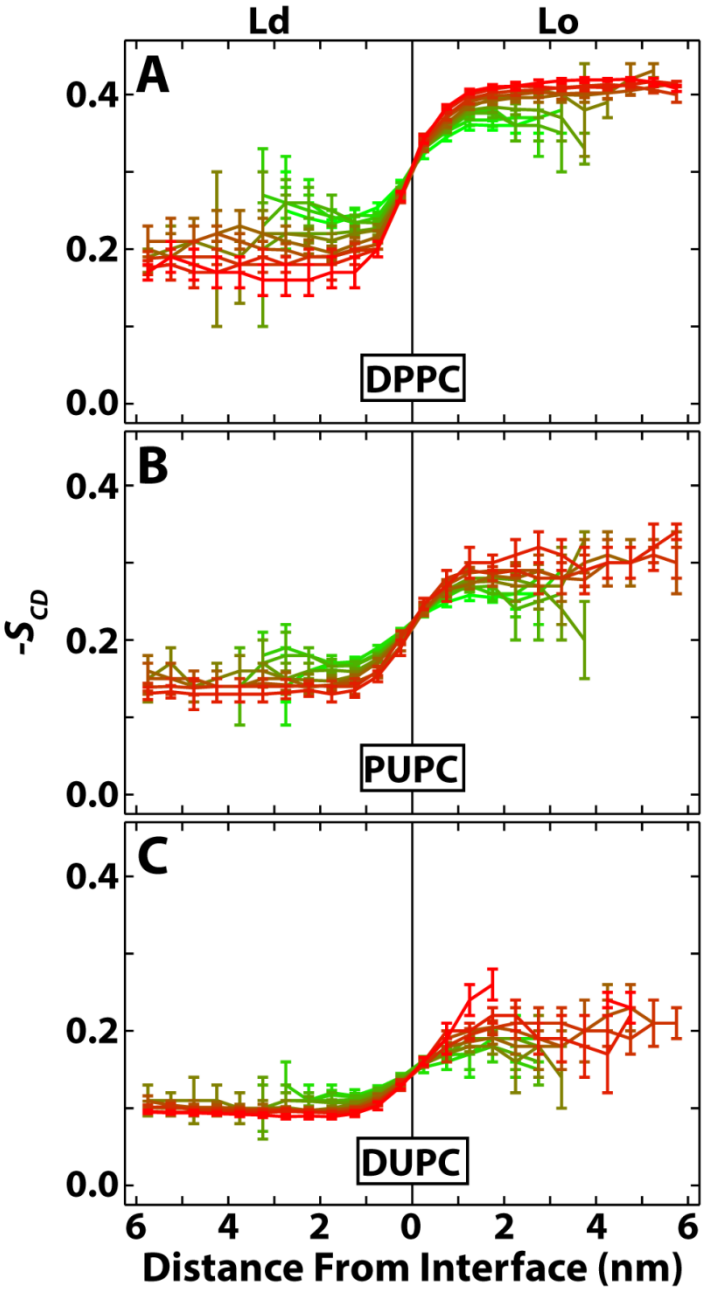

Figure B.6 The order of all UA PCs is only perturbed within ~ 2 nm from the interface into each phase. $-S_{CD}$ averaged over all methylenes in both chains of A) DPPC, B) PUPC and C) DUPC as a function of distance from the phase interface. Colors correspond to ρ values from ρ = 0 (green) to ρ = 1 (red). PCs in both phases reach equilibrium within ~ 2 nm of the interface, regardless of ρ.

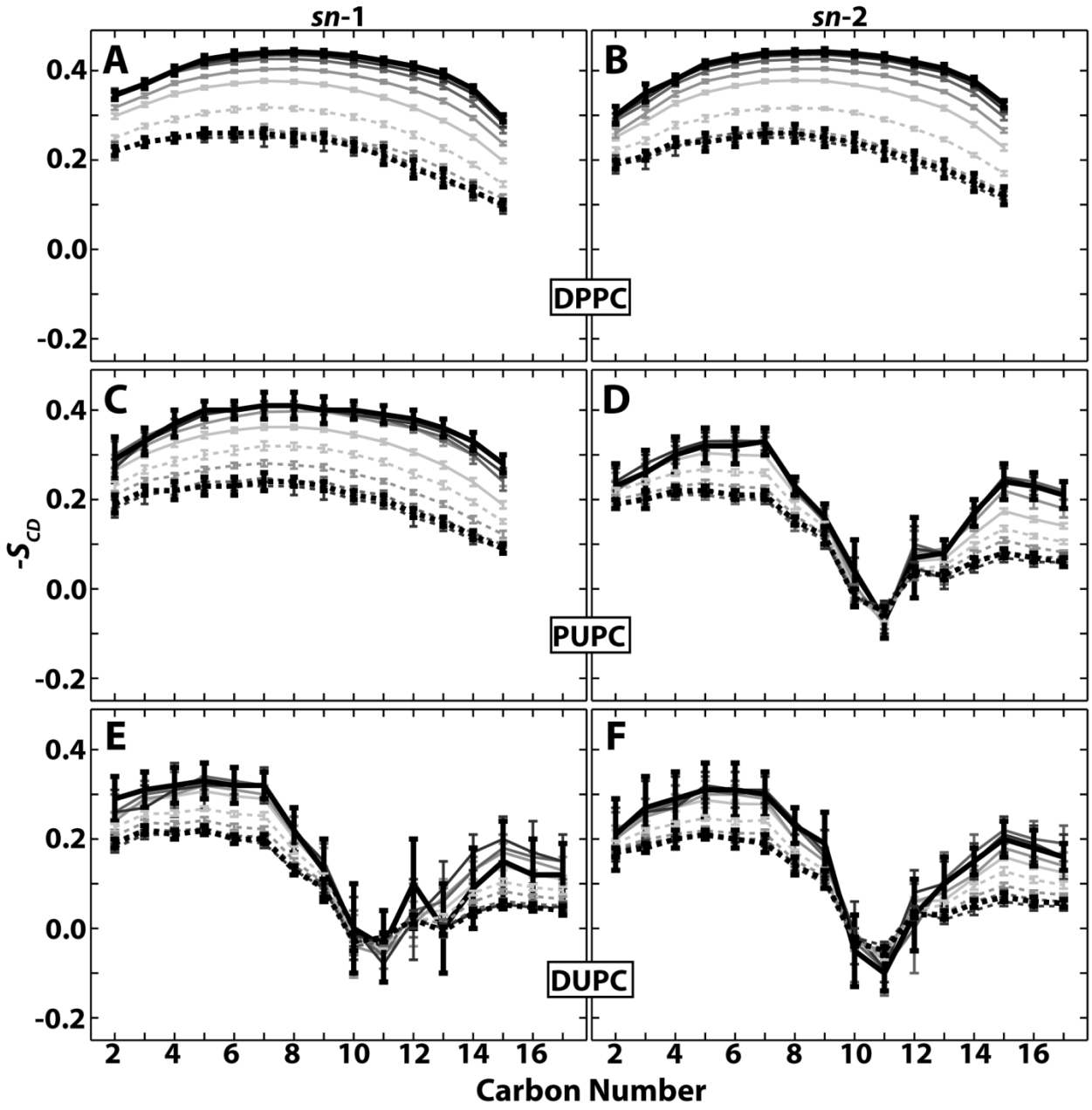

Figure B.7 UA DPPC, PUPC and DUPC carbons are nearly uniformly perturbed regardless of phase or distance from the phase interface. Order parameters are plotted for PC *sn*-1 and *sn*-2 carbons for Ld lipids (dashed) and Lo lipids (solid) with increasing darkness indicating increasing distance from the interface in increments of 0.5 nm. Thicker black curves are averaged over all PCs farther than or equal to 2 nm from the interface. Results shown for $\rho = 0.5$ for A,B) DPPC, C,D) PUPC and E,F) DUPC. The large variation in DUPC carbon order in the Lo phase is due to the few DUPCs in that phase.

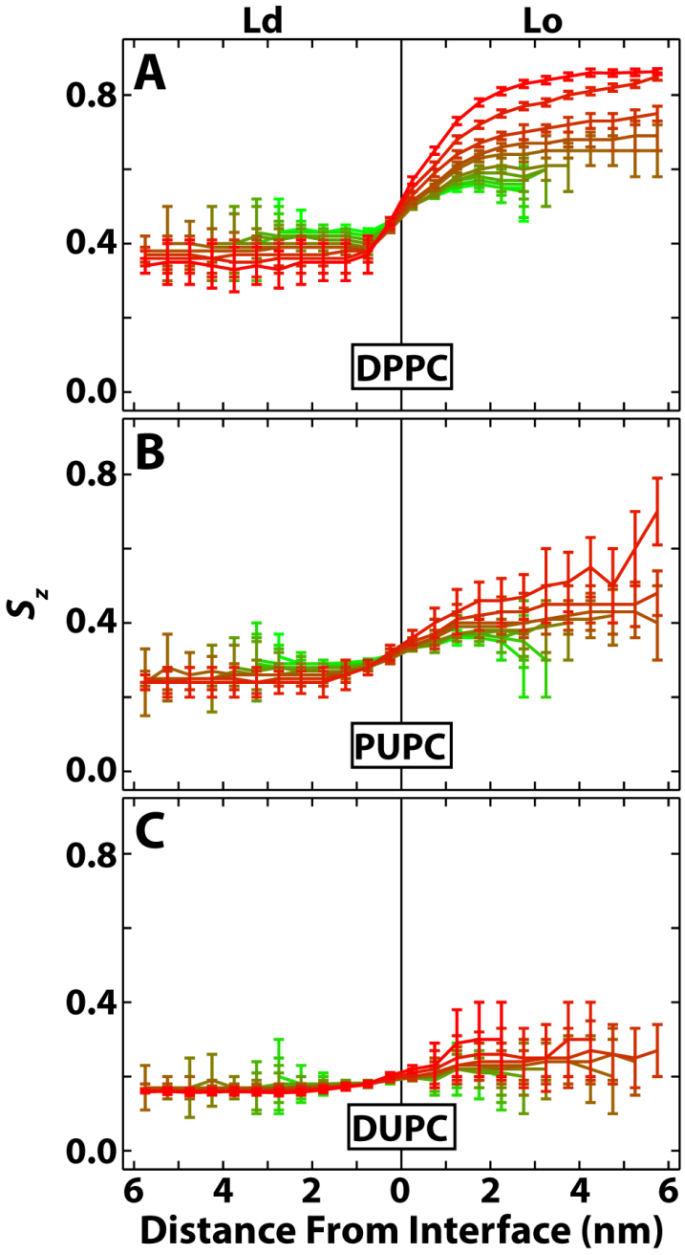

Figure B.8 The order of CG PCs in both phases reach equilibrium within ~ 2 nm of the interface, regardless of ρ. The order of all CG PCs is perturbed further into the Lo phase than the Ld phase.

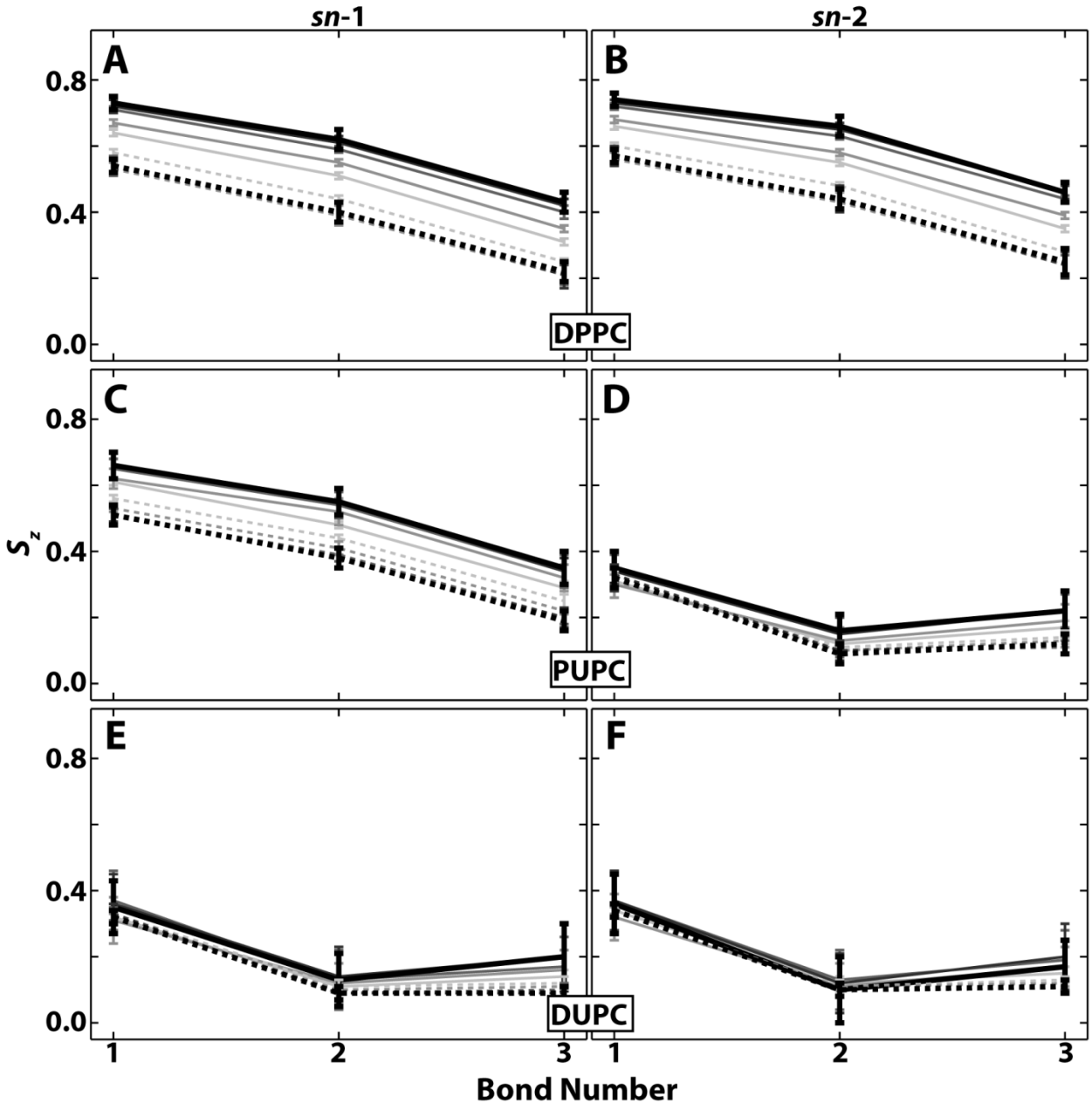

Figure B.9 CG DPPC, PUPC and DUPC saturated chains (A-C) are nearly uniformly perturbed regardless of phase or distance from the phase interface. Order parameters are plotted for PC *sn*-1 and *sn*-2 bonds for Ld lipids (dashed) and Lo lipids (solid) with increasing darkness indicating increasing distance from the interface in increments of 0.5 nm. Thicker black curves are averaged over all PCs farther than or equal to 2 nm from the interface. Results shown for $\rho = 0.5$ for A,B) DPPC, C,D) PUPC and E,F) DUPC.

B.4 Lipid tilts

The PC lipid tilt vector ($\vec{t}$) is defined in Section 3.4.5. $\vec{t}$ for cholesterol is along the long axis of cholesterol, joining atom C20 to atom C5 (4). The angle between $\vec{t}$ and the bilayer normal (θ) for all lipids reaches equilibrium within ~ 2 nm of the phase interface, regardless of equilibrium tilts in the Lo and Ld phases (Figure B.10). Compared to the other lipids, we also see that cholesterol tilts significantly more in the Ld phase.

The orientation of lipid tilt (φ) is defined to be the angle between $\vec{t}$ projected onto the xy plane and the vector pointing from the center of mass of the lipid to the nearest phase interface (see Figure 3.8*A*). φ for all lipids is plotted in Figure B.11. For higher ρ values, lipids near the interface in the Ld phase tend to tilt away from the interface (φ > 90°). Conversely, lipids near the interface in the Lo phase tend to tilt towards the interface (φ < 90°). At high ρ, the preferential orientation extends for several nanometers into the Lo phase. The extent and persistence of this preferred orientation is less significant at low ρ.

For comparison, we plot the corresponding CG tilt results in Figures S12 and S13. CG lipid tilts were calculated analogously to UA lipid tilts, as described in reference (4). θ behavior is qualitatively similar for CG and UA DPPC and cholesterol, but CG PUPC and DUPC show a smaller and almost negligible change in tilt than their UA counterparts. Conversely, φ behavior for CG and UA lipids differs both qualitatively and quantitatively. For instance, CG lipids in the Lo phase tilt *away* from the interface. We do not currently have an explanation for this difference in tilts, aside from the possibility that it is simply due to differences in the CG and UA force fields and lipid models.

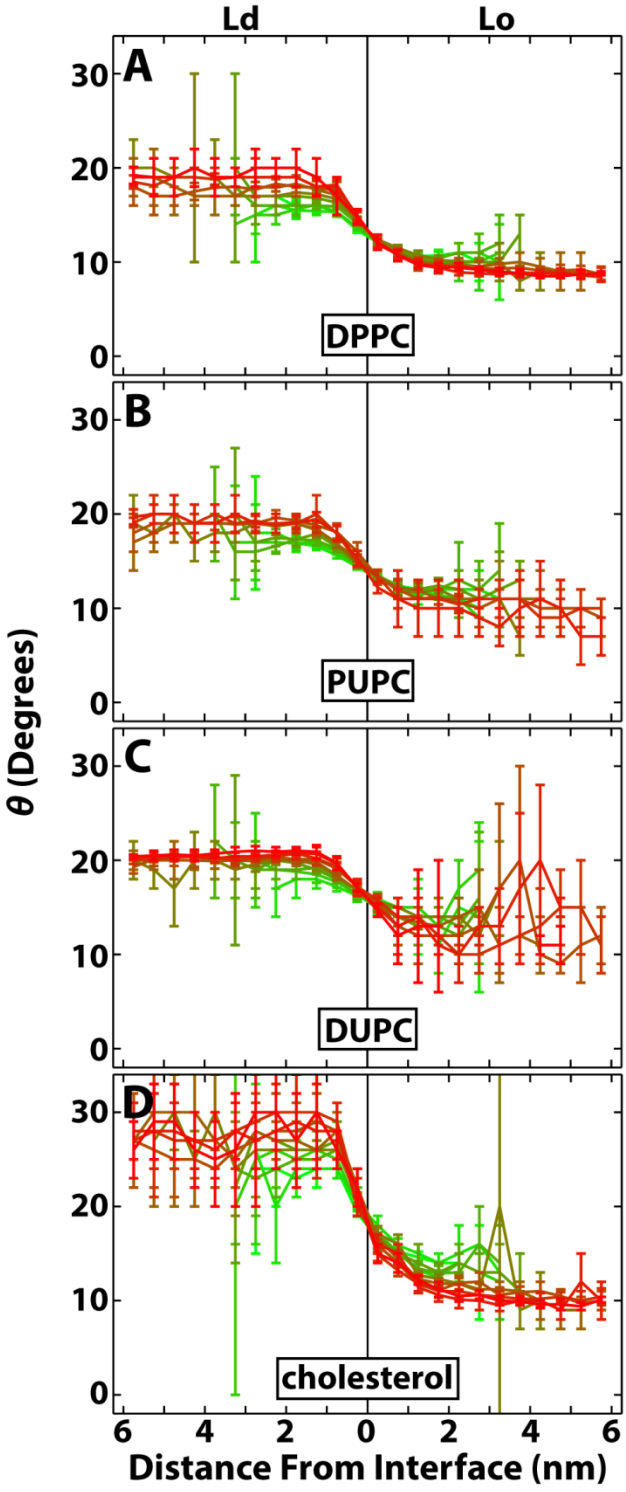

Figure B.10 All UA lipids tilt more in the Ld phase than in the Lo phase. The transition in $\boldsymbol{\theta}$ occurs over a span of ~ 2 nm into each phase. Results shown for A) DPPC, B) PUPC, C) DUPC and D) cholesterol from $\rho = 0$ (green) to $\rho = 1$ (red).

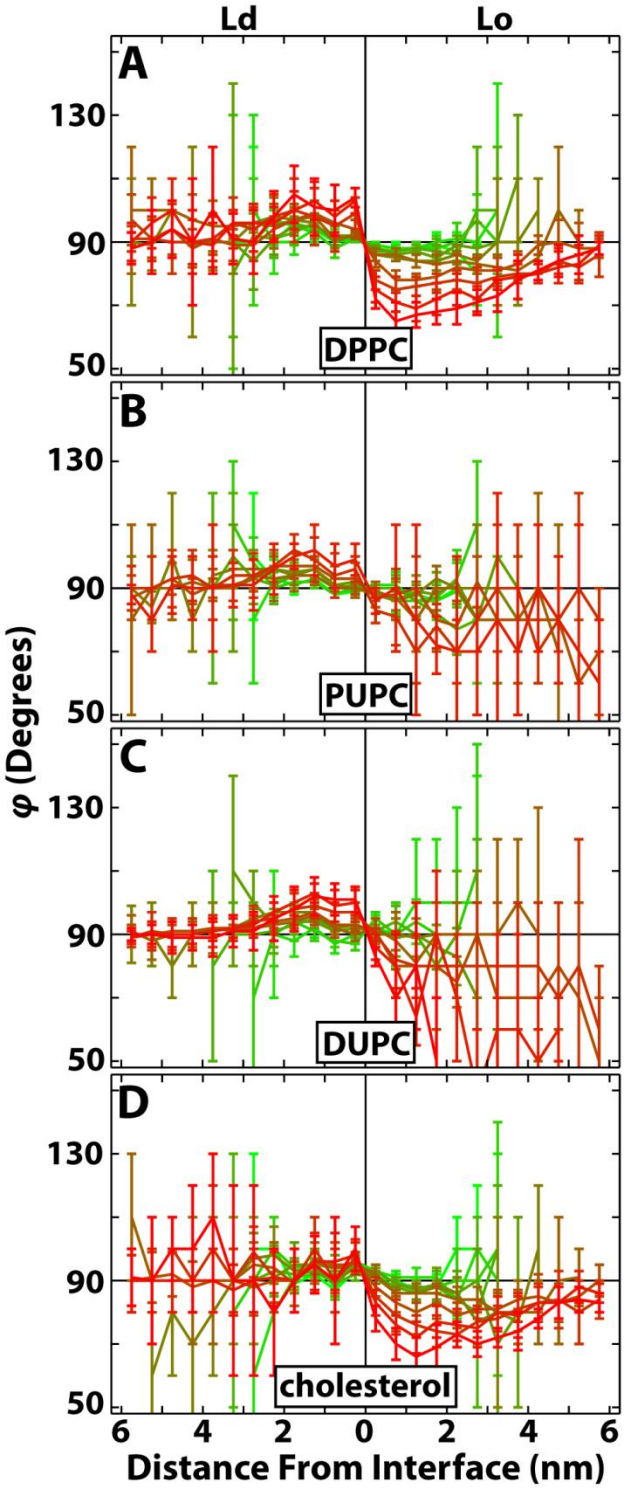

Figure B.11 UA lipids tilt toward the Ld phase. Near the interface, lipids tilt away from the interface in the Ld phase ($\varphi > 90°$) but towards the interface in the Lo phase ($\varphi < 90°$). Results shown for A) DPPC, B) PUPC, C) DUPC and D) cholesterol from $\rho = 0$ (green) to $\rho = 1$ (red).

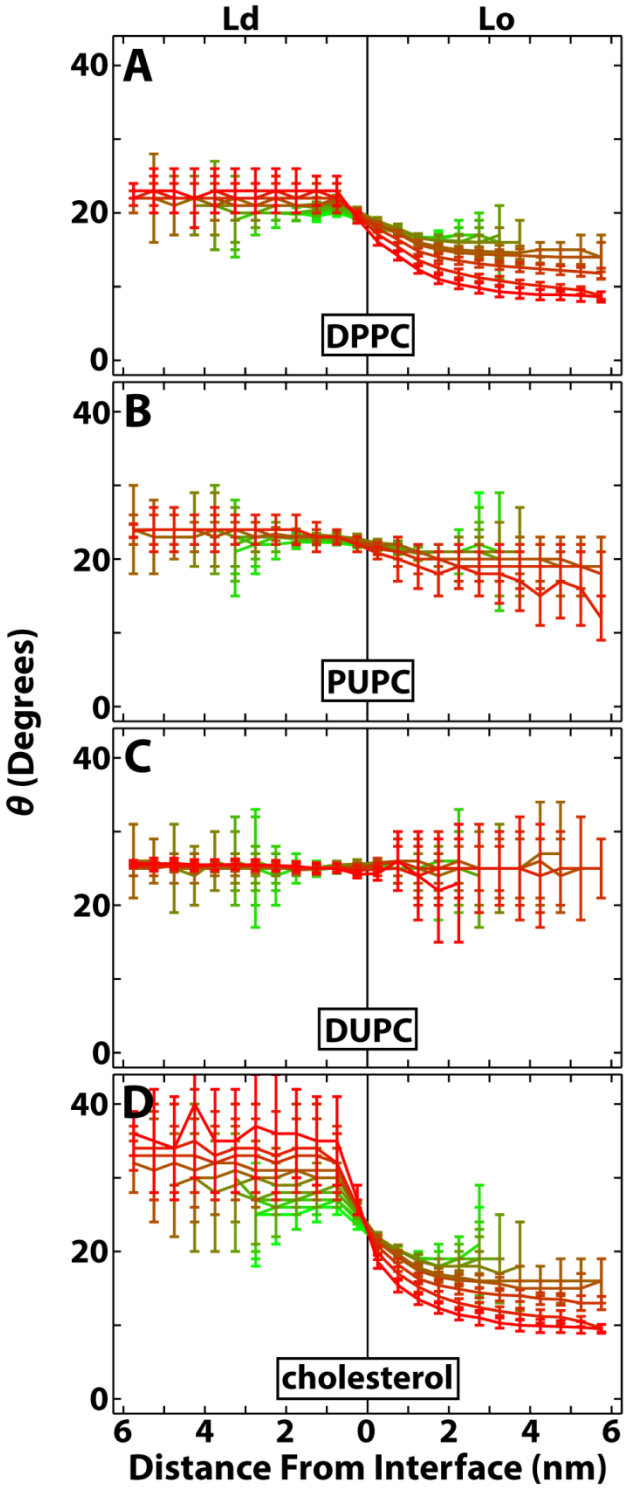

Figure B.12 CG DPPC and cholesterol tilt more in the Ld phase than in the Lo phase, while PUPC and DUPC tilts are more constant. The $\boldsymbol{\theta}$ transition for DPPC and cholesteroloccurs over a short distance into each phase. Results shown for A) DPPC, B) PUPC, C) DUPC and D) cholesterol from $\rho = 0$ (green) to $\rho = 1$ (red).

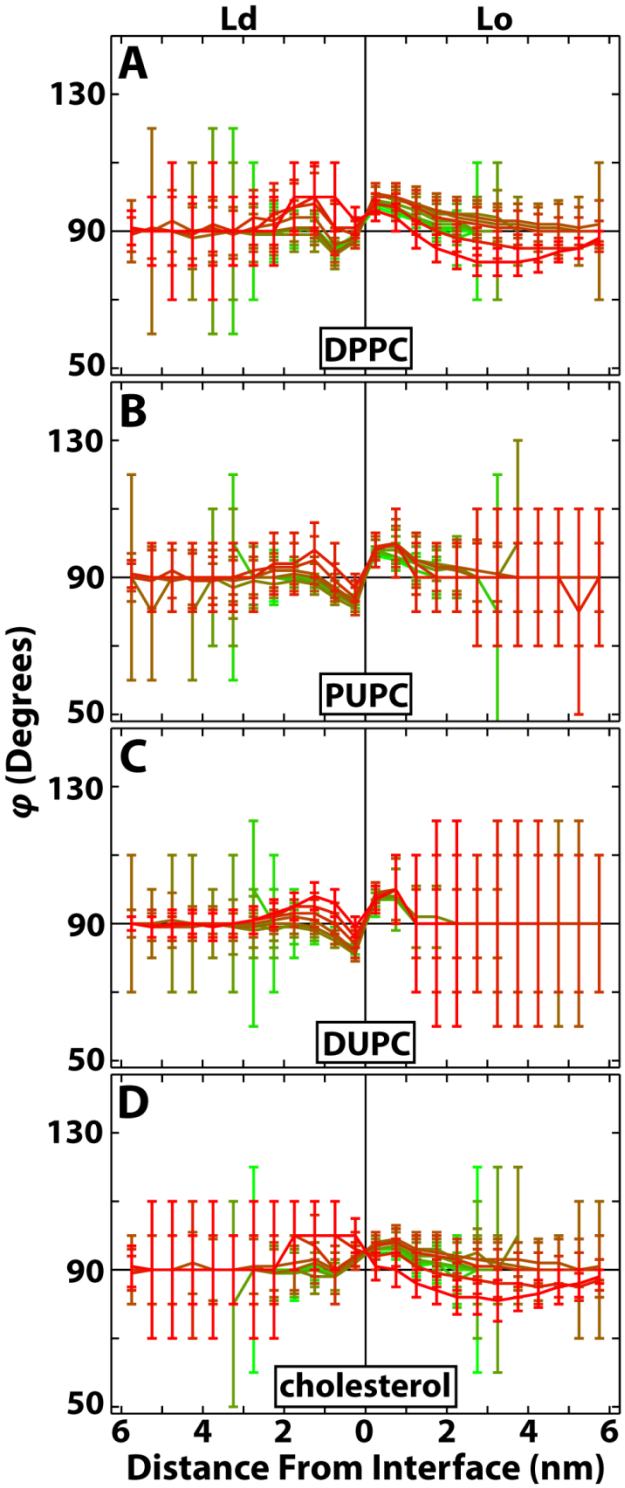

Figure B.13 CG lipid tilt orientation differs from corresponding UA lipid tilt orientation. Near the interface, CG lipids tilt away from the interface in the Lo phase ($\varphi > 90°$), while behavior in the Ld phase show lipids tilt both towards and away from the interface. Results shown for CG lipids A) DPPC, B) PUPC, C) DUPC and D) cholesterol from $\rho = 0$ (green) to $\rho = 1$ (red).

B.5 Lipid thickness and unsaturation locations

Thickness mismatch between coexisting phases could be an important factor in phase morphology. As an analog for monolayer thickness, we plot CG lipid thickness in Figure B.14. Here we define CG lipid thickness as the maximum distance between the PO4 headgroup bead and any other bead in the lipid, measured along the bilayer normal; a distance is positive (negative) if the PO4 bead is further from (closer to) the bilayer center than the other bead. As ρ increases, the lipid thickness difference between Lo and Ld phases increases. This implies that the monolayer thickness difference between Lo and Ld phases also increases with ρ. An increasing CG monolayer thickness difference with ρ is also evident in the mass density profiles of the Lo and Ld phases (Figure B.15*A*). As ρ increases, the overall Lo mass density becomes thicker and the overall Ld mass density becomes thinner: the thickness difference between the phases increases with ρ. In addition to an increasing thickness mismatch with ρ, the density of unsaturations in the Lo (Ld) phase decreases (increases) with ρ (Figure B.15*B*).

We note that the mass densities, measured with respect to the z-coordinate of the local bilayer center of mass, are likely convoluted with the fact that the Lo and Ld domain alignment increases along the ρ-trajectory. Since the thickness and mass density profile of the two phases differ, the z-coordinate of the local bilayer center of mass will inherently vary depending on alignment of the phases. We do not account for this, but the lipid thickness provides further support that the Lo phase becomes thicker while the Ld phase becomes thinner along a ρ-trajectory.

UA lipid thicknesses are plotted in Figure B.16. While the lipid thickness difference, and in turn monolayer thickness difference, between Lo and Ld phases increases with ρ for all PC lipids, equilibrium is always reached within 2 nm of the phase interface.

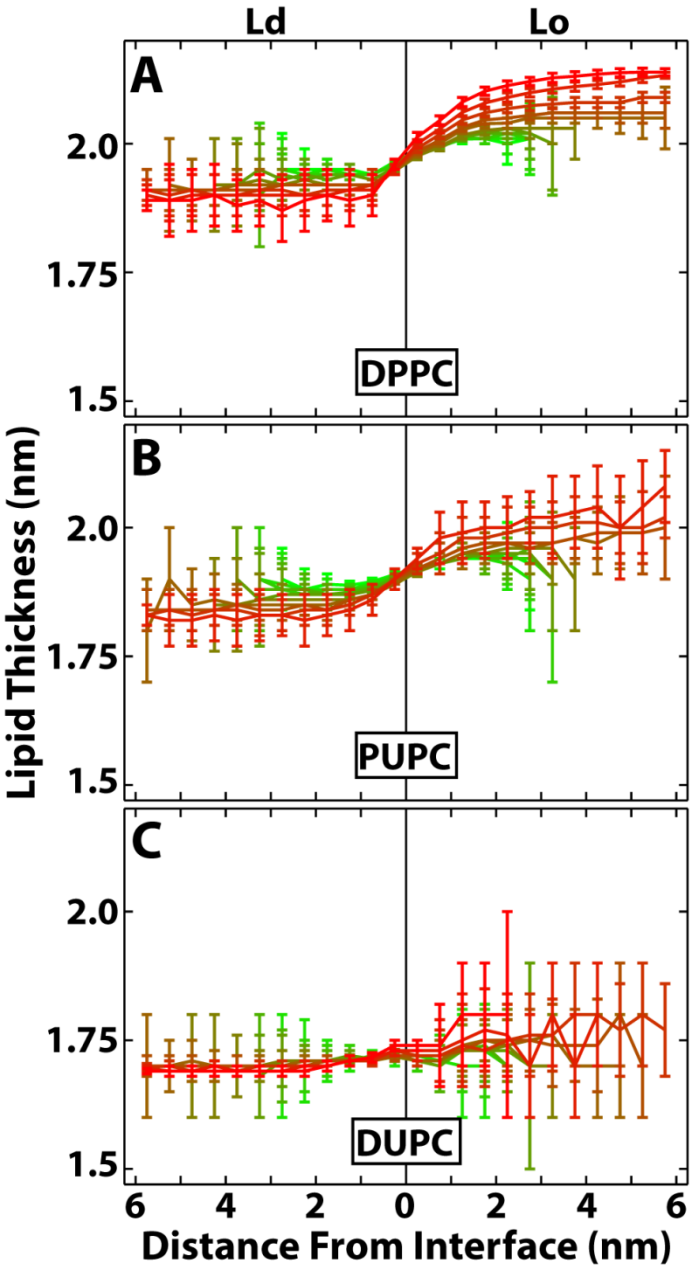

Figure B.14 CG lipid thickness mismatch increases with ρ. Lipid thickness is defined as the largest distance between the PO4 headgroup bead and any other bead in the lipid, measured along the bilayer normal, with positive distances being those with the PO4 bead further from the bilayer center than the other bead (and vice versa). Results shown for A) DPPC, B) PUPC and C) DUPC from ρ = 0 (green) to ρ = 1 (red).

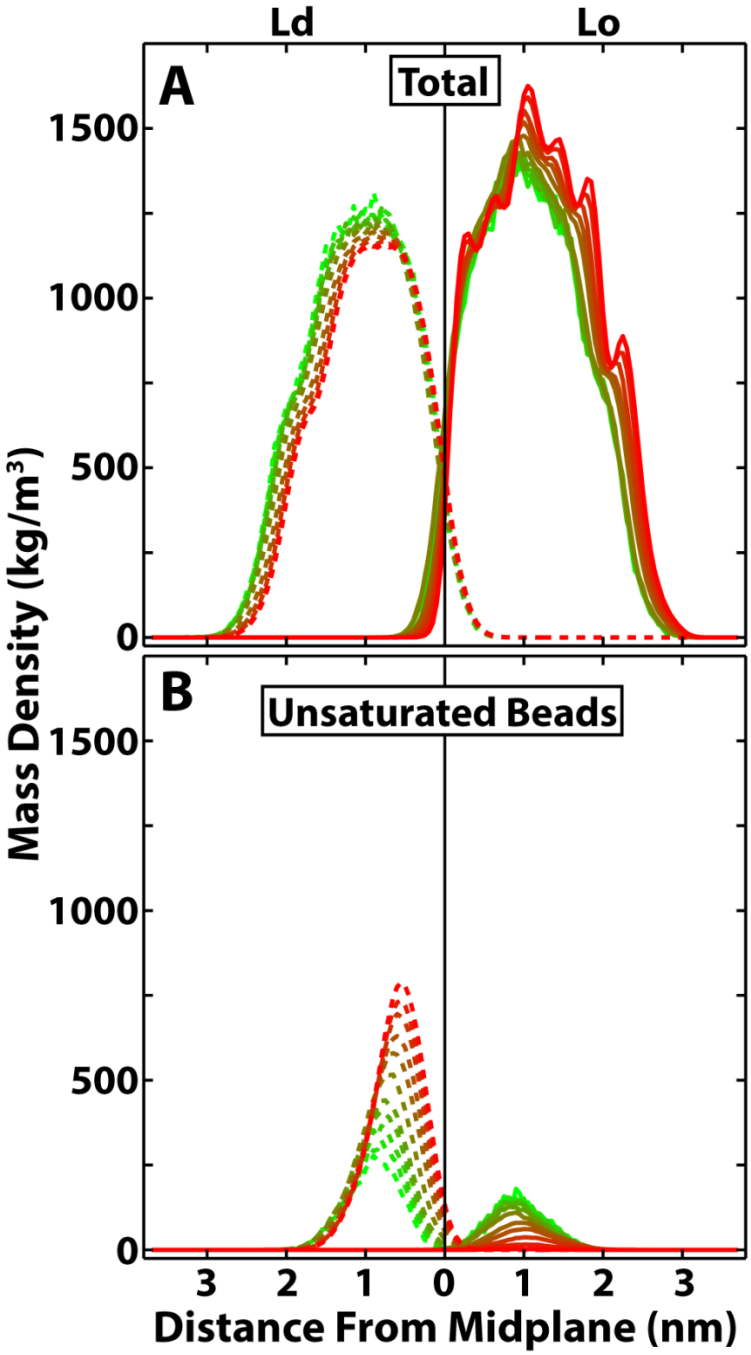

Figure B.15 Difference in CG mass densities for coexisting Lo and Ld phases increases with ρ. A) Total mass density profile of the Ld phase (left, dashed) and the Lo phase (right, solid). As ρ increases, the decreasing (increasing) width of the profiles for the Ld (Lo) phases indicates that monolayer thickness mismatch also increases. B) Mass density of unsaturated beads near the bilayer center increases in the Ld phase (left, dashed), and decreases in the Lo phase (right, solid), as ρ increases. All results shown are from ρ = 0 (green) to ρ = 1 (red) and only for lipids farther than or equal to 2 nm from the phase interface.

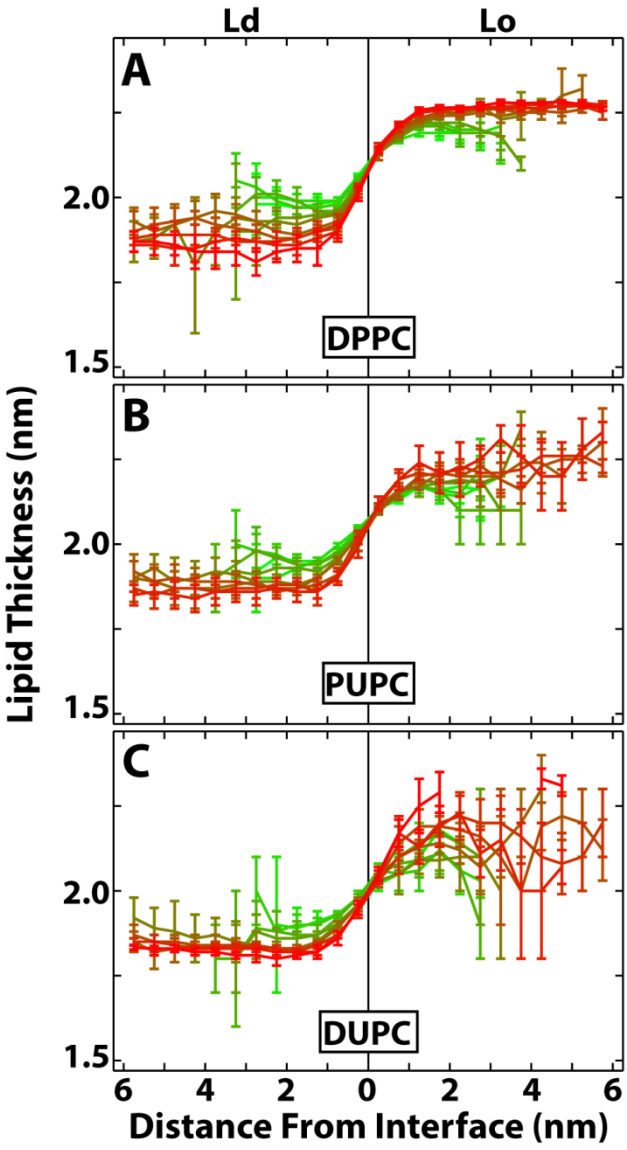

Figure B.16 UA lipid thickness mismatch increases with ρ. Lipid thickness is defined as the largest distance between the headgroup phosphorus atom and any other atom in the lipid, measured along the bilayer normal, with positive distances being those with the phosphorus atom further from the bilayer center than the other atom (and vice versa). Results shown for A) DPPC, B) PUPC and C) DUPC from ρ = 0 (green) to ρ = 1 (red).

REFERENCES

1. Wassenaar, T.A., K. Pluhackova, R.A. Böckmann, S.J. Marrink, and D.P. Tieleman. 2013. Going Backward : A Flexible Geometric Approach to Reverse Transformation from Coarse Grained to Atomistic Models. J. Chem. Theory Comput. 10: 676–690.

2. Hakobyan, D., and A. Heuer. 2013. Phase separation in a lipid/cholesterol system: comparison of coarse-grained and united-atom simulations. J. Phys. Chem. B. 117: 3841–51.

3. Schäfer, L. V, D.H. de Jong, A. Holt, A.J. Rzepiela, A.H. de Vries, B. Poolman, J.A. Killian, and S.J. Marrink. 2011. Lipid packing drives the segregation of transmembrane helices into disordered lipid domains in model membranes. Proc. Natl. Acad. Sci. U.S.A. 108: 1343–8.

4. Khelashvili, G., B. Kollmitzer, P. Heftberger, G. Pabst, and D. Harries. 2013. Calculating the Bending Modulus for Multicomponent Lipid Membranes in Different Thermodynamic Phases. J. Chem. Theory Comput. 9: 3866–3871.

APPENDIX C
Supporting information for Chapter 4

C.1 Equilibration and correlation

Equilibration of box areas, interface length and overlap fraction occurs during the first 5 μs of the simulations (Figure C.1). For the shorter simulations, we therefore use the final 5 μs (5-10 μs) for analysis. For the longer simulations, we allow for a prolonged period of equilibration (15 μs) and use the final 10 μs (15-25 μs) for analysis.

The parameters of interest become sufficiently uncorrelated over a timescale of 250 ns (Figure C.2). Thus we split the simulations into 250 ns chunks for the purposes of error calculations.

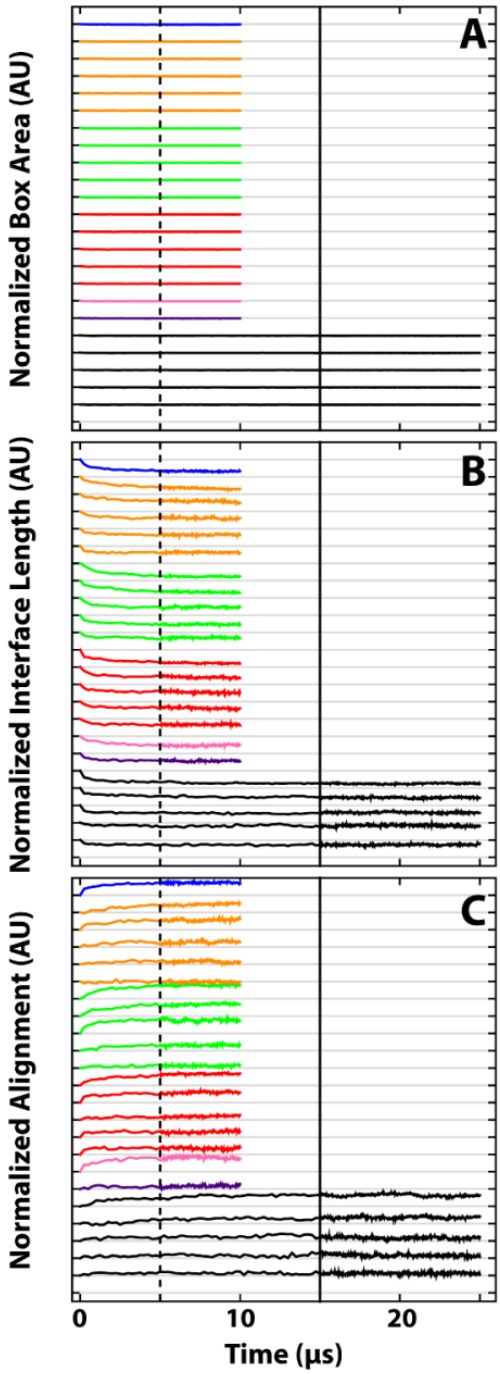

Figure C.1 Equilibration occurs within 5 μs. A) Box area, B) interface length and C) alignment fraction normalized by their values at 0 μs, with each subsequent dataset shifted vertically by 1 for clarity. Results colored as follows: peptide-free (black), 2 mol% WALP-17 (red), 2 mol% WALP-23 (green), 2 mol% WALP-29 (orange), 0.5 mol% WALP-23 (purple), 1 mol% WALP-23 (pink) and 4 mol% WALP-23 (blue). All values become sufficiently equilibrated by 5 μs (dashed black line). For the peptide-containing bilayers, which were run for 10 μs, only the last 5 μs were used for analysis. The peptide-free bilayers were run for 25 μs (as described in Chapter 4), and so we allowed for further equilibration up to 15 μs (solid black line) before data was collected for analysis.

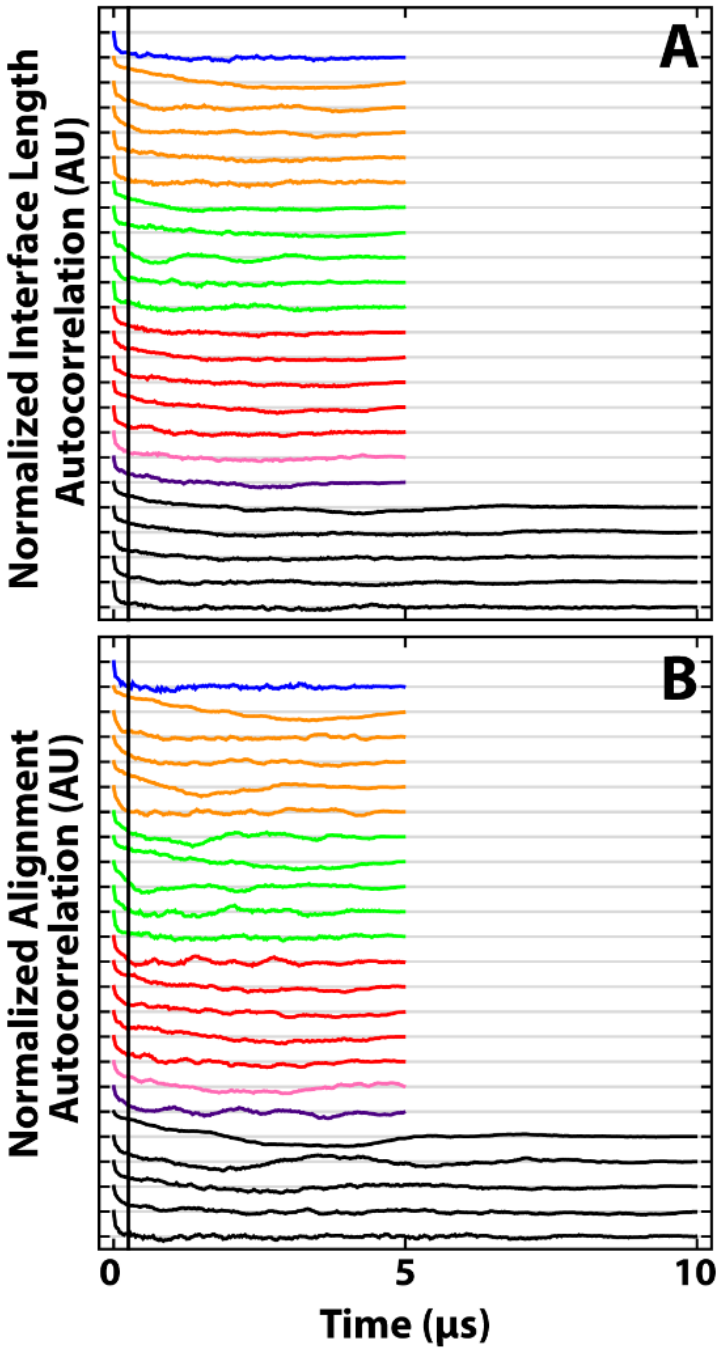

Figure C.2 Correlation times are generally less than 250 ns. Autocorrelations of A) interface length and B) overlap fraction for the range of data being analyzed (see Figure C.1), with each subsequent dataset shifted vertically by 1 for clarity. Results colored as follows: peptide-free (black), 2 mol% WALP-17 (red), 2 mol% WALP-23 (green), 2 mol% WALP-29 (orange), 0.5 mol% WALP-23 (purple), 1 mol% WALP-23 (pink) and 4 mol% WALP-23 (blue). Data become sufficiently uncorrelated by 250 ns (black line) and so we split the data into 250 ns subsets, considered independent for the purposes of error estimation.

C.2 Preliminary asymmetry results

We have begun to test the ability of WALPs to induce phase separation in more biologically relevant asymmetric bilayers. We simulated asymmetric bilayers with a top leaflet at $\rho = 1$ which strongly phase separates, and a bottom leaflet at $\rho = 0.4$ which weakly phase separates. Two simulations were performed, one lipid-only mixture and one with 2 mol% WALP-23. Preliminary results indicate that the presence of WALPs is able to drive larger-scale domain formation in both leaflets, and increased alignment between the leaflets. In particular, we found that the $\rho = 0.4$ leaflet had a normalized interface length of 18.2 ± 0.2 without peptide and 15.4 ± 0.2 with peptide: a decrease of ~ 15%. The $\rho = 1$ leaflet normalized interface length decreased by ~ 18%, from 6.10 ± 0.08 without peptide to 5.03 ± 0.08 with peptide. The normalized alignment fraction increased by ~ 14% in the presence of peptide, going from 0.661 ± 0.008 without peptide to 0.755 ± 0.004 with peptide. Since cholesterol redistributed itself significantly between the leaflets, more controls need to be run to determine whether the measured changes are due to intraleaflet or interleaflet effects of WALP addition.